SYNTHESIS AND CHARACTERIZATION OF CORRELATED ELECTRON MATERIALS BY NOVEL SOFT-CHEMISTRY TOPOTACTIC TECHNIQUES

By

Colin K. Blakely

A DISSERTATION

Submitted to
Michigan State University
In partial fulfillment of the requirements
for the degree of

Chemistry – Doctor of Philosophy

2014

ABSTRACT

SYNTHESIS AND CHARACTERIZATION OF CORRELATED ELECTRON MATERIALS BY NOVEL SOFT-CHEMISTRY TOPOTACTIC TECHNIQUES

By

Colin K. Blakely

A series of soft-chemistry, topotactic, multistep synthesis methods were developed to synthesize a variety of metastable functional materials. Throughout the thesis, a focus is placed on how crystal structure, bonding, and atomic interactions play a role on determining function or properties of the material. Materials synthesized were fully characterized, including Rietveld refinement (with high-resolution diffraction data were available), stoichiometry characterization by ICP and titration, thermal stability, and decomposition products. Properties investigation was completed where applicable, including electrochemical cycling of Li-ion cathode material candidates and magnetic properties characterization for frustrated magnetic systems with competing coupling pathways.

The first method presented – solvothermal reduction – was used for the exploratory synthesis of materials with NiO_2 square planar units in an extended lattice. As phases with square planar CuO_2 units garnered much attention in the 1990s as high-temperature superconductors, NiO_2 analogs may exhibit similar properties. Synthesis of the infinite-layer compound $La_4Ni_3O_8$ was used as the test case for the solvothermal reduction method. A full discussion on reaction variables as well as reactions routes is presented.

A family of fluorinated materials is also presented, prepared using multistep fluorination methods. The oxyfluoride $SrFeO_2F$ was prepared via the infinite-layer intermediate $SrFeO_2$, the first phase with FeO_2 square planar units in an extended lattice. An investigation of the effects of experimental conditions on local coordination is presented for this material. The multistep fluorination of $La_4Ni_3O_8$ is also presented, where two different fluorinated phases were prepared – $La_4Ni_3O_8F_1$ and $La_4Ni_3O_8F_2$. The complex and anisotropic structure of these phases is discussed, including the interesting T to T' transformation. Lastly, a solvothermal fluorination method is developed and demonstrated in the synthesis of $Sr_2Co_2O_5F$. The effect of the low-temperature synthesis on product purity is discussed as well as the importance of experimental conditions.

The third technique described in this thesis is the multistep reductive exchange (MURE) method for the synthesis of novel layered materials with spin frustrated Cd-I_2 type layers. A series of materials with different transition metals is presented, focusing on the topotactic nature of the reactions. The synthesis of a group of $Co^{2+/3+}$ phases allowed for the further exploration of the low temperature magnetic phase diagram for $Co^{2.5+}/Co^{4+}$ in layered phases with Cd-I_2 type layers. Thermal stability, electrochemistry, and reaction kinetics were also investigated.

Lastly, the Whole Powder Pattern Modeling algorithms are described and shown to be a powerful tool for nanoparticle analysis. Particle size and strain values were extracted from powder patterns of nanoparticles with high accuracy.

Copyright by
COLIN K. BLAKELY
2014

This dissertation is dedicated to my family and friends who helped make this happen.

ACKNOWLEDGEMENTS

I would like to expressly acknowledge my advisor, Prof. Viktor Poltavets, for his advice and attention to details as well as my coworker Dr. Shaun Bruno for the stimulating conversation during my graduate tenure. I would also like to thank my committee members for their guidance, including Prof. Thomas J. Pinnavaia, Prof. Tom Hamann, Prof. Tim Hogan, and Prof. Greg Baker.

TABLE OF CONTENTS

LIST OF TABLES x

LIST OF FIGURES xiv

Chapter 1. Introduction to soft chemistry and experimental methods 1
1.1 Introduction to solid state and soft chemistry methods 1
1.2 Contents of dissertation 3
1.3 General experimental methods and characterization 11
1.3a Powder diffraction theory and instrumentation 11
1.3b In-house powder diffraction 14
1.3c Synchrotron diffraction at Argonne National Lab 15
1.3d Diffraction data workup software 16
1.3e Thermogravimetric analysis 16
1.3f ICP optical emission spectroscopy 18
1.3g Electrochemical characterization 19
REFERENCES 23

Chapter 2. Low-temperature solvothermal reduction method 30
2.1 Introduction 30
2.2 Description of the novel solvothermal method 33
2.2a Experimental methods for the test case of $La_4Ni_3O_{10}$ 33
2.2b Results of the reduction of $La_4Ni_3O_{10}$ 36
2.2c Discussion on the role of pressure in the reaction 45
2.3 $LaNiO_2$ – square planar Ni^{1+} 47
2.3a Literature background of $LaNiO_2$ 47
2.3b Reaction pathways for the formation of $LaNiO_2$ 50
2.3c Synthesis and characterization of $LaNiO_2$ 52
2.3d Reinvestigating the magnetic properties of $LaNiO_2$ 60
2.3e Comparison of solid-solid and solid-gas mechanisms 66
2.3f DFT study on $LaNiO_2$ and $CaCuO_2$ similarities 71
2.4 Reduction of $EuNiO_3$ 74
2.4a Solvothermal synthesis of $EuNiO_3$ 74

2.4b Discussion on the reduction of $EuNiO_3$ 78
2.5 Chapter conclusions..... 84
2.6 Future work on this topic 85
REFERENCES 86

Chapter 3. Soft chemistry synthesis of extended oxyfluoride materials 92
3.1 Survey of synthesis methods of inorganic oxyfluorides 92
3.2 Novel multistep oxyfluoride synthesis procedure 94
3.2a Multistep synthetic route and experimental methods .. 94
3.2b Synthesis and characterization of $SrFeO_2F$ 98
3.2c Full magnetic properties investigation 105
3.2d Local coordination control using ^{57}Fe Mössbauer 108
3.2e DFT structure optimization of ordered $SrFeO_2F$ 113
3.2f Concluding remarks for $SrFeO_2F$ 116
3.3 Synthesis of complex oxyfluorides $La_4Ni_3O_8F_x$ (x = 1,2) 117
3.3a Solid state synthesis using XeF_2 118
3.3b Structural characterization of $La_4Ni_3O_8F_x$ (x = 1,2) 121
3.3c Discussion on the T to T' transformation 129
3.3d Concluding remarks for $La_4Ni_3O_8F_x$ (x = 1,2) 130
3.4 Novel solvothermal synthesis of complex oxyfluorides 131
3.4a Description of the solvothermal fluorination method .. 132
3.4b Proof-of-principle: synthesis of $Sr_2Co_2O_5F$ 134
3.4c Exploring the importance of experimental conditions 137
3.5 Chapter conclusions..... 147
3.6 Future work on this topic 148
REFERENCES 149

Chapter 4. MuRE – A multistep topotactic synthetic method 158
4.1 Literature background on α-$NaFeO_2$ type phases 158
4.1a Review of $NaFeO_2$ type and similar structures 163
4.1b Dependence of oxidation state on properties 174
4.2 The multistep reductive exchange (MuRE) method 186
4.3 $Fe^{2.5+}$ phases prepared with the MuRE method 192
4.3a $Ca_{0.50}FeO_2$ characterization and intercalation 194
4.3b Magnetic measurements of $Fe^{2.5+}$ phases..... 212
4.3c Electrochemical cycling of $Li_{0.50}Ca_{0.50}FeO_2$ 216

4.4 $Co^{2+/3+}$ phases prepared with the MuRE method 221
4.4a Structure characterization of $A_xCa_yCoO_2$ phases 221
4.4b Thermal analysis and stability investigation 233
4.4c Magnetic properties - completing the phase diagram 238
4.4d Electrochemical cycling of layered cobaltates 243
4.4e Intercalation kinetics exploration 248
4.5 Possibility of lower oxidation states with extended MuRE ... 251
4.6 Chapter conclusions 253
4.7 Future work on this topic 254
REFERENCES 256

Chapter 5. Particle size analysis using Whole Powder Pattern Modeling ... 266
5.1 Introduction to particle size analysis 266
5.2 Effects of milling and annealing on stannate nanoparticles . 269
5.2a Experimental methods and WPPM input 271
5.2b Effect of impact milling on particle size and strain 275
5.2c Direct control over size and strain with annealing 279
5.2d Concluding remarks and observations 281
5.3 Using WPPM to characterize synthesized nanoparticles 284
5.3a Direct synthesis of stannate nanoparticles 284
5.3b Microscopy investigation of particle size 287
5.3c Particle size distributions of stannate nanoparticles .. 289
5.4 Efficacy of WPPM on lower symmetry oxides 291
5.4a Introduction to delafossite type $CuAlO_2$ 291
5.4b Synthesis of nanoparticle $CuAlO_2$ 294
5.4c Particle size distribution of $CuAlO_2$ nanoparticles 294
5.5 Chapter conclusions 296
REFERENCES 297

LIST OF TABLES

Table 2-1. Vapor pressure, enthalpy of vaporization, and calculated pressures at given temperatures for solvents used in solvothermal reduction reactions. Chemical data obtained from the 2013 CRC handbook online. 36

Table 2-2. Products of $La_4Ni_3O_{10}$ reduction by different techniques. Autogenous pressures were calculated using either the Clausius-Clapeyron equation or the van der Waals equation depending on the critical point temperature of the solvent. 40

Table 2-3. Products of the solvothermal reaction of $LaNiO_3$ with NaH at 150 °C. Calculated autogenous internal pressure was approximately 10 atm..... 56

Table 2-4. Products of the solvothermal reaction of $LaNiO_3$ with NaH at 200 °C. Calculated autogenous internal pressure was approximately 60 atm..... 56

Table 2-5. Cell parameter comparison for $LaNiO_2$. Three literature reported cell parameter values as well as the cell parameters refined in this thesis are presented 60

Table 2-6. Bragg reflections of $LaNiO_2$ and selected reflections of $La_2Ni_2O_5$ that appear at similar d spacing, thereby complicating the multiphase refinement 63

Table 3-1. Unit cell parameters for $SrFeO_{3-x}$, $SrFeO_2$, and $SrFeO_2F$. Previously reported literature cell parameters for $SrFeO_2F$: $Pm\bar{3}m$, a = 3.956 Å (*6*, *7*). 103

Table 3-2. Atomic positions obtained from the Reitveld refinement of synchrotron diffraction data for $SrFeO_2F$ with refined occupancies..... 105

Table 3-3. $SrFeO_2F$ Mössbauer spectrum fit parameters obtained using the Fit:o) software package (*35*). 110

Table 3-4. Atomic parameters of $La_4Ni_3O_8F_1$ from Rietveld refinement of synchrotron powder diffraction data in the space group I4/mmm with *a* = 3.931(8) Å and *c* = 27.66(1) Å 123

Table 3-5. Refined cell parameters of the $La_4Ni_3O_xF_y$ family of compounds prepared. Cell parameters obtained for $La_4Ni_3O_8F_2$ via LeBail refinement of synchrotron data 128

Table 3-6. Structure parameters of $Sr_2Co_2O_5F$ based on Rietveld refinement of powder diffraction data in the space group $Pm\bar{3}m$ with *a* = 3.8549(1) Å 136

Table 3-7. Percent formation of $Sr_2Co_2O_5F$ via the fluorination of $Sr_2Co_2O_5$ over time using four different methods. The total percent of unreacted $Sr_2Co_2O_5$ is the difference between the listed value below and 100 140

Table 4-1. Summary of structure types, space groups, cation coordination, and the Co oxidation state in the three layer and two layer families of the Na_xCoO_2 system 177

Table 4-2. Unit cell parameters of sodium parent phases and calcium exchange phases discussed in this chapter (53, 57). Notice the topotactic nature of the aliovalent exchange preserves the structural type between sodium and calcium phases. 183

Table 4-3. Cell parameters of $Ca_{0.50}FeO_2$ obtained from the LeBail refinement of powder x-ray and neutron diffraction data at different temperatures (61). Full Rietveld refinement was undertaken as well. 196

Table 4-4. Refined atomic positions for $Ca_{0.50}FeO_2$ obtained by Rietveld refinement of NPD data. 198

Table 4-5. Observed and calculated Bragg reflections for $Ca_{0.50}FeO_2$ in the C2/m space group as proof of correct indexing. Indexing of the PXD data was done using the TOPAS software package. 199

Table 4-6. Values for profile fitting parameters used in the Rietveld refinement of $Ca_{0.50}FeO_2$ NPD data collected at both 75 K and 12 K 203

Table 4-7. A comparison of the nuclear and incommensurate magnetic cell parameters of $Ca_{0.50}FeO_2$ obtained from refinement of NPD data 205

Table 4-8. Atomic positions for $Na_{0.50}Ca_{0.50}FeO_2$ from Rietveld refinement of PXD data 209

Table 4-9. Atomic positions for $Li_{0.50}Ca_{0.50}FeO_2$ from Rietveld refinement of PXD data 209

Table 4-10. Unit cell parameters for $Ca_{0.50}FeO_2$ and the intercalated compounds demonstrating the symmetry preservation throughout the MuRE reactions 211

Table 4-11. FeO_6 interplanar distances comparison for the Fe series of compounds synthesized with the MuRE method 211

Table 4-12. Rietveld refined atomic positions for $Li_{0.75}Ca_{0.25}CoO_2$ from PXD data 223

Table 4-13. Cell parameters of the materials with transition metals in the 2+/3+ oxidation state couple prepared with the MuRE method next to the cation coordination type and Co oxidation state 227

Table 4-14. CoO_6 interplanar spacings for all Co-containing layer phases prepared with the MuRE method 229

Table 4-15. Particle size distributions obtained using the WPPM algorithms implemented in the PM2K software suite. PM2K results gave the shortest length (height of platelet) for platelet type particles ... 231

Table 4-16. Electrochemical properties of common Li-ion cathode materials compared to the novel cobaltates presented in this thesis 244

Table 4-17. Compound stoichiometry over intercalation time for the preparation of the reduced phases presented in the manuscript. Bolded numbers are stopping points for the preparation each compound 250

Table 5-1. Particle sizes and crystallite strain values calculated using the PM2K software for $BaSnO_3$ and $SrSnO_3$ samples milled for different time periods 278

Table 5-2. Particle sizes and crystallite strain values calculated using the PM2K software for $BaSnO_3$ and $SrSnO_3$ samples thermally treated for 24 hours at varied temperatures..... 282

LIST OF FIGURES

Figure 1-1. Structural transformation from the perovskite $SrFeO_3$ to the infinite layer $SrFeO_2$ via reduction with CaH_2 (*50*). The colored balls represent the following atoms: blue - Fe, red - O, grey - Sr..... 4

Figure 1-2. Results of topotactic and non-topotactic chemistry performed on a pristine Jenga game, illustrating the power and tunability of topotactic techniques..... 5

Figure 1-3. α-$NaFeO_2$ type crystal structure, the parent of the phases presented in Chapter 4 and synthesized using the MuRE method. The structure consists of alternating layers of edge shared FeO_6 and NaO_6 octahedra (teal and blue polyhedra, respectively). 9

Figure 1-4. Actual coin cell setup using for all electrochemical measurements performed and described in this thesis. These split cells were purchased from MTI-XTL 22

Figure 2-1. Structure models of $La_4Ni_3O_{10}$ (left) and $La_4Ni_3O_8$ (right) with denoted layers and structural blocks: P, perovskite; RS, rock salt; IL, infinite layer; F, fluorite. Yellow, cyan, and red balls represent La, Ni, and O atoms, respectively 38

Figure 2-2. Phase composition versus reaction time during the reduction of $La_4Ni_3O_{10}$ with NaH at 200 °C: (a) solid state reaction, (b) solvothermal conditions. $La_4Ni_3O_{10}$, black squares; $La_4Ni_3O_9$, red circles; $La_4Ni_3O_8$, blue triangles. Relative phase content is normalized to 100% total..... 41

Figure 2-3. Representative PXD patterns for the reduction products prepared by different experimental methods. $La_4Ni_3O_9$, red circles; $La_4Ni_3O_8$, blue triangles..... 44

Figure 2-4. Refinement of PXD data for $La_4Ni_3O_8$ using the TOPAS software suite. The sample was prepared via the solvothermal reduction route. 45

Figure 2-5. d orbital manifold diagram of the crystal field splitting for a transition metal in square planar configuration..... 48

Figure 2-6. Powder X-ray diffraction patterns of products obtained by the reaction between $LaNiO_3$ and CaH_2 at various reaction temperatures using Cu $K_{\alpha 1}$ radiation. Reproduced with permission from (31). 51

Figure 2-7. Crystal structures of a) $LaNiO_3$ and b) $LaNiO_2$. Grey spheres represent La^{3+}, teal spheres represent Ni^{3+} ($LaNiO_3$) or Ni^{1+} ($LaNiO_2$), and red spheres are O^{2-} 53

Figure 2-8. PXD pattern of the perovskite $LaNiO_3$ after Pechini synthesis and thermal treatment for 240 hours at 850 °C under an O_2 atmosphere. Diffraction pattern was taken on a D2 Phaser. ... 54

Figure 2-9. PXD pattern of the perovskite $LaNiO_3$ and the reduced infinite-layer type phase $LaNiO_2$ synthesized via the solvothermal reduction method at 200 °C for 10 days. 58

Figure 2-10. Rietveld refinement of $LaNiO_2$ obtained from the solvothermal reduction of $LaNiO_3$ at 200 °C for 10 days using NaH. Phase analysis lead to a $LaNiO_2$:$La_2Ni_2O_5$:Ni (metal) product ratio of 500:12.35:1 61

Figure 2-11. Susceptibility (closed circles) and inverse susceptibility (open circles) data collected on a sample of $LaNiO_2$ under a 1000 Oe field using a SQUID magnetometer. 64

Figure 2-12. Effective magnetic moment of $LaNiO_2$ across the temperature range studied. A horizontal line was drawn in blue at 1.73 μ_B – the effective magnetic moment of an S = ½ ion (Ni^{1+}). 65

Figure 2-13. Literature fitted molar paramagnetic susceptibility of $LaNiO_2$ from the Hayward group. Adapted with permission from (9). Copyright 2013 American Chemical Society..... 66

Figure 2-14. TGA/DSC data for the reduction of $LaNiO_3$ under a 40:20 H_2:N_2 atmosphere from 25 – 1000 °C. The sample holder was loaded under N_2. 69

Figure 2-15. TGA/DSC data for the calorimetry experiment of $LaNiO_3$ under a N_2 atmosphere from 25 – 1000 °C. The sample holder was loaded under N_2. 70

Figure 2-16. Comparison of calculated LDA projected paramagnetic DOS $LaNiO_2$ (upper panel) and $CaCuO_2$ (lower panel) using DFT.

Reproduced with permission from (*37*). Copyright 2012 by The American Physical Society. 74

Figure 2-17. Crystal structure of the perovskite $EuNiO_3$ (*Pbnm*, *a* = 5.2984(3) Å, *b* = 5.4572(2) Å, *c* = 7.5365(3) Å) obtained via solvothermal synthesis. 77

Figure 2-18. TGA data for $EuNiO_3$ recorded under different atmospheres. . 80

Figure 2-19. PXD spectra after decomposition of $EuNiO_3$ at 950 °C in O_2, N_2, and H_2. Tickmarks refer to cubic Eu_2O_3 (wine, top), Ni metal (olive, middle), and Ni (navy, bottom). All other reflections were indexed as monoclinic Eu_2O_3. 82

Figure 3-1. Multistep synthetic route for the preparation of the $SrFeO_2F$ oxyfluoride. The previously known literature method using PVDF at 400 °C is also highlighted (6). 95

Figure 3-2. Comparison of PXD patterns of the $SrFeO_{3-x}$ perovskite (bottom pattern), the $SrFeO_2$ infinite-layer compound (middle), and the $SrFeO_2F$ oxyfluoride (top). 97

Figure 3-3. Rietveld refinement of the synchrotron powder x-ray diffraction data of $SrFeO_2F$ showing the observed pattern (black crosses), fitted pattern (red trace), difference curve (gray trace, below), and Bragg peak positions (magenta tickmarks, below) 101

Figure 3-4. Thermogravimetric analysis of the fluorinated product $SrFeO_2F$ under an O_2 and N_2 atmospheres. Positive slope in the DSC curve represents endothermic signals, while negative slope represents exothermic signals..... 106

Figure 3-5. DC magnetization at H = 1000 Oe (a), DC field dependence (b), AC magnetic susceptibility (c, d) and specific heat measurement (a) results for $SrFeO_2F$ collected on a Quantum Design PPMS system..... 109

Figure 3-6. Fit (black line) of room temperature ^{57}Fe Mössbauer spectrum of $SrFeO_2F$ with denoted contributions from Fe sites: Fe1 (blue line), Fe2 (red line), Fe3 (green line)..... 110

Figure 3-7. Left: Potential energy surface of varied a/c structures. The minimum position of the surface is highlighted by the white circle. Right: Contour plot zoomed in around the minimum energy

extracted from the potential surface shown on the left. The dark blue area represents the minimum energy 114

Figure 3-8. Topotactic transformation of $La_4Ni_3O_8$ to $La_4Ni_3O_8F_2$. The structure shown for $La_4Ni_3O_8F_2$ depicts O/F ordering. Colored balls represent the following atoms: yellow – La, red – O, teal – Ni, green – F 119

Figure 3-9. Rietveld refinement profile for the synchrotron powder X-ray diffraction data of $La_4Ni_3O_8F_1$. Observed intensities (crosses), calculated pattern (solid line), and difference curve (bottom solid line). Tickmarks represent the following phases: $La_4Ni_3O_8F_1$ – magenta (top), $La_4Ni_3O_8F_2$ – green (middle), $La_4Ni_3O_8$ – blue (bottom) 122

Figure 3-10. Electron diffraction patterns of $La_4Ni_3O_8F_2$ (left column) and $La_4Ni_3O_8F_1$ (right column) 125

Figure 3-11. Rietveld refinement of the NPD data of $La_4Ni_3O_8F_1$. Observed intensities (crosses), calculated pattern (solid line), and difference curve (bottom solid line). Tickmarks represent the following phases: $La_4Ni_3O_8F_1$ – magenta (top), $La_4Ni_3O_8F_2$ – green (middle), $La_4Ni_3O_8$ – blue (bottom) 126

Figure 3-12. X-ray absorption spectra for $La_4Ni_3O_{10}$, $La_4Ni_3O_8$, $La_4Ni_3O_8F_1$, $La_4Ni_3O_8F_2$ as well as applicable standards 129

Figure 3-13. Comparison of the two known methods for the preparation of the oxyfluoride $Sr_2Co_2O_5F$. Colored balls represent the following atoms: blue – Co, red – O, white – Sr, green – F, and purple – O/F disorder 133

Figure 3-14. Observed (green trace), calculated (crosses), and difference (grey trace, below) XRD profiles obtained from Rietveld refinement of PXD data for $Sr_2Co_2O_5F$ made at 100 °C. Magenta tickmarks denote Bragg reflections. 135

Figure 3-15. DC magnetic susceptibility measurements of $Sr_2Co_2O_5F$. Insets show the field and temperature dependence on magnetization in terms of magnetic moment per Co. Data collected on a Quantum Design PPMS system..... 137

Figure 3-16. Fluorination rates over time for the fluorination of $Sr_2Co_2O_5$ using XeF_2 as a fluorine source under different experimental conditions. The blue lines show the % of $Sr_2Co_2O_5F$ at any given time 139

Figure 3-17. Possible bonding interaction between XeF_2 and two adjacent CoO_4 tetrahedra in the brownmillerite structure $Sr_2Co_2O_5$. A full description is presented in the text. Bond lengths were obtained from the literature (*20*, *28*, *66*, *74*, *75*) 142

Figure 4-1. Different structure variations found in the α-$NaFeO_2$ system based on the coordination of the alkali metal – O for octahedral and P for trigonal prismatic. A further description of the naming convention is given in the text 158

Figure 4-2. Rouxel type plot of bond ionicities vs. alkali metal/alkaline earth metal. Dotted line separates P type (left side) from O type phases. Bond ionicities were calculated using the Pauling method (Equation 4-1) (4) 162

Figure 4-3. Graph of the figure-of-merit Z values for the in Na_xCoO_2 series of layered cobaltates. Used with permission from (52)..... 176

Figure 4-4. Magnetic susceptibility (x) of $Na_xCoO_2 \cdot yH_2O$. Filled circles, zero-field cooling; open circles, field cooling. The susceptibility was measured in a magnetic field of 20 Oe. The inset shows x measured under various magnetic fields by the zero-field cooling process. Reused without adaptation from (56)..... 181

Figure 4-5. Schematic of the general four step MuRE method. In the chemical formulae, M represents any 3d transition metal. Colored spheres represent the following atoms: grey – Na^{1+}, teal – M^{x+}, blue – Ca^{2+}, yellow – Na^{1+}/Li^{1+}. MO_6 octahedra are shown in teal for clarity. 185

Figure 4-6. Rietveld refinement PXD data for α-$NaFeO_2$ performed using the GSAS software package. Peak anisotropy from preferred orientation is shown in the difference plot (grey line). 193

Figure 4-7. PXD spectra of the Fe based family of materials prepared using the MuRE method presented in this chapter. The background (broad hump, peak near 16 °2θ) in $Na_{0.50}Ca_{0.50}FeO_2$ was due to the dome-type sample holder used during collection. 195

Figure 4-8. Rietveld refinement of the PXD data of $Ca_{0.50}FeO_2$ showing the observed pattern (black crosses), refined fit (red trace), difference curve (grey below), and Bragg diffraction positions (magenta tickmarks, below) 197

Figure 4-9. Rietveld refinement of NPD of $Ca_{0.50}FeO_2$ collected at 75 K at Oak Ridge National Laboratory SPS showing the observed pattern (black crosses), fit pattern (red trace), difference curve (grey line, below), and Bragg peak positions (magenta tickmarks, below). The refined unit cell is present in the top right corner showing the topotactically preserved layered structure 202

Figure 4-10. Rietveld refinement of NPD of $Ca_{0.50}FeO_2$ collected at 12 K at Oak Ridge National Laboratory SPS showing the observed pattern (black crosses), fit pattern (red trace), difference curve (grey line, below), and Bragg peak positions (magenta tickmarks, below). The second line of magenta tickmarks represents the magnetic cell observed. The first few reflections of the magnetic cell are labeled 204

Figure 4-11. Refinement of PXD of $Na_{0.50}Ca_{0.50}FeO_2$. Contribution from the sample holder is the reason for the unindexed peaks/amorphous background 207

Figure 4-12. DC magnetic susceptibility data collected for $NaFeO_2$, $Ca_{0.50}FeO_2$, and $Na_{0.50}Ca_{0.50}FeO_2$ collected under a 1000 Oe field..... 212

Figure 4-13. Effective magnetic moment for $NaFeO_2$, $Ca_{0.50}FeO_2$, and $Na_{0.50}Ca_{0.50}FeO_2$ calculated from magnetic susceptibility data 213

Figure 4-14. Dependence of magnetization on applied field of $Na_{0.50}Ca_{0.50}FeO_2$ collected at 300 K and 5 K..... 215

Figure 4-15. Partially optimized charge-discharge curve of $Li_{0.50}Ca_{0.50}FeO_2$ cycled from 2.2 V to 3.8 V vs. a Li-metal anode 218

Figure 4-16. Secondary electron SEM of $Ca_{0.50}FeO_2$ prepared using the MuRE method 220

Figure 4-17. PXD spectra of the $Na_{0.50}CoO_2$ based family of materials prepared using the MuRE method presented in this chapter 222

Figure 4-18. PXD spectra of the $NaCoO_2$ based family of materials prepared using the MuRE method presented in this chapter 224

Figure 4-19. PXD spectra of the $Na_{0.37}CoO_2$ family of materials prepared using the MuRE method presented in this chapter 216

Figure 4-20. SEM image of $Na_{0.59}Ca_{0.37}CoO_2$ using back scattered electrons (top) and secondary electrons (bottom) showing the large anisotropy in crystal dimensions resulting in platelets. Clearly, the ridges on the larger particles are actually many different platelets 232

Figure 4-21. TGA and DSC curves of $Li_{0.75}Ca_{0.25}CoO_2$ under O_2 and N_2 atmospheres. Negative signals in the DSC are exothermic .. 233

Figure 4-22. DSC curves of the Na^{1+} intercalated products of Ca_xCoO_2 (x = 0.50, 0.37, 0.25) under an N_2 atmospheres. Negative signals in the DSC are exothermic 234

Figure 4-23. Magnified differential scanning calorimetry trace of $Na_{0.31}Ca_{0.50}CoO_2$ with the first derivative of the trace 236

Figure 4-24. Molar magnetic susceptibility of the Na^{1+} intercalated cobaltates synthesized with the MuRE method obtained under an applied field of 0.1 T 238

Figure 4-25. Magnetization dependence on field traces of the Na^{1+} intercalated cobaltates synthesized with the MuRE method obtained at 5 K 240

Figure 4-26. Low-temperature magnetic phase diagram of layered oxide phases with Co in different oxidation states 242

Figure 4-27. Charge-discharge curves of $Li_{0.47}Ca_{0.50}CoO_2$ showing two separate discharge events at 2.9 V and 3.2 V vs Li metal..... 245

Figure 4-28. Per-cycle capacity of $Li_{0.75}Ca_{0.25}CoO_2$ measured at a C/5 rate against a Li metal anode 247

Figure 4-29. A schematic diagram demonstrating the theoretical extendibility of the MuRE method to produce phases with transition metal oxidation states between 2+ and 2.5+ 251

Figure 5-1. Powder x-ray diffraction patterns of a) $BaSnO_3$ and b) $SrSnO_3$ as well as the corresponding calculated particle size distributions in c) and d), respectively 276

Figure 5-2. Williamson-Hall plots of a) $BaSnO_3$ and b) $SrSnO_3$ obtained using the WPPM methods. The particle strain can be extracted from the slope of the line using equation (5-5) 279

Figure 5-3. Williamson-Hall plots of $BaSnO_3$ and $SrSnO_3$ particles after thermal annealing for 24 hrs at various temperatures. The particle strain can be extracted from the slope of the line using equation (5-5)..... 280

Figure 5-4. The left 6 TEM micrograms represent $BaSnO_3$, while the right 6 vertical panels show $SrSnO_3$ particles. The labels a) - f) refer to milling times: a) none, b) 30 min, c) 1 hr, d) 2 hr, e) 4hr, and f) 8 hr..... 283

Figure 5-5. TEM (top, left) and HRTEM (top, right) micrographs of $BaSnO_3$ nanoparticles synthesized using procedure I and TEM (bottom, left) and HRTEM (bottom, right) micrographs of $BaSnO_3$ nanoparticles synthesized using procedure II. Both materials were fired at 650 °C for 60 hrs 286

Figure 5-6. (a) & (b) TEM and HRTEM micrographs of $SrSnO_3$ nanoparticles synthesized at 650 °C for 72 hr (obtained from procedure I), (c) & (b) TEM and HRTEM micrographs of $SrSnO_3$ nanoparticles..... 288

Figure 5-7. Particle size distributions of the prepared $BaSnO_3$ and $SrSnO_3$ nanoparticles obtained using the WPPM method..... 290

Figure 5-8. Transmission electron microscopy pictures of $CuAlO_2$ nanoparticles prepared at 775 °C under a controlled partial oxygen pressure atmosphere (a,b), 800 °C under ultrapure N_2 (c,d), and 950 °C under ultrapure N_2 (e,f)..... 293

Figure 5-9. Particle size distribution of $CuAlO_2$ nanoparticles prepared at 775 °C, 800 °C, and 950 °C. Distribution plots calculated using the PM2K software package. 295

Chapter 1: Introduction to soft chemistry and experimental methods

1.1 Introduction to solid state and soft chemistry methods

For over a hundred years, the solid state chemist has mixed simple metal or binary reagents and heated the mixture to a high enough temperature in hopes of preparing a thermodynamically stable phase. Unfortunately, many of the most interesting functional materials are kinetically stable rather than thermodynamically stable; therefore, they can only be prepared using much softer synthetic techniques. The soft-chemistry ideals borrow heavily from organic chemists, truly the masters of efficient atomic substitution and movement in a specific and planned fashion. Many very complex natural products have been published in the literature in just the past year (*1–12*). These materials were produced starting from simple, common materials, via a planned series of steps executed in a specific order, demonstrating the true dominance of organic chemistry techniques over atomic framework. Obviously, organic chemists have one very important advantage over the solid-state community - in general, organic molecules are easily accessed when suspended or dissolved in some type of solution. Solid state chemists are required to fight both the slow kinetics of solid-solid reactions as well as the inability to access specific atoms in a crystal lattice due to the extended nature of any crystal.

In an effort to prepare functional materials, solid state chemists began to assimilate synthetic techniques from other disciplines into the main stream solid state toolbox about two decades ago (*13*). Multiple very nice literature reviews

have covered the most common topotactic reactions: intercalation, ion-exchange, substitution, pillaring, layer construction, exfoliation, deintercalation, and grafting (*13*, *14*). Annual reports of soft-chemistry and topotactic chemistry in solid-state materials synthesis have skyrocketed in the past few years with many new groups joining the field led by the Kageyama, Cava, Wiley, Schaak, and Hayward research labs (*15*–*37*). High temperature analogs of many of the soft-chemistry techniques are known, especially ion-exchange and substitution; however, the low-temperature alternatives allow for much greater control over specific structural components (*38*, *39*).

The ideals of the soft-chemistry mantra run deep in this thesis - a majority of the chemistry presented employs topotactic methods to specifically modify structures in a planned fashion to synthesize phases with desired properties.

1.2 Contents of dissertation

This thesis is divided into five main sections: the first gives an introduction to general experimental methods used, the following three introduce and discuss novel synthetic techniques developed, and a fifth focuses on methods to extract particle information from powder x-ray diffraction patterns.

Chapter 2 presents a novel solvothermal reduction method to produce phases with transition metals in infinite-layer coordination environments. The infinite layer structure is represented in Figure 1-1, in which the primitive cell (P4/mmm) of ABX_2 is shown with A in cubical coordination and BX_2 shown as infinite square planar units. This structure was proposed by Buckman as essentially a thought experiment in a paper published in 2006, dubbing the structure "Kentuckia" (*40*); however, the high-temperature superconducting cuprates initially synthesized in 1988 all have infinite-layer CuO_2 sheets (*38*). Considering the superconducting nature of $CaCuO_2$ (T_c = 40 - 89 K), many different variations and dopings of this parent phase were investigated in attempts to synthesize a room temperature superconductor (*41–49*).

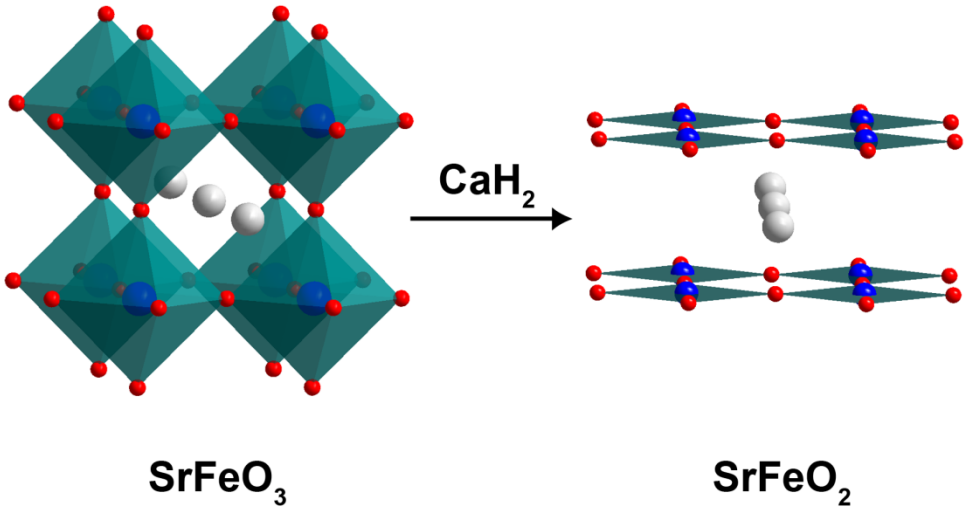

Figure 1-1. Structural transformation from the perovskite $SrFeO_3$ to the infinite layer $SrFeO_2$ via reduction with CaH_2 (*50*). The colored balls represent the following atoms: blue - Fe, red - O, grey - Sr.

More recently, infinite-layer compounds with transition metals other than Cu have been synthesized using low-temperature methods. The synthesis of $LaNiO_2$, with Ni^{1+} in square-planar geometry, has been attempted with mixed success multiple times in the literature over the past two decades (*29*, *51–53*). Due to the metastability of $LaNiO_2$ - and many other infinite layer materials where the transition metal is not Cu - topotactic methods are generally employed to directly control the final product. Topotactic reactions - reactions in which small modifications are made to the crystal lattice while the general structure is preserved - have grown in use in the recent solid state literature, showing a movement away from standard "heat-and-beat" approaches (*15*, *18*, *21*, *23 –25*,

60, *61*). The concept of topotactic chemistry is depicted in Figure 1-2, using an analogy to the common Jenga game.

Figure 1-2. Results of topotactic and non-topotactic chemistry performed on a pristine Jenga game, illustrating the power and tunability of topotactic techniques.

The novel solvothermal method presented in Chapter 2 is investigated using the literature reduction of $La_4Ni_3O_{10}$ as a test case. The roles of the different experimental variables including: solvent, reductant, reductant concentration, temperature, and autogeneous pressure are established. After establishing the method, the reduction of $LaNiO_3$ is attempted to produce the pure phase nickelate without the Ni and $La_2Ni_2O_5$ impurities seen in previous literature reports. A full

reaction pathway discussion on the formation of $LaNiO_2$ and an investigation into why certain impurities plague the synthesis is described. A magnetic properties comparison to previous data is also presented, confirming the higher purity sample prepared using the solvothermal reduction method presented. Lastly, a comparison of physical and chemical properties between $LaNiO_2$ and the superconducting cuprates is discussed.

The last section of Chapter 2 explores the synthesis of $EuNiO_2$, a theoretical compound with cuboidal Eu^{2+} and Ni^{2+} in square planar configuration. The difficult synthesis of $EuNiO_3$ is discussed, as are results from reduction attempts using the solvothermal method. Future directions of this project are presented as well, based on recent literature publications on isolated square planar units.

In Chapter 3, the common theme of topotactic, soft-chemistry reactions is applied to synthesizing novel oxyfluoride materials using simple, less hazardous reaction conditions. First, the synthesis of $SrFeO_2F$ via the infinite layer $SrFeO_2$ is presented using a multistep synthetic method. Full structural and magnetic investigation of $SrFeO_2F$ was performed with high-intensity radiation sources, AC and DC magnetic measurements, DFT calculations, and Mössbauer spectroscopy. A comparison between the properties of the previously synthesized $SrFeO_2F$ and the $SrFeO_2F$ synthesized herein is made with a clear conclusion that low-temperature, topotactic reactions give much more control over phase structure and configuration than the analogous higher temperature methods.

The multistep synthesis for the preparation of $La_4Ni_3O_8F_1$ and $La_4Ni_3O_8F_2$ is also presented in Chapter 3. Structural characterization using synchrotron and

neutron diffraction patterns were performed. An interesting discussion on structure and the possible structural transformations in these materials is included.

The last third of Chapter 3 describes and demonstrates the fluorinating power of the novel solvothermal fluorination method developed. The details behind how the method was established and why it allows for the preparation of complex oxyfluorides without byproducts are discussed. Furthermore, the relationship between fluorine-source concentration and experimental volume is thoroughly investigated to pinpoint the general reaction mechanism in the fluorination of the brownmillerite phase $Sr_2Co_2O_5$.

In Chapter 4, the third topotactic method developed is presented: multistep reductive exchange (MuRE). This method, compiled of four different steps that have been individually well-studied in the literature, is an extremely powerful tool in the preparation of layered phases with transition metals in lower oxidation states than previously reported. Because of the complexity of the system, an in-depth literature background is presented to familiarize the reader with both the rich literature, as well as the importance of this method as a synthetic tool in creating new, and, more importantly interesting phases. The parent structure of all of the phases synthesized is presented in Figure 1-3.

Following the introduction into the many nuances of the structure and synthetic procedures, experimental details of the MuRE synthetic method are presented. The procedure is then used to synthesize an array of phases with different transition metals in AMO_2 (A = Na, Li, Ca; M = Co, Fe) type layered structures, where M is in the 2+/3+ oxidation state couple. The topotactic nature of the

reactions is corroborated via multiple techniques including titration, inductively coupled plasma emission spectroscopy, powder x-ray diffraction, and neutron diffraction. Intercalation rates and possible intermediate phases are also presented. Thermal analysis was performed in efforts to determine if the phases were truly metastable, or if they could be directly prepared and were actually just low temperature (kinetic) phases.

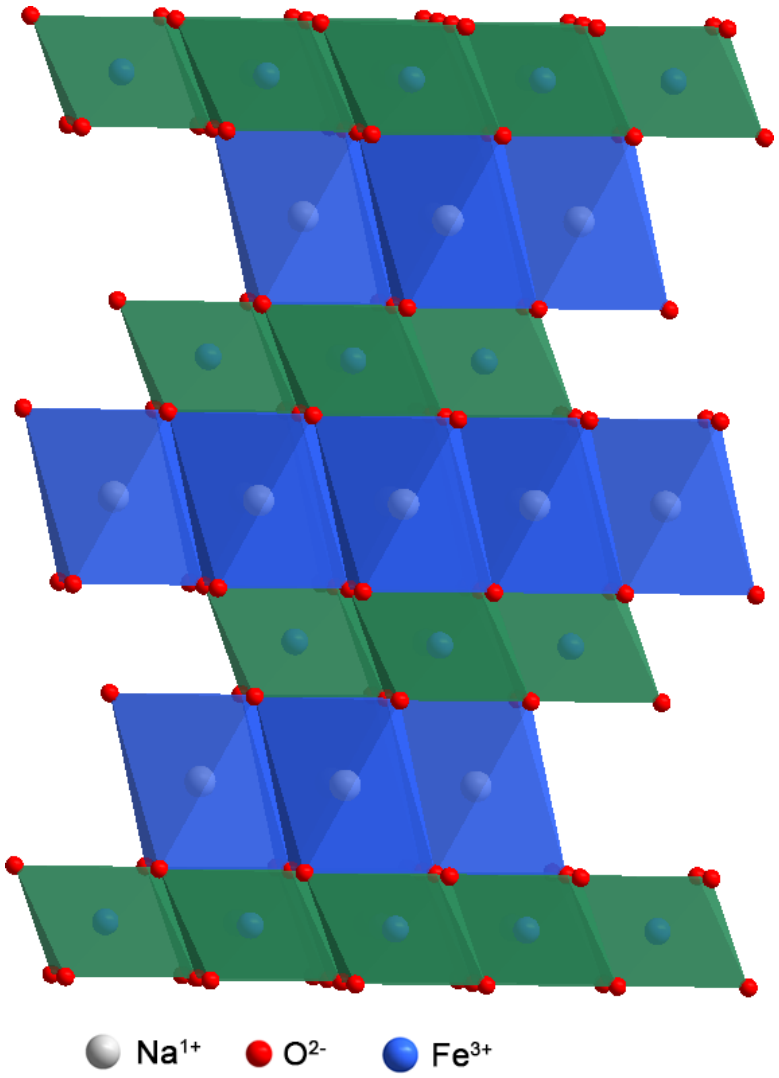

Figure 1-3. α-$NaFeO_2$ type crystal structure, the parent of the phases presented in Chapter 4 and synthesized using the MuRE method. The structure consists of alternating layers of edge shared FeO_6 and NaO_6 octahedra (green and blue polyhedra, respectively).

As the common theme of this thesis is investigating the relationship between structure and function, a range of properties were investigated for these materials, including electrochemical, magnetic, and thermoelectric. Phases containing Li^{1+}

were considered as candidates for Li-ion cycling cathode materials, while Na^{1+} phases underwent magnetic properties characterization and a small investigation into thermal conductivity. The chapter concludes with a discussion on the future direction of the MuRE project, as well as a proposal for reaching oxidation states below 2.5+ - the current lower bound of the 4 step MuRE technique.

In the fifth and final chapter, a technical powder diffraction modeling method called Whole Powder Pattern Modeling (WPPM) is described (*56*). The method and implementation of WPPM in the PM2K software suite is briefly described, then validated using alkaline earth stannates and delafossite $CuAlO_2$ as case studies (*57*, *58*). Crystallite parameters including average particle size, strain, or even defect density can be calculated using the PM2K software, with multiple examples presented in this chapter.

1.3 General experimental methods and characterization

The following experimental methods are general guidelines; the experimental synthesis and characterization methods used for each compound in this thesis will be explicitly discussed.

1.3a Powder diffraction theory and instrumentation

In a powder poly-crystalline sample, the assumption is that, due to the large number of crystals in random orientation relative to the number of possible diffraction planes of the sample, the reciprocal space lattice can be condensed from three-dimensional to a single-dimension projection. Given a reciprocal lattice coordination system using spherical coordinates (r^*, θ^*, ϕ^*), the reciprocal lattice of a real space unit cell defined by the primitive vectors (a_1, a_2, a_3) can be generated by determining the reciprocal space primitive vectors (b_1, b_2, b_3) via the following:

$$b_1 = \frac{a_2 \times a_3}{a_1 \cdot (a_2 \times a_3)} \tag{1-1}$$

$$b_2 = \frac{a_1 \times a_3}{a_2 \cdot (a_1 \times a_3)} \tag{1-2}$$

$$b_3 = \frac{a_1 \times a_2}{a_3 \cdot (a_1 \times a_2)} \tag{1-3}$$

Due to the random orientation of the polycrystallites in the sample being measured, the resultant diffraction pattern taken using a plate detector is a series of concentric rings with a spacing directly related to the angle between the beam

axis and the ring, known as the 2θ angle. Each diffraction ring can be represented by a reciprocal lattice vector as described previously. The relationship between the location of the diffraction ring in real space to the reciprocal space lattice vector can be extracted from the general reciprocal lattice vector equation, the Laue equation, and the theory of elastic scattering, as follows.

$$G=hA+kB+lC \tag{1-4}$$

$$G\cdot(a+b+c)=2\pi(h+k+l) \tag{1-5}$$

The general reciprocal lattice vector G for a crystal lattice with primitive vectors a, b, c, and reciprocal lattice indices (hkl) can be defined by both equations 1-4 and 1-5 by exploiting the Laue equations for integer value reflections (consistent with Bragg's Law) shown in equation 1-6.

$$a\cdot\Delta k=2\pi h b\cdot\Delta k=2\pi k c\cdot\Delta k=2\pi l \tag{1-6}$$

Rearrangement of the three Laue conditions to form a three dimensional reciprocal lattice vector results in equation 1-7 and furthermore 1-8, which essentially dictates that constructive interference of diffracted radiation (and a resulting diffractogram) can only occur at integer (hkl) values.

$$\Delta k\cdot(a+b+c)=2\pi(h+k+l) \tag{1-7}$$

$$\Delta k=G \tag{1-8}$$

Realizing that Δk is a measure of the difference between the incident radiation wave vector k_i and the diffracted wave vector k_o (1-9) allows for rearrangement of 1-8 to arrive at the general diffraction condition 1-10.

$$\Delta k= k_o-k_i \tag{1-9}$$

$$k_o - k_i = G \quad (1\text{-}10)$$

Squaring both sides of the equation (1-11) and applying the simplification that $(k_o)^2 = (k_i)^2$ for elastic scattering leads to equation 1-12, which is directly related to Bragg's Law (1-13) where $k = 2\sin(\theta)/\lambda$ under the Bragg condition and $G = 2\pi/d$ (conversion from reciprocal to real space).

$$k_0^2 - 2k_0k_i + k_i^2 = G^2 \quad (1\text{-}11)$$

$$2k_i \cdot G = G^2 \quad (1\text{-}12)$$

$$2d\sin(\theta) = n\lambda \quad (1\text{-}13)$$

When multiple diffractograms taken with different incident radiation wavelengths (for example, synchrotron and lab powder diffraction) are to be compared, the Q space definition derived from 1-12 where Q = G should be employed to allow for plotting diffractograms as a function of the scattering vector Q (1-14).

$$Q = \frac{4\pi\sin\theta}{\lambda} \quad (1\text{-}14)$$

The ability to convert between real space and reciprocal space is paramount to the theory of powder diffraction because in reciprocal space, or momentum space, the momentum difference between incoming and diffracted radiation is defined by a reciprocal lattice vector; therefore, the atomic positions in a unit cell are determinable by combining chemical compositional knowledge and a diffraction pattern with known incident radiation wavelength.

1.3b In-house powder diffraction

The in-house diffractometer that the majority of the PXD scans presented in this thesis were run on was a Bruker D2 Phaser with LYNXEYE detector. This diffractometer is optimized for rapid acquisition of diffractograms with electronic fluorescence control to increase the signal-to-noise ratio. Sample preparation for measurement was slightly different depending on the air-sensitivity of the compound being measured.

For an air-stable material, 100 mg – 150 mg were weighed out and placed in the middle of an etched silicon wafer sample holder. The powder was lightly tamped with a glass slide to prevent anomalous peak intensity errors due to sample displacement. The majority of the diffractograms were obtained with a 2θ range of 10 °2θ to 70 °2θ for both air-stable and air-sensitive samples. The presence of straight-through beam intensity below 10 °2θ and lack of diffraction resolution above 70 °2θ were instrumental parameters that dictated the experimentally chosen diffraction range. When diffractograms of air-sensitive materials were needed, the D2 Phaser was placed inside of a sealed N_2 filled glovebox. Samples were prepared in a similar manner but with a smaller sample holder to accommodate the smaller amount of mass present (generally 30 mg – 50 mg). Diffractogram scans for both air-stable and air-sensitive samples were run with a step size of 0.02 °2θ per second. Publication quality results were obtained with a step size 0.02 °2θ per 10 seconds. For exceptionally air-sensitive samples, a dome-shaped plastic sample holder was loaded under N_2 and sealed.

The glovebox environment created to house the D2 Phaser was a custom job completed in collaboration with Plas-Labs from Lansing. Plas-Labs fabricated the stainless steel shell with hatch door and placed four KF45 fittings in the back based on blueprints drafted. After taking delivery of the shell, KF connection feed-throughs were made to pass power, Ethernet, and a chilling system into the glovebox. Due to the minimal airflow and high heat output from the D2 Phaser, a multi-faceted chilling setup was devised. The glovebox was cooled by a radiator type system with 5 gal/min constant flow that was passed through 50 ft. of aluminum pipe outside of the glovebox, as well as a radiator housed in a bucket of circulating chilled water. The D2 Phaser was also cooled by an external chiller with constant recirculation set at 19 °C. These two methods combined held the box temperature at 30 °C during long measurements.

1.3c Synchrotron diffraction at Argonne National Lab

The Synchrotron Powder x-ray Diffraction (SPXD) pattern was collected on the Argonne National Lab Synchrotron BM-11 beam line via the sample mail-in program using a 0.8 mm kapton capillary with an approximately 100 mg sample. The sample was loaded into the sample holder under an inert atmosphere. The synchrotron source wavelength was 0.373822 Å with a sample measurement time of 30 minutes. Data was worked up using the GSAS software package.

1.3d Diffraction data workup software

Two software packages, Bruker TOPAS and GSAS/EXPGUI, were employed to extract sample information from the recorded diffractograms. TOPAS was used exclusively to index diffractograms due to its indexing and cell parameter interface, while GSAS was used for all Rietveld refinements.

1.3e Thermogravimetric analysis

Thermogravimetric analysis (TGA) and differential scanning calorimetry (DSC) measurements were performed on a Netsch Jupiter STA 499 F3 system located in a custom-fitted purge glovebox. All gas and cooling flow to and from the instrument was passed through air-tight feedthroughs in the back of the glovebox. Air or moisture sensitive samples were loaded into the sealed glovebox using standard air-sensitive techniques.

The Netsch Jupiter STA 449 F3 is a vacuum tight, top-down simultaneous TGA/DSC instrument with a balance sensitive from the g to μg level. 99.999% ultrapure N_2 or Ar was used as the protective gas in all experiments, safely protecting the balance from exposure to decomposition products and allowing for a baseline calibration curve to remove gas buoyancy effects. Calibration curves were created for sample heating rates of 5 °C/min and 1 °C/min with a maximum sample temperature of 1300 °C.

TGA is a simple yet powerful technique in which the sample mass is continuously recorded as the sample temperature changes – allowing for the calculation of decomposition products by mass changes. DSC analysis

instruments constantly record the difference in heat required to raise the temperature of the unknown sample compared to a known reference sample with a well-defined heat capacity. From the DSC results, information such as melting, phase transition temperatures, or enthalpies of transitions can be calculated ($\Delta H = KA$; K = calorimetric constant, A = area under DSC curve).

The typical sample introduction and measurement procedure for an air-sensitive sample is described herein. 100 mg of the sample loaded under N_2 in a paraffin wrapped vial is placed in the antechamber of the purging Jupiter STA 449 F3 glovebox at a purge rate of approximately 2 L/min of ultrapure N_2 generated by a Cryo Industries XG350 N_2 generator. Concurrently, an alumina sample holder is heated to 300 °C for 10 min to remove any moisture adsorbed on the surface, placed in a vial, and loaded into the antechamber. After purging for 2 hrs, both the sample and the sample holder are brought in to the purge box. Approximately 25 – 40 mg of sample is loaded into the sample holder, and the sample holder is loaded onto the TGA balance. After sealing the system with the sample on the balance and the protective N_2 gas flowing, the active gas is introduced to the sample at a defined flow rate based on the buoyancy calibration curve (generally 40 mL/min protective / 20 mL/min active). After completion of the heating program, the sample is furnace cooled to room temperature, loaded into a paraffin-wrapped vial, and moved into the glovebox containing the Bruker D2 diffractometer for post-TGA phase characterization in order to further understand the decomposition products.

All TGA and DSC data was worked up using the Netzsch Proteus software package, which provided the necessary tools to extract pertinent data.

1.3f ICP optical emission spectroscopy

Inductively Coupled Plasma - Optical Emission Spectroscopy (ICP-OES) is a technique used to determine the concentrations of different elements in a sample. ICP-OES can be used to find exact concentrations of elements (quantitative ICP) or relative molar ratios (qualitative ICP), depending on the requirements of the experiment.

An ICP instrument works on the principle of optical emission - when atoms are ionized they emit radiation specific to each element. The intensity of the emitted radiation can then be used to calculate the concentration of each element in the sample. An Ar plasma is generated in an ICP by passing Ar gas through a coil with a large electromagnetic field created by induction using high power RF. The initial plasma is ignited with a discharge from a Tesla coil. As the sample of interest is passed through the plasma, the atoms are ionized and the resultant emission is channeled to a detector via plasma separation or optical fibers. Photomultiplier tubes or other detectors can be used to quantify the intensity of the emission signal.

Sample preparation for ICP analysis is simple for the majority of ceramic oxides. A 10 mg sample of the oxide was weighed out in the glovebox and transferred to a 20 mL glass vial. The vial was then filled with spectrophotometric grade concentrated nitric acid. After stirring and slight heating, 90% of all samples dissolve. Samples including Cu or main group elements required the addition of

HCl to generate aqua regia. The resulting solution has a concentration of approximately 500 ppm, which is 10x too high to inject into the ICP instrument. Following complete dissolution of the sample, 1 mL of this mixture was transferred to a 15 mL test tube filled with spectrophotometric grade water. The sample concentration of the test tube at this point is approximately 35 ppm in 5% nitric acid.

The sample is introduced into the ICP instrument with a 5% nitric acid carrier solution via a peristaltic pump.

1.3g Electrochemical characterization

The optimized procedure for preparing a sample for electrochemical characterization is summarized in this section. As each sample is different at both the macroscopic and microscopic scales, small sample-based changes to this method may be required for optimal results. However, if followed verbatim, the below procedure will result in initial measurements that assist in identifying the ideal measurement voltage range or scanning speed.

Initial sample preparation is key to acquiring good electrochemical characterization data using Li-ion coin cell setups. The biggest disadvantage of many of the materials presented in this thesis, with respect to electrochemical performance as Li-ion cathode materials, is the very low electronic conductivity intrinsic with semiconducting/insulating phases. The easiest way to approach this deficiency is by intimately mixing the material with a conductive powder (for example, carbon) in the form of acetylene black or Timcal SuperC 65.

The first step in preparing the sample for measurement is intimate mixing with the carbon additive, a binding additive, and a solvent. Example binding additives include polytetrafluoroethylene (PTFE), polyvinylidene fluoride (PVDF), and poly(3-methylthiophene) (*59*). PVDF was used as the binder in the following guide for two reasons: lower capacity fade rate upon subsequent charging, and high solubility in polar, aprotic solvents (*60*). From both literature and experience, a good starting ratio for active material:carbon additive:binder additive is 80:12:8 (*61*). Depending on the conductivity of the sample, the carbon content can be reduced down to as low as 2% by mass (*62*, *63*). This powder mixture is then placed in a 20 mL vial with a stir bar in the glovebox. To this vial, approximately 2 mL of N-methyl-2-pyrrolidone (NMP) is added, then the slurry is stirred for 12 hrs. NMP is a polar, aprotic solvent that PVDF is readily soluble in, as opposed to the other binder additives. MP also has relatively low surface tension – an important characteristic during the film phase of sample preparation.

After the paste has stirred for 12 hours, the film is made using a doctor blade tool. A piece of battery grade Al foil (99.99% MTI-XTL) is cut into an 8”x4” rectangle and placed longwise on a piece of tempered glass. Approximately 3 mL of paste is applied drop wise 3" from the left edge of the Al foil and 2" from the bottom, forming a hemisphere shape with 1" diameter. The doctor blade tool is then set to between 200 and 250 microns and slowly moved across the paste. A drag speed of 1" per minute is optimal. As the doctor blade passes over the paste a uniform layer will form. This step is repeated until the desired paste area is achieved while leaving a clean 1" edge along the entire Al sheet. After forming the film, it must be

cured to remove the NMP and densify the film. The Al sheet and tempered glass plate are then loaded into the antechamber and heated to 130 °C, followed by evacuation to 20 inHg. Allen keys should be placed along the clean edges of the Al foil to prevent it from moving during evacuation. The heating under vacuum treatment should continue for a minimum of 6 hours - generally overnight.

Once the film is removed from the antechamber it must be cut to size for coin cell fabrication. Using the die press in the glovebox, cut a 19 mm chip of the active material. The chip is then pressed with a pressure of 2000 lb/in^2. This chip, along with an equivalent 19 mm Celgard polyethylene membrane, are placed - active material below - in a split-cell type setup (Figure 1-4). Approximately 2 mL of selected electrolyte is then added to the cell, followed by a Li chip (99%, MTI-XTL). The cell is sealed according to Figure 1-4 and the potentiostat leads are connected. Review the Gamry software package tutorial for setting up and initializing experiments.

Figure 1-4. Actual coin cell setup used for all electrochemical measurements performed and described in this thesis. These split cells were purchased from MTI-XTL.

REFERENCES

REFERENCES

(1) Larson, R. T.; Clift, M. D.; Thomson, R. J. Total synthesis of the Galbulimima alkaloid (-)-GB17. *Angew. Chem. Int. Ed. Engl.* **2012**, *51*, 2481–4.

(2) Deng, J.; Zhu, B.; Lu, Z.; Yu, H.; Li, A. Total synthesis of (-)-fusarisetin A and reassignment of the absolute configuration of its natural counterpart. *J. Am. Chem. Soc.* **2012**, *134*, 920–3.

(3) Michels, T. D.; Dowling, M. S.; Vanderwal, C. D. A synthesis of echinopine B. *Angew. Chem. Int. Ed. Engl.* **2012**, *51*, 7572–6.

(4) Jakubec, P.; Hawkins, A.; Felzmann, W.; Dixon, D. J. Total synthesis of manzamine A and related alkaloids. *J. Am. Chem. Soc.* **2012**, *134*, 17482–5.

(5) Faber, J. M.; Eger, W. A.; Williams, C. M. Enantioselective total synthesis of the mexicanolides: khayasin, proceranolide, and mexicanolide. *J. Org. Chem.* **2012**, *77*, 8913–21.

(6) Enomoto, M.; Morita, A.; Kuwahara, S. Total synthesis of the tremorgenic indole diterpene paspalinine. *Angew. Chem. Int. Ed. Engl.* **2012**, *51*, 12833–6.

(7) Tian, S.; Zi, W.; Ma, D. Potentially biomimetic total synthesis and relative stereochemical assignment of (±)-gracilamine. *Angew. Chem. Int. Ed. Engl.* **2012**, *51*, 10141–4.

(8) Diethelm, S.; Carreira, E. M. Total synthesis of (±)-Gelsemoxonine. *J. Am. Chem. Soc.* **2013**, *135*, 8500–3.

(9) Bonazzi, S.; Cheng, B.; Wzorek, J. S.; Evans, D. A. Total synthesis of (-)-nakadomarin A. *J. Am. Chem. Soc.* **2013**, *135*, 9338–41.

(10) Mukai, K.; Urabe, D.; Kasuya, S.; Aoki, N.; Inoue, M. A convergent total synthesis of 19-hydroxysarmentogenin. *Angew. Chem. Int. Ed. Engl.* **2013**, *52*, 5300–4.

(11) Tsuna, K.; Noguchi, N.; Nakada, M. Convergent total synthesis of (+)-ophiobolin A. *Angew. Chem. Int. Ed. Engl.* **2011**, *50*, 9452–5.

(12) Frederich, J. H.; Harran, P. G. Modular access to complex prodiginines: total synthesis of (+)-roseophilin via its 2-azafulvene prototropisomer. *J. Am. Chem. Soc.* **2013**, *135*, 3788–91.

(13) Schaak, R. E.; Mallouk, T. E. Perovskites by Design: A Toolbox of Solid-State Reactions. *Chem. Mater.* **2002**, *14*, 1455–1471.

(14) Ranmohotti, K. G. S.; Josepha, E.; Choi, J.; Zhang, J.; Wiley, J. B. Topochemical manipulation of perovskites: low-temperature reaction strategies for directing structure and properties. *Adv. Mater.* **2011**, *23*, 442–60.

(15) Sivakumar, T.; Wiley, J. Topotactic route for new layered perovskite oxides containing fluorine: $Ln_{1.2}Sr_{1.8}Mn_2O_7F_2$ (Ln=Pr, Nd, Sm, Eu, and Gd). *Mater. Res. Bull.* **2009**, *44*, 74–77.

(16) Seddon, J.; Suard, E.; Hayward, M. A. Topotactic reduction of $YBaCo_2O_5$ and $LaBaCo_2O_5$: square-planar Co(I) in an extended oxide. *J. Am. Chem. Soc.* **2010**, *132*, 2802–10.

(17) Hayward, M. A. Phase Separation during the Topotactic Reduction of the Pyrochlore $Y_2Ti_2O_7$. *Chem. Mater.* **2005**, *17*, 670–675.

(18) Muguerra, H.; Colin, C.; Anne, M.; Julien, M.-H.; Strobel, P. Topotactic synthesis, structure and magnetic properties of a new hexagonal polytype of silver cobaltate(III) $AgCoO_{2+\delta}$. *J. Solid State Chem.* **2008**, *181*, 2883–2888.

(19) Blakely, C. K.; Bruno, S. R.; Poltavets, V. V. Low-temperature solvothermal approach to the synthesis of $La_4Ni_3O_8$ by topotactic oxygen deintercalation. *Inorg. Chem.* **2011**, *50*, 6696–700.

(20) Overton, A. J.; Best, J. L.; Saratovsky, I.; Hayward, M. a. Influence of Topotactic Reduction on the Structure and Magnetism of the Multiferroic $YMnO_3$. *Chem. Mater.* **2009**, *21*, 4940–4948.

(21) Hyett, G.; Barrier, N.; Clarke, S. J.; Hadermann, J. Topotactic oxidative and reductive control of the structures and properties of layered manganese oxychalcogenides. *J. Am. Chem. Soc.* **2007**, *129*, 11192–201.

(22) Hadermann, J.; Abakumov, A. M.; Adkin, J. J.; Hayward, M. A. Topotactic reduction as a route to new close-packed anion deficient perovskites: structure and magnetism of 4H-$BaMnO_{2+x}$. *J. Am. Chem. Soc.* **2009**, *131*, 10598–604.

(23) Saratovsky, I.; Lockett, M. A.; Rees, N. H.; Hayward, M. A. Preparation of $Sr_7Mn_4O_{13}F_2$ by the topotactic reduction and subsequent fluorination of $Sr_7Mn_4O_{15}$. *Inorg. Chem.* **2008**, *47*, 5212–7.

(24) Dixon, E.; Hayward, M. A. The Topotactic Reduction of $Sr_3Fe_2O_5Cl_2$-Square Planar Fe(II) in an Extended Oxyhalide. *Inorg. Chem.* **2010**, *49*, 9649–54.

(25) Tassel, C.; Kageyama, H. Square planar coordinate iron oxides. *Chem. Soc. Rev.* **2012**, *41*, 2025–35.

(26) Toda, K. Room temperature synthesis and characterization of perovskite compounds. *Solid State Ionics* **2002**, *154-155*, 393–398.

(27) Blakely, C. K.; Bruno, S. R.; Poltavets, V. V. Multistep soft chemistry method for valence reduction in transition metal oxides with triangular (CdI_2-type) layers. *Chem. Commun. (Camb).* **2014**, 2–5.

(28) Tassel, C.; Watanabe, T.; Tsujimoto, Y.; Hayashi, N.; Kitada, A.; Sumida, Y.; Yamamoto, T.; Kageyama, H.; Takano, M.; Yoshimura, K. Stability of the infinite layer structure with iron square planar coordination. *J. Am. Chem. Soc.* **2008**, *130*, 3764–5.

(29) Takamatsu, T.; Kato, M.; Noji, T.; Koike, Y. Low-temperature synthesis of the infinite-layer compound $LaNiO_2$ using CaH_2 as reductant. *Phys. C Supercond.* **2010**, *470*, S764–S765.

(30) Ma, R.; Liu, Z.; Takada, K.; Iyi, N.; Bando, Y.; Sasaki, T. Synthesis and exfoliation of Co^{2+}-Fe^{3+} layered double hydroxides: an innovative topochemical approach. *J. Am. Chem. Soc.* **2007**, *129*, 5257–63.

(31) Stoltz, C.; Ramesha, K.; Sirchio, S. a; Gönen, Z. S.; Eichhorn, B. W.; Salamanca-Riba, L.; Gopalakrishnan, J. Topochemical anion metathesis routes to the Zr_2N_2S phases and the Na_2S and ACl derivatives (A = Na, K, Rb). *J. Am. Chem. Soc.* **2003**, *125*, 4285–92.

(32) Badri, V. Topochemical oxygen deintercalation in oxides using butyllithium. *Phys. C Supercond.* **2000**, *339*, 106–112.

(33) Viciu, L.; Kodenkandath, T. A.; Wiley, J. B. Construction of a double-layered tetrahedral network within a perovskite host: Two-step route to the alkali-metal-halide layered perovskite, $(Li_xCl)LaNb_2O_7$. *J. Solid State Chem.* **2007**, *180*, 583–588.

(34) Neiner, D.; Spinu, L.; Golub, V.; Wiley, J. B. Ferromagnetism in Topochemically Prepared Layered Perovskite $Li_{0.3}Ni_{0.85}La_2Ti_3O_{10}$. *Chem. Mater.* **2006**, *18*, 518–524.

(35) Mcintyre, R. A.; Falster, A. U.; Li, S.; Simmons, W. B.; Connor, C. J. O.; Wiley, J. B. Opening a Perovskite to Valence Manipulation : Two-Step Topotactic Route to a New Mixed-Valence Titanate, $Na_{1-x+y}Ca_{x/2}LaTiO_4$. *J. Am. Chem. Soc.* **1998**, *7863*, 217–218.

(36) Choi, J.; Zhang, X.; Wiley, J. B. Building alkali-metal-halide layers within a perovskite host by sequential intercalation: $(A_2Cl)LaNb_2O_7$ (A = Rb, Cs). *Inorg. Chem.* **2009**, *48*, 4811–6.

(37) Schaak, R. E.; Mallouk, T. E. Prying Apart Ruddlesden–Popper Phases: Exfoliation into Sheets and Nanotubes for Assembly of Perovskite Thin Films. *Chem. Mater.* **2000**, *12*, 3427–3434.

(38) Francesconi, M. G.; Greaves, C. Anion substitutions and insertions in copper oxide superconductors. *Phys. C* **1997**, *10*, 29–37.

(39) Clearfield, A. Role of ion exchange in solid-state chemistry. *Chem. Rev.* **1988**, *88*, 125–148.

(40) Bucknum, M. J.; Castro, E. A. Kentuckia: A 4,6,8-connected tetragonal structural pattern in space group P4/nmm. *Russ. J. Gen. Chem.* **2006**, *76*, 265–266.

(41) Slater, P. R.; Hodges, J. P.; Francesconi, M. G.; Greaves, C.; Slaskic, M. Fluorination of the Ruddlesden – Popper type cuprates , LnACuO (Ln = La , Nd ; A = Ca , Sr). *Structure* **1997**, *7*, 2077–2083.

(42) Nakayama, R.; Tanaka, Y.; Yui, H.; Yamauchi, H.; Baron, A. Q. R.; Sasagawa, T. Preparation of infinite layer cuprate compounds $(Sr_{1-x}La_x)CuO_2$ and detailed phonon properties in x = 0. *Mater. Sci. Eng. B* **2010**, *173*, 41–43.

(43) Sachdev, S. Where is the quantum critical point in the cuprate superconductors? *Phys. Status Solidi* **2010**, *247*, 537–543.

(44) Iyo, A.; Hirai, M.; Tokiwa, K.; Watanabe, T.; Tanaka, Y. Preparation of polycrystals with various Tc and single crystal growth of $Ba_2Ca_3Cu_4O_8(O_{1-y}F_y)_2$ under high pressure. *Phys. C Supercond.* **2003**, *392-396*, 140–144.

(45) Hadermann, J.; Van Tendeloo, G.; Abakumov, A. M.; Rozova, M. G.; Antipov, E. V. HREM Study of Fluorinated Nd_2CuO_4. *J. Solid State Chem.* **2001**, *157*, 56–61.

(46) AI-Mamouri, M.; Edwards, P. P.; Greaves, C.; Slaski, M. Synthesis and superconducting properties of the strontium copper oxyfluoride $Sr_2CuO_2F_{2+\delta}$. *Nature* **1994**, *369*, 382–384.

(47) Zhao, H.; Shen, J.-L.; Zhao, Z. X. Proximity effect in layered high T_c superconductors. *Phys. C Supercond.* **2000**, *333*, 242–252.

(48) Choy, J.-H.; Park, N.-G.; Hwang, S.-J.; Kim, D.-H.; Hur, N. H. New Superconducting Intercalation Compounds: $(HgX_2)_{0.5}Bi_2Sr_2CaCu_2O_y$ (X = Br and I). *J. Am. Chem. Soc.* **1994**, *116*, 11564–11565.

(49) Shimizu, S.; Mukuda, H.; Kitaoka, Y.; Iyo, a.; Tanaka, Y.; Kodama, Y.; Tokiwa, K.; Watanabe, T. Uniform Mixing of Antiferromagnetism and High-Temperature Superconductivity in Electron-Doped Layers of Four-Layered $Ba_2Ca_3Cu_4O_8F_2$: A New Phenomenon in an Electron Underdoped Regime. *Phys. Rev. Lett.* **2007**, *98*, 60–63.

(50) Tsujimoto, Y.; Tassel, C.; Hayashi, N.; Watanabe, T.; Kageyama, H.; Yoshimura, K.; Takano, M.; Ceretti, M.; Ritter, C.; Paulus, W. Infinite-layer iron oxide with a square-planar coordination. *Nature* **2007**, *450*, 1062–5.

(51) Hayward, M. A.; Green, M. A.; Rosseinsky, M. J.; Sloan, J. Sodium Hydride as a Powerful Reducing Agent for Topotactic Oxide Deintercalation: Synthesis and Characterization of the Nickel(I) Oxide $LaNiO_2$. *J. Am. Chem. Soc.* **1999**, *121*, 8843–8854.

(52) Crespin, M.; Isnard, O.; Dubois, F.; Choisnet, J.; Odier, P. LaNiO: Synthesis and structural characterization. *J. Solid State Chem.* **2005**, *178*, 1326–1334.

(53) Crespin, M.; Levitz, P.; Gatineau, L. Reduced Forms of $LaNiO_3$ Perovskite. **1983**, 1181–1194.

(54) Shimakawa, Y.; Inoue, S.; Haruta, M.; Kawai, M.; Matsumoto, K.; Sakaiguchi, A.; Ichikawa, N.; Isoda, S.; Kurata, H. Topotactic Changes in Thin Films of Brownmillerite $SrFeO_{2.5}$ Grown on $SrTiO_3$ Substrates to Infinite-Layer Structure $SrFeO_2$. *Cryst. Growth Des.* **2010**, *10*, 4713–4715.

(55) Pralong, V.; Reddy, M. A.; Caignaert, V.; Malo, S.; Lebedev, O. I.; Varadaraju, U. V; Raveau, B.; Crismat, L.; Mar, B.; Caen, F.-. A New Form

of $LiNbO_3$ with a Lamellar Structure Showing Reversible Lithium Intercalation. *Chem. Mater.* **2011**, *23*, 1915–1922.

(56) Leoni, M.; Scardi, P. Nanocrystalline domain size distributions from powder diffraction data research papers. *J. Appl. Crystallogr.* **2004**, *37*, 629–634.

(57) Blakely, C. K.; Bruno, S. R.; Baum, Z. J.; Poltavets, V. V. Effects of ball milling and thermal annealing on size and strain of $ASnO_3$ (A = Ba, Sr) ceramics. *Solid State Sci.* **2013**, *15*, 110–114.

(58) Leoni, M.; Confente, T.; Scardi, P. PM2K: a flexible program implementing Whole Powder Pattern Modelling. *Zeitschrift für Krist. Suppl.* **2006**, *2006*, 249–254.

(59) Xu, W.; Read, A.; Koech, P. K.; Xiao, J. Effects of Substitution Positions, Electrolytes, and Binders on the Performance of Anthraquinone-based Cathode Materials. *Chem. Eng.* 2011.

(60) Barsykov, V.; Khomenko, V. The Influence of Polymer Binders on the Performance of Cathodes for Lithium-Ion Batteries. *Sci. J. Riga Tech. Univ.* **2010**, *21*, 67–71.

(61) Chou, S.; Wang, J.; Liu, H.; Dou, S. Rapid Synthesis of $Li_4Ti_5O_{12}$ Microspheres as Anode Materials and Its Binder Effect for Lithium-Ion Battery. **2011**, 16220–16227.

(62) Chu, C.-M.; Liu, C.-Y.; Wang, Y.-Y.; Wan, C.-C.; Yang, C.-R. On the evaluation of the factors influencing the rate capability of a $LiCoO_2$|Li battery. *J. Taiwan Inst. Chem. Eng.* **2012**, *43*, 201–206.

(63) Yamada, A.; Chung, S. C.; Hinokuma, K. Optimized $LiFePO_4$ for Lithium Battery Cathodes. *J. Electrochem. Soc.* **2001**, *148*, A224.

Chapter 2 : Low-temperature solvothermal reduction method

2.1 Introduction

Conventional high-temperature (≥750 °C) solid state synthetic techniques result in the preparation of thermodynamically stable products, while the low-temperature chimie douce (soft chemistry) approach allows for the formation of new metastable phases with unique structural features. Because extensive parts of the structure are retained during soft chemistry reactions, these reactions are topotactic in nature. In spite of the low diffusion coefficients of ions in solids at lower temperatures, there are many examples of topotactic reactions performed at or even below room temperature. For example, alkali metal intercalation can be performed at –78 °C in NH_3(l), as in the case of the synthesis of $Li_xMo_2SbS_2$ (*2*).

Due to a large ionic radius and double charge, the diffusion of O^{2-} can be expected to be prohibitively slow for any reaction to occur at room temperature; however, it has been shown that it takes only 12 h to transform $SrCoO_{2.5}$ into $SrCoO_3$ by oxidation in a sodium hypobromite solution at 0 °C (*3*). These reaction conditions are in sharp contrast with the traditional high oxygen pressure method of $SrCoO_3$ preparation (2000 bar at 300 °C) (*4*). This anomaly can be attributed to the strong oxidation power of sodium hypobromite, as well as the higher stability of $SrCoO_3$ at lower temperatures. While oxygen intercalation reactions can be performed at 0 °C, the inverse process – topotactic oxygen deintercalation – always requires higher temperature. Oxygen deintercalation is conventionally

performed by reaction in flowing H_2 or NH_3 at temperatures above 300 °C (*5*, *6*), or using metal getters like Zr (*7*, *8*). Recently, metal hydrides were introduced as powerful low-temperature agents for topotactic oxygen deintercalation (*9*–*12*). These reagents gave access to new metastable compounds inaccessible by reduction with flowing H_2, such as $La_3Ni_2O_6$ (*11*), $SrFeO_2$ (*13*), and $CaFeO_2$ (*14*). Solid state reductions have become possible at temperatures as low as 210 °C due to the high chemical activity of NaH and CaH_2 (*15*). Novel highly reduced phases with unusual coordination polyhedrons were prepared by this topotactic method – for example, $LaBaCoO_{4.25}$ with Co(I) in square planar coordination and $Sr_3LaFe_{1.5}Co_{1.5}O_{7.5}$ with three-coordinate Fe(II)/Co(II) (*15*, *16*).

Solid state reduction using metal hydrides generally requires intimately grinding the reagents, and sealing the reaction mixture in glass ampoules, and often involves intermediate regrinding/resealing steps. Unreacted metal hydrides and metal hydroxide byproducts must be removed by washing with methanol or saturated NH_4Cl in methanol solution (*13*).

One can consider performing topotactic oxygen deintercalation in the presence of organic solvents in order to improve reaction kinetics and eliminate the necessity of grinding/sealing operations. Reduction using metal hydrides in solvents is a classical method in organic chemistry; nevertheless, to the best of our knowledge, this technique has never been employed for the topotactic oxygen deintercalation of extended oxides. While $NaBH_4$ has been employed for metal oxides reduction in aqueous solution (*17*–*22*) and organic solvents (*23*), it was used as a source of

H_2, and reduction did not occur in a topotactic manner. Considering that topotactic oxygen deintercalation at temperatures below 200 °C is an unexplored area, it is possible that many new metastable transitional metal oxides can be prepared in the 50–150 °C temperature range. With this fact in mind, a new, lower temperature method of oxygen deintercalation is needed. In this chapter, the relative efficiency of a novel topotactic oxygen deintercalation method that exploits the reductive power of metal hydrides in common organic solvents is investigated. The results obtained from this method are compared with more conventional experimental techniques, including reduction in the solid state using metal hydrides and H_2 gas, as well as metal hydride reduction in organic solvents at ambient pressure.

2.2 Description of the novel solvothermal methods

$La_4Ni_3O_{10}$ was synthesized by the sol–gel Pechini technique as described previously (*24*). The final sintering was performed under oxygen flow at 1150 °C for 200 hrs with 4 intermittent grindings.

2.2a Experimental methods for the test case of $La_4Ni_3O_{10}$

Four different experimental reduction methods - solid state utilizing NaH or H_2, solution, and solvothermal - were used. For solid state reactions where H_2 was used as the reducing agent, 400 mg (0.449 mmol) of $La_4Ni_3O_{10}$ was finely ground and then spread evenly on the bottom of an alumina boat. The materials were fired at 200 °C, 250 °C, or 300 °C for up to 15 days under dried H_2 flow. In the solid state reaction employing NaH as a reducing agent, 400 mg (0.449 mmol) of $La_4Ni_3O_{10}$ was ground with NaH (13.47 mmol) under a nitrogen atmosphere in a glovebox and then loaded into a glass ampoule and covered with a vacuum adapter. The ampoule was removed from the glovebox, evacuated, and flame sealed. Samples were annealed at 100–200 °C for up to 10 days with intermediate regrinding/resealing every 24–48 hrs. Products were washed with anhydrous methanol under a nitrogen atmosphere to remove any remaining NaH or NaOH and then dried under vacuum for 1 h.

In the solution-based reactions, high-boiling solvents including triethylene glycol dimethyl ether (b.p. = 216 °C), diethylene glycol dimethyl ether (b.p. = 162 °C), and ethylene glycol (b.p. = 197 °C) were used. A 200 mg (0.22 mmol) sample

of $La_4Ni_3O_{10}$ with an excess of NaH (0.66–13.2 mmol) was loaded into a 100 mL Schlenk flask in a nitrogen glovebox. The flask was then charged with 20 mL of a high-boiling solvent and a Teflon stir bar, fitted with a reflux condenser, and placed in a temperature-regulated (25 °C – 200 °C) oil bath. Aliquots were periodically removed, washed with anhydrous methanol, and analyzed to determine phase composition.

The solvothermal reactions proceeded as follows: 200 mg (0.22 mmol) of $La_4Ni_3O_{10}$ and NaH (2.22 mmol – 6.6 mmol) were added to a 45 mL Teflon sleeve to avoid reaction with the steel vessel. The Teflon sleeve was then charged with 20 mL of anhydrous pentane, after which it was inserted into a steel autoclave and treated solvothermally at either 150 °C or 200 °C for up to 10 days. The products were washed under nitrogen with multiple aliquots of anhydrous methanol to remove any unreacted NaH or NaOH and then dried for 1 h under vacuum to remove any solvent. All samples were stored in a glovebox under nitrogen atmosphere.

The samples were characterized by powder X-ray diffraction (PXD) on a Bruker D8 Advanced with a DAVINCI design diffractometer using Cu Kα radiation. The patterns were recorded at room temperature with a step size of 0.02° (2Θ) on a zero background sample holder. Relative amounts of $La_4Ni_3O_{10}$, $La_4Ni_3O_9$, and $La_4Ni_3O_8$ have been estimated as a ratio of the main peak intensities.

Internal autogenous pressure of the autoclave at a given temperature was calculated either by the Clausius-Clapeyron relation (Equation 2-1), for

temperatures below the critical point of the solvent, or the Van-der-Waals equation (Equation 2-2), if the reaction temperature exceeded the critical point of the solvent. The only solvent used at a temperature higher than its critical point was pentane (critical point = 196 °C); therefore, the Van-der-Waals a and b constants used for pentane were 19.26 L^2bar/mol^2 and 0.146 L/mol respectively, as recorded in the 2013 CRC. Calculated pressures and enthalpies for the solvents used during reduction are presented in Table 2-1.

$$\ln\frac{P_1}{P_2} = \frac{-\Delta H_{vap}}{R}\left(\frac{1}{T_2} - \frac{1}{T_1}\right) \quad (2\text{-}1)$$

$$\left(P + \frac{n^2 a}{V^2}\right)(V - nb) = nRT \quad (2\text{-}2)$$

For the Clausius-Clapeyron relation, P and T refer to pressure in bar and temperature in Kelvin, R is the gas law constant 8.31447 J/molK, and ΔH_{vap} is the enthalpy of formation in units of J/mol. In the Van-der-Waals equation, P and T also refer to pressure in bar and temperature in Kelvin, n is the number of moles of solvent present, and V is the volume of the autoclave sleeve in L, while a and b are Van-der-Waals constants that vary depending on the solvent present. The a value describes the intermolecular attractive forces between particles while the nb term describes the total volume per mole occupied by the gas.

Table 2-1. Vapor pressure, enthalpy of vaporization, and calculated pressures at given temperatures for solvents used in solvothermal reduction reactions. Chemical data obtained from the 2013 CRC handbook online.

Solvent	P_{vapor} (atm)	ΔH_{vap} (kJ/mol)	P_{150} (atm)	P_{200} (atm)
Diglyme	2.10×10^{-3}	48.0	0.6895	2.9155
Triglyme	1.31×10^{-6}	63.7	0.0873	0.5916
Tetraglyme	2.48×10^{-8}	76.9	0.0068	0.0692
Pentane	5.61×10^{-1}	26.2	15.65	59.738
Heptane	5.82×10^{-2}	36.6	4.3158	12.956
Decane	1.04×10^{-3}	51.5	0.4579	2.1508

2.2b Results of the reduction of $La_4Ni_3O_{10}$

The crystal structure of the Ruddlesden–Popper (RP) nickelate $La_4Ni_3O_{10}$ can be described as an intergrowth of rock salt and perovskite blocks (Figure 2-1). As shown earlier, the low-temperature reduction of $La_4Ni_3O_{10}$ proceeds through oxygen deintercalation from the LaO layers in the perovskite blocks of the structure and results in two distinct line phases: $La_4Ni_3O_9$ and $La_4Ni_3O_8$ (*24*). Apart from the presence of oxygen vacancies, $La_4Ni_3O_9$ is structurally similar to $La_4Ni_3O_{10}$. On the contrary, formation of $La_4Ni_3O_8$ occurs through an oxygen deintercalation followed by a structural change in the $(LaO)_2$ part of the structure, resulting in a transformation from rock salt to fluorite arrangement (Figure 2-1) (*1*, *24*). As a result of this structural transformation, the so-called triple layer T′-type structure is

formed with infinite NiO_2 planes, where nickel is exclusively in square-planar coordination. While both reduced nickelates, $La_4Ni_3O_9$ and $La_4Ni_3O_8$, can be prepared by reduction of $La_4Ni_3O_{10}$ under H_2 flow at 350 °C, different concentrations of H_2 have to be utilized. $La_4Ni_3O_9$ is produced when 5–10% H_2 is used, while synthesis of $La_4Ni_3O_8$ requires pure H_2 flow. Reaction at higher temperatures results in complete decomposition of both phases with La_2O_3 and Ni as the decomposition products.

In the following experiments, the topotactic reduction of $La_4Ni_3O_{10}$ was chosen as a model system. This selection was based on the existence of two possible reduction products ($La_4Ni_3O_9$ and $La_4Ni_3O_8$), which can qualitatively indicate the activity of the reducing agents. The progress of each reaction was monitored via PXD, since the main peaks of all three nickelates can be easily distinguished in powder diffraction patterns (*1*).

Reduction of $La_4Ni_3O_{10}$ in flowing H_2 (100%) at different temperatures has been utilized as a benchmark for comparison with other techniques. The final composition of the reactions clearly demonstrates a rapid decrease in H_2 activity with decreasing temperatures (Table 2-1). While the most reduced $La_4Ni_3O_8$ nickelate can be prepared at 300 °C, only $La_4Ni_3O_9$ formed at 250 °C. No reaction was detected at 200 °C, confirmed by the sole presence of $La_4Ni_3O_{10}$.

NaH showed high activity in the solid state reduction of $La_4Ni_3O_{10}$ at 200 °C, where $La_4Ni_3O_8$ was the major product (Table 1, Figure 2a). While unable to prepare a pure phase sample even after annealing for 10 days with 5 intermediate

grindings, a ΔT of −100 °C in comparison with the H_2 reaction is rather impressive. The activity of NaH in solid state reduction reactions declines sharply at lower temperatures, with no reaction observed at 150 °C.

Surprisingly, the reduction of $La_4Ni_3O_{10}$ by NaH in triglyme at 200 °C resulted in the intermediate nickelate $La_4Ni_3O_9$ as the most reduced reaction product (Table 2-1). While a pure phase sample can be prepared faster (in 4 days) and easier (no regrinding/resealing) than in the case of the reported solid state reduction, the inability to form the most reduced product is essentially a failure of the method.

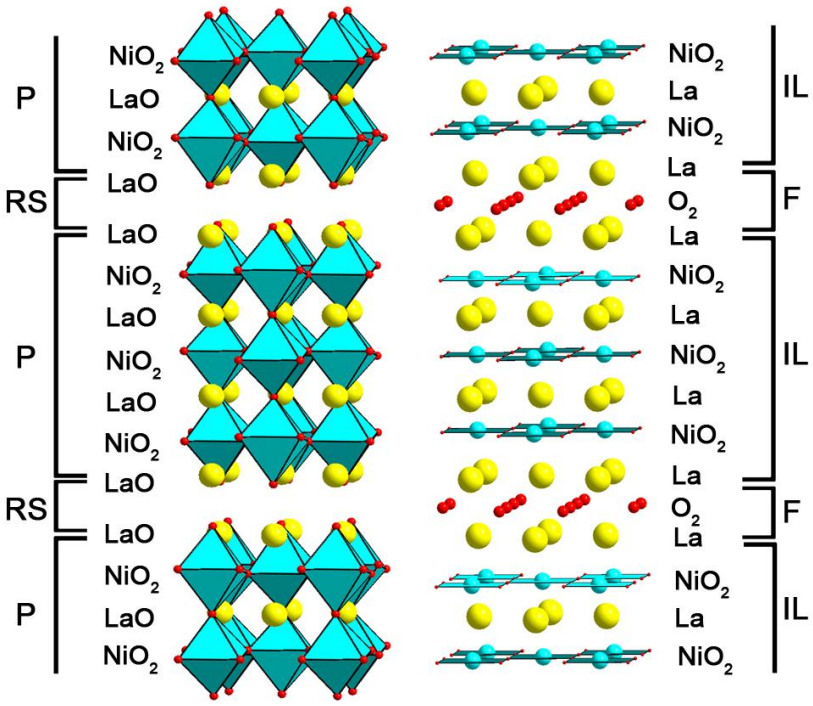

Figure 2-1. Structure models of $La_4Ni_3O_{10}$ (left) and $La_4Ni_3O_8$ (right) with denoted layers and structural blocks: P, perovskite; RS, rock salt; IL, infinite layer; F, fluorite. Yellow, cyan, and red balls represent La, Ni, and O atoms, respectively.

At 150 °C, reduction with NaH in triglyme under ambient pressure produces almost pure $La_4Ni_3O_9$. By these results, one can see that oxygen diffusion in nickelates is sufficient at this temperature for oxygen deintercalation to occur. Since no reaction was observed in the solid state reduction at 150 °C, there must be a limiting process absent in the presence of solvent.

The reaction of $La_4Ni_3O_{10}$ with NaH is summarized below:

$$La_4Ni_3O_{10} + NaH \rightarrow La_4Ni_3O_9 + NaOH \quad (2\text{-}3)$$

$$La_4Ni_3O_9 + NaH \rightarrow La_4Ni_3O_8 + NaOH \quad (2\text{-}4)$$

Since the eutectic temperature in the NaH–NaOH system, 450 °C (*25*), is much higher than the reaction temperature under consideration, reduction without the presence of a solvent is a purely solid state process, and involves diffusion of NaH through NaOH(s) to the nickelate surface. Due to the relatively high solubility of NaOH in glyme ethers, the nickelate particle surface opens up constantly for further reaction with NaH. Even at a lower temperature of 100 °C, $La_4Ni_3O_9$ forms slowly in the reaction with NaH/diglyme.

Reduction in autoclaves was initially tried as a convenient alternative to reaction in the presence of solvents under reflux. A large array of solvents can be used at temperatures above their boiling points, *i.e.* solvothermal conditions. Reduction of $La_4Ni_3O_{10}$ by NaH in diglyme (bp = 162 °C) at 200 °C led to the most reduced nickelate, $La_4Ni_3O_8$, as the major phase. Therefore, at 200 °C, the

reducing activity of NaH in diglyme under solvothermal conditions is comparable with that of solid NaH, and higher than NaH in triglyme at ambient pressure.

Table 2-2. Products of $La_4Ni_3O_{10}$ reduction by different techniques. Autogenous pressures were calculated using either the Clausius-Clapeyron equation or the van der Waals equation depending on the critical point temperature of the solvent.

reagent/solvent	**reaction temperature (reaction time), autogenous pressure**	**relative content (%) of $La_4Ni_3O_{10}$/$La_4Ni_3O_9$/$La_4Ni_3O_8$ (normalized to 100% total)**
H_2	300 °C (100 h)	0/0/100
	250 °C (120–360 h)	0/100/0
	200 °C (360 h)	no reaction
NaH	200 °C (240 h)	0/30/70
	150 °C (240 h)	no reaction
NaH/triglyme	200 °C (168 h)	0/100/0
	150 °C (120 h)	10/90/0
NaH/diglyme	200 °C (168 h), 2.9 atm	0/30/70
	150 °C (240 h)	0/90/10
NaH/pentane	200 °C (240 h), 59.7 atm	0/0/100
	150 °C (72 h), 15.7 atm	0/25/75

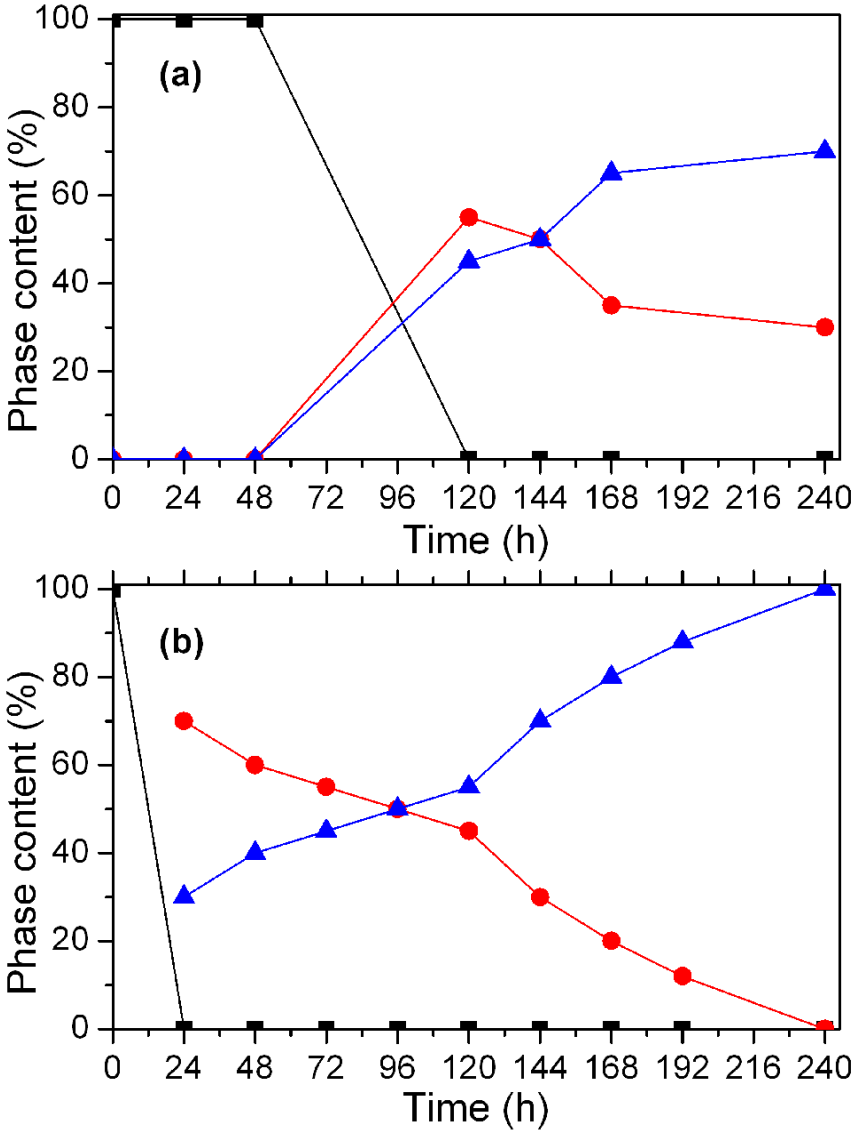

Figure 2-2. Phase composition versus reaction time during the reduction of $La_4Ni_3O_{10}$ with NaH at 200 °C: (a) solid state reaction, (b) solvothermal conditions. $La_4Ni_3O_{10}$, black squares; $La_4Ni_3O_9$, red circles; $La_4Ni_3O_8$, blue triangles. Relative phase content is normalized to 100% total.

The solvothermal reduction performed with NaH in pentane (bp = 36.1 °C) at 200 °C resulted in pure phase $La_4Ni_3O_8$. While the reaction is kinetically hindered and takes 10 days to prepare the single phase, in this case, simplicity of procedure and the purity of the product are advantageous over solid state reduction with NaH.

Representative PXD patterns for the reduction products prepared by four different experimental methods are shown in Figure 2-3. Pure $La_4Ni_3O_8$ without any peaks of admixture phases can be prepared by reduction with H_2 at 325 °C or by reduction with NaH under solvothermal condition at 200 °C. Highly crystalline products are formed in both cases. The full width at half maximum (FWHM) for the main $La_4Ni_3O_8$ reflections, (1 1 0) and (1 0 7), were 0.113(8)° and 0.131(5)° 2Θ for the H_2 reduction product, and 0.111(4)° and 0.146(3)° 2Θ for $La_4Ni_3O_8$ prepared by the solvothermal reduction method (Figure 2-4). Cell parameters were refined as a = 3.9708(1) Å and c = 26.106(1) Å after reaction with H_2 at 325 °C, and a = 3.9705(2) Å and c = 26.103(2) Å after solvothermal preparation at 200 °C.

$La_4Ni_3O_8$ was also obtained as a main phase by the solvothermal reduction with NaH in pentane at 150 °C. The solubility of both NaH and NaOH was expected to be much lower (or zero for NaH) in nonpolar solvents like pentane than in the polar glyme ethers; therefore, the reducing power of NaH in pentane cannot be attributed to reagent/product solubility. There is a clear correlation between formation of $La_4Ni_3O_8$ and autogenous pressure in autoclaves (Table 2-2). The pressure inside of the autoclaves was calculated by employing the Clausius–Clapeyron equations. Above the critical temperature of pentane (196.7 °C), the

van der Waals equation was used with a = 18.99 L^2 atm mol^{-2} and b = 0.146 L mol^{-1} as reported in the 2013 CRC. The effect of pressure could be related to many factors: changes in relative surface energy of the nickelates, an increase in solubility of either the reagent or the byproduct, and/or changes in the oxygen diffusion coefficients. Since the autogenous pressure was important for both polar and nonpolar solvents, it is not likely that surface energies or NaOH and NaH solubilities played the determining role.

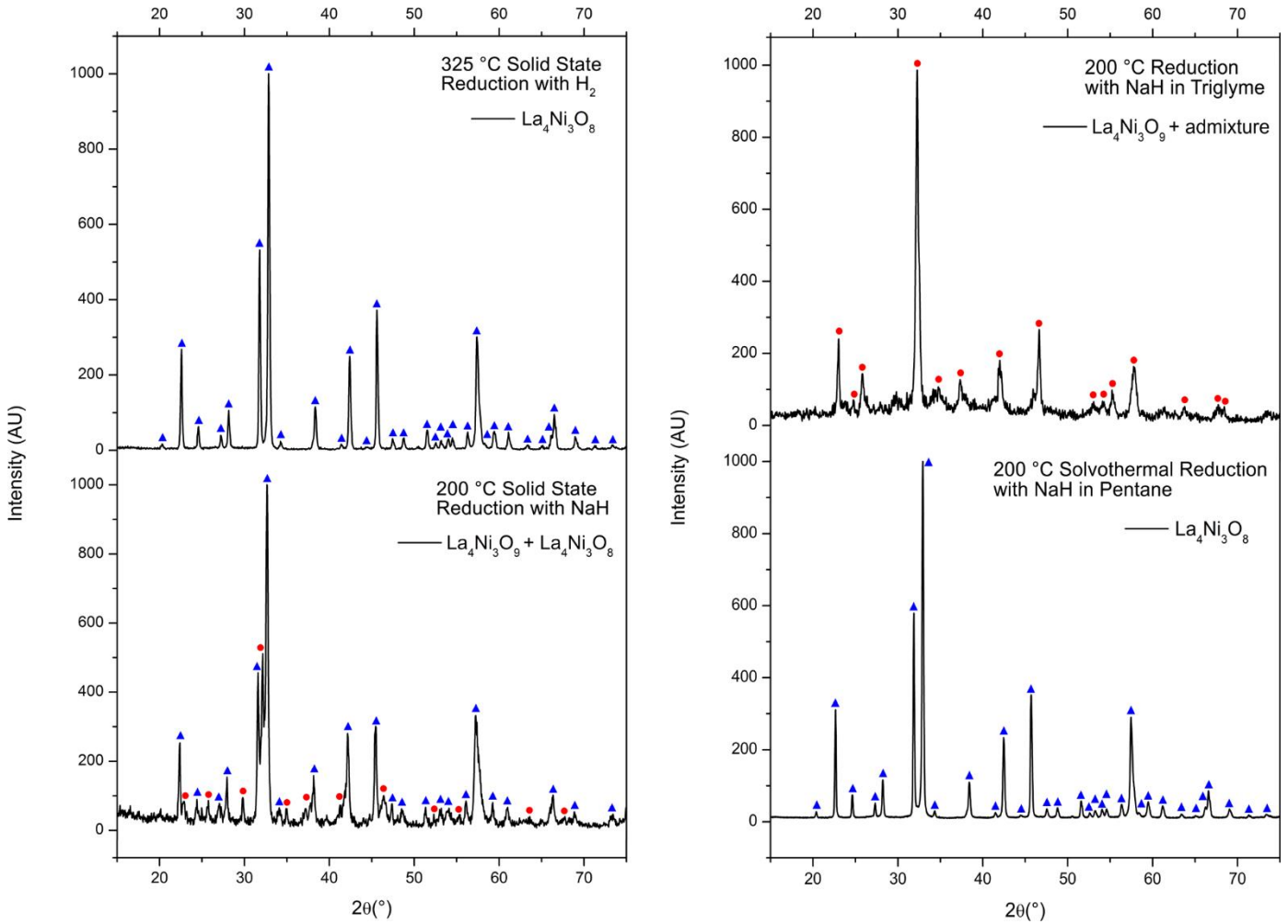

Figure 2-3. Representative PXD patterns for the reduction products prepared by different experimental methods. $La_4Ni_3O_9$, red circles; $La_4Ni_3O_8$, blue triangles.

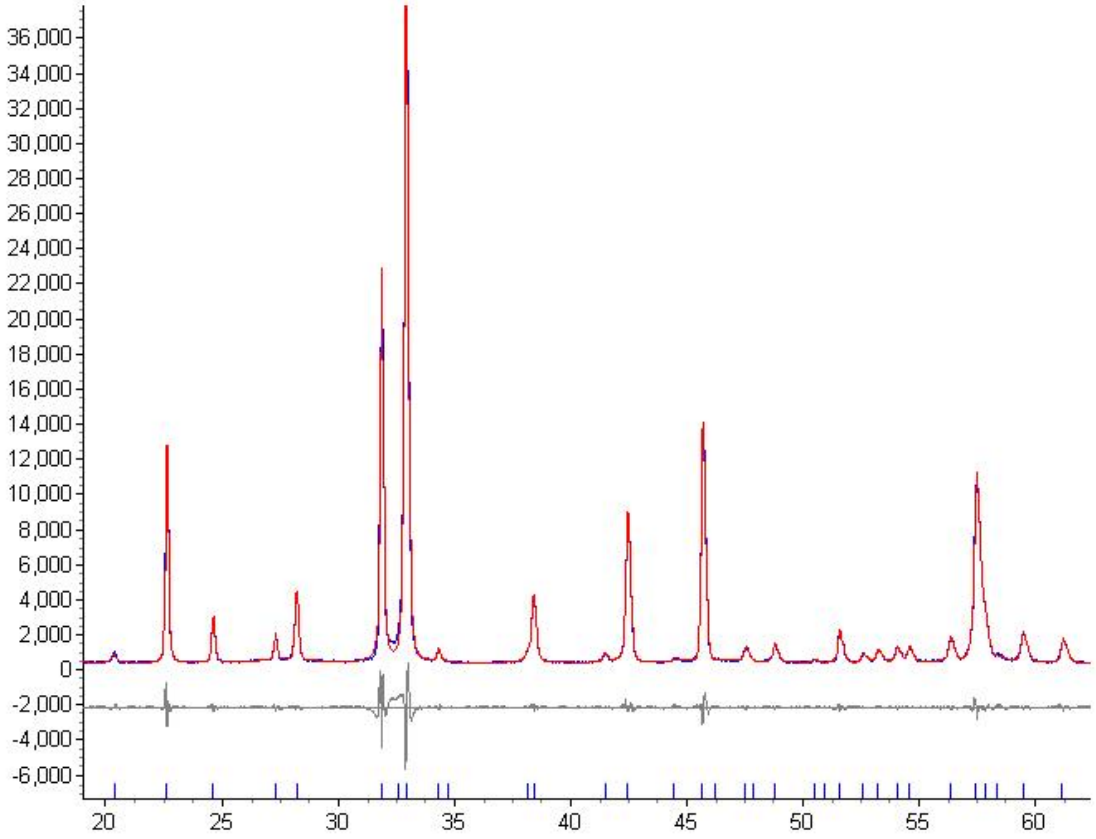

Figure 2-4. Refinement of PXD data for $La_4Ni_3O_8$ using the TOPAS software suite. The sample was prepared via the solvothermal reduction route.

2.2c Discussion on the role of pressure

Nucleation of a new phase can be a limiting step for topotactic transformations at such low reaction temperatures. In a solid–solid nucleation, a change in specific volume that occurs must be accommodated elastically, leading to a strain energy effect. Oxygen diffusion coefficients in ab planes can be expected to be much higher than in the c direction in the nickelates under consideration; therefore, the

seeds of reduced nickelates presumably form epitaxially on any crystal facets except (00l). In previously reported oxygen deintercalation reactions of these nickelates, large changes in *c* cell parameters were observed. For example, the *c* parameter decreases by 1.9% during reduction of $La_4Ni_3O_{10}$ to $La_4Ni_3O_9$. Further oxygen deintercalation of $La_4Ni_3O_9$ to $La_4Ni_3O_8$ leads to a striking 4.9% decrease in the *c* parameter. Formation of strained coherent interfaces raises the free energy of the system and can hinder the homogeneous nucleation. It is possible that the pressure during reduction under solvothermal conditions decreases the nucleation energy of the reduced nickelates—an effect that should be particularly important at lower temperatures. While it is not possible to uniquely attribute the pressure effect to increased reduction activity, the results presented in this chapter give direction for further development of this low-temperature topotactic oxygen deintercalation method. Higher pressure is favorable for this reaction to occur. At the same time, the autogenous pressure becomes lower at lower temperatures; therefore, reduction under an externally generated pressure of inert gas might allow extending reaction to lower temperatures.

2.3 $LaNiO_2$ – Square Planar Ni^{1+}

2.3a Literature background of $LaNiO_2$

Before proceeding into the experimental methods of the synthesis of $LaNiO_3$, it is important to emphasize the reasoning behind the choice of $LaNiO_3$ as a reduction target to form the infinite-layer type phase $LaNiO_2$. In $LaNiO_2$, the paramagnetic d9 Ni^{1+} metal exists in square planar configuration with the d_{x2-y2} singly filled and the rest of the d orbitals doubly filled (the square planar orbital manifold diagram is presented in Figure 2-5), and is both isoelectronic and isostrucural to Cu^{2+} in the high temperature cuprate superconductors with infinite layer CuO_2 ($CaCuO_2$, Sr_2CuO_4, $YBa_2Cu_3O_7$, etc.) (*26*–*28*). Considering that the Cu^{2+} infinite-layer compounds have been extensively studied, the synthesis of $LaNiO_2$ would provide a simple model for the study of a monovalent transition metal d^9 ion – something essentially nonexistent in bulk materials (*29*, *30*).

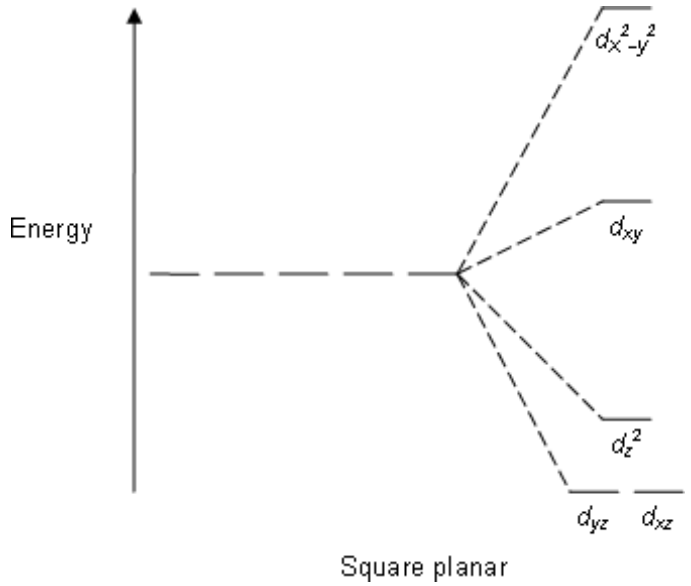

Figure 2-5. d orbital manifold diagram of the crystal field splitting for a transition metal in square planar configuration.

The first literature report of the synthesis of $LaNiO_2$ was published in 1983 by Crespin and Gatineau at the Université Paris-Sud using a very complex vacuum system with circulation loop to explicitly control the amount of hydrogen that was exposed to the $LaNiO_3$ starting material (*5*). According to the literature preparation, 500 mg of $LaNiO_3$ was introduced into the recirculation loop and oxidatively cleaned for 15 hrs at 670 K. The loop was then evacuated and filled with an exact amount of purified and dried H_2 gas and held at 397 °C until exactly 1 molar equivalent of H_2 was consumed, as measured by a monometer attached to the system, resulting in what was believed to be pure phase $LaNiO_2$. However, similarities in the K absorptions edge of the as-prepared $LaNiO_2$ and Ni metal

highlight the possible Ni^0 impurity in the sample, which would be invisible to x-ray diffraction techniques due to its amorphous nature at low temperature.

Fifteen years after the first reported synthesis of $LaNiO_2$, Hayward published a seminal work on the reduction of solid state materials to form metastable phases using NaH as a reducing agent (*9*). Hayward reacted $LaNiO_3$ with an excess of NaH in an evacuated glass ampoule between 165 °C and 250 °C to investigate the reducing power of NaH. When the reaction was performed at 210 °C, a mixture of $LaNiO_2$, $La_2Ni_2O_5$, and Ni metal was produced in a ratio of 80:15:5 by PXD peak intensity. Although this impure sample had the highest $LaNiO_2$:impurity ratio, the method allowed, for the first time, the reproducible synthesis of $LaNiO_2$ using simple techniques and common reagents.

The most recent report of the synthesis of $LaNiO_2$ was from the Koike group at Tohoku University in Japan (*31*). Rather than using NaH as the reducing agent, the less active CaH_2 was employed; therefore, the reaction temperature had to be increased to 400 °C before $LaNiO_2$ was produced as the major product. The experimental setup was identical to that proposed by Hayward - a glass ampoule was loaded with the starting materials then sealed under vacuum and heated to 300 °C for 24 hrs. The reaction products of the reduction between 150 °C and 400 °C are shown in Figure 2-6 – focus should be drawn to the presence of Ni metal in every reduction attempt. Just as in previous literature reports, the presence of Ni metal, and the reason for the over-reduction was mentioned, at most in passing. This will be further explored in the following section.

2.3b Reactions pathways for the formation of $LaNiO_2$

While planning the experimental conditions for the synthesis of $LaNiO_2$ from $LaNiO_3$, it was important to understand the multiple different reaction routes that could occur and to eliminate temperature and pressure regions that modulate the reaction energetics down the wrong pathway. The reduction of $LaNiO_3$ can be explained using 4 different pathways:

$$2LaNiO_3 + 2H_2 \rightarrow La_2NiO_4 + Ni + 2H_2O \quad (2\text{-}6)$$

$$4LaNiO_3 + 4H_2 \rightarrow La_2Ni_2O_5 + 2Ni + La_2O_3 + 4H_2O \quad (2\text{-}7)$$

$$2LaNiO_3 + 3H_2 \rightarrow La_2O_3 + 2Ni + 4H_2O \quad (2\text{-}8)$$

$$LaNiO_3 + H_2 \rightarrow LaNiO_2 + H_2O \quad (2\text{-}9)$$

As previously discussed, the effects of temperature on the reduction of $LaNiO_3$ with H_2 have been explored in the literature (*5*, *9*, *31*). Above 425 °C, the brownmillerite phase $La_2Ni_2O_5$ forms as oxygen is removed from the crystal lattice of $LaNiO_3$, resulting in Ni disproportionation to Ni^0 metal (Equation 2-6) (*8*). As the temperature is increased, the brownmillerite further decomposes to Ni metal and La_2O_3 (Equation 2-8). At temperatures above 700 °C, the thermodynamically stable spinel type structure La_2NiO_4 is formed (Equation 2-6). Lastly, under ambient pressure, $LaNiO_2$ is formed via reaction with H_2 between 350 °C and 400 °C (Equation 2-9) (*32*).

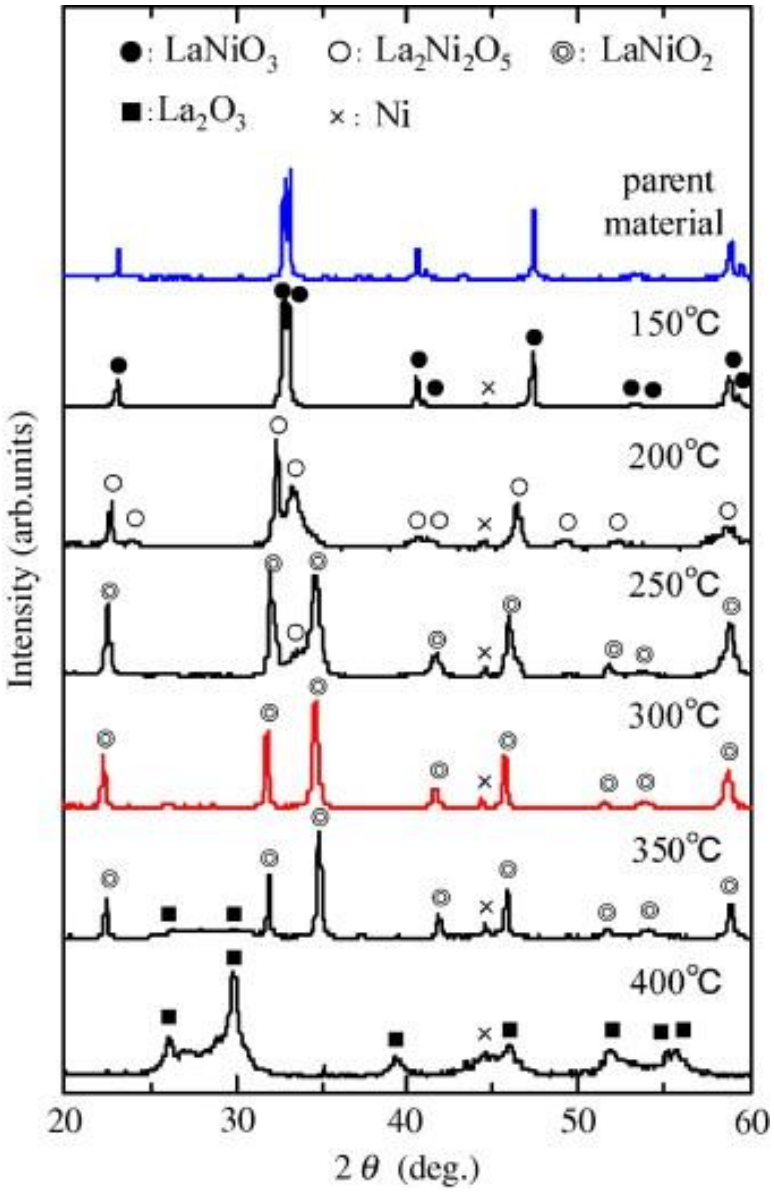

Figure 2-6. Powder X-ray diffraction patterns of products obtained by the reaction between $LaNiO_3$ and CaH_2 at various reaction temperatures using Cu $K\alpha_1$ radiation. Reproduced with permission from (*31*).

The effect of pressure on the reactant energetics and $LaNiO_2$ stabilization has been much less studied, in which the Hayward and Koike groups were the only ones previously to investigate both pressure and temperature effects concurrently on the reduction of $LaNiO_3$. From the Koike group, a simple phase diagram could be inferred relating pressure and temperature of the reaction of $LaNiO_3$ and CaH_2 (PXD patterns show in Figure 2-6) (*31*). Unfortunately, no real qualitative trends could be observed due to the lack of different pressures at each temperature point. That being said, the influence of both pressure and temperature on the reduction of $LaNiO_3$ to $LaNiO_2$ were investigated.

2.3c Synthesis and characterization of $LaNiO_2$

The parent oxygen-deficient perovskite $LaNiO_3$ adopts a highly symmetric geometry with 12-coordinate La^{3+} and corner sharing NiO_6 octahedra. Topotactic oxygen deintercalation of the parent led to the removal of the apical O^{2-} from the NiO_6 octahedra to form the tetragonal infinite-layer compound $LaNiO_3$ with Ni in the 1+ oxidation state (Figure 2-7). The Pechini method was used for the synthesis of $LaNiO_3$: 2.780 g (30 mmol) $Ni(OH)_2$, 4.89 g (15 mmol) La_2O_3, 30 g citric acid, 5

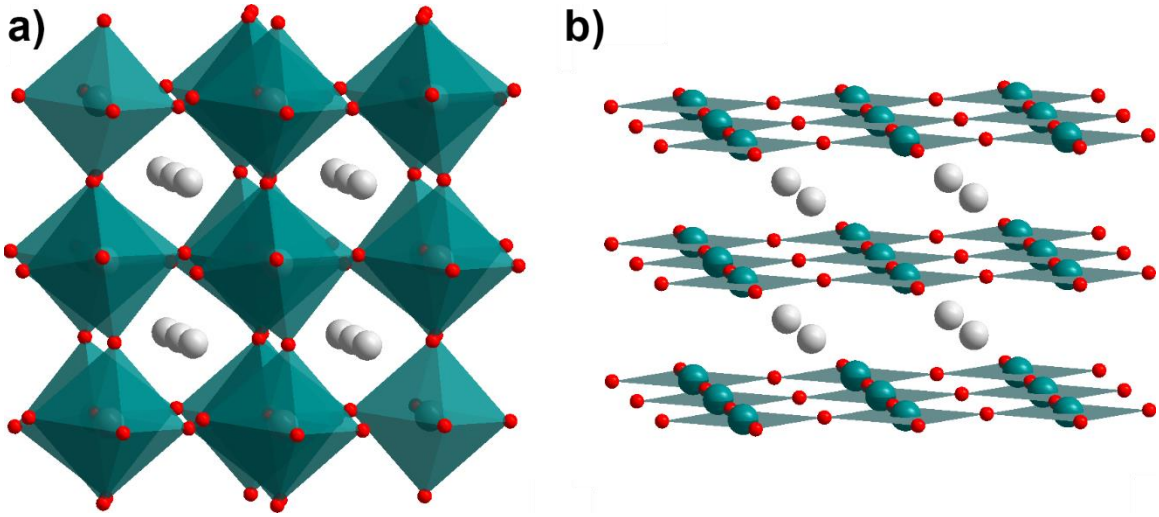

Figure 2-7. Crystal structures of a) $LaNiO_3$ and b) $LaNiO_2$. Grey spheres represent La^{3+}, teal spheres represent Ni^{3+} ($LaNiO_3$) or Ni^{1+} ($LaNiO_2$), and red spheres are O^{2-}.

mL ethylene glycol, 3 mL nitric acid, and 150 mL water were added to a stirring 250 mL ceramic evaporating dish. The dish was allowed to stir at room temperature for 48 hours after which the solution became transparent green then was heated to 300 °C. Any remaining organic matter was burned off by firing the dish at 600 °C for 2 hours. The ash was then ground with an agate mortar and pestle and pelleted into 3/4" pellets. The pellets were placed into an alumina boat and heated to 850 °C for 160 hours under flowing O_2. The resulting material – a mixture of $LaNiO_3$, La_2O_3, and NiO – was reground and pelletted, then fired for another 80 hours. The final product was stored in a vial inside of the glovebox.

A PXD diffractogram of pure $LaNiO_3$ prepared by the above method is presented in Figure 2-8, with the diffraction lines denoted by magenta tickmarks.

TGA analysis under oxygen showed no mass gain, confirming the $LaNiO_3$ stoichiometry compared to an oxygen deficient $LaNiO_{3-x}$.

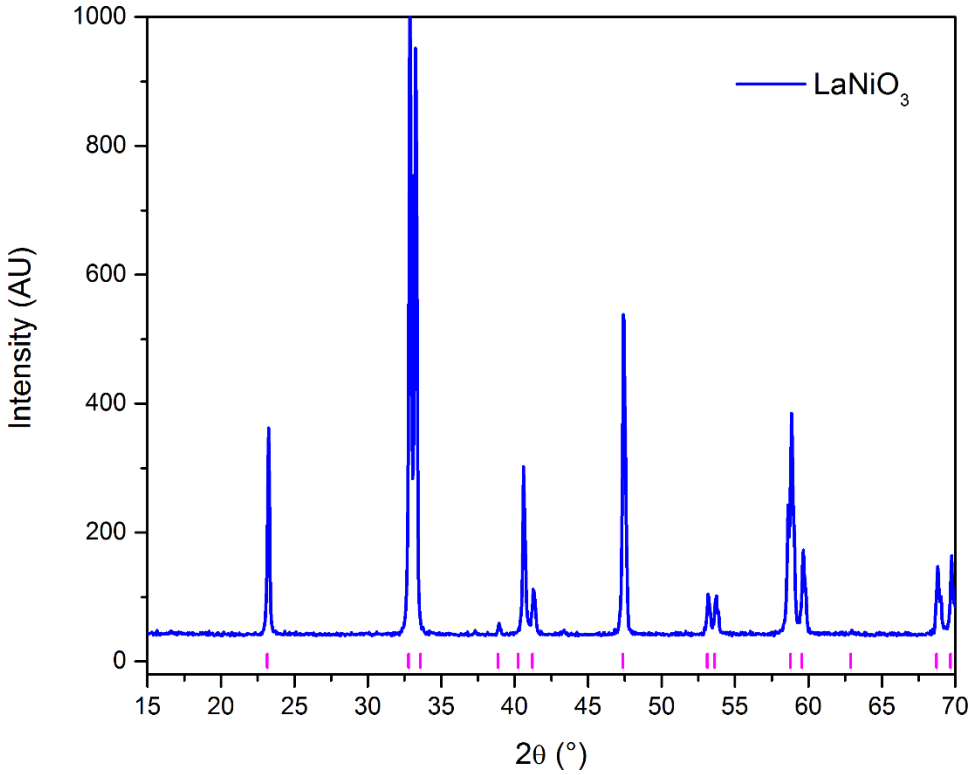

Figure 2-8. PXD pattern of the perovskite $LaNiO_3$ after Pechini synthesis and thermal treatment for 240 hrs at 850 °C under an O_2 atmosphere. Diffraction pattern was taken on a D2 phaser.

With the knowledge that the reduction of $LaNiO_3$ to $LaNiO_2$ occurs at 210 °C with NaH (*9*), initial attempts focused on reduction in high boiling solvents in an attempt to mitigate the formation of $La_2Ni_2O_5$ and Ni metal as reduction products. Reaction of $LaNiO_3$ with 30 molar equivalents of NaH in 20 mL of triglyme (b.p.

216 °C) at 200 °C for 7 days under N_2 led to an approximate 50:50 mixture of $LaNiO_3$ and $La_2Ni_2O_5$ by peak intensity. Increasing the temperature to 225 °C and swapping triglyme for tetraglyme (b.p. 275 °C) to maintain ambient pressure conditions produced a very similar mixture of $LaNiO_3$ and $La_2Ni_2O_5$.

To understand the effects of pressure on the reaction, a solvothermal approach was attempted. $LaNiO_3$ and 30 equivalents of NaH were intimately ground then loaded into a 45 mL Parr autoclave with 20 mL of anhydrous pentane. The autoclave was sealed under N_2 and placed in the glovebox at 150 °C. The reaction was duplicated 5 times and the autoclaves were held for 24 hrs, 72 hrs, 120 hrs, 168 hrs and 240 hrs to investigate the reduction products over time – as summarized in Table 2-3. The reduced intermediate $La_2Ni_2O_5$ began to appear after only 24 hours – a much shorter time frame compared to the 15 day analogous solid-state reduction reaction. Up until 72 hrs, only $LaNiO_3$ and $La_2Ni_2O_5$ are present; however, after 120 hrs diffraction peaks representing Bragg reflections from the tetrahedral space group P4/mmm ($LaNiO_2$) begin to appear. After 10 days, and furthermore, after 1 month, pure phase $LaNiO_2$ is never obtained at 150 °C.

Table 2-3. Products of the solvothermal reaction of $LaNiO_3$ with NaH at 150 °C. Calculated autogenous internal pressure was approximately 10 atm.

Time (hrs)	Phase % (Main peak intensity ratio)		
	$LaNiO_3$	$La_2Ni_2O_5$	$LaNiO_2$
24	80	20	0
72	65	35	0
120	15	70	15
168	0	80	20
240	0	25	75

Table 2-4. Products of the solvothermal reaction of $LaNiO_3$ with NaH at 200 °C. Calculated autogenous internal pressure was approximately 60 atm.

Time (hrs)	Phase % (Main peak intensity ratio)		
	$LaNiO_3$	$La_2Ni_2O_5$	$LaNiO_2$
24	55	35	10
72	25	60	15
120	10	40	50
168	0	20	80
240	0	< 5	> 95

The same reactions were repeated at 200 °C to understand the effect of temperature on the reduction products. As seen in Table 2-4, $LaNiO_2$ is present in an appreciable amount after only 24 hours; while after 10 days, the product mixture is primarily $LaNiO_2$ (Figure 2-9) with a very small (2.5% by Rietveld refinement) mixture of $La_2Ni_2O_5$. Although only the temperature was changed between these sets of reactions, from 150 °C to 200 °C the autogenous pressure inside of the autoclave increased dramatically from 15 atm to 60 atm. From previous experiments (reduction of $LaNiO_3$ at 225 °C with tetraglyme and NaH, ambient pressure) it can be deduced that the increase in reductive power is due to the increase in experimental pressure rather than temperature.

When a more nucleophilic hydride was used as the reducing agent, $LiAlH_4$, at 125 °C in tetraglyme while stirring for 48 hrs, the major reduction products were $La_2Ni_2O_5$, Ni metal, and $LaNiO_2$. Although NaH is a better reducing agent when described via electronegativity arguments, the solubility of $LiAlH_4$ allows for the solid-solid reaction mechanism to occur much faster, as will be discussed later. However, the increase in reduction also lead to a 25% mixture of Ni metal at 125 °C. When the temperature was lowered to 100 °C, very little reduction occurred - resulting in a product mixture of 90%:10% $LaNiO_3$:$La_2Ni_2O_5$.

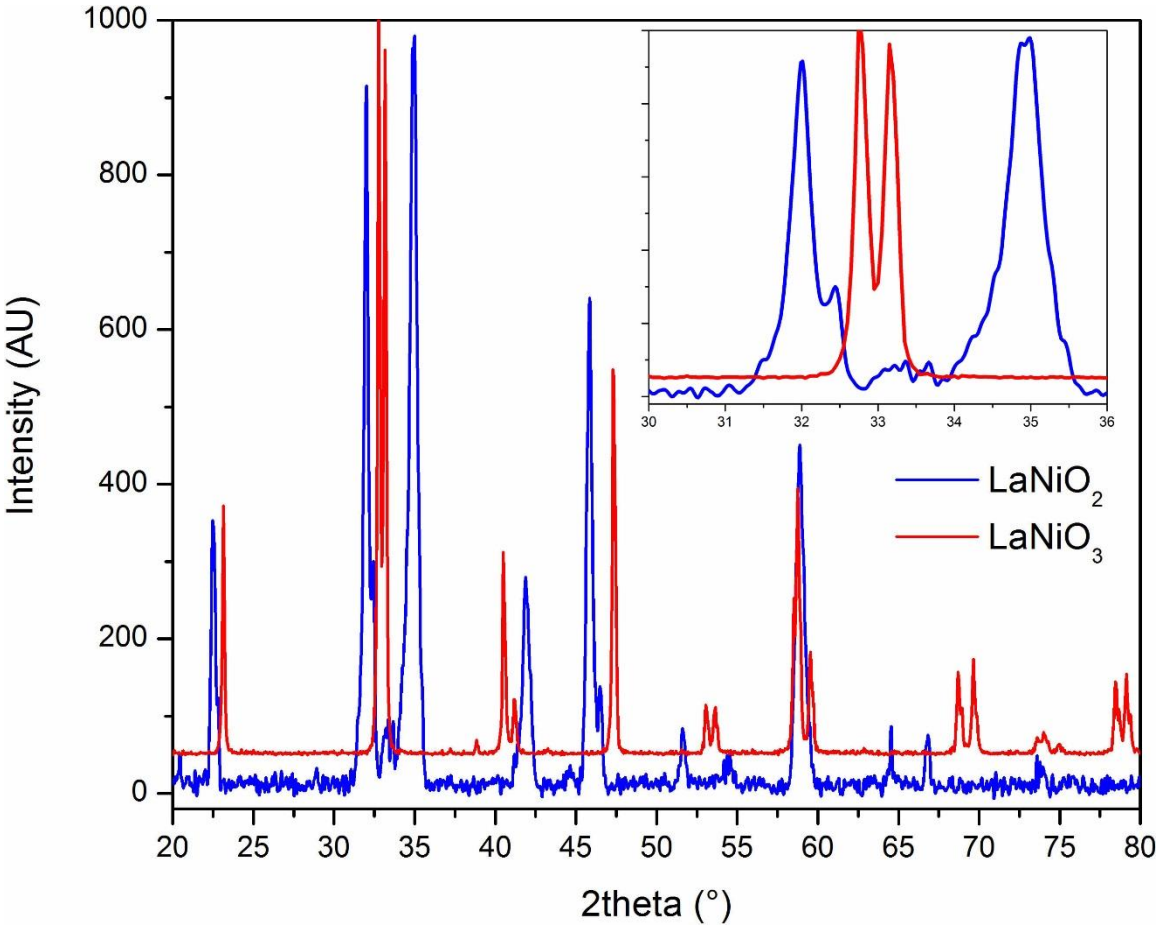

Figure 2-9. PXD pattern of the perovskite $LaNiO_3$ and the reduced infinite-layer type phase $LaNiO_2$ synthesized via the solvothermal reduction method at 200 °C for 10 days.

The multi-phase refinement of $LaNiO_2$ obtained solvothermally was especially difficult due to the peak overlap between $LaNiO_2$ and $La_2Ni_2O_5$ (Table 2-5 presents all of the Bragg reflections of $LaNiO_2$ and reflections of $La_2Ni_2O_5$ that appear at the same d spacing). As seen in Figure 2-10, the peak profile was difficult to fit, resulting in residuals at the most intense peaks (fluctuations in the grey difference

line below the plot). Initial refinement attempts were made using a Gaussian type peak profile that gave a refinement R_{wp} = 7.82 – a poor refinement for high symmetry compounds and good diffraction statistics. Introduction of a Lorentzian component to the peak shape lowered the R_{wp} value to 2.65. A small amount of preferred orientation was present that could not be appropriately fit, manifested in the refinement as imperfect intensity fittings of the (h00) peaks of $LaNiO_2$. Although Ni was included in the plot of the Rietveld refinement (Figure 2-10 – magenta tick marks), inclusion of the phase in the actual refinement did not statistically improve the fit; therefore, it was only included as a reference to show that no unique diffraction peaks from Ni are present. A compilation of cell parameters for $LaNiO_2$ synthesized previously in the literature, as well as in this thesis, is presented in Table 2-5. Cell parameters obtained from the refinement of $LaNiO_2$ in this work match closest to the data from Crespin, deemed the most pure sample of the three in the literature. The larger *c* parameters in the Hayward and Koike samples may be due to Ni in-plane disorder resulting from O non-stoichiometry (*9*, *33*).

Table 2-5. Cell parameter comparison for $LaNiO_2$. Three literature reported cell parameter values as well as the cell parameters refined in this thesis are presented.

Source	Space Group	*a* (Å)	*b* (Å)	*c* (Å)	Volume (Å^3)
Crespin	P4/mmm	3.966	3.966	3.376	53.10
Hayward	P4/mmm	3.958	3.395	3.381	52.96
Koike	P4/mmm	3.964	3.964	3.399	53.40
Blakely	P4/mmm	3.962	3.962	3.378	53.03

2.3d Reinvestigating the magnetic properties of $LaNiO_2$

The magnetic susceptibility of $LaNiO_2$ is presented in Figure 2.11 along with the inverse magnetic susceptibility. The material can be easily broken down into three different temperature regimes: a Curie-Weiss paramagnet between 5 K and 60 K, a temperature independent paramagnetic state between 60 K and 225 K, and a second Curie-Weiss paramagnetic regime with a very large Weiss constant above 225 K. Between 5 K and 60 K, the magnetization data was modeled with a simple Curie-Weiss fit (C = 0.385) with Θ = -91.62 K denoting antiferromagnetically coupled spins in the paramagnetic state. In this temperature regime the μ_{eff} is ~ 0.5 β lower than the expected 1.73 β for a Ni^{1+} ion (Figure 2-12).

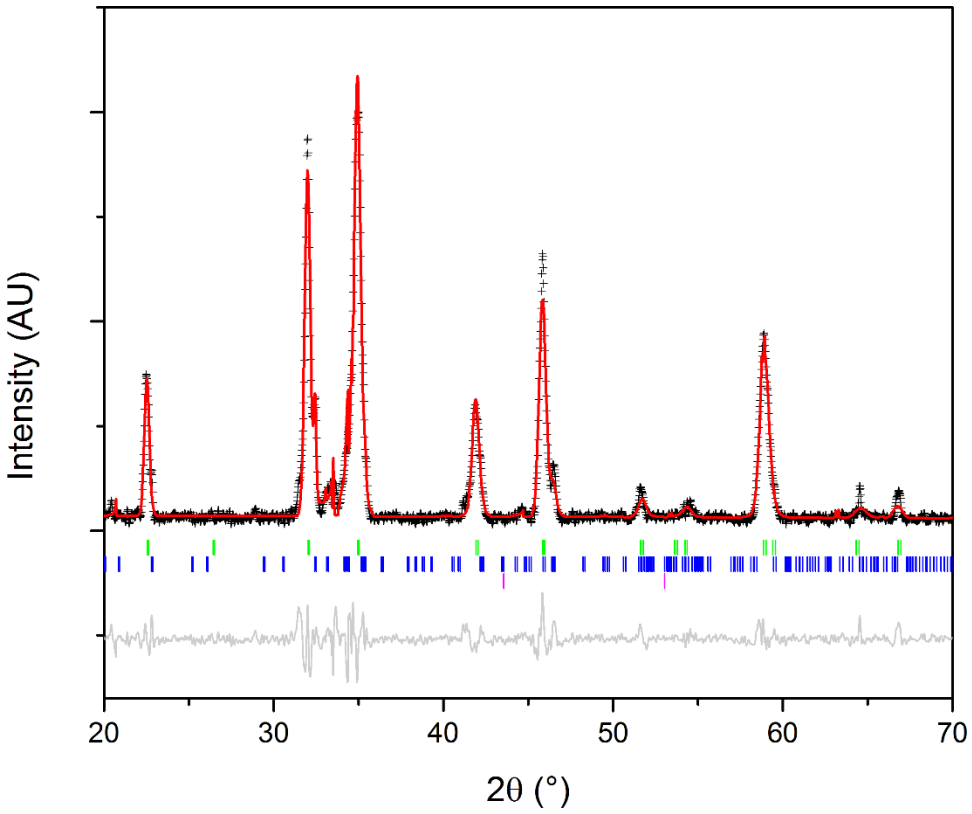

Figure 2-10. Rietveld refinement of $LaNiO_2$ obtained from the solvothermal reduction of $LaNiO_3$ at 200 °C for 10 days using NaH. Phase analysis lead to a $LaNiO_2$:$La_2Ni_2O_5$:Ni (metal) product ratio of 500:12.35:1.

In the temperature independent paramagnetic region (50 K – 225 K), the data does not follow Curie-Weiss law. The most probable cause for this temperature independent paramagnetism is a spin glass state with the low temperature spin glass feature hidden by the Ni impurity signal.

Between 225 K and 400 K, the magnetization data follows Curie-Weiss law with an exceptionally high Weiss temperature of -302 K – indicative of highly correlated electrons and spins. The high effective magnetic moment may be due to a mixture

of superparamagnetic Ni with very small particle sizes on the order of 10 nm or less, which would cause an increase in the overall effective moment. Considering that the critical radius for Ni nanoparticles with a blocking temperature of 50 K is approximately 30 nm, this assumption is appropriate (*34*). Using the magnetic data as a phase purity test, which is not a guide due to the inaccuracies brought on by the superparamagnetic Ni, while locking the effective magnetic moment to 1.73 bohr magnetons and setting the effective moment of the superparamagnetic Ni to 1.3 bohr magnetons (*35*), a phase ratio of 1:0.036:0.036 $LaNiO_2$:$La_2Ni_2O_5$:Ni.

Table 2-6. Bragg reflections of $LaNiO_2$ and selected reflections of $La_2Ni_2O_5$ that appear at similar d spacing, thereby complicating the multiphase refinement.

$LaNiO_2$		**$La_2Ni_2O_5$**	
d (Å)	**hkl**	**d (Å)**	**hkl**
3.968	010	3.898	200
3.376	001	3.455	021
2.804	110	2.789	-202
2.571	011	2.551	221
2.157	111	2.171	222
1.983	200	1.954	400
1.773	120	1.778	-402
1.708	021	1.709	-241
1.685	002	1.682	-332
1.569	121	1.563	242
1.444	112	1.447	314
1.401	220	1.409	243
1.285	022	1.281	334
1.175	131	1.175	154

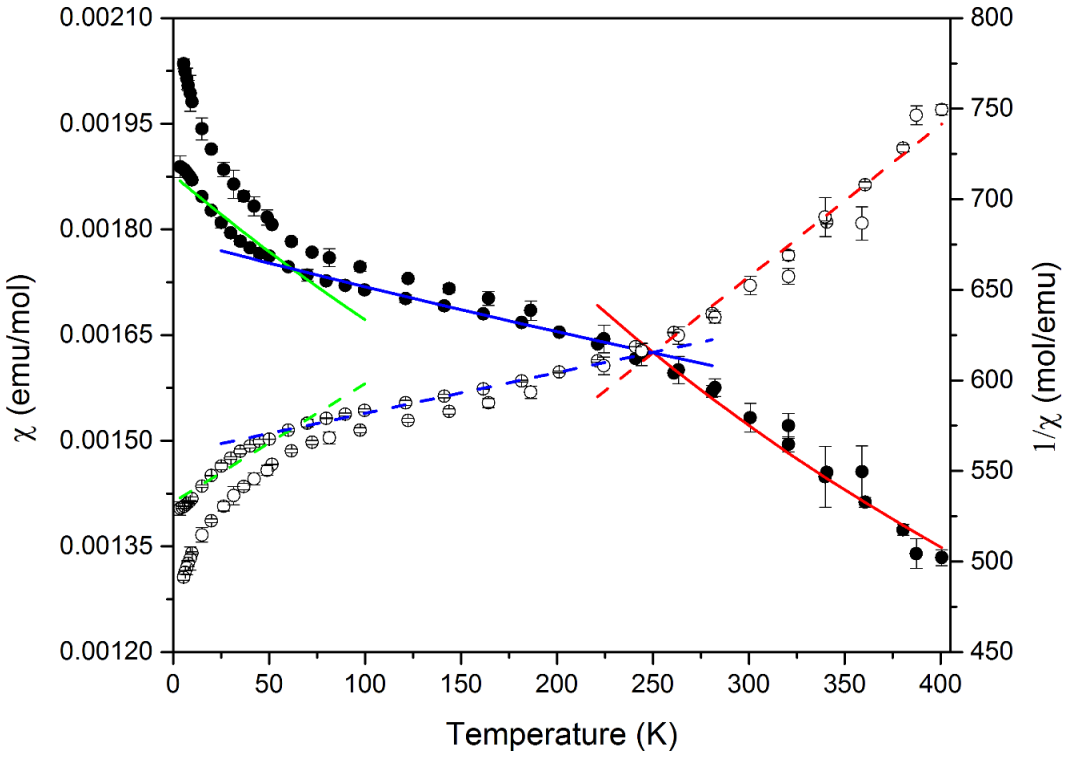

Figure 2-11. Susceptibility (closed circles) and inverse susceptibility (open circles) data collected on a sample of $LaNiO_2$ under a 1000 Oe field using a SQUID magnetometer.

The magnetic data obtained for $LaNiO_2$ can then be compared with previous reports in the literature (*9*). As seen in Figure 2-13, the general shape of the susceptibility curve is similar for the sample made by Hayward in 1999; however, the fit is substantially different (*9*). Due to the large Ni impurity and the assumption that the Ni impurity was in a ferromagnetic state (an impossibility considering that the Ni particle size would have to be significantly larger than the critical radius for a superparamagnetic at 300 K of 40 nm), both fits – represented by b) and c) in

Figure 2-13 – required the use of a temperature independent term to achieve reasonable values (*9*). The sample of $LaNiO_2$ presented in this thesis is of a much higher purity based on the magnetic measurements than previous reports (with the exception of Crespin, who did not characterize the magnetic properties), leading to the conclusion that the phase purity presented in this thesis is of higher purity than many of the literature accounts.

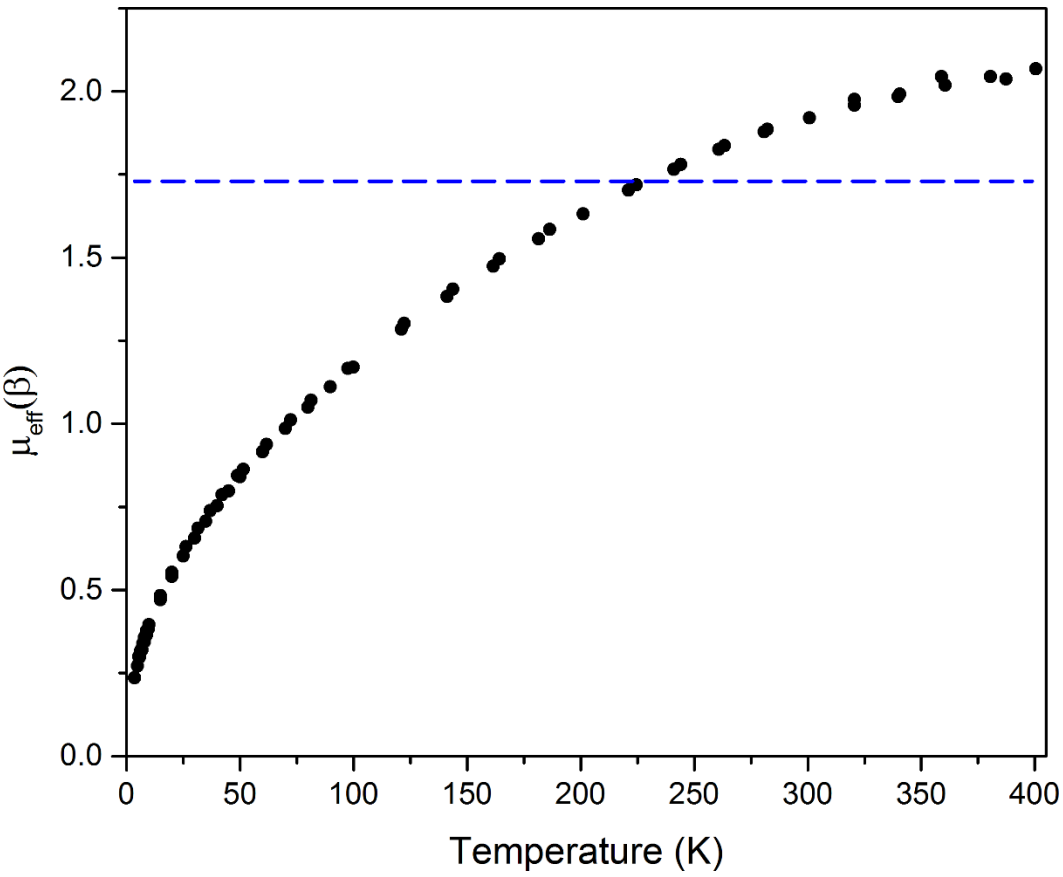

Figure 2-12. Effective magnetic moment of $LaNiO_2$ across the temperature range studied. A horizontal line was drawn in blue at 1.73 μ_B – the effective magnetic moment of an S = ½ ion (Ni^{1+}).

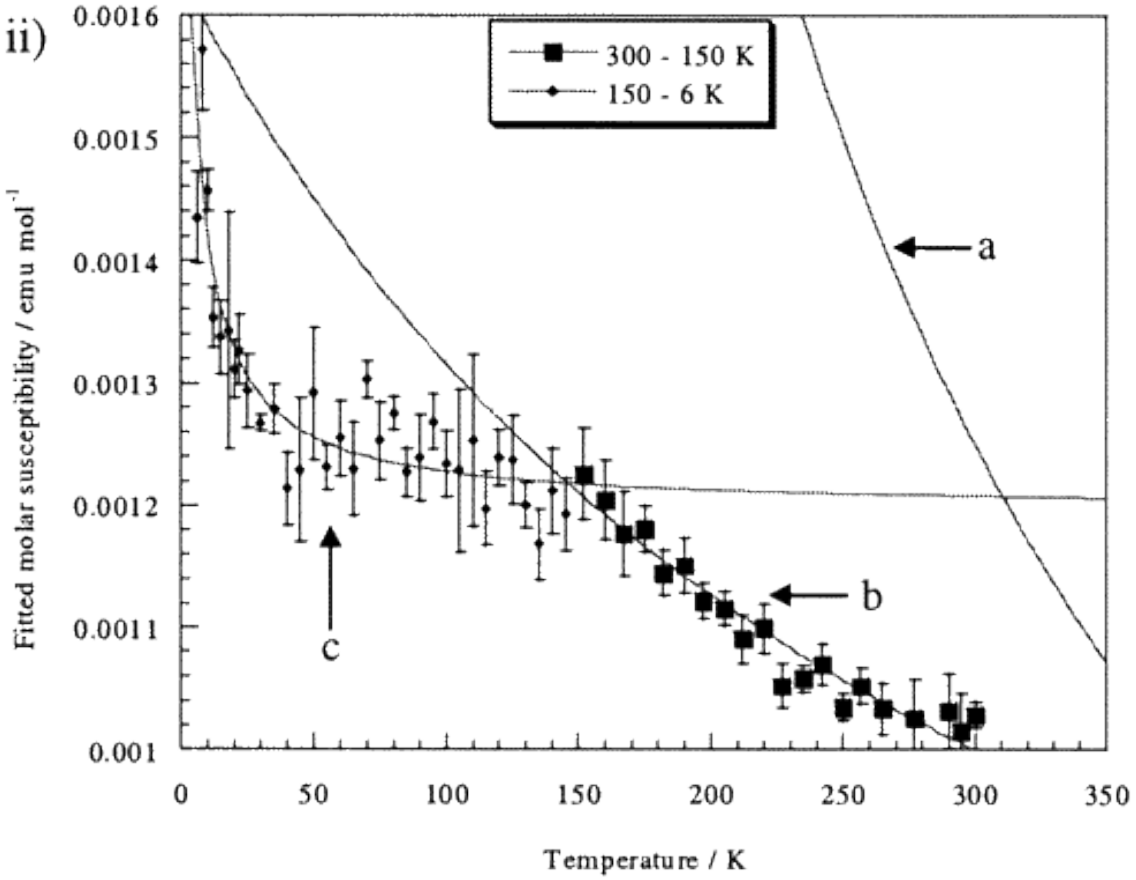

Figure 2-13. Literature fitted molar paramagnetic susceptibility of $LaNiO_2$ from the Hayward group. Adapted with permission from (*9*). Copyright 2013 American Chemical Society.

2.3e Comparison of solid-solid and solid-gas reaction mechanisms

The mechanism of formation of $LaNiO_2$ can be approached differently than discussed earlier ((2-6) – (2-9)) by looking at the possible reduction interfaces: a solid-solid reaction (2-11) or a solid-gas reaction (2-10, 2-12).

$$LaNiO_3(s) + 2NaH(s) \rightarrow 2Na(s) + H_2(g) + LaNiO_2(s)$$
$$\rightarrow NaOH(s) + NaH(s) + LaNiO_2(s) \quad (2\text{-}10)$$

$$LaNiO_3(s) + NaH(s) \rightarrow 2NaH(s) + 1/2O_2(g) + LaNiO_2(s)$$
$$\rightarrow NaOH(s) + LaNiO_2(s) \quad (2\text{-}11)$$

$$LaNiO_3(s) + NaH(s) \rightarrow NaOH(s) + LaNiO_2(s) \quad (2\text{-}12)$$

The solid-gas reaction using H_2 (2-10) can be ruled out from occurring below 250 °C by the TGA reduction of $LaNiO_3$ in 10% H_2, which shows that $LaNiO_3$ is stable towards reduction until about 250 °C (Figure 2-14). In this TGA, the first reduction step corresponds to the formation of $La_2Ni_2O_5$ (350 °C) and the second reduction step (500 °C) represents decomposition to La_2O_3 and Ni. When $LaNiO_3$ and the reductant were physically separated during the solvothermal reaction via a teflon cup in the autoclave, very little reduction occurred until 225 °C when $La_2Ni_2O_5$ began to appear. This was anomalous until the decomposition temperature of NaH(s) into Na(s) and H_2(g) was investigated under pressure – and shown that NaH decomposes between 210 °C and 225 °C resulting in the reduction of $LaNiO_3$ to $La_2Ni_2O_5$ by H_2. This fact also rules out the solid-gas reaction presented in (2-10).

The second solid-gas reaction listed (2-11) relies on the release of oxygen from the crystal lattice of $LaNiO_3$ under a reducing atmosphere. This pathway can be easily ruled out by the TGA of $LaNiO_3$ under nitrogen (Figure 2-15) which shows a negligible mass loss; therefore, oxygen is not released upon heating at 200 °C.

Since pathways (2-10) and (2-11) are ruled out, the solid-solid reaction mechanism (2-12) was analyzed. If the reduction of $LaNiO_3$ occurred via a solid-solid route, the reaction rate would be dependent on the crystallite size of the starting material as well as the reaction mixture intimacy.

To test this hypothesis $LaNiO_3$ was ball-milled for 30 minutes, 1 hour, and 2 hours, then reduced under the same conditions (200 °C, 10 d, pentane, hand-ground to mix) as previously discussed. Without ball milling, no Ni metal was present in the PXD pattern; however, after ball-milling for any appreciable amount of time, a large peak (~10% by intensity) of Ni metal was present, accompanied by both $La_2Ni_2O_5$ and La_2O_3 – essentially following the solid-solid reduction reaction pathway articulated by (2-7). One final proof of the solid-solid reaction mechanism is the molar dependence of NaH on the reaction rate. When a fourfold or tenfold molar excess of NaH was used, the major phase present after 10 days was $La_2Ni_2O_5$. On the other hand, when 30 equivalents of NaH were added to the autoclave the reaction went to completion, resulting in $LaNiO_2$ as the major phase under the same reaction conditions. Since the reaction rate was dependent on both the particle size as well as the local reductant concentration, the solid-solid reaction pathway is the most likely mechanism.

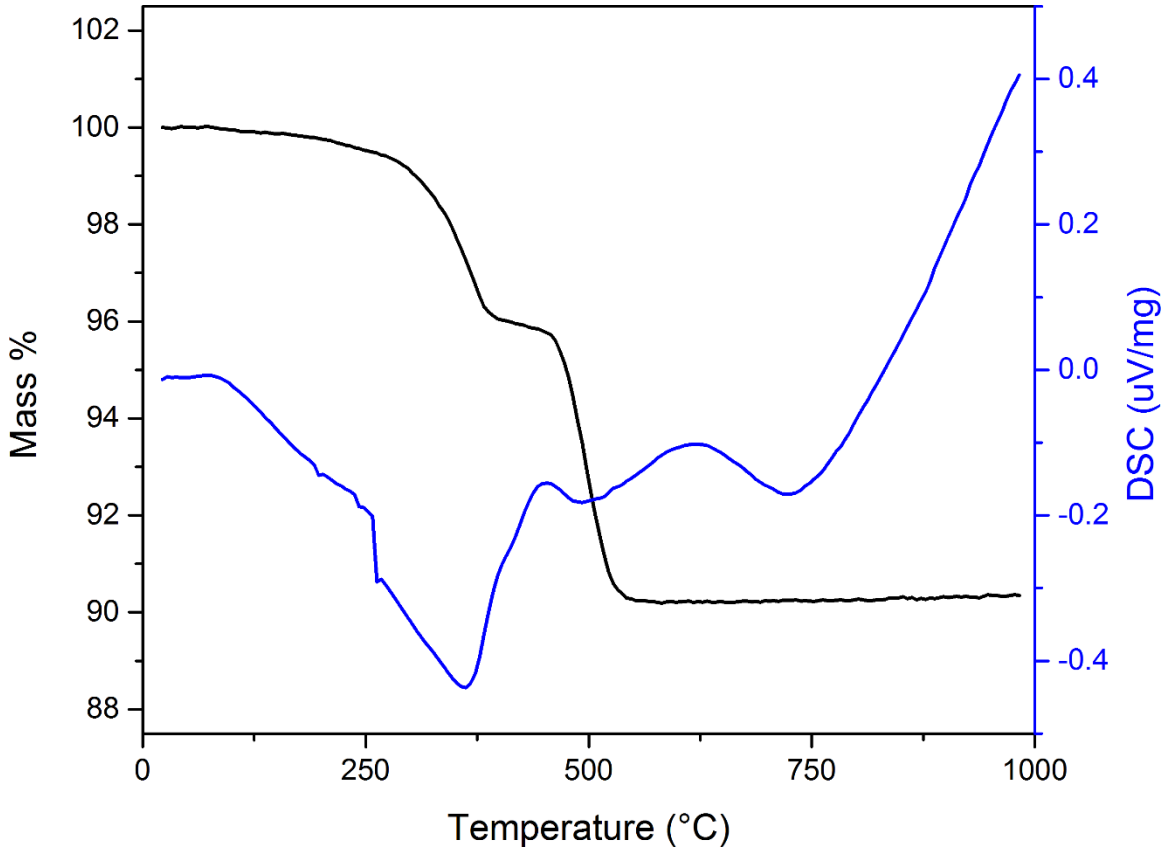

Figure 2-14. TGA/DSC data for the reduction of $LaNiO_3$ under a 40:20 H_2:N_2 atmosphere from 25 – 1000 °C. The sample holder was loaded under N_2.

Interestingly, the previous discussion on the solid-solid vs. sold-gas reaction mechanism only applies when NaH is used as the reducing agent. Below the decomposition temperature of 210 °C, the basicity of NaH dominates its reactivity and the hydride ion acts as the reductant rather than H_2 gas. The reduction of $LaNiO_3$ to $LaNiO_2$ reported by Koike at 400 °C using CaH_2 presumably follows a solid-gas reduction pathway considering the decomposition of CaH_2 to form Ca (s) and H_2 (g) begins at 240 °C and at 400 °C a large overpressure of H_2 would be

present (*36*). This idea is corroborated by the TGA reduction of $LaNiO_3$ in H_2 (Figure 2-14) where the first reduction from $LaNiO_3$ to $La_2Ni_2O_5$ occurs at 275 °C followed by a negative slope plateau at approximately 400 °C. This discussion applies to the other reducing agents used, $LiAlH_4$ and $NaBH_4$, as well.

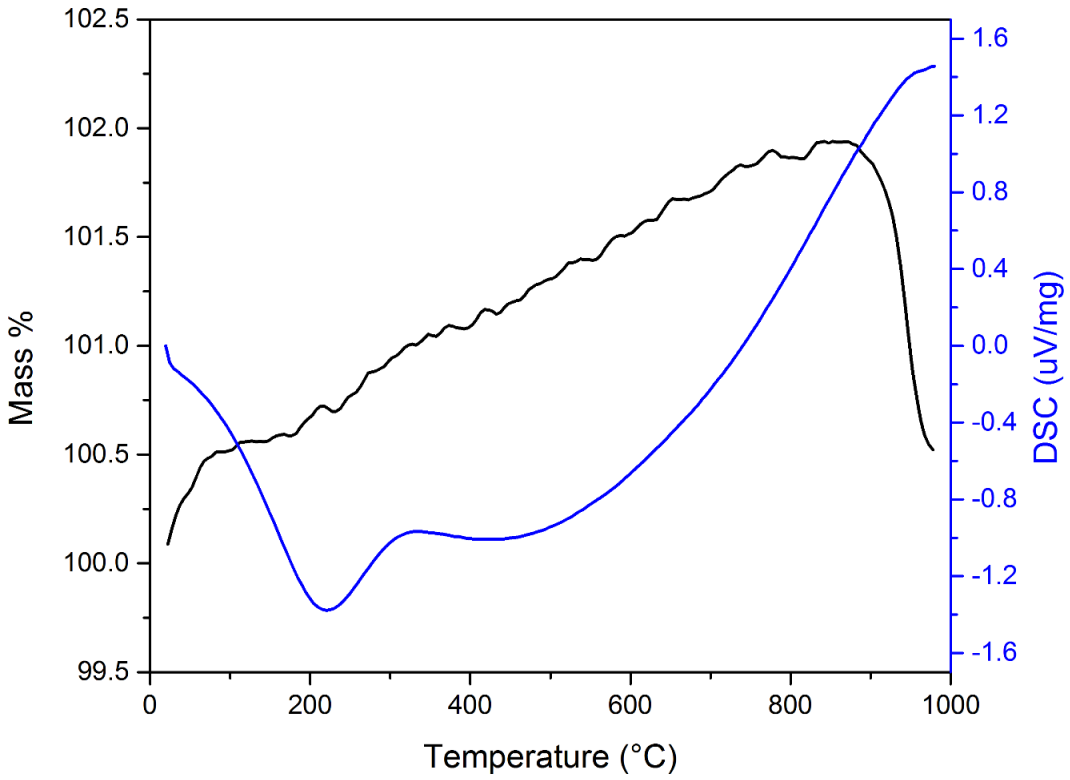

Figure 2-15. TGA/DSC data for the calorimetry experiment of $LaNiO_3$ under a N_2 atmosphere from 25 – 1000 °C. The sample holder was loaded under N_2.

2.3f DFT study on $LaNiO_2$ and $CaCuO_2$ similarities

Pickett and Lee published an in-depth work in the computational study of $LaNiO_2$ comparing Ni^{1+} to Cu^{2+} in the infinite-layer $CaCuO_2$ where the correlation effects and electronic properties of both were compared (*37*). In comparing the density of states (DOS) plots in Figure 2-16, it is apparent that intimate mixing of the Cu 3d states with the O 2p states occurs just below the Fermi level in $CaCuO_2$; however, there is a large energy separation between the centers (3eV - 4eV) of the Ni 3d and O 2p states in $LaNiO_2$. The “pinning” of the Cu 3d orbitals to the O 2p orbitals below the Fermi level – causing a high degree of 2p-3d hybridization – in the high-temperature superconducting cuprates has been heavily investigated as the source of the superconductive properties.

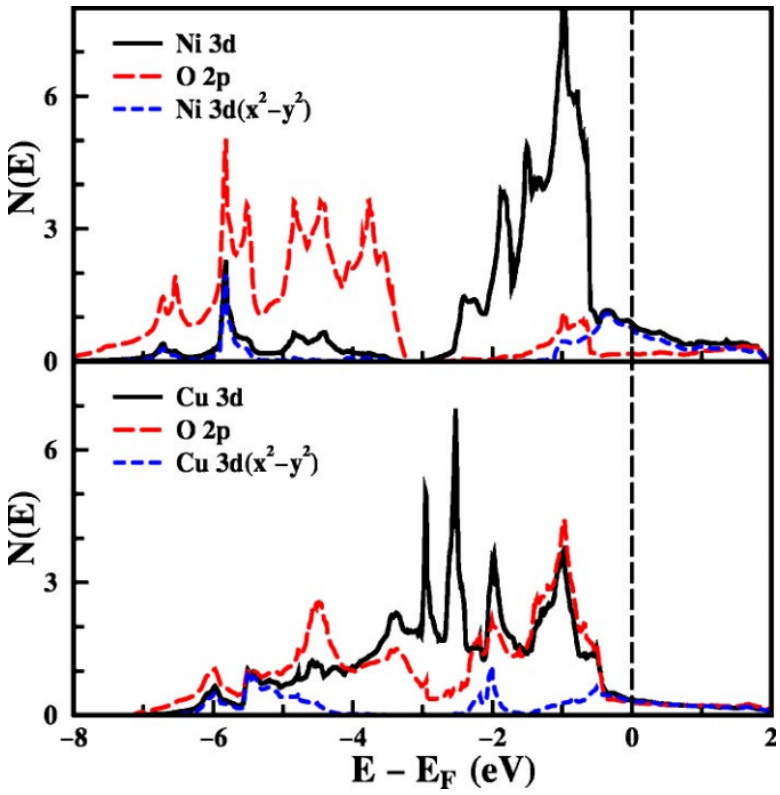

Figure 2-16. Comparison of calculated LDA projected paramagnetic DOS $LaNiO_2$ (upper panel) and $CaCuO_2$ (lower panel) using DFT. Reproduced with permission from (*37*). Copyright 2012 by The American Physical Society.

Apart from the isostrucural and isoelectronic similarities between $LaNiO_2$ and $CaCuO_2$, the overall magnetic features and behavior of $LaNiO_2$ are markedly different. $LaNiO_2$ is an apparent bad metal (lower resistivity than expected from the band diagram due to electron-electron interactions) – the temperature dependence of the paramagnetic susceptibility as well as the resistivity corroborate with the 3d orbitals of Ni crossing the Fermi level – as opposed to the insulating nature of $CaCuO_2$. There is no observed long range ordering of the spins in $LaNiO_2$ from

either the magnetic susceptibility measurements recorded from samples synthesized using the solvothermal method or those presented in the literature; a refinement of neutron data by Hayward also failed to elucidate any type of spin ordering (*9*, *31*). This is markedly different from the essentially universal antiferromagnetic spin ordering of the high-T_c superconducting cuprates (*38–40*). The lack of long range magnetic ordering in $LaNiO_2$ may be a result of two different scenarios – a small amount of Ni^{2+} exists in the lattice, resulting in a general formula of $LaNiO_{2+x}$ where x is small enough to not break the crystal symmetry, or the exceptionally long Ni – O bonds (1.974(2) Å refined in this work, 1.979 Å reported (*9*)). The presence of Ni^{2+} – most likely from oxidation during sample transport or measurement preparation – could introduce a high enough number of hole carriers to suppress long range ordering, as seen in $La_{2-x}Sr_xCuO_4$, where the introduction of 3% by mole Cu^{3+} suppresses the antiferromagnetic long range ordering, lowering the Nèel temperature from 250 K to 6 K (*41*). The decrease in covalency caused by the long Ni-O bonds would lead to the weakening of the superexchange mechanism between O – Ni – O; therefore, compared to the exceptionally strong superexchange mechanism (resulting in the antiferromagnetic spin ground state) in $CaCuO_2$ where the O 2p and Cu 3d orbitals overlap very well, no long range magnetic ordering is seen in $LaNiO_2$.

2.4 Reduction of $EuNiO_3$

All known nickelates with infinite NiO_2 layers - $Ln_3Ni_2O_6$, $Ln_4Ni_3O_8$, and $LnNiO_2$ (Ln = La, Nd) - contain nickel in formal oxidation states between 1.5+ and 1+. Considering that there are no perovskite related nickelates in which the subsequent reduction would result in a Ni^{2+} IL perovskite phase where only the Ni oxidation state is reduced, we examined $EuNiO_3$ as a possible precursor for the formation of the infinite layer compound $EuNiO_2$. In this case, both Eu and Ni are expected to be reduced from the 3+ to 2+ oxidation state during topotactic oxygen deintercalation. $EuNiO_2$ would be the first perovskite infinite layer structure with Ni in the 2+ oxidation state. The high-pressure synthesis presented in the following sections was done in collaboration with Dr. Jai Prakash at MSU.

2.4a Solvothermal synthesis of $EuNiO_3$

$EuNiO_3$ was synthesized by a flux method using high purity Eu_2O_3 (99.99%, Strem) and NiO (99.8%, Sigma-Aldrich) as reactants and a LiCl (99%, Sigma-Aldrich) and KCl (ACS grade, Columbus Chemical Industries) mixture (4:6) as the flux. $EuNiO_3$ and NiO were preheated to remove adsorbed water at 900 °C and 400 °C, respectively. The reactants were weighed according to the stoichiometric ratio and mixed with a LiCl/KCl flux in a N_2-filled glovebox with a ratio of flux to reactants fixed to 5:1 by weight. The reaction was carried out under an O_2 pressure of 180 bar at 400 °C for 16 days and then cooled to room temperature under 180 bar of oxygen pressure. A high pressure autoclave (Parr model 4652) was used

for all of the high pressure experiments. The products were washed with 0.2 M HCl to remove the flux (LiCl/KCl) and un-reacted oxides, and then dried in air at 50 °C to afford a black powder.

An attempt at the synthesis of $EuNiO_3$ using lower temperatures was made by employing a molten NaOH/KOH eutectic mixture as a solvent to dissolve the otherwise insoluble Eu_2O_3. The use of fluxes at low temperatures allows for the stabilization of kinetically metastable phases as compared to the thermodynamic sinks favored when reacting at high temperatures. Stoichiometric amounts of Eu_2O_3 and NiO were ground together under inert atmosphere, placed in an alumina boat with a twofold excess of dry NaOH/KOH in a 50:50 mixture, and loaded into a tube furnace in a fused silica tube. The reactants were heated to 300 °C at a heating rate of 70 °C/min under flowing oxygen and held for 120 hrs. After the reaction cooled to room temperature, the product mixture was washed with water to remove the hydroxides, resulting in a mixture of the layered α-$NaFeO_2$ type phases $NaNiO_2$ and Na_xNiO_2 ($0.80 < x < 1.00$), Eu_2O_3, and NiO. Interestingly, synthesis of the layered phases Na_xNiO_2 has only been reported above 700 °C; however, the changed energetics under molten salt conditions stabilized the layered phase at a much lower temperature. The same reaction was attempted solvothermally at 200 °C in the presence of 5 mL of water, resulting in starting materials only.

To understand whether $EuNiO_3$ can be produced at a lower oxygen pressure than 180 bar, a 45 mL Parr autoclave was loaded with stoichiometric amounts of

Eu_2O_3 and NiO, as well as a molar equivalent of $KMnO_4$ to generate oxygen pressure in-situ according to the following reaction above 200 °C under ambient pressure:

$$2KMnO_4 \rightarrow K_2MnO_4(s) + MnO_2(s) + O_2(g) \qquad (2\text{-}13)$$

The autoclave was heated to 225 °C and held for 72 hours. An autogenous pressure of 7.35 atm was generated upon decomposition of the permanganate assuming ideal gas conditions as well as full decomposition based on the study done by Weissman, neither of which are entirely accurate (*42*). Since the $KMnO_4$ was physically separated from the Eu_2O_3 and NiO via a Teflon cup, no separation techniques were required to isolate the product mixture. Only starting materials and an unknown, low symmetry phase were present after the reaction.

Reduction of $EuNiO_3$ was attempted through two routes: solid state reduction using 100% H_2, and a solvothermal route similar to the reduction of $La_4Ni_3O_{10}$ to $La_4Ni_3O_8$. For the solid state reduction reactions, $EuNiO_3$ was finely ground and loaded into an alumina boat, which was centered in a 3' quartz tube. Alumina boats filled with P_2O_5 were placed at either end of the quartz tube to absorb any released water and the tube was sealed with glass barbed fittings. Pure hydrogen was passed over the sample while the reaction temperature was modulated to elucidate a possible synthetic route to the reduction of $EuNiO_3$ while avoiding complete decomposition.

The solvothermal reactions were prepared in a nitrogen filled glovebox while utmost care was taken to avoid exposing any of the metal hydride reducing agents

to air or oxidizing solvents. A 45 mL Teflon lined Parr 4744 autoclave was charged with a 30 molar excess of a reducing agent (CaH_2, NaH), 250 mg of finely ground $EuNiO_3$, and 20 mL of anhydrous pentane. The autoclave was sealed inside of the glovebox and placed in a top-down furnace. Both time (24 hours to 240 hours) and temperature (100 °C - 200 °C) were varied in attempts to obtain the infinite layer $EuNiO_2$ phase via the solvothermal reduction route.

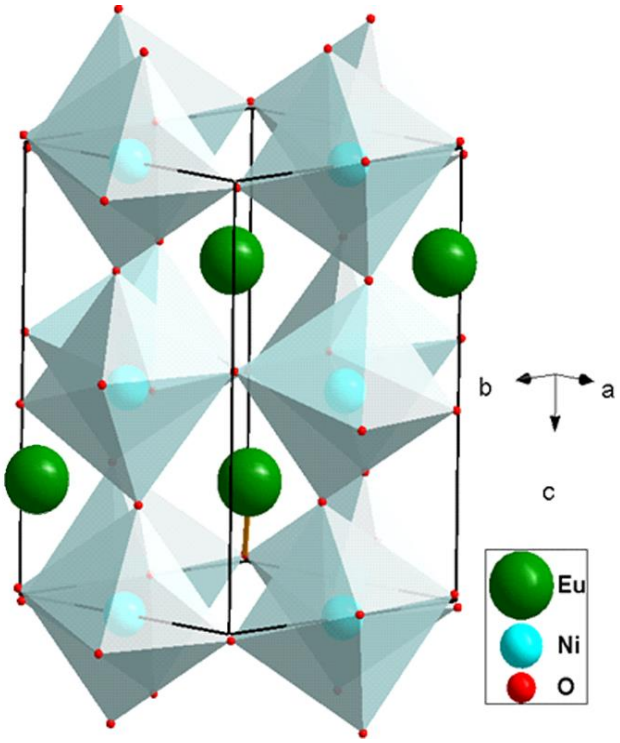

Figure 2-17. Crystal structure of the perovskite $EuNiO_3$ (*Pbnm*, *a* = 5.2984(3) Å, *b* = 5.4572(2) Å, *c* = 7.5365(3) Å) obtained via solvothermal synthesis.

The synthesis of $EuNiO_3$ at 400 °C and 1 bar of O_2 pressure in a LiCl/KCl flux was unsuccessful. The PXD pattern of the washed product showed the presence

of Eu_2O_3 and NiO reagents, indicating the necessity for high O_2 pressure during the synthesis of this compound.

Synthesis of $EuNiO_3$ at 400 °C and 180 bar O_2 pressure lead to the formation of the perovskite phase (Figure 2-17). The products were shiny black in color and were found to be stable under ambient condition and towards water. PXD pattern show very sharp diffraction peaks reflecting the good crystalline nature of the samples. All observed reflections could be indexed on the basis of an orthorhombic *Pbnm* structure. Refined lattice parameters of $EuNiO_3$ were found to be a = 5.2984(3) Å, b = 5.4572(2) Å, and c = 7.5365(3) Å, which are in good agreement with previous reports (*43*, *44*).

2.4b Discussion on the reduction of $EuNiO_3$

During TGA analysis of $EuNiO_3$, the mass of the samples under an O_2 atmosphere remains constant until 950 °C, indicating the absence of any oxygen vacancies, as well as absence of a decomposition process (Figure 2-18). This is in striking contrast with the high pressure conditions required for these compounds. Therefore, annealing of $EuNiO_3$ at 950 °C in O_2 flow for 3 hours was performed. PXD of the annealed product confirmed full $EuNiO_3$ decomposition attributing the TGA experiment results to the relative kinetic stability of $EuNiO_3$ under the experimental conditions used.

The DSC curve for $EuNiO_3$ showed an endothermic peak at 186.5 °C, corresponding to the metal-to-insulator transition and agreed well with previous

reports (*43*, *44*). TGA analysis of $EuNiO_3$ under a N_2 atmosphere showed no change in the sample weight until 772 °C. Above this temperature, thermal decomposition occurred in one well-defined step which starts at 772 °C and ends at 900 °C. The observed weight loss on the TG curve was 3.10%, very close to the 3.09% weight loss of 0.25 O_2. To check the final products after decomposition of $EuNiO_3$ under a N_2 atmosphere, the sample was subjected to heat treatment at 950 °C for 3 hrs, resulting in decomposition to Eu_2O_3 and NiO. TGA and PXD results for $EuNiO_3$ suggests the following reaction under a N_2 environment:

$$EuNiO_3 \rightarrow 0.5Eu_2O_3 + NiO + 0.25O_2 \qquad (2\text{-}14)$$

The TGA of $EuNiO_3$ under a reducing atmosphere of hydrogen (10% H_2/N_2) is shown in Figure 2-18. The mass of $EuNiO_3$ remains nearly constant until 384 °C, above which a clear weight loss step occurs starting from 384 °C and ending at 570 °C. The sample weight above 570 °C remains constant until the final temperature (950 °C). The observed weight loss (9.04%) corresponds to a composition of "$EuNiO_{1.5}$", indicating the formation of Eu_2O_3 and Ni. Data obtained from both TGA and PXD (Figure 2-19) measurements for $EuNiO_3$ suggests the following chemical reaction under a H_2 environment:

$$EuNiO_3 + 1.5H_2 \rightarrow 0.5Eu_2O_3 + Ni + 1.5H_2O \qquad (2\text{-}15)$$

Utilization of the LiCl/KCl flux has allowed for a drastic decrease in the temperature required to prepare $EuNiO_3$ (from 1000 °C to 400 °C). While pressure is needed to prepare $EuNiO_3$, a reaction at lower temperature allows for the use of

less expensive and commercially available autoclaves with large internal volumes. The developed method is expected to be suitable for the preparation of other rare-earth based nickelates.

We hoped that the reduction of $EuNiO_3$, in a similar manner to the reduction of $LaNiO_3$ discussed earlier, would lead to the formation of $EuNiO_2$, a new compound with both Eu and Ni in the 2+ oxidation state. This compound would be the first infinite layer structure with Ni in the 2+ oxidation state. Unfortunately, the employed experimental conditions did not indicate the possibility of such phase preparation due to the metastability of oxygen deficient $EuNiO_{3-x}$.

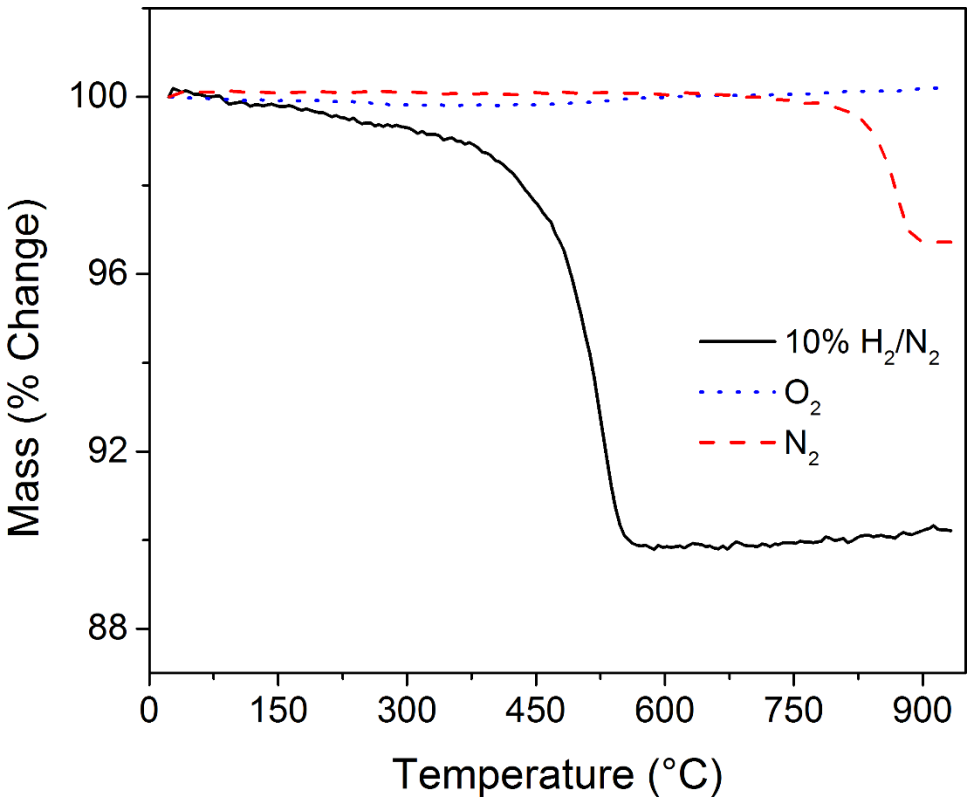

Figure 2-18. TGA data for $EuNiO_3$ recorded under different atmospheres.

Reduction of $EuNiO_3$ using the solid state method employing H_2 as a reducing agent was attempted in the temperature range of 200 °C to 300 °C with a firing time of 36 hours and a heating ramp of 4 hours. Between 200 °C and 235 °C, no decomposition products were observed and $EuNiO_3$ was phase pure after 36 hours. Beginning at 240 °C, the reduction of $EuNiO_3$ resulted in the presence of small amounts of Eu_2O_3 in the PXD pattern. From 260 °C - 280 °C, decomposition was the primary reaction occurring, while small amounts of $EuNiO_3$ were present after 36 hours. Complete decomposition at 300 °C was confirmed by the presence of Eu_2O_3 and Ni without any traces of $EuNiO_3$ in the PXD pattern.

Under solvothermal experimental conditions, decomposition to Eu_2O_3 and Ni metal began to occur at 150 °C when $EuNiO_3$ was reduced with NaH after 168 hours. Interestingly, $EuNiO_3$ was also present in this sample, confirming the fact that if any oxygen-deficient phases of $EuNiO_{3-x}$ exist, they are exceptionally metastable and might be isolated using other, currently undeveloped, techniques.

As the solvothermal reaction temperature approached 200 °C, complete decomposition of $EuNiO_3$ was observed. At 100 °C, a small amount of NaOH was present in the PXD pattern after 168 hours, indicating reduction had occurred; however, there were no new diffraction peaks associated with either an oxygen-deficient perovskite $EuNiO_{3-x}$ structure or the decomposition products Eu_2O_3 or Ni.

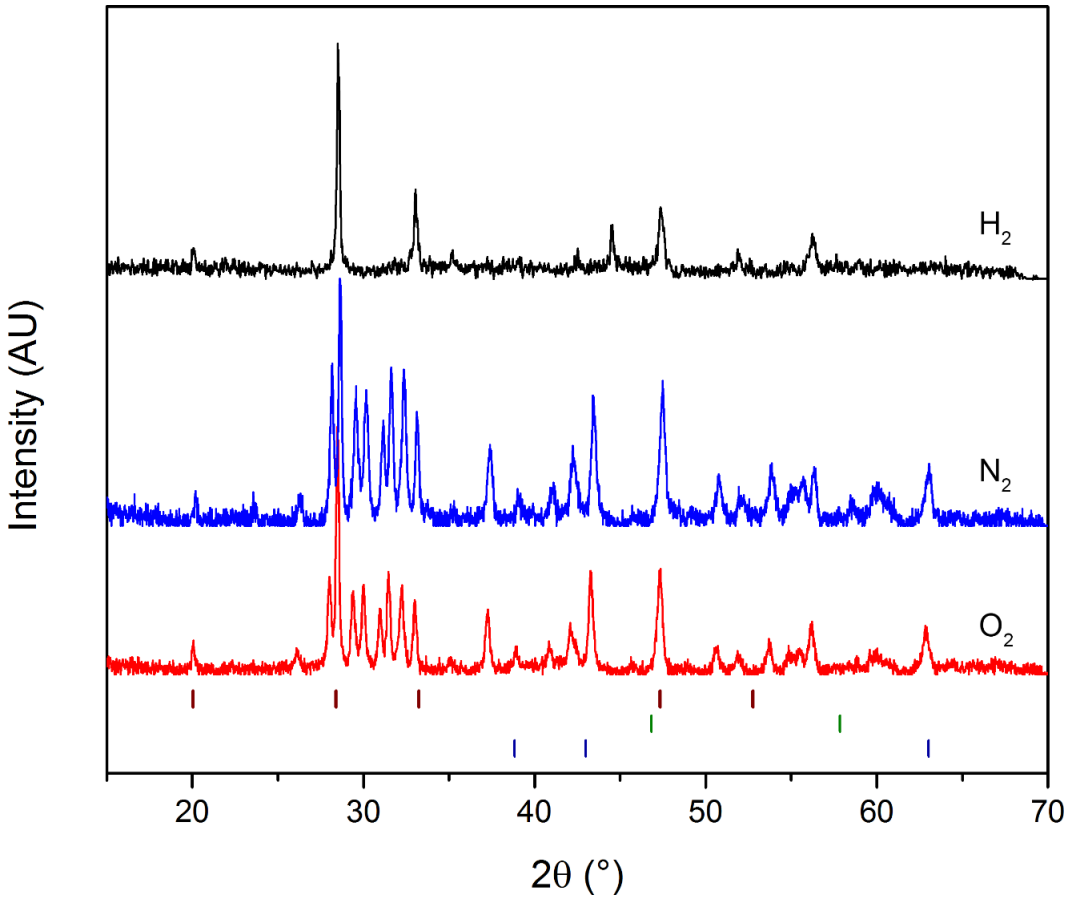

Figure 2-19. PXD spectra after decomposition of $EuNiO_3$ at 950 °C in O_2, N_2, and H_2. Tickmarks refer to cubic Eu_2O_3 (wine, top), Ni metal (olive, middle), and Ni (navy, bottom). All other reflections were indexed as monoclinic Eu_2O_3.

This result can be attributed to a small amount of decomposition of $EuNiO_3$, resulting in nanoparticles of Eu_2O_3 and Ni that are in amounts undetectable via the D2-Phaser diffractometer employed. The autogenous pressures associated with the solvothermal experiments at 100 °C, 150 °C and 200 °C were 12.38 atm, 15.65 atm, and 59.74 atm, respectively.

In conclusion, no oxygen-deficient phases of $EuNiO_3$ were observed under TGA conditions, solid state reduction conditions, or solvothermal conditions.

2.5 Chapter Conclusions

A novel solvothermal topotactic oxygen deintercalation method employing metal hydrides and organic solvents was described and validated via reduction of $La_4Ni_3O_{10}$ to $La_4Ni_3O_8$ at 150 °C. The relative reduction activities of different conventional solid state reduction techniques were compared to determine the reductive power of the proposed solvothermal method. Introduction of pressure is favorable and leads to formation of pure $La_4Ni_3O_8$ at lower temperatures than previously reported.

Nearly pure phase $LaNiO_2$ was synthesized using the solvothermal method developed. The material was fully characterized, including a reinvestigation of the magnetic properties and comparison to previously published results. According to the Rietveld refinement and magnetic properties, the $LaNiO_2$ sample prepared by the solvothermal method saw an approximately fourfold increase in purity compared to literature reports (by ratio of $LaNiO_2$:$La_2Ni_2O_5$).

Multiple attempts were made to synthesize Ni^{2+} in square planar configuration in $EuNiO_2$. The parent phase, $EuNiO_3$, was synthesized via a simple solvothermal method that was substantially easier than literature methods. Reduction of $EuNiO_3$ to $EuNiO_2$ using multiple methods was unsuccessful as shown by multiple characterization methods.

2.6 Future Work on this Topic

Recent literature has presented other 3d transition metals in square planar configuration, including Mn in $BiMn_7O_{12}$ (*45*), Co in $YBaCo_2O_5$ (*15*), and Fe in $SrFeO_2$ (*46*). Investigation of the reduction of perovskites and perovskite-related phases with these metals would be an interesting continuation of this project. Due to the exploratory type of this project and the high-risk, high-reward nature of metastable phase synthesis, a full thesis could be written on this topic alone.

REFERENCES

REFERENCES

(1) Blakely, C. K.; Bruno, S. R.; Poltavets, V. V. Low-temperature solvothermal approach to the synthesis of $La_4Ni_3O_8$ by topotactic oxygen deintercalation. *Inorg. Chem.* **2011**, *50*, 6696–700.

(2) Lappas, A.; Nuttall, C. J.; Fthenakis, Z. G.; Pomjakushin, V. Y.; Roberts, M. A. Topotactic Intercalation of a Metallic Dense Host Matrix Chalcogenide with Large Electron–Phonon Coupling: Crystal Structures and Electronic Properties of $Li_xMo_2SbS_2(0 \leq x < 0.7)$. *Chem. Mater.* **2007**, *19*, 69–78.

(3) Nemudry, A.; Rudolf, P.; Schoollhorn, R. Topotactic Electrochemical Redox Reactions of the Defect Perovskite $SrCoO_{2.5+x}$. **1996**, *4756*, 2232–2238.

(4) Taguchi, H.; Shimada, M.; Koizumi, M. The Effect of Oxygen Vacancy on the Magnetic Properties in the System $SrCoO_{3\text{-delta}}$. *J. Solid State Chem.* **1979**, *225*, 221–225.

(5) Crespin, M.; Levitz, P.; Gatineau, L. Reduced Forms of $LaNiO_3$ Perovskite. **1983**, 1181–1194.

(6) Poeppelmeier, K. R.; Leonowicz, M. E.; Scanlon, J. C.; Longo, J. M.; Yelon, B. Structure Determination of $CaMnO_3$ and $CaMnO_{2.5}$ by X-Ray and Neutron Methods. *J. Solid State Chem.* **1982**, *79*, 71–79.

(7) Yamamoto, T.; Kageyama, H. Hydride Reductions of Transition Metal Oxides. *Chem. Lett.* **2013**, *42*, 946–953.

(8) Alonso, J. A.; Martinez-Lope, M. J.; Garcia-Munoz, J. L.; Fernandez-Diaz, M. T. A structural and magnetic study of the defect perovskite $LaNiO_{2.5}$ from high-resolution neutron diffraction data. *J. Phys. Condens. Matter* **1997**, *9*, 6417–6426.

(9) Hayward, M. A.; Green, M. A.; Rosseinsky, M. J.; Sloan, J. Sodium Hydride as a Powerful Reducing Agent for Topotactic Oxide Deintercalation: Synthesis and Characterization of the Nickel(I) Oxide $LaNiO_2$. *J. Am. Chem. Soc.* **1999**, *121*, 8843–8854.

(10) Hayward, M. A.; Rosseinsky, M. J. Synthesis of the infinite layer Ni(I) phase $NdNiO_{2+x}$ by low temperature reduction of $NdNiO_3$ with sodium hydride. *Solid State Sci.* **2003**, *5*, 839–850.

(11) Poltavets, V. V; Lokshin, K. A.; Dikmen, S.; Croft, M.; Egami, T.; Greenblatt, M. $La_3Ni_2O_6$: a new double T'-type nickelate with infinite $Ni^{1+/2+}O2$ layers. *J. Am. Chem. Soc.* **2006**, *128*, 9050–1.

(12) Poltavets, V. V.; Lokshin, K. A.; Egami, T.; Greenblatt, M. The oxygen deficient Ruddlesden–Popper $La_3Ni_2O_{7-\delta}$ (δ=0.65) phase: Structure and properties. *Mater. Res. Bull.* **2006**, *41*, 955–960.

(13) Tsujimoto, Y.; Tassel, C.; Hayashi, N.; Watanabe, T.; Kageyama, H.; Yoshimura, K.; Takano, M.; Ceretti, M.; Ritter, C.; Paulus, W. Infinite-layer iron oxide with a square-planar coordination. *Nature* **2007**, *450*, 1062–5.

(14) Tassel, C.; Pruneda, J. M.; Hayashi, N.; Watanabe, T.; Kitada, A.; Tsujimoto, Y.; Kageyama, H.; Yoshimura, K.; Takano, M.; Nishi, M.; Ohoyama, K.; Mizumaki, M.; Kawamura, N.; Iñiguez, J.; Canadell, E. $CaFeO_2$: a new type of layered structure with iron in a distorted square planar coordination. *J. Am. Chem. Soc.* **2009**, *131*, 221–9.

(15) Seddon, J.; Suard, E.; Hayward, M. A. Topotactic reduction of $YBaCo_2O_5$ and $LaBaCo_2O_5$: square-planar Co(I) in an extended oxide. *J. Am. Chem. Soc.* **2010**, *132*, 2802–10.

(16) Bowman, A.; Allix, M.; Pelloquin, D.; Rosseinsky, M. J. Three-coordinate metal centers in extended transition metal oxides. *J. Am. Chem. Soc.* **2006**, *128*, 12606–7.

(17) Zhu, Y. T.; Manthiram, A. A New Route for the Synthesis of Tungsten Oxide Bronzes. *J. Solid State Chem.* **1994**, *110*, 187–189.

(18) Tsang, C.; Lai, S. Y.; Manthiram, A. Reduction of Aqueous Na_2WO_4 by $NaBH_4$ at Ambient Temperatures To Obtain Lower Valent Tungsten Oxides. *Inorg. Chem.* **1997**, *36*, 2206–2210.

(19) Tsang, C.; Dananjay, A.; Kim, J.; Manthiram, A. Synthesis of Lower Valent Molybdenum Oxides by an Ambient Temperature Reduction of Aqueous K_2MoO_4 by KBH_4. *Inorg. Chem.* **1996**, *35*, 504–509.

(20) Hwang, S.-J.; Choy, J.-H. Local Atomic Arrangement and Electronic Structure of Nanocrystalline Transition Metal Oxides Determined by X-ray Absorption Spectroscopy. *J. Phys. Chem. B* **2003**, *107*, 5791–5796.

(21) Manthiram, A.; Tsang, C. Synthesis of Amorphous MoO_{2+x} and Its Electrode Performance in Lithium Batteries. *J. Electrochem. Soc.* **1996**, *143*, 10–12.

(22) Tsang, C. F.; Manthiram, A. Synthesis of lower-valent molybdenum oxides in aqueous solutions by reducing Na_2MoO_4 with $NaBH_4$. *J. Mater. Chem.* **1997**, *7*, 1003–1006.

(23) Zhou, C. X.; Wang, Y. X.; Yang, L. Q.; Lin, J. H. Syntheses of hydrated molybdenum bronzes by reduction of MoO_3 with $NaBH_4$. *Inorg. Chem.* **2001**, *40*, 1521–6.

(24) Poltavets, V. V; Lokshin, K. A.; Croft, M.; Mandal, T. K.; Egami, T.; Greenblatt, M. Crystal structures of $Ln_4Ni_3O_8$ (Ln = La, Nd) triple layer T'-type nickelates. *Inorg. Chem.* **2007**, *46*, 10887–91.

(25) Gnanasekaran, T. Thermochemistry of binary Na–NaH and ternary Na–O–H systems and the kinetics of reaction of hydrogen/water with liquid sodium – a review. *J. Nucl. Mater.* **1999**, *274*, 252–272.

(26) Wen, X.-D.; Cahill, T. J.; Gerovac, N. M.; Bucknum, M. J.; Hoffmann, R. Playing the quantum chemical slot machine: an exploration of ABX_2 compounds. *Inorg. Chem.* **2010**, *49*, 249–60.

(27) Al-Mamouri, M.; Edwards, P. P.; Greaves, C.; Slaski, M. Synthesis and superconducting properties of the strontium copper oxyfluoride $Sr_2CuO_2F_{2+\delta}$. *Nature* **1994**, *369*, 382–384.

(28) Slakle, J. M. S. Crystal chemical substituents and doping of $YBa_2Cu_3O_x$ and related superconductors. *Mater. Sci. Eng. R Reports* **1998**, 1–40.

(29) Schlesslnger, R. H.; Burk, D.; Lobo, A. P.; Nordlander, J. E.; Roberts, J. D.; Gosselink, D. W.; Kaczynski, J. A.; Mckinley, V.; Beck, K. R.; Grutzner, J. B.; Ferber, G. J.; Kiinck, R. E.; Stothers, J. B. Nickel Phsophine Complexes. *145*, 5187–5189.

(30) Hayes, W.; Wilkens, J. An Investigation of the Ni^+ Ion in Irradiated LiF and NaF. *Proc. R. Soc. A Math. Phys. Eng. Sci.* **1964**, *281*, 340–365.

(31) Takamatsu, T.; Kato, M.; Noji, T.; Koike, Y. Low-temperature synthesis of the infinite-layer compound $LaNiO_2$ using CaH_2 as reductant. *Phys. C Supercond.* **2010**, *470*, S764–S765.

(32) Crespin, M.; Isnard, O.; Dubois, F.; Choisnet, J.; Odier, P. LaNiO: Synthesis and structural characterization. *J. Solid State Chem.* **2005**, *178*, 1326–1334.

(33) Alonso, J. A.; Martínez-Lope, M. J.; García-Muñoz, J. L.; Fernández, M. T. Crystal structure and magnetism in the defect perovskite $LaNiO_{2.5}$. *Phys. B Condens. Matter* **1997**, *234-236*, 18–19.

(34) Fonseca, F.; Goya, G.; Jardim, R.; Muccillo, R.; Carreño, N.; Longo, E.; Leite, E. Superparamagnetism and magnetic properties of Ni nanoparticles embedded in SiO_2. *Phys. Rev. B* **2002**, *66*, 104406.

(35) Knickelbein, M. B. Nickel clusters: The influence of adsorbed CO on magnetic moments. *J. Chem. Phys.* **2001**, *115*, 1983.

(36) Tse, J.; Klug, D.; Desgreniers, S.; Smith, J.; Flacau, R.; Liu, Z.; Hu, J.; Chen, N.; Jiang, D. Structural phase transition in CaH_2 at high pressures. *Phys. Rev. B* **2007**, *75*, 134108.

(37) Lee, K.-W.; Pickett, W. Infinite-layer $LaNiO_2$: Ni^{1+} is not Cu^{2+}. *Phys. Rev. B* **2004**, *70*, 165109.

(38) Poltavets, V.; Greenblatt, M.; Fecher, G.; Felser, C. Electronic Properties, Band Structure, and Fermi Surface Instabilities of Ni^{1+}/Ni^{2+} Nickelate $La_3Ni_2O_6$, Isoelectronic with Superconducting Cuprates. *Phys. Rev. Lett.* **2009**, *102*, 046405.

(39) Nakayama, R.; Tanaka, Y.; Yui, H.; Yamauchi, H.; Baron, A. Q. R.; Sasagawa, T. Preparation of infinite layer cuprate compounds $(Sr_{1-x}La_x)CuO_2$ and detailed phonon properties in x = 0. *Mater. Sci. Eng. B* **2010**, *173*, 41–43.

(40) Sachdev, S. Where is the quantum critical point in the cuprate superconductors? *Phys. Status Solidi* **2010**, *247*, 537–543.

(41) Budnick, J. I.; Chamberland, B.; Yang, D. P.; Niedermayer, C.; Golnik, A.; Recknagel, E.; Rossmanith, M.; Weidinger, A. Dependence of the Nèel-Temperatures of La_2CuO_4 on Sr-Doping Studied by Muon Spin Rotation. *Europhys. Lett.* **1988**, *5*, 651–656.

(42) Herbstein, F. H.; Ron, G.; Weissman, A. The thermal decomposition of potassium permanganate and related substances. Part I. Chemical aspects. *J. Chem. Soc. A Inorganic, Phys. Theor.* **1971**, 1821.

(43) Alonso, J. A.; Martinze-Lope, M. J.; Rasines, I. Preperation, Crystal Structure, and Metal-to-Insulator Transition of $EuNiO_3$. *J. Solid State Chem.* **1995**, *120*, 170–174.

(44) Torrance, J. B.; Lacorre, P.; Nazzal, A. I.; Ansaldo, E.; Niedermayer, C. Systematic study of insulator-metal transitions in perovskites $RNiO_3$ (R=Pr,Nd,Sm,Eu) due to closing of charge-transfer gap. *Phys. Rev. B* **1992**, *45*, 8209–8212.

(45) Okamoto, H.; Imamura, N.; Karppinen, M.; Yamauchi, H.; Fjellvag, H. Square Coordinated MnO_2-Units in $BiMn_7O_{12}$. *Solid State Ionics* **2010**, 8709–8712.

(46) Seinberg, L.; Yamamoto, T.; Tassel, C.; Kobayashi, Y.; Hayashi, N.; Kitada, A.; Sumida, Y.; Watanabe, T.; Nishi, M.; Ohoyama, K.; Yoshimura, K.; Takano, M.; Paulus, W.; Kageyama, H. Fe-site substitution effect on the structural and magnetic properties in $SrFeO_2$. *Inorg. Chem.* **2011**, *50*, 3988–95.

Chapter 3 : Soft chemistry synthesis of extended oxyfluoride materials

3.1 Survey of solid-state synthesis of inorganic oxyfluorides

Topotactic reactions, when extensive parts of the original framework are retained and only minor structural rearrangements take place, allows for greater control of the final product structures. Tuning the transition metal oxidation state via cation exchange is a well-studied and exploited method in the literature (*1–3*). Modification of the anion lattice primarily focuses on the preparation of oxyfluorides by fluorination of perovskite and related structures (Dion-Jacobson, Ruddlesden-Popper, etc.) where $NaCaNb_2O_6F$, $PbFeO_2F$, $Sr_2LaCu_2O_5F$, and $Sr_2MnGa(O,F)_6$ are the most studied examples (*4–9*). Applications of oxyfluorides include: high temperature superconductors, electrochromic glasses, next-generation lithium ion battery materials, and ferroelectrics (*10–14*). During the replacement of O^{2-} for F^{1-} crystal structure motifs are often preserved due to the similarity of ionic radii. Unfortunately, powder x-ray and neutron diffraction cannot differentiate between O^{2-} and F^{1-} positions in the structure thus preventing the establishment of O/F ordering (15).

Solid state synthesis methods employing pure F_2 as the fluorination agent are notoriously demanding and dangerous due to the high oxidizing potential of F_2 gas (*15*). Recently, fluorination methods involving less severe conditions have been proposed. Greaves and coworkers have reported oxyfluoride preparations using mixtures of the starting materials and transition metal fluorides MF_2 (M = Cu, Zn,

Ni, Ag) utilized as fluorination reagents (*16*). These reactions result in unwanted admixtures of the corresponding metal oxide byproducts, thus fluorinated polymers as sources of fluorine were also studied. Slater et al investigated the potential of poly(vinylidene fluoride) (PVDF) as a low temperature fluorinating agent in the synthesis of $Sr_2TiO_3F_2$ as well as $Ca_2CuO_2F_2$ from the parent materials Sr_2TiO_4 and Ca_2CuO_3, respectively, in a non-oxidative fashion (*17*, *18*). Oxidative fluorine intercalation has also been performed on the $Ln_{1.2}Sr_{1.8}Mn_2O_7$ (Ln = La, Pr, Nd, Sm, Eu, and Gd) system by decomposing PVDF at 400 °C to form $Ln_{1.2}Sr_{1.8}Mn_2O_7F_1$ (*19*). XeF_2 has seen more use in the recent literature as a powerful source of fluorine without the production of admixture M_xO_y or MF_2 byproducts. Due to the relatively high vapor pressure of XeF_2 , the temperatures required to perform fluorination using this reagent are in the 100 °C - 300 °C range, allowing for topotactic intercalation of fluorine into anion vacancies (*20*).

There are multiple examples of oxygen/fluorine ordering in the literature including $Sr_{3-x}Ba_xAlO_4F$, $Sr_7Mn_4O_{13}F_2$, and $Nb_3O_5F_5$ (*21*, *22*). When trying to achieve anion ordering during synthesis, it is important to perform anion intercalation at as low a temperature as possible to avoid thermal randomization of the anions (*21*, *23*, *24*).

The focus of this chapter is on the preparation of oxyfluoride materials by multiple different synthetic methods including a multistep fluorination method employing XeF_2 and a novel solvothermal method. Multiple proof-of-principle

cases are presented to demonstrate the fluorinating power of each of the approaches.

3.2 Novel multistep oxyfluoride synthesis procedure

In this section, a novel low temperature fluorination method employing XeF_2 for the synthesis of the oxyfluoride $SrFeO_2F$ via the recently discovered infinite layer compound $SrFeO_2$ is presented. Characterization of $SrFeO_2F$ was accomplished using Rietveld refinement of synchrotron powder diffraction data, Mössbauer spectroscopy, AC and DC magnetometry, and heat capacity measurements. The prepared $SrFeO_2F$ does not have long range O/F ordering but demonstrates differences in both magnetic properties and Mössbauer spectrum in comparison with the earlier reported disordered $SrFeO_2F$, lending credence to the idea that the chosen synthetic approach has an effect on short range O/F ordering and, consequently, on the properties of the compound (*7*).

3.2a Multistep synthetic route and experimental methods

All reagents were of analytical grade purity or higher and were used without further purification. $SrCO_3$ (99.9%), Fe_2O_3 (99.99%), and XeF_2 (99.9%) were obtained from Alfa Aesar. CaH_2 (99%) was purchased from Sigma Aldrich packed as a suspension in mineral oil. The CaH_2 was washed with anhydrous pentane under nitrogen to remove the mineral oil, resulting in a fine white powder. *Utmost care should be taken to avoid exposing the XeF_2 to moisture, as hazardous HF will form.*

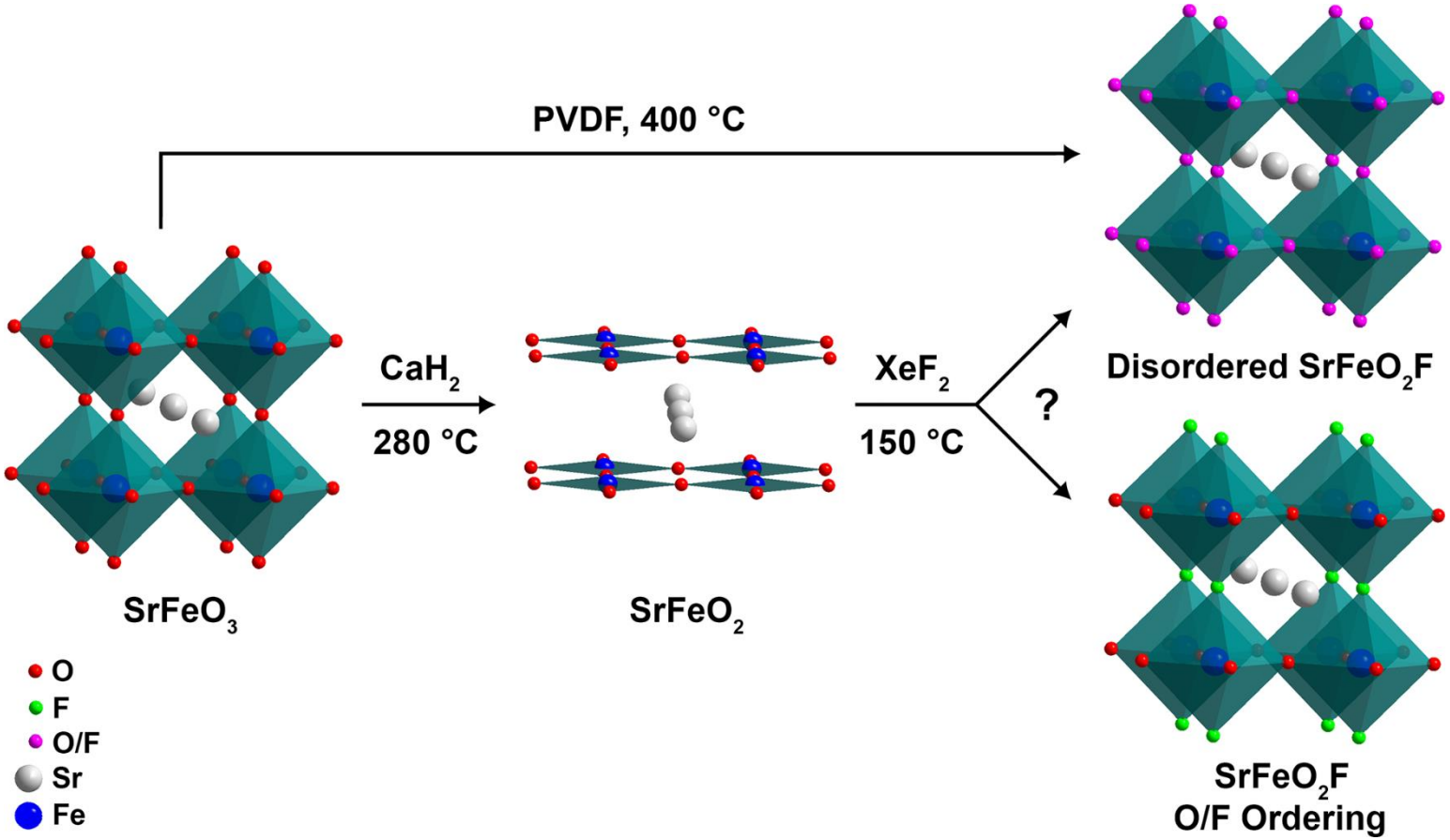

Figure 3-1. Multistep synthetic route for the preparation of the $SrFeO_2F$ oxyfluoride. The previously known literature method using PVDF at 400 °C is also highlighted (*6*).

The parent cubic perovskite $SrFeO_{3-x}$ was synthesized by the reaction of $SrCO_3$ and Fe_2O_3. 0.739 g (5 mmol) of $SrCO_3$ was coarsely mixed with 0.399 g (2.5 mmol) Fe_2O_3 then ball milled in agate jars for 30 minutes with four 6 mm agate balls using a Fritsch Planetary ball mill. The powder was then pelletted in 3/4" pellets under 5 tons pressure and fired at 1000 °C in air for 48 hours. $SrFeO_2$ was prepared via a modified literature method (*25*), described below, where large quantities of sample were produced per batch to avoid batch inconsistencies. 4.75 g (25 mmol) of previously synthesized $SrFeO_{3-x}$ was intimately ground with 4.20 g (100 mmol) of CaH_2 in a nitrogen filled glovebox. The precursor mixture was loaded into an ampoule then connected to a silicon oil bubbler, removed from the glovebox and lowered through the top of a muffle furnace. The material was fired at 280 °C for 48 hours with no intermittent grindings. The ampoule was connected to a silicon oil bubbler to release the hydrogen pressure. After completion of the reaction, the product was washed with four 100 mL aliquots of a saturated NH_4Cl in methanol solution to remove any remaining CaH_2 as well as the CaO reduction byproduct.

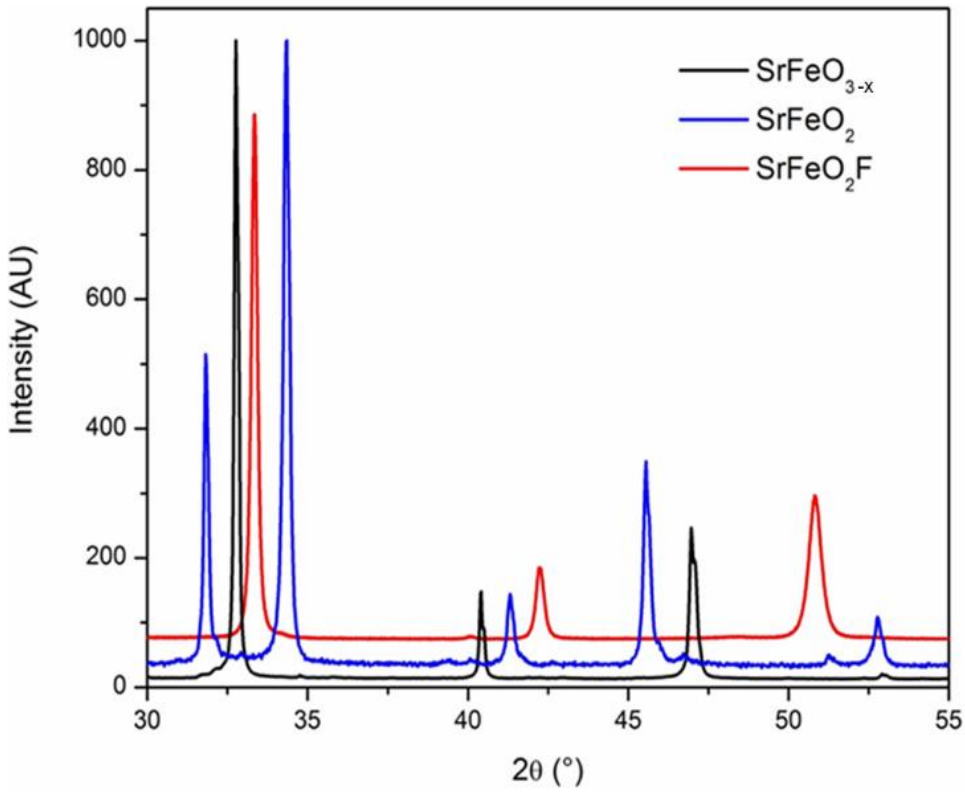

Figure 3-2. Comparison of PXD patterns of the $SrFeO_{3-x}$ perovskite (bottom pattern), the $SrFeO_2$ infinite-layer compound (middle), and the $SrFeO_2F$ oxyfluoride (top).

The oxyfluoride phase $SrFeO_2F$ was prepared via the reaction of the infinite-layer $SrFeO_2$ with XeF_2. 500 mg (2.87 mmol) of $SrFeO_2$ was weighed out in a glovebox and loaded into a teflon sleeve along with 289 mg (1.70 mmol) of XeF_2, previously weighed under N_2 using a teflon spoon and a Ni weighing dish. The sleeve was sealed in a steel autoclave then removed from the glovebox and placed in a furnace. The mixture was heated for 48 hours at 150 °C, after which the

product was stored under N_2 due to the extremely moisture sensitive nature of the oxyfluoride.

3.2b Synthesis and characterization of $SrFeO_2F$

Powder X-ray Diffraction (PXD) patterns were obtained on a Bruker D8 Advanced New diffractometer using Cu radiation with a $K_{\alpha 1}$ wavelength of 1.5418 Å. The Synchrotron Powder x-ray Diffraction (SPXD) pattern was collected on the Argonne National Lab Synchrotron BM-11 beam line using a 0.8 mm kapton capillary. The sample was first sealed in a 0.6 mm glass capillary then placed in the kapton capillary and held with wax. The synchrotron source wavelength was 0.373822 Å.

Rietveld refinement and structure analysis were completed using the GSAS software package. Peak positions, unit cell parameters, background parameters, and profile parameters were refined one by one, followed by a refinement of all parameters.

Average Fe oxidation state was determined by iodometric titration. The iodometric titration procedure has been described previously (*26*). Care was taken to avoid exposure to oxygen by blowing nitrogen over the flask. Fluorine content was investigated by ion selective electrode (ISE) technique. ISE measurements were performed using a Hanna Instruments HI 4110 Fluoride Combination ISE electrode with an ion-activity buffer (TISAB II) by the calibration curve method. Careful attention was paid to both the temperature of the material and the electrode

equilibration time before recording the voltage response. Inductively coupled plasma (ICP) spectroscopy was performed on a Vista-MPX CCD Simultaneous ICP-OES instrument (Varian Inc.).

The parent oxygen-deficient perovskite $SrFeO_{3-x}$ adopts a highly symmetric cubic geometry with 12-coordinate Sr^{2+} and corner sharing FeO_6 octahedra. Topotactic oxygen deintercalation of the parent led to the removal of the apical O^{2-} from the FeO_6 octahedra to form the tetragonal infinite-layer compound $SrFeO_2$.

While the reaction temperature and time used for the preparation of $SrFeO_2$ were the same as previously reported by Tsujimoto et al. (*25*), instead of using a sealed Pyrex tube the ampoule was connected to a bubbler filled with silicon oil. $Ca(OH)_2$ formed during reaction with the oxide phase further reacted with CaH_2, leading to the formation of CaO and H_2. Utilizing a bubbler prevents H_2 pressure build up and allows for scaling up of the synthesis in a safe manner; therefore, multiple grams of $SrFeO_2$ can be prepared in one batch instead of a few hundred milligrams as previously reported. From this it can be concluded that H_2 pressure is not required for $SrFeO_2$ formation as the reduction process occurs through the direct reaction of 2 solids.

Fluorination, the third step in the multistep synthesis route, resulted in the oxidative insertion of F^{1-} to give the final cubic oxyfluoride phase $SrFeO_2F$. The reaction temperature was critical in obtaining phase pure oxyfluoride. When fired at 250 °C, a small admixture of SrF_2 was always present regardless of the excess amount of XeF_2 used, which manifested as broad SrF_2 reflections in the powder x-

ray diffraction pattern due the poor crystallinity of the admixture. Reacting the starting materials at 150 °C resulted in $SrFeO_2F$ with no traces of SrF_2. Comparing this result with the literature data where $SrFeO_2F$ was prepared at 400 °C by fluorination of $SrFeO_{3-x}$ with poly(vinylidene fluoride) we can conclude that the appearance of SrF_2 at 250 °C is not related to the insufficient kinetic stability of the metastable $SrFeO_2F$ product but rather to the energetic ease of SrF_2 formation when the $SrFeO_2$ precursor is used.

PXD patterns indicating pure phases of $SrFeO_{3-x}$, $SrFeO_2$, and $SrFeO_2F$ are compared in Figure 3-2. The $SrFeO_2F$ pattern was readily refined in the cubic space group $Pm\bar{3}m$ (a = 3.955 Å), similar to the parent perovskite phase $SrFeO_{3-x}$, with an R_{wp} value of 1.68 %. Observed, calculated, and difference plots for the Rietveld refinement of $SrFeO_2F$ are shown in Figure 3-3. An anion disordered structure was used in the refinement due to the similar scattering factors of O^{2-} and F^{1-}. Refinement of the anion sites led to complete occupancy.

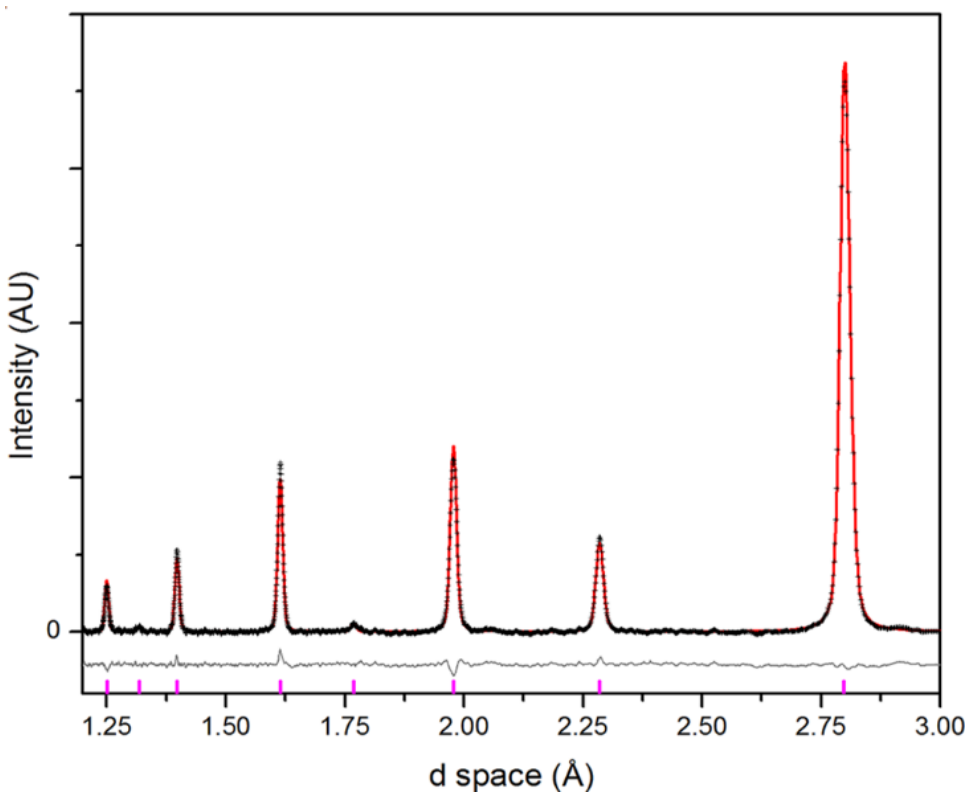

Figure 3-3. Rietveld refinement of the synchrotron powder x-ray diffraction data of $SrFeO_2F$ showing the observed pattern (black crosses), fitted pattern (red trace), difference curve (gray trace, below), and Bragg peak positions (magenta tickmarks, below).

Unit cell parameters for $SrFeO_{3-x}$, $SrFeO_2$, and $SrFeO_2F$ as well as the structural data for $SrFeO_2F$ are presented in Tables 3-1 and 3-2, respectively. Large thermal parameters for the anion position in $SrFeO_2F$ might indicate a minute shift of O/F atoms from the special position. However, refinements with anions in a lower symmetry position did not lead to lower goodness-of-fit parameters.

Due to the presence of trivalent fluorine-complexing ions (Fe^{3+}), the use of a fluoride ion-selective electrode resulted in underestimated F content values even when an ion-activity buffer (TISAB II) was added.

Because fluorination reactions can lead to fluorine insertion into interstitial positions as well as fluorine-for-oxygen substitution, prepared oxyfluorides can be represented by the general formula $SrFeO_xF_y$. Due to the presence of two unknown variables, O_x and F_y, two different compositional analysis methods must be corroborated to deduce the actual composition. Using ICP spectroscopy, the molar mass of the oxyfluoride, 194.5 g/mol, was quantitatively deduced from the Sr and Fe content and known initial sample mass assuming the presence of 1 Sr and 1 Fe ion per oxyfluoride formula unit, as in the initial $SrFeO_3$ and intermediate $SrFeO_2$ compounds. This assumption is assured by the fact that no impurities containing Sr or Fe were found in the synchrotron data. The average Fe oxidation state (2.99+) was determined by iodometric titration. As a result of these two experiments, both O_x and F_y can be solved, resulting in a stoichiometry of $Sr_{1.00(1)}Fe_{1.00(1)}O_{2.01(1)}F_{0.99(1)}$.

The *a* parameter increased to 3.955 Å in the oxyfluoride phase relative to 3.851 Å in the parent perovskite $SrFeO_{3-x}$ due to the size difference between Fe^{3+} and Fe^{4+}. Direct establishment of O/F ordering by diffraction techniques is not possible due to the similar X-ray form factors and neutron coherent scattering lengths (O^{2-} = 5.803 fm, F^{1-} = 5.654 fm) for these anions (*27*). However, there is a subtle difference in the ionic radii in a 6 coordinate environment: O^{2-} = 1.26 Å while F^{1-} =

1.19 Å (*28*); therefore, layered O/F ordering in $SrFeO_2F$ might lead to a tetragonal distortion with different values for the *a* and *c* cell parameters. This hypothesis was confirmed by DFT calculations as discussed above. No tetragonal distortion was observed for $SrFeO_2F$ by PXD or by SPXD. Therefore, there is no long range layered anion ordering in the prepared oxyfluoride and an anion disordered structure was formed in spite of using a precursor with ordered O vacancies ($SrFeO_2$). As the Sr/Fe cationic sublattice was preserved during fluorination, this reaction can be considered topotactic; however, O/F mixing in $SrFeO_2F$ over the same anionic crystallographic position indicates that both anions are mobile during the fluorination procedure. Mobility of the anion sublattice in $SrFeO_2$ has been previously investigated, where during O intercalation the intermediate $Sr_2Fe_2O_5$ brownmillerite phase forms (*29*, *30*). The difference in O vacancy ordering in $SrFeO_2$ and $Sr_2Fe_2O_5$ requires substantial anion lattice rearrangement during the reaction.

Table 3-1. Unit cell parameters for $SrFeO_{3-x}$, $SrFeO_2$, and $SrFeO_2F$. Previously reported literature cell parameters for $SrFeO_2F$: $Pm\bar{3}m$, *a* = 3.956 Å (*6*, *7*).

Compound	Space Group	Unit Cell Parameters (Å)	Volume (Å^3)
$SrFeO_{3-x}$	$Pm\bar{3}m$	*a* = 3.851	55.11
$SrFeO_2$	P4/mmm	*a* = 3.991 *c* = 3.478	55.35
$SrFeO_2F$	$Pm\bar{3}m$	*a* = 3.955(1)	61.86(4)

Table 3-2. Atomic positions obtained from the Reitveld refinement of synchrotron diffraction data for $SrFeO_2F$ with refined occupancies.

Atom	Wyckoff Position	x	y	z	Occ.	$10^2 U_{iso}$ (Å^2)
Sr	1b	0.5	0.5	0.5	1	0.03(2)
Fe	1a	0	0	0	1	0.13(4)
O/F	3d	0	0	0.5	0.66 / 0.33	0.96(2)

Collected thermograms (Figure 3-4) for $SrFeO_2F$ under both O_2 and N_2 in the range of 300-1200 K were analyzed based on total weight loss due to the complexity of the decomposition pathways.

Under an O_2 atmosphere, the final mass was 99.47%, giving a total weight loss of 0.53% as described in reaction (3-1) below, which is dominated by the formation of SrF_2 and the stable parent perovskite $SrFeO_{3-x}$. When the oxyfluoride was heated under a reducing N_2 environment, a mass loss of 2.09% was observed, pointing again to the formation of SrF_2 as well as the more reduced iron oxide Fe_3O_4 and the stable brownmillerite phase $Sr_2Fe_2O_5$ as shown in reaction (3-2) below.

$$2\ SrFeO_2F \rightarrow SrFeO_{3-x} + SrF_2 + 0.50\ Fe_2O_3 \quad (3\text{-}1)$$

$$SrFeO_2F \rightarrow 0.25\ Sr_2Fe_2O_5 + 0.50\ SrF_2 + 0.16\ Fe_3O_4 + 0.11\ O_2 \quad (3\text{-}2)$$

The mass gain under an O_2 atmosphere seen from 1000 K to 1100 K followed by an equal mass loss to give the final mixture is attributed to a higher oxygen

activity at 1000 K, leading to fewer oxygen vacancies (lower x value) in $SrFeO_{3-x}$. At 1100 K the oxygen activity decreases and the more stable $SrFeO_{3-x}$ ($0.25 > x > 0.15$) perovskite forms (*31*). The majority of the mass loss under an N_2 atmosphere is due to the loss of oxygen at higher temperatures. TGA decomposition products were confirmed by PXD.

An endothermic peak in the DSC curve under an N_2 atmosphere at 510 K might indicate a local O/F order-disorder transition. This peak is absent in the O_2 DSC curve. The small number of O vacancies formed in $SrFeO_2F$ on heating under N_2 flow is apparently important for O/F rearrangement to occur.

3.2c Full magnetic properties investigation

The temperature dependence of DC magnetic susceptibility was measured on powder samples with a Quantum Design SQUID magnetometer at H = 1000 Oe in the temperature range 4 - 400 K. Samples were loaded into gelatin capsules under N_2, placed into a plastic sample holder and cooled to 4 K under zero magnetic field. All measurements were performed by warming the samples in the applied field after cooling to 4 K in zero field (ZFC, zero field cooling) and by cooling the samples in the applied measuring field (FC, field cooling).

The field dependence of DC magnetic susceptibility, AC magnetization, and specific heat measurements were performed on a powder sample with a Quantum Design PPMS. AC magnetic susceptibility data was collected between 4 K and 310 K by varying the frequency from 50 Hz to 10000 Hz.

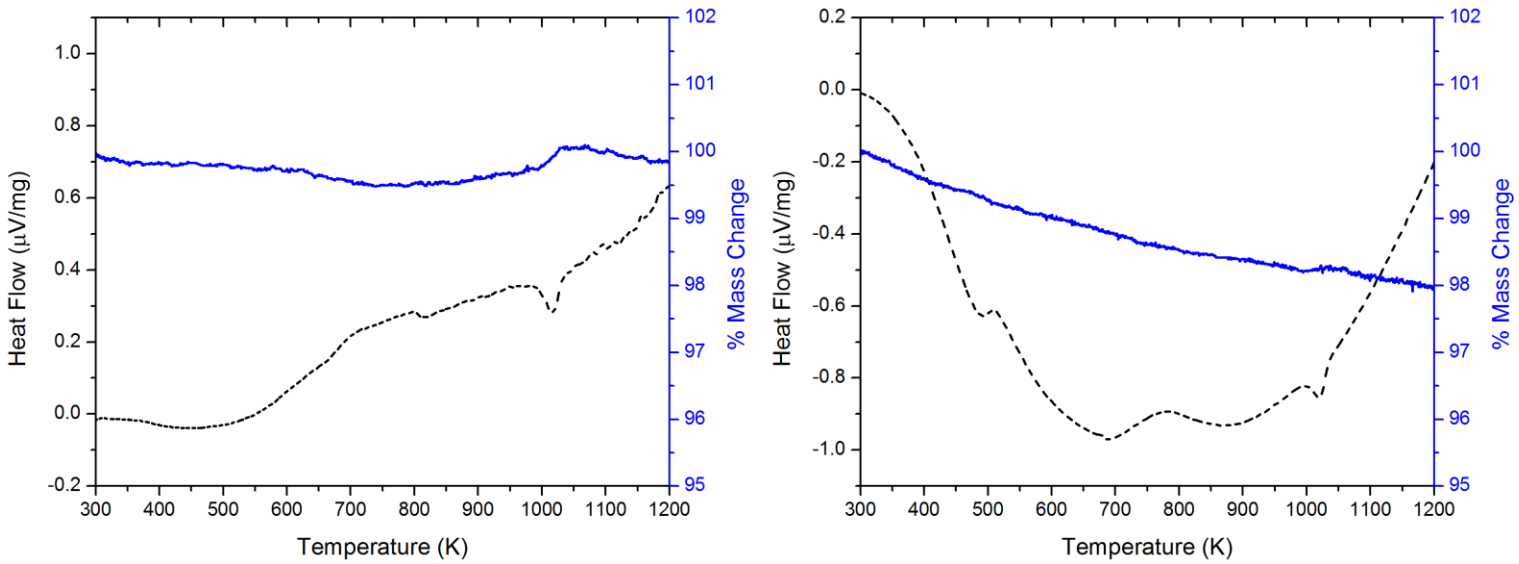

Figure 3-4. Thermogravimetric analysis of the fluorinated product $SrFeO_2F$ under an O_2 and N_2 atmospheres. Positive slope in the DSC curve represents endothermic signals, while negative slope represents exothermic signals.

The magnetic susceptibility and specific heat measurement results are shown in Figure 4. The small divergence between ZFC and FC curves at 300 K (Figure 3-5a) is due to SQUID instrument measurement noise as confirmed by the M vs. H measurement on a PPMS system at 300 K (Figure 3-5b). No magnetization frequency dependence was observed in the AC susceptibility data above 60 K (Figure 3-5c, 3-5d). Finally, the specific heat data did not reveal any convincing transitions in the temperature range studied (Figure 3-5a).

A cusp in the AC magnetization at about 60 K and dependence of the cusp position on the frequency of the AC susceptibility measurements are characteristic features of a spin-glass like transition (Figure 3-5c, 3-5d) (*32*–*34*). The divergence of the ZFC and FC susceptibility curves below 60 K (Figure 3-5a) and non-linear magnetization on magnetic field dependence at 10 K (Figure 3-5b) are in agreement with the spin-glass like state as well. Above 60 K the magnetic properties presented here (Figure 3-4a, 3-4b) are drastically different from reported for $SrFeO_2F$ prepared directly from $SrFeO_3$ at 400 °C (7). For the literature sample, a spin-glass transition at 300 K was reported based on the bifurcation of ZFC and FC data and a nonlinear change of magnetization vs. magnetic field at 300 K (7). In our sample, there was no magnetization frequency dependence in the AC magnetization data between 310 K and 60 K which eliminates the possibility of a spin-glass state. Considering that the $SrFeO_2F$ cell parameters and composition reported here and in (*6*, *7*) are virtually identical, it is unexpected to see such distinct magnetic properties. The difference in properties can be related to

differences in O/F ordering due to both the preparation approaches (direct vs. multistep) and synthesis temperature (400 °C vs. 150 °C).

3.2d Local coordination control using ^{57}Fe Mössbauer

^{57}Fe Mössbauer spectroscopy was carried out utilizing a ^{57}Co-source in a rhodium matrix at room temperature. The measured spectrum was evaluated using Fit;o) - a Mössbauer spectrum fitting program (*35*).

Local Fe environments in $SrFeO_2F$ were studied by Mössbauer spectroscopy. The room temperature ^{57}Fe Mössbauer spectrum of $SrFeO_2F$ is shown on Figure 3-6 and Mössbauer spectrum fitting parameters are given in Table 3-3. It was necessary to introduce 3 Fe sites in the refinement to fit the spectrum (χ^2= 3.7). Unlike the previously reported oxyfluoride $PbFeO_2F$ (*36*), no asymmetry of the main sextet peaks was observed in our case. Nevertheless, attempts to add an extra Fe site in order to use two Fe sites with close quadrupole splitting parameters to fit the main sextets similarly to Inaguma *et al.* were undertaken (*36*). Such attempts did not lead to a better fit and the refined area for an extra Fe site was below 2%, which is within error.

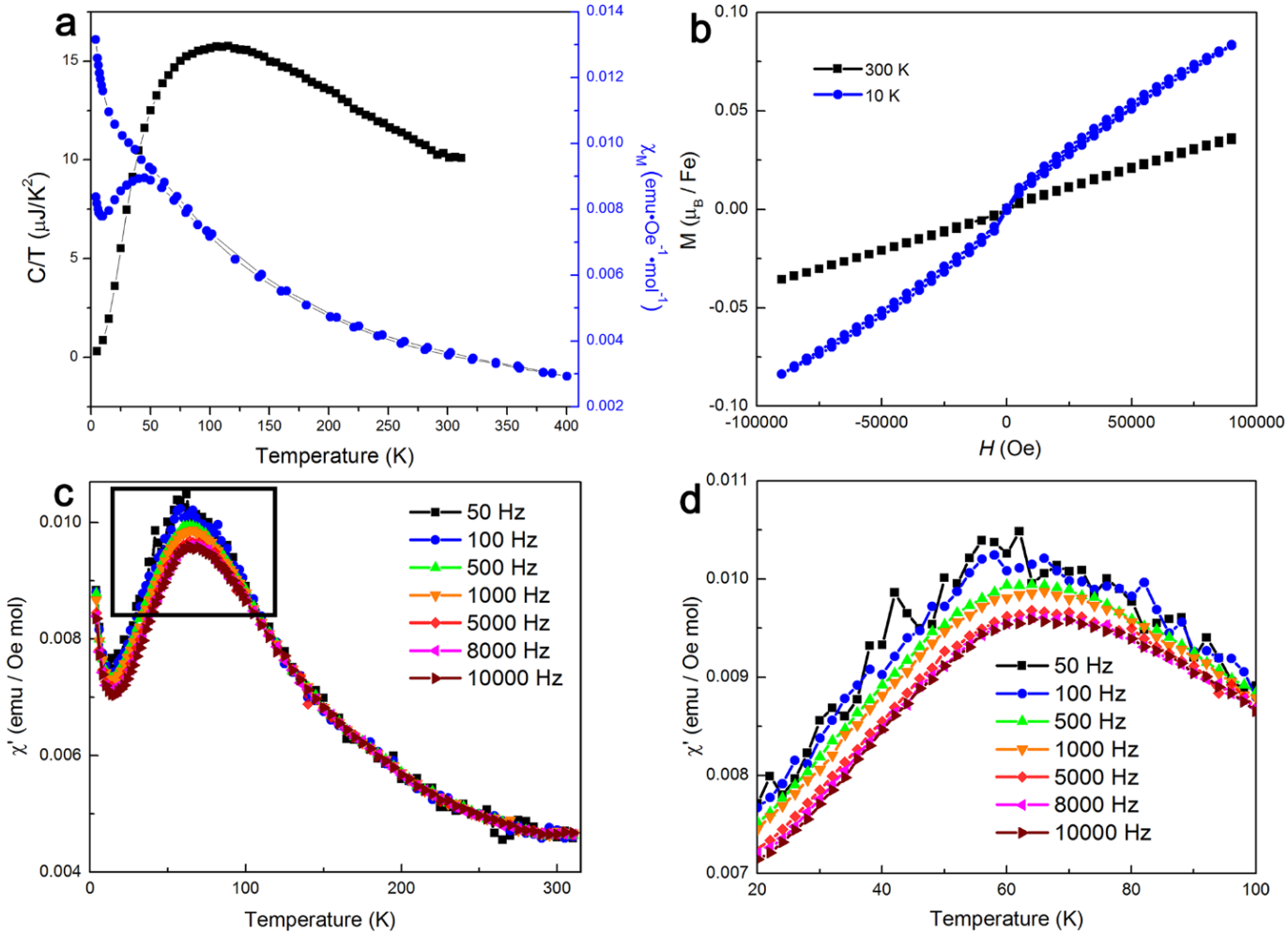

Figure 3-5. DC magnetization at H = 1000 Oe (a), DC field dependence (b), AC magnetic susceptibility (c, d) and specific heat measurement (a) results for $SrFeO_2F$ collected on a Quantum Design PPMS system.

Table 3-3. $SrFeO_2F$ Mössbauer spectrum fit parameters obtained using the Fit:o) software package (*35*).

Site	Isomer Shift ± 0.02 (mm/s)	Quadrupole Splitting ± 0.02 (mm/s)	Hyperfine Magnetic Field ± 0.08 (T)	Line Width ± 0.02 (mm/s)	Area ± 2 (%)
Fe1	0.42	0.11	51.43	0.79	41
Fe2	0.33	0.04	49.29	0.80	46
Fe3	0.42	1.04	-	0.81	13

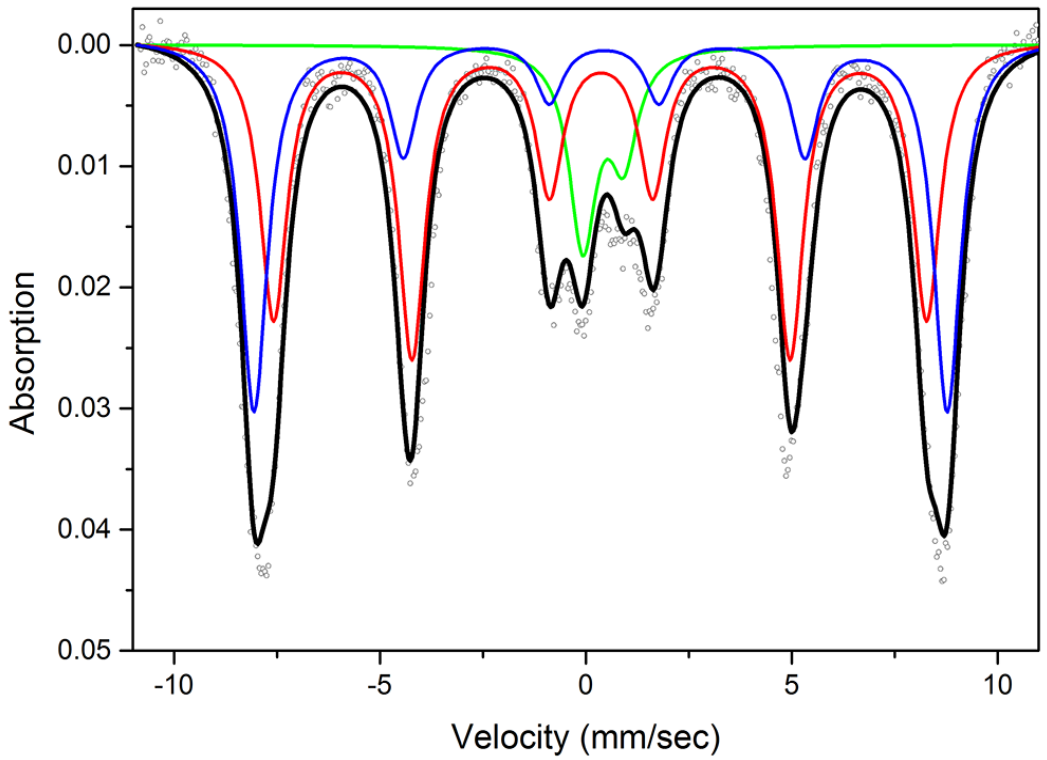

Figure 3-6. Fit (black line) of room temperature ^{57}Fe Mössbauer spectrum of $SrFeO_2F$ with denoted contributions from Fe sites: Fe1 (blue line), Fe2 (red line), Fe3 (green line).

Mössbauer spectroscopy was utilized to study the local Fe environments, O/F ordering, and Fe spin states in $SrFeO_2F$ prepared by the multistep procedure reported here. A slightly broader range of isomer shifts (0.33 – 0.42 mm/s) for Fe positions was found in our sample in comparison with the data (0.34 – 0.39 mm/s) of Berry (*7*). The simultaneous presence of Fe sites with zero and non-zero hyperfine fields in the single phase O/F disordered $SrFeO_2F$ sample was reported earlier between 200 and 317 K *(7)*. All isomer shift values for Fe sites in our fit can be assigned to Fe^{3+} (HS) states. For the spherical Fe^{3+} ($3d^5$) ion, quadrupole splitting (QS) can only arise due to non-cubic symmetry of the lattice contribution to the electric field gradient (EFG) (*36*). Random O/F distribution in Fe oxyfluorides should lead on average to FeO_4F_2 polyhedra with 2 possible O/F arrangements: trans - FeO_4F_2 with F^{1-} ions at opposite corners of the octahedron and cis - FeO_4F_2 arrangement with 2 F^{1-} at adjacent octahedron corners. The value of QS for the non-magnetic Fe3 site (1.04 mm/s) is similar to that (0.96 mm/s) reported for disordered $SrFeO_2F$ (*7*). It is not possible to uniquely deduce the coordination nature of the nonmagnetic Fe3 site which can consist of cis-, trans- or, most probably, a mixture of both anion arrangements. In the presence of a magnetic hyperfine field (B_{HF}), as is observed for the Fe1 and Fe2 sites, the QS value depends on the angle (Θ) between the principal axis of the EFG (V_{zz}) and the direction of B_{HF}: $\Delta = ½\ \Delta_0\ (3\cos^2\Theta - 1)$, where Δ and Δ_0 are QS value with and without a magnetic hyperfine field, respectively. The expected values of QS for magnetic sites can be estimated following the excellent discussion of Berry (*7*).

Accepting Δ_0 equal to 1.04 mm/s and Θ values of 45° and 90°, the calculated QS values for the cis-arrangement are 0.26 mm/s and -0.52 mm/s. The 45° Θ value corresponds to the cis-configurations with one of the F1- ion situated on the z axis, while the 90° Θ value is for cis-configuration with 2 F1- ions in the equatorial positions. Similarly, for the trans-FeO_4F_2 Δ_0 equal to -1.04 mm/s (an opposite QS sign is expected for cis- and trans- configurations) and Θ values of 0° and 90°, the calculated QS values are -1.04 mm/s and 0.52 mm/s. The calculated QS values for the trans-configuration are much larger than the observed ones for the Fe1 and Fe2 sites. After comparing the absolute values of calculated QS with the fit results (Table 3-3), the cis-configuration can uniquely be assigned to the Fe1 and Fe2 sites. Even more specifically, the cis-configurations with one of the F^{1-} anions on V_{zz} can be selected. The difference between the calculated QS value of 0.26 mm/s for one of the cis-configurations and the experimentally observed ones (~0.1 mm/s) for Fe1 and Fe2 can be attributed to subtle octahedra distortion resulting in the angle between V_{zz} and B_{HF} of ~51° instead of the ideal value of 45°. Considering the magnetic character of Fe1 and Fe2 sites, as well as an absence of the divergence of the ZFC and FC susceptibility and linear character of magnetic field dependence at room temperature, we propose a cluster of spins state above 60 K. The reverse magnetic susceptibility vs. temperature dependence is linear between 60 and 400 K. The effective magnetic moment μ_{exp} per Fe ion calculated from the Curie-Weiss model was 3.44 μ_B, which is substantially smaller than the expected spin only values of 5.92 μ_B (S = 5/2) for Fe^{3+} (d^5) in high spin

configuration. The lower effective magnetic moment is in agreement the proposed spin cluster model. The presence of some amount of FeO_5F and FeO_3F_3 polyhedra can be assumed in the sample. Attempts to take into accounts these configurations by adding extra sites to the fit led to peak areas below 2%, i.e. below the fit error, and thus were excluded from the fit.

As was discussed in great detail by Berry *et al. (7)* for a disordered $SrFeO_2F$ phase, the area ratio for cis- and trans- configurations is expected to be 67% : 33%. A close ratio (65% : 35%) was indeed observed experimentally in their case. In our case, even if we ascribe the Fe3 site completely to trans-configuration, the cis- to trans- peak area is 81% : 19%; much higher than for disordered oxyfluorides. The ratio may be even higher since the Fe3 site can be a mixture of cis- and trans- configurations. Thus, the multistep low temperature preparation technique used resulted in the predominance of cis fluorine configuration in the FeO_4F_2 polyhedra.

3.2e DFT structure optimization for ordered $SrFeO_2F$

The structure optimization of the ordered $SrFeO_2F$ was performed using the Wien2K 11.1 computational package (*37*). The tetragonal structural model with layered O and F ordering was generated and total energy was computed for structures with varied *a*/*c* ratios in order to determine the most stable structure model. Beginning from the cell parameters for the disordered phase (*a* = 3.955 Å, *a*/*c* = 1), the *a*/*c* parameter ratio was varied by 1% in a grid of 20x20 structures with the original structure held at the center.

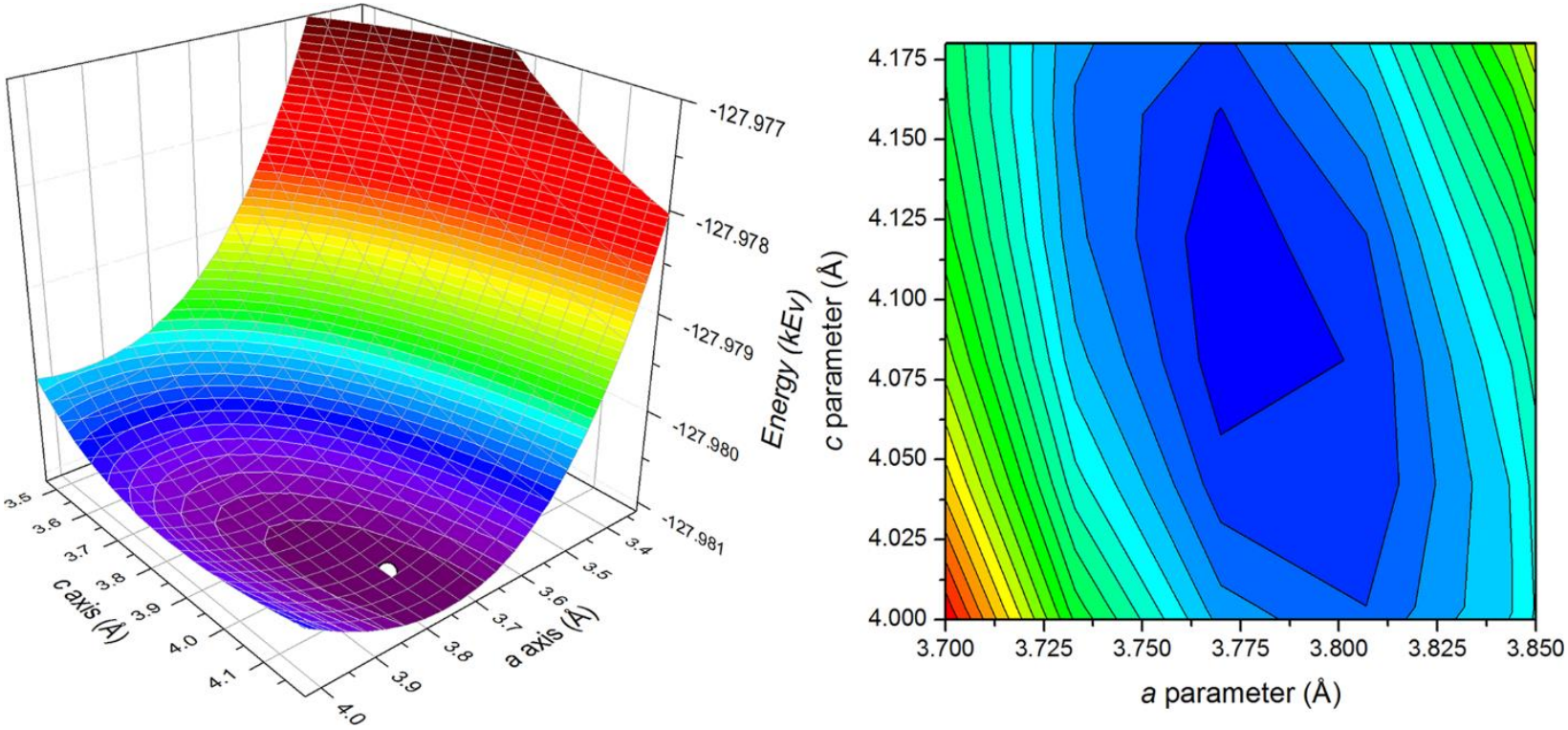

Figure 3-7. Left: Potential energy surface of varied a/c structures. The minimum position of the surface is highlighted by the white circle. Right: Contour plot zoomed in around the minimum energy extracted from the potential surface shown on the left. The dark blue area represents the minimum energy.

The energies of the structures were each calculated with an RK_{max} of 8, a G_{max} of 15, 5000 k-points, a core separation of -7.0 Ry and a muffin tin sphere reduction of 10% to allow for expansion and contraction of the spheres during optimization.

Relaxation of the ordered structure of $SrFeO_2F$ was also performed using the Vienna Ab-initio Simulation Package (VASP) 5.2.12 with the projector augmented wave method and the Perdew-Burke-Enzerholf '96 functional utilizing a conjugate-gradient algorithm for the ionic relaxation (*38–40*). The internal positions and cell parameters were allowed to relax. A gamma point centered pack of 1000 k-points were used in each calculation with an energy cut-off (En_{cut}) value of 400 eV.

The results of the structure optimization of the ordered $SrFeO_2F$ using the Wien2K package is shown in Figure 3-7 where the energies of structures with different *a* and *c* parameters are plotted. The figure clearly shows a local minimum at *a* = 3.775 Å and *c* = 4.120 Å. VASP was used to verify that the large tetragonal distortion should be expected for the ordered $SrFeO_2F$ with layered O/F ordering. The cell parameters for the VASP relaxed structure are *a* = 3.786 Å and *c* = 4.086 Å, validating the expected tetragonal distortion.

Considering similar ionic radii for O^{2-} and F^{1-} ions, a large theoretically predicted cell parameter difference is rather unexpected for the Fe^{3+} (d^5) compound, especially since half-filled *d* electronic orbitals possess spherical symmetry around the atomic nucleus (34). At the same time, an apparent failure of the effective ionic radii concept in oxyfluorides was shown experimentally previously for LaOF. In LaOF the La – O distance (2.42 Å) is substantially shorter than for La – F (2.60 Å)

(*42*). Interestingly, the predicted distance difference between Fe – O and Fe – F bonds in the ordered $SrFeO_2F$ (0.17 Å) is similar to La – O and La – F distance difference in LaOF with metal – fluorine distances longer in both cases.

3.2f Concluding remarks for $SrFeO_2F$

A low temperature multi-step synthesis of the $SrFeO_2F$ oxyfluoride using XeF_2 was presented. According to Rietveld refinement of SPXD data, the oxyfluoride crystallizes in a cubic perovskite structure ($Pm\bar{3}m$ space group, a = 3.955 Å) without long range O/F ordering. A large thermal parameter for the O/F crystallographic position indicated local disorder and differences in Fe-O and Fe-F bond lengths. Unexpectedly, for $SrFeO_2F$ with layered O/F ordering, DFT calculations predict Fe-F bonds significantly longer than Fe-O ones. When synthesized at 150 °C using the method described herein, a preference for cis fluorine configuration in local FeO_4F_2 polyhedra was extrapolated from Mössbauer spectroscopy data, demonstrating the effects of experimental conditions on local Fe coordination.

3.3 Synthesis of complex oxyfluorides $La_4Ni_3O_8F_x$ (x = 1,2)

The infinite NiO_2 square-planar layer is a very rare structural element in solids in spite of the well-known stability of Ni^{2+} cations in square-planar coordination. All nickelates with infinite NiO_2 layers are metastable and can be prepared only by low temperature reduction of the parent phases (*43–48*). Further information on these phases can also be found in Chapter 2 of this thesis. Such nickelates belong to the so-called T′-type $Ln_{n+1}Ni_nO_{2n+2}$ (Ln = La,Nd; n = 2,3,∞) homologous series (*49*).The physical properties of the T′-type nickelates are of great interest due to the $3d^9/3d^8$ electronic configuration of Ni^{1+}/Ni^{2+}, the same as that of Cu^{2+}/Cu^{3+} in the high-temperature superconductors (*50*, *51*). The n = 2 homologue, $La_3Ni_2O_6$, demonstrates multiply degenerate magnetic ground state while a spin density wave transition was observed for the n = 3 phase, $La_4Ni_3O_8$. (*46*, *52*, *53*). Depending on the homologue synthesized, the Ni oxidation state varies between 1+ and 1.5+. Synthesizing infinite layer phases with higher Ni oxidation states than 1.5+ is difficult due to the limited solubility range of alkaline earth metals in the A position; however, as discussed in Chapter 2 of this thesis, Eu^{2+} in $EuNiO_2$ may be a viable route to synthesizing an infinite-layer phase with Ni in the 2+ oxidation state. As the direct synthesis of any of the metastable phases presented in this section is thermodynamically hindered, a multistep route was taken in the synthesis of the oxyfluorides $La_4Ni_3O_8F_x$ (x = 1,2). The experimental conditions were carefully optimized to increase the purity an crystallinity of each phase in the series.

Tying in with the general theme of this thesis, the ability to topotactically intercalate F^{1-} into certain positions in the crystal structure of $La_4Ni_3O_8$ would allow for the establishment of a structure-function relationship based on F^{1-} stoichiometry. As the oxidation of $La_4Ni_3O_8$ to $La_4Ni_3O_{10}$ is easily performed under an O_2 atmosphere at relatively low temperature, fluorine should also be easily intercalated into the vacancies. However, oxyfluorides are often only kinetically stable and decompose to the thermodynamically stable phases as temperature is increased. Indeed, the reaction of $La_4Ni_3O_8$ with XeF_2 at 350 °C led to the formation of LaOF and an amorphous mixture, demonstrating that the oxyfluoride LaOF is the more stable product at that temperature. This work was done in collaboration with Dr. Artem Abakumov (electron diffraction), Dr. Joke Hadermann (electron diffraction), Dr. Jason Hodges (neutron diffraction), and Dr. Matthew Suchomel (synchrotron diffraction).

3.3a Solid state synthesis using XeF_2

All fluorinated samples were treated with the utmost care to limit exposure to moisture due to the hazards related to HF. All sample manipulations were done under an N_2 atmosphere in a glovebox. XeF_2 was weighed using a nickel boat and teflon spoon to avoid oxidation of equipment in the glovebox.

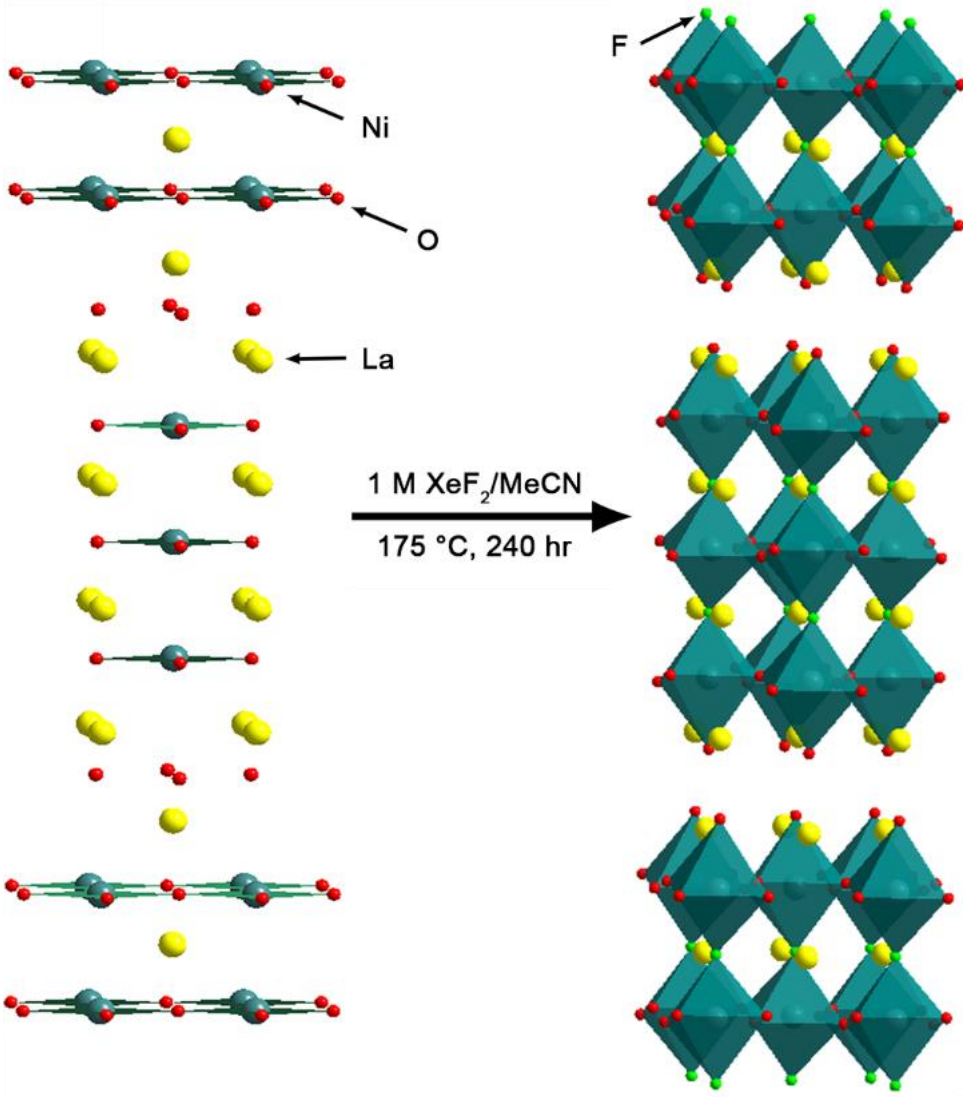

Figure 3-8. Topotactic transformation of $La_4Ni_3O_8$ to $La_4Ni_3O_8F_2$. The structure shown for $La_4Ni_3O_8F_2$ depicts O/F ordering. Colored balls represent the following atoms: yellow – La, red – O, teal – Ni, green – F.

La_2O_3 (Alfa Aesar, 99.9%) and $Ni(OH)_2$ (Sigma Aldrich, 99.9%) were both stored under nitrogen to avoid water absorption. XeF_2 (Alfa Aesar, 98%) was used as received without further purification.

$La_4Ni_3O_{10}$ was synthesized by the Pechini method: 7.310 g (22.43 mmol) La_2O_3 was mixed with 3.12 g (33.6 mmol) $Ni(OH)_2$ in a 200 mL ceramic bowl. An excess of citric acid, 5 mL of ethylene glycol, and 1 mL of concentrated HNO_3 were added. The bowl was filled with deionized water and allowed to stir for 48 hrs. After a gel had formed, the sample was fired at 600 °C for 2 hours to remove any remnant organics. The resulting black mixture was intimately ground, pelleted into 3/4" pellets then fired at 1150 °C for 468 hours with five intermittent grindings.

3.80 g (4.26 mmol) of finely ground $La_4Ni_3O_{10}$ was loaded into an alumina crucible and fired at 310 °C for 142 hours with one intermittent grinding, resulting in the pure phase $La_4Ni_3O_8$. Extreme care was taken during the use of pure hydrogen due to the extreme flammability of the gas.

For the solid state fluorination of $La_4Ni_3O_8$ to afford $La_4Ni_3O_8F_1$, a nickel crucible was charged with 2.00 g (2.3 mmol) of $La_4Ni_3O_8$ then placed inside a teflon lined stainless steel autoclave. A second nickel crucible was loaded with 0.220 g XeF_2 (1.3 mmol, 2.6 mmol F) using a teflon spoon then placed in the same teflon lined autoclave. The autoclave was sealed inside the glovebox to limit exposure to air then placed in a muffle furnace. A 48 hr temperature ramp was set to a final temperature of 250 °C then held for 72 hrs followed by furnace cooling to room temperature. The autoclave was then transferred back to the glovebox and was evacuated to remove any excess F_2 gas. After two intermittent grindings and recharges of XeF_2, a pure phase sample was obtained with a total firing time of 460 hrs. A similar experimental method was used in the synthesis of $La_4Ni_3O_8F_2$

as that for $La_4Ni_3O_8F_2$. Two nickel crucibles, one containing 2.00 g (2.325 mmol) $La_4Ni_3O_8$ and the other containing 0.473 g (2.79 mmol) XeF_2, were loaded into a teflon lined stainless steel autoclave. The autoclave was fired for a total of 296 hrs at 250 °C with three intermittent grindings and XeF_2 recharges. The final samples were stored under nitrogen at all times.

3.3b Structural characterization of $La_4Ni_3O_8F_x$ (x = 1,2)

Diffraction patterns, refinements, and other structural features of $La_4Ni_3O_{10}$ and $La_4Ni_3O_8$ are located in Chapter 2 of this thesis. Curious readers should review the full description in the first few sections of that chapter.

Initially, a well crystallized product was obtained by fluorination of the T′-type parent phase $La_4Ni_3O_8$ at 250 °C for 48 hrs. This product was investigated by electron diffraction (ED) and energy dispersive X-ray (EDX) analysis. ED patterns taken from different crystallites can be separated into two groups according to distinct *c/a* ratio: ~7.0 for one phase and ~7.3 for the second phase. These phases were often present in one crystallite as micro-domains. According to the EDX analysis, both phases have the same La:Ni ratio and contain some amount of fluorine – a quantitative analysis of fluorine content is difficult with EDX due to the low number of electrons. However, taking a qualitative approach, the estimated F content is clearly higher for the phase with the larger *c/a* ratio. It can be concluded that a mixture of two oxyfluorides was obtained by the fluorination of $La_4Ni_3O_8$.

Optimization of the synthetic conditions allowed the preparation of $La_4Ni_3O_8F_1$ and $La_4Ni_3O_8F_2$ separately.

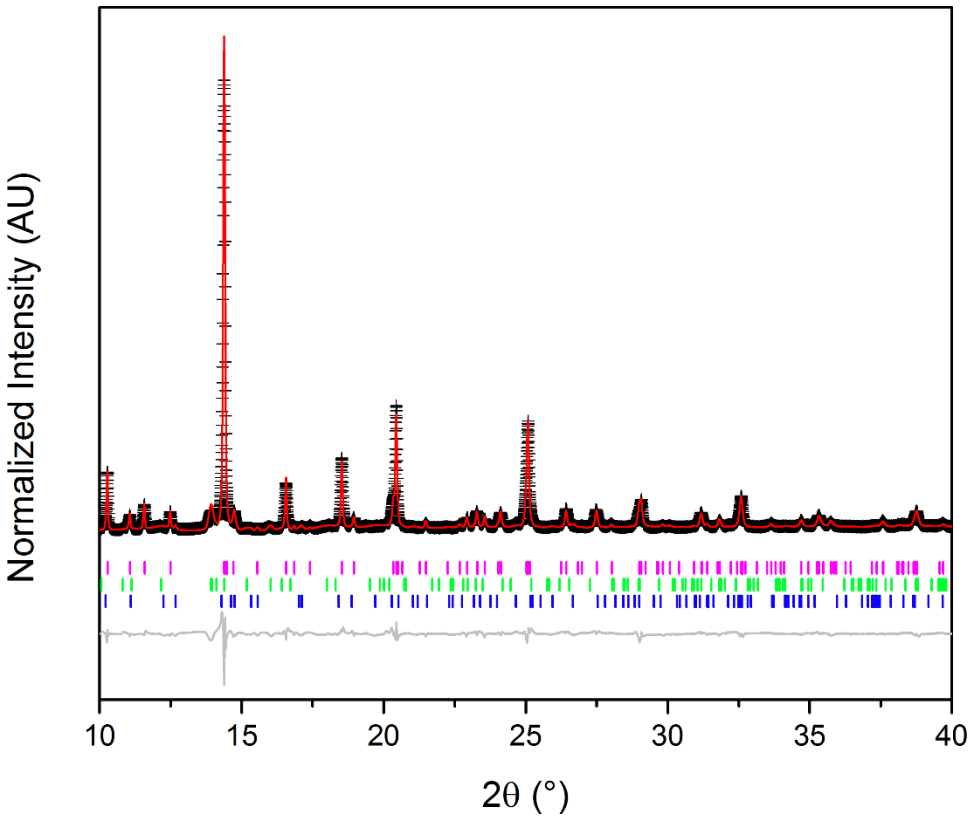

Figure 3-9. Rietveld refinement profile for the synchrotron powder X-ray diffraction data of $La_4Ni_3O_8F_1$. Observed intensities (crosses), calculated pattern (solid line), and difference curve (bottom solid line). Tickmarks represent the following phases: $La_4Ni_3O_8F_1$ – magenta (top), $La_4Ni_3O_8F_2$ – green (middle), $La_4Ni_3O_8$ – blue (bottom).

Table 3-4. Atomic parameters of $La_4Ni_3O_8F_1$ from Rietveld refinement of synchrotron powder diffraction data in the space group I4/mmm with *a* = 3.931(8) Å and *c* = 27.66(1) Å.

Atom	Site	*x*	*y*	*z*	U_{iso} (10^2 Å^2)
La1	4e	0	0	0.4335(2)	1.16(1)
La2	4e	0	0	0.3022(3)	1.01(2)
Ni1	2a	0	0	0	0.83(1)
Ni2	4e	0	0	0.1356(2)	0.27(2)
O1	4c	0	0.5	0	2.09(8)
O2	4e	0	0.5	0.8627(5)	1.08(4)
O3	8g	0	0	0.2216(8)	1.68(2)
F1	4e	0	0	0.0729(1)	1.89(7)

The space groups of the prepared nickel oxyfluorides were determined by Rietveld refinement of synchrotron powder X-ray diffraction data (Figure 3-9). An idealized (space group I4/mmm) structure of an n=3 RP phase was used for a starting model preparation. The symmetry of the starting model was lowered to several possible space groups as determined by ED. Typical ED patterns of nickel oxyfluorides material are shown in Figure 3-10. The ED patterns are characterized by sharp spots that correlate to an c/a ratio of 7.02 – 7.10 for $La_4Ni_3O_8F_1$ and 7.22 – 7.28 for $La_4Ni_3O_8F_2$. ED measurements of $La_4Ni_3O_8F_1$ point to an I4/mmm lattice structure with a faint orthorhombic superstructure present. The reflection

conditions found for $La_4Ni_3O_8F_2$ were hkl: h+k=2n; 0kl: k,l =2n; h0l: h=2n; h00: h=2n; 0k0: k=2n; 00l: l=2n; therefore, Cc-- is the only possible extinction symbol. For Ccc- there is disagreement with h0l: h,l=2n, which would not allow for any of the weaker reflections to be present, nor could they then be due to double diffraction or twinning. $Ccm2_1$ (36), Cc2m (40) and Ccmm (63) are possible subgroups of the Cc-- extinction symbol. To distinguish between these, convergent beam electron diffraction would be needed for determining whether the point group is mm2 (36), 2mm (40) or mmm (63). Due to observed crystal twinning, the results from such experiment would be unreliable.

Rietveld refinement of the synchrotron diffraction data for $La_4Ni_3O_8F_1$ converged successfully with a three phase refinement, shown in Figure 3-11. Fittings parameters of $\chi^2 = 4.82$ and $R_{wp} = 2.86$ % were obtained, showing a very good refinement of the high resolution data. Atom positions of $La_4Ni_3O_8F_1$ (I4/mmm, *a* = 3.931(8), *c* = 27.66(1)) are presented in Table 3-4. Although both O^{2-} and F^{1-} are isoelectronic and cannot be directly distinguished in synchrotron diffraction data, F^{1-} appears to sit in a unique crystallographic site. When F^{1-} is introduced shared position with O^{2-} atoms, the refinement quickly diverged or negative thermal parameters were reported. Furthermore, F^{1-} occupancy was able to be refined, resulting in a fluorine stoichiometry of F1.11 – slightly higher than the $La_4Ni_3O_8F_1$ ideal stoichiometry. Other atom occupancies were rounded to the appropriate value for the parent phase $La_4Ni_3O_8$. The phases $La_4Ni_3O_8F_2$ and the parent $La_4Ni_3O_8$ were both included in the refinement, with a normalized refined

phase composition ratio of 0.947:0.041:0.012 for $La_4Ni_3O_8F_1$:$La_4Ni_3O_8F_2$:$La_4Ni_3O_8$, respectively.

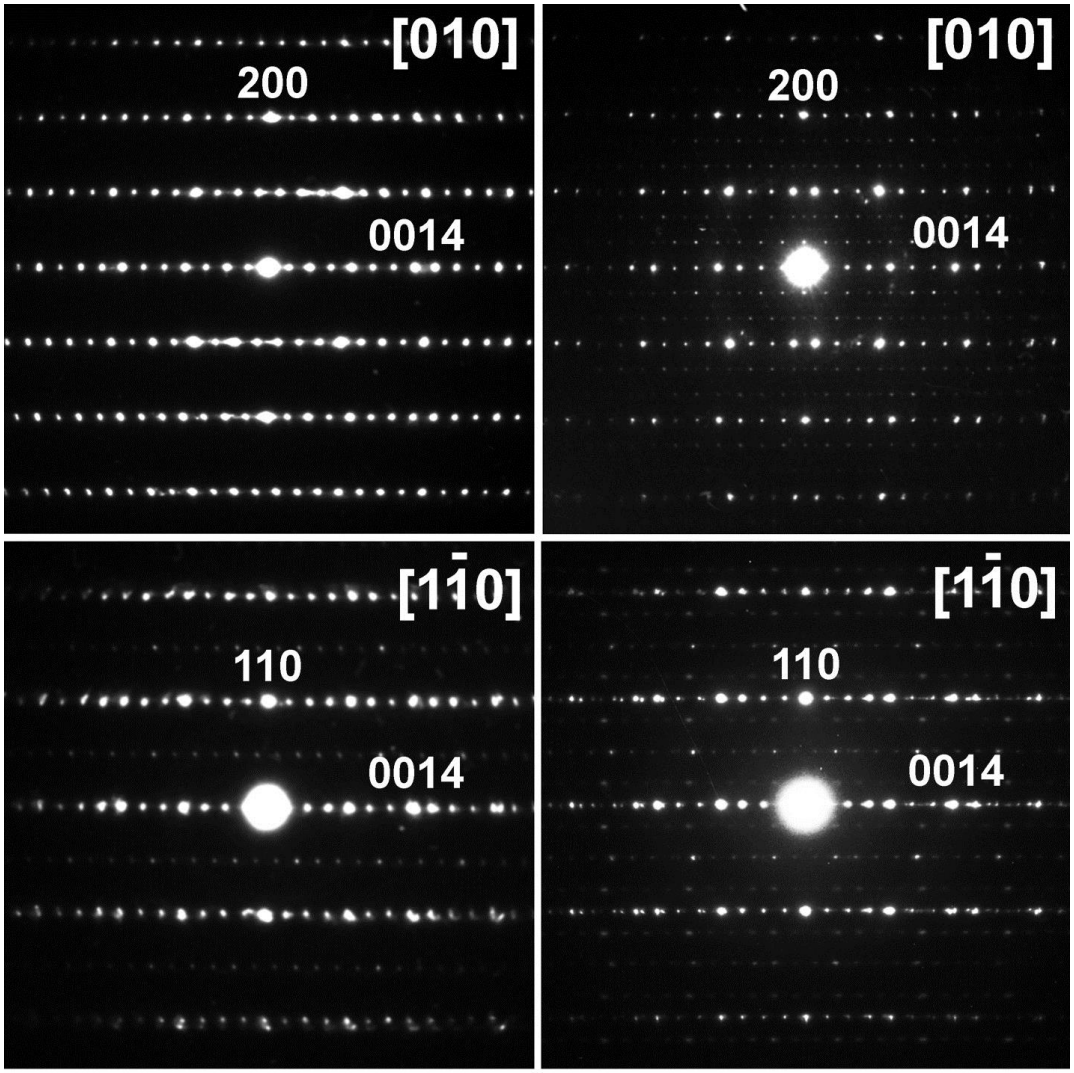

Figure 3-10. Electron diffraction patterns of $La_4Ni_3O_8F_2$ (left column) and $La_4Ni_3O_8F_1$ (right column).

To further investigate the possibility of O^{2-}/F^{1-} ordering, neutron diffraction measurements were taken of $La_4Ni_3O_8F_1$ at Oak Ridge National Lab under the guidance of Dr. Jason Hodges (Figure 3-11). Unfortunately, as a consequence of the similar neutron cross sections between O^{2-} and F^{1-} and the extremely poor counting statistics of the data, no further information on anion ordering was obtained (*27*).

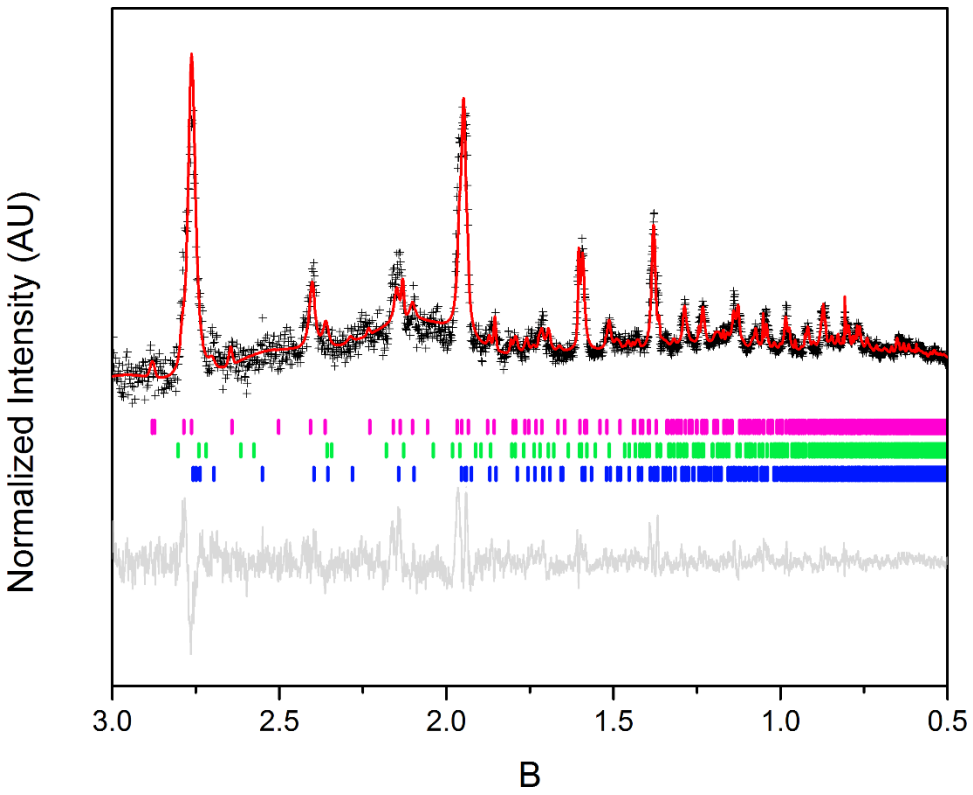

Figure 3-11. Rietveld refinement of the NPD data of $La_4Ni_3O_8F_1$. Observed intensities (crosses), calculated pattern (solid line), and difference curve (bottom solid line). Tickmarks represent the following phases: $La_4Ni_3O_8F_1$ – magenta (top), $La_4Ni_3O_8F_2$ – green (middle), $La_4Ni_3O_8$ – blue (bottom).

Synchrotron powder diffraction, neutron powder diffraction, and electron diffraction were all performed on $La_4Ni_3O_8F_2$. Unfortunately, only the SPXD pattern had good enough counting statistics to use, and only for LeBail refinement to obtain the cell parameters (*54*). A very wave-like background and exceptionally broad peaks were present in the SPXD data. Refinement of the background and acceptable peak profiles simultaneously resulted divergence of the Rietveld refinement. The NPD was of similar quality to that of $La_4Ni_3O_8F_1$ presented in Figure 3-11; however, the lack of an initial model system (as was available for $La_4Ni_3O_8F_1$ from refinement of the high-resolution synchrotron diffraction data) greatly hindered any attempts at Rietveld refinement of $La_4Ni_3O_8F_2$ from neutron diffraction data. A combination of the LeBail refinement of cell parameters from the synchrotron data and the *c*/*a* ratio obtained from the ED results led to a Ccmm crystal symmetry assignment with a = 3.977(7) Å, b = 3.898(1) Å, and c = 28.90(4) Å. As the diffraction positions produced by this space group appeared to correlate with the broad peaks in the diffraction pattern, a high-resolution neutron diffraction study may lead to a successful Rietveld refinement of atomic positions.

A comparison of the cell parameters, volumes, and *c*/*a* ratios for all four of the phases prepared in this section is shown in Table 3-5.

Table 3-5. Refined cell parameters of the $La_4Ni_3O_xF_y$ family of compounds prepared. Cell parameters obtained for $La_4Ni_3O_8F_2$ via LeBail refinement of synchrotron data.

Phase	Space Group	Cell Parameters (Å)	Volume (Å³)	c/a
$La_4Ni_3O_{10}$	Bmab	*a* = 5.412(2) *b* = 5.467(3) *c* = 27.96(1)	827.3(4)	5.168
$La_4Ni_3O_8$	I4/mmm	*a* = 3.969(2) *c* = 26.11(4)	411.3(1)	6.579
$La_4Ni_3O_8F_1$	I4/mmm	*a* = 3.931(8) *c* = 27.66(1)	427.4(6)	7.036
$La_4Ni_3O_8F_2$	Ccmm	*a* = 3.977(7) *b* = 3.898(1) *c* = 28.90(4)	445.7(2)	7.271

Nickel oxidation states of the compounds prepared were confirmed using Ni K-edge X-ray absorption spectroscopy measurements (Figure 3-12) were performed. When the data is viewed at an absorption coefficient of 0.5, it is apparent that the Ni oxidation state trends as the relative energy of the Ni K-edge increases. For example, the Ni K-edge energy of $La_3Ni_2O_6$ is lower in energy compared to $LaNiO_3$ because of the lower oxidation state ($Ni^{1.5+}$ vs Ni^{3+}) in $La_3Ni_2O_6$. The Ni K-edge for the prepared oxyfluoride $La_4Ni_3O_8F_2$ falls near and of higher energy to $La_3Ni_2O_7$. From this, a Ni oxidation state of approximately 2+ can be established. As this oxidation is not exact, it cannot be used to back-calculate F^{1-} stoichiometry. Quantitative ICP analysis was completed on $La_4Ni_3O_8F_2$, resulting in a stoichiometry of $La_4Ni_3O_8F_{2.01(1)}$ in which La, Ni, and O stoichiometries were fixed. The Ni-K XAS results are consistent with Ni oxidation state changes by the

multistep synthesis and provide additional evidence of F^{1-} incorporation into the crystal structure.

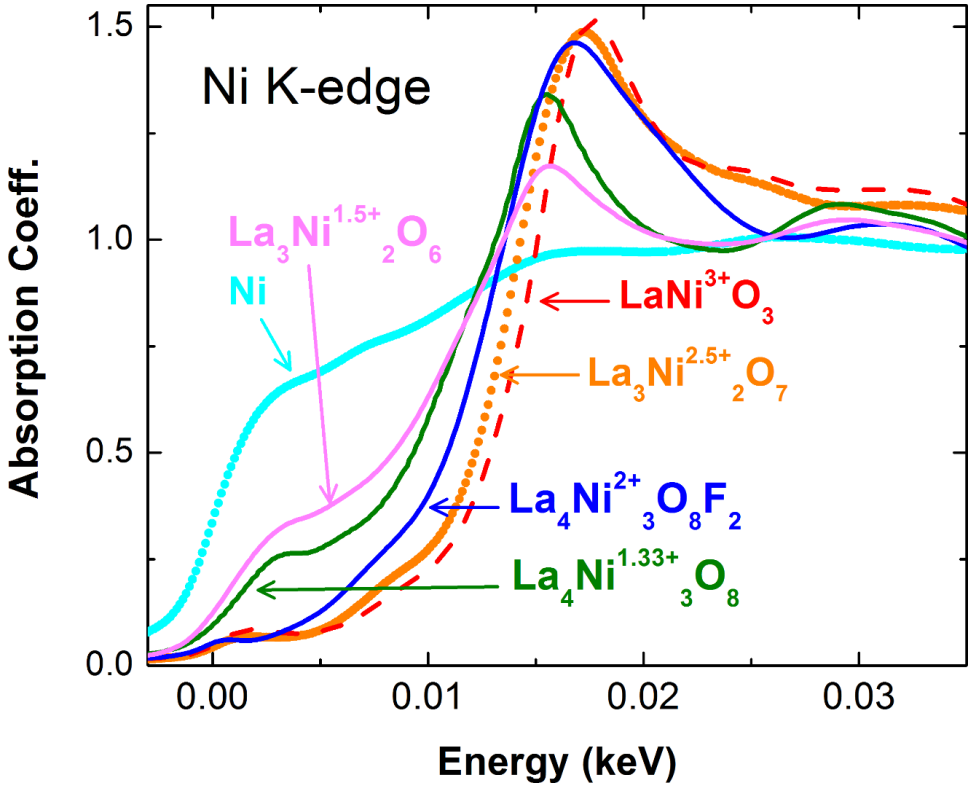

Figure 3-12. X-ray absorption spectra for $La_4Ni_3O_{10}$, $La_4Ni_3O_8$, $La_4Ni_3O_8F_1$, $La_4Ni_3O_8F_2$ as well as applicable standards.

3.3c Discussion on the T to T' transformation

The layered structures of the RP and the T′-type phases can be described as intergrowth of perovskite and rock- salt (in RP) and infinite layer and fluorite (in T′-type) structural blocks. The formation of the T′-type nickelates from the parent RP phases occurs as a result of an oxygen deintercalation and a structural

rearrangement in the $(LaO)_2$ blocks. Oxygen atoms are deintercalated exclusively from LaO layers between NiO_2 planes. Due to the drastic decrease of the distance between adjacent NiO_2 layers the $La_4Ni_3O_8$ structure does not allow oxygen vacancies despite its preparation by oxygen deintercalation. During the structural rearrangement of the $(LaO)_2$ blocks, oxygens shift in between La layers, transforming the rock-salt type block into a fluorite analog. The driving force for this T-to-T′ transformation is attributed to release of structural stress and is discussed in detail in the literature (*49*). As a result of the described structural changes, Ni exclusively adopts square-planar coordination in the infinite NiO_2 layers in $La_4Ni_3O_8$.

3.3d Concluding remarks for $La_4Ni_3O_8F_x$ (x = 1,2)

The syntheses presented for the oxyfluorides $La_4Ni_3O_8F_1$ and $La_4Ni_3O_8F_2$ is a rare example of a 4 step synthetic procedure in solid-state chemistry. $La_4Ni_3O_8F_1$ shows a tendency towards O/F ordering based on the refinement of high-resolution synchrotron data. Rietveld refinement of $La_4Ni_3O_8F_2$ was hindered based on poor counting statistics and high peak broadening. Electron diffraction measurements of both phases corroborated the cell parameters refined from the diffraction patterns. The synthesized phases $La_4Ni_3O_8F_1$ and $La_4Ni_3O_8F_2$ with infinite-layer NiO_2 would be the first phases synthesized with Ni in a higher oxidation state than 1.5+ with this coordination.

3.4 Novel solvothermal synthesis of complex oxyfluorides

Although many complex materials can be directly prepared via standard solid-state ceramic methods, compounds with low thermodynamic stability relative to their formation kinetics must be synthesized using soft chemistry techniques. Solvothermal chemistry has been employed with much success to produce metastable phases difficult or impossible to obtain by high-temperature methods including $NaFeSO_4F$, $Rb_2Hg_3Te_4$, $LaSrMnO_4F$ and $LiMnPO_4$ (*16*, *19*, *48*, *55–58*). However, very rarely are solvothermal conditions used to perform topotactic modifications on extended solids in which the cation and/or anion framework is preserved. Unlike conventional solid state methods, where direct control over atom connectivity and crystal structure is largely dictated by thermodynamics, topotactic strategies allow for the intelligent design of complex oxides beginning from a precursor host through multiple synthetic steps including ion exchange, intercalation, substitution, grafting, etc.(*1*, *59–61*)

Multiple reaction pathways for the low-temperature oxidative intercalation of fluorine into perovskite and perovskite-related hosts have been reported in the literature, in which a majority focus on the use of F_2 gas, NH_4F, and MF_2 (M = Cu, Zn, Ni, Ag) as sources of fluorine (*21*, *62–64*). Although relatively effective, the exceptionally hazardous nature of F_2 gas and the unwanted MO by-products formed during fluorination when using MF_2 reagents leaves much to be desired when performing topotactic fluorination. Very recently, a solvothermal fluorination method was published by Sheng (*65*) wherein NH_4HF_2 in absolute ethanol was

used to synthesize the superconductor $Sr_2Cu(O,F)_{4+\delta}$ with T_c = 38 K. As with previously reported fluorination techniques, the unwanted by-products SrF_2 and CuO were formed according to the following reaction (*65*):

$$Sr_2CuO_3 + 2HF \rightarrow Sr_2Cu(O,F)_{4+x} + SrF_2 + CuO + H_2O \quad (3\text{-}3)$$

The presence of water during the synthesis of oxyfluorides is especially alarming considering that many metastable oxyfluorides slowly hydrolyse in the presence of water to make HF. The solvothermal fluorination method employing XeF_2 as the oxidative fluorine source reported herein relies on a much simpler reaction pathway because of the nature of the reactants:

$$Sr_2Co_2O_5 + 0.5XeF_2 \rightarrow Sr_2Co_2O_5F + 0.5Xe \quad (3\text{-}4)$$

Assuming the reaction conditions (time, temperature, pressure, XeF_2 concentration) are optimized, unwanted by-products can be avoided to afford pure product. The fluorination of the Brownmillerite $Sr_2Co_2O_5$ was performed in a steel autoclave as a validation case for the novel solvothermal fluorination method proposed.

3.4a Description of the solvothermal fluorination method

The solvothermal method differs from the sole previous report of solvothermal fluorination in the fluorine source – XeF_2. The solubility of XeF_2 is fairly high in HF – 192 g/100 mL at 29.95 °C (*66*). It is also reasonably soluble in chloroform, dichloromethane, tetrachloromethane, fluorotrichloromethane, and acetonitrile; however, both proton-fluorine and chlorine-fluorine exchange was observed in the

halogenated solvents while the exchange in acetonitrile was negligible (*67*, *68*). Acetonitrile was chosen as the solvent for the low reactivity and the environmentally friendly aspect.

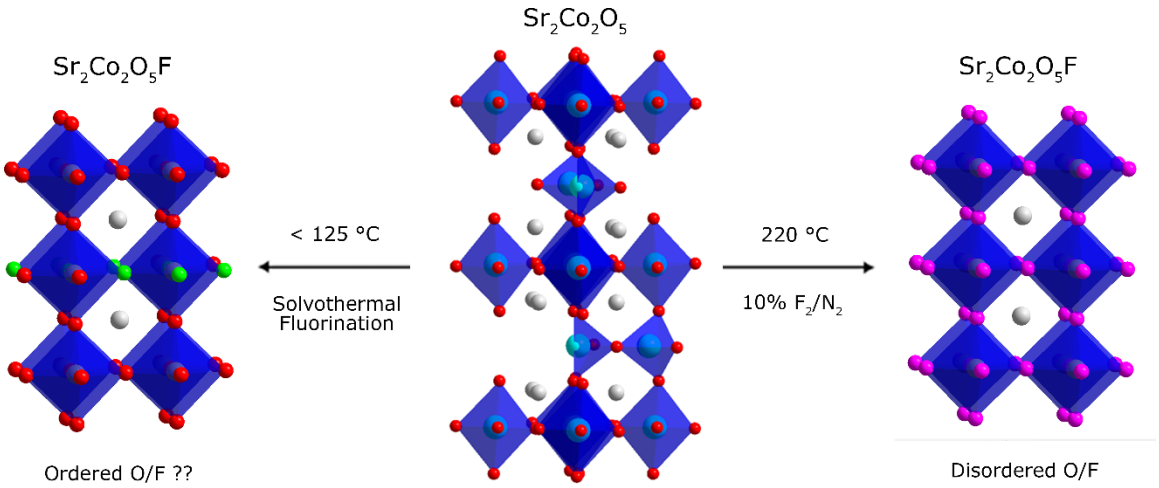

Figure 3-13. Comparison of the two known methods for the preparation of the oxyfluoride $Sr_2Co_2O_5F$. Colored balls represent the following atoms: blue – Co, red – O, white – Sr, green – F, and purple – O/F disorder.

Approximately 250 mg of the parent phase is weighed out in a glovebox and added to a 45 mL teflon sleeve, followed by 3 mL of anhydrous acetonitrile and 507 mg XeF_2 – generating a 1 M solution of XeF_2 with approximately 5x molar excess fluorine in solution. This concentration may need to be changed depending on the formula weight of the parent phases to maintain the 5x molar excess. The teflon sleeve was capped and inserted into a stainless steel autoclave, sealed, and loaded into a temperature controlled oven. Depending on the stability of the phase, a temperature range between 50 °C and 225 °C can be used. Before performing

any of these experiments, the autogenous pressure generated during reaction from both the solvent and complete decomposition of the XeF_2 must be calculated.

Once the reaction is completed, the products were washed three times with anhydrous acetonitrile to remove any excess XeF_2 then dried under vacuum.

3.4b Proof-of-principle: solvothermal synthesis of $Sr_2Co_2O_5F$

The brownmillerite phase $Sr_2Co_2O_5$ was synthesized using previous literature methods (*69*). Stoichiometric amounts of $SrCO_3$ and Co_3O_4 were fired for 24 hours at 1000 °C in air then quenched into liquid nitrogen to avoid the formation of the thermodynamically stable cubic structure. However, as the resulting product is not anion ordered, using the cubic perovskite $SrCoO_{3-x}$ as the precursor phase is feasible and synthetically easier.

The brownmillerite lattice is perovskite-like in structure but differs in local coordination. In brownmillerite phases, oxygen vacancies are ordered within planes, generating two different vertex-linked transition metal coordination environments: tetrahedral chains along the a axis and tetrahedral/octahedral layers along the c axis, as depicted in Figure 3-13.

$Sr_2Co_2O_5F$ was first synthesized in 2012 by the Greaves group (*70*). A sample of undisclosed mass was reacted at 200 °C for 15 minutes under a 10% F_2/N_2 stream. The sample was then ground and fired at 220 °C for 90 minutes in static 10% F_2/N_2. $Sr_2Co_2O_5F$ produced by this method was poisoned with a substancial amount of the parent brownmillerite, probably due to fluorination on the surface.

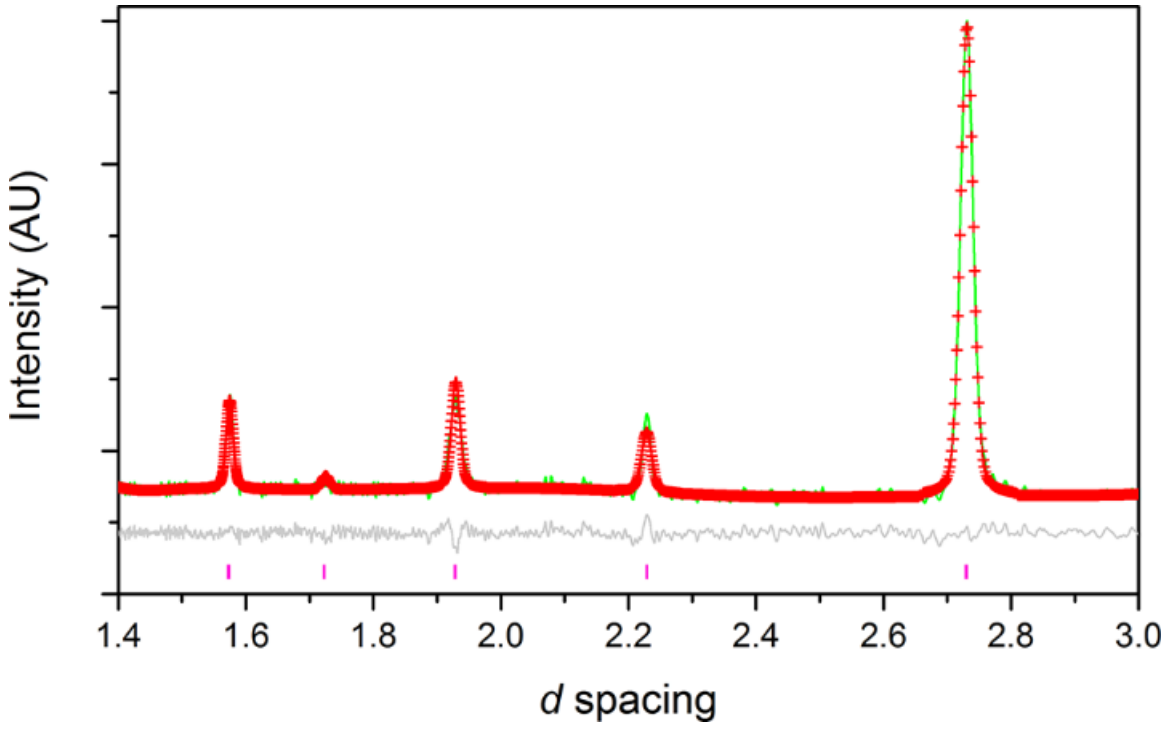

Figure 3-14. Observed (green trace), calculated (crosses), and difference (grey trace, below) XRD profiles obtained from Rietveld refinement of PXD data for $Sr_2Co_2O_5F$ made at 100 °C. Magenta tickmarks denote Bragg reflections.

The refinement of $Sr_2Co_2O_5F$ converged with $\chi^2 = 0.491$ and $R_{wp} = 2.21$ % with a very good fit between the calculated and observed patterns as shown in Figure 3-14. The refined cell parameter *a* = 3.8549(1) Å was very similar to the literature value of *a* = 3.8574 Å (*70*) as well as the literature value for the cubic disordered perovskite $SrCoO_3$ (*a* = 3.855 Å) (*71*). Addition of SrF_2 did not result in a change of any fitting parameters or a relative phase percent of more than 0.34% SrF_2. This finding also validates the fact that the solvothermal method leads to the synthesis

of metastable phases without the byproducts generally associated with solid state fluorination. The refined atomic positions of $Sr_2Co_2O_5F$ are shown in Table 3-6.

Table 3-6. Structure parameters of $Sr_2Co_2O_5F$ based on Rietveld refinement of powder diffraction data in the space group $Pm\bar{3}m$ with *a* = 3.8549(1) Å.

Name	Site	*x*	*y*	*z*	U_{iso} (10^2 Å^2)
Sr	1a	0	0	0	1.022
Co	1b	0.5	0.5	0.5	0.542
O/F	3c	0	0.5	0.5	1.328

The temperature dependence of DC magnetic susceptibility measured at a 3000 Oe field is presented in Figure 3-15. The increase of magnetic susceptibility at low temperatures is associated with a canted antiferromagnetism state. A bifurcation of the FC and ZFC magnetic susceptibility curves occurs at T ~ 30 K, similar to what was previously reported. The top inset displays an expanded view of the isothermal magnetization measurement M(H) at 2 K with the magnetic field H swept between +9 T and -9 T, where a hysteresis loop is obviously observed - a feature previously argued to originate from the existence of a ferromagnetic component in $Sr_2Co_2O_5$ (*70*). However, the hysteresis behavior only occurs below 30 K, found by measuring the M(H) curves from 9 T to 0 T at various temperatures (insets of Figure 3-15). The remnant magnetization decreases with increasing temperature and becomes zero above 30 K; therefore, instead of being genuinely

ferromagnetic, $Sr_2Co_2O_5F$ may form a spin-glass like magnetic state with a glass transition temperature of 30 K, which is presumably attributed to the magnetic frustration or disorder originating from the complex magnetic interactions involving Co^{4+} and Co^{3+} mixed states.

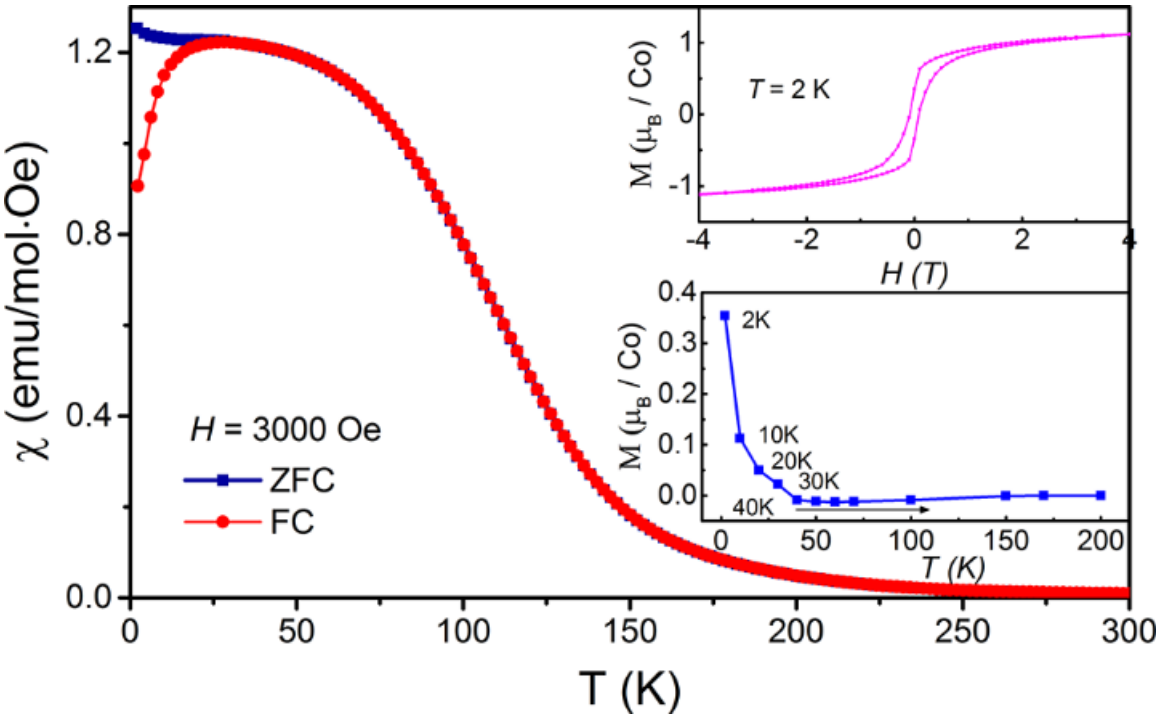

Figure 3-15. DC magnetic susceptibility measurements of $Sr_2Co_2O_5F$. Insets show the field and temperature dependence on magnetization in terms of magnetic moment per Co. Data collected on a Quantum Design PPMS system.

3.4c Exploring the importance of experimental conditions

To further understand the fluorination reaction mechanism in this solvothermal method, a series of experimental setups was devised. The initial hypothesis of a

solution based fluorination as opposed to gas based reaction was first adopted. Following, four different experimental conditions were drawn up, including the initial solvothermal method described previously. Two solid state reactions - one using the standard 45 mL autoclave and one with a reduced volume of approximately 10 mL - as well as a solvothermal method using 20 mL MeCN to dilute the XeF_2 concentration. Each method was tested using an experimental time of 1, 3, 5, 7, and 10 days at 100 °C. This lower temperature was chosen to subdue the fluorination rate, which allowed for a more precise comparison over time.

The two solid state type reactions were competed to understand whether the fluorination occurred via F_2 gas as opposed to a soluble fluorine source. For the standard volume solid state reactions, 250 mg (0.798 mmol) of $Sr_2Co_2O_5$ and 0.677 mg (4 mmol) XeF_2 were loaded into a 45 mL teflon sleeve, capped, and placed in a stainless steel autoclave followed by thermal treatment at 100 °C. In the reduced volume solid state reactions, a teflon insert was added to the 45 mL sleeve after the reactants had been added. The teflon insert displaced approximately 35 mL of sleeve volume. The sleeve was then capped and placed in a stainless steel autoclave. The two solvothermal type reactions were completed using the same parameters as explained above with a change in solvent volume for the 20 mL case.

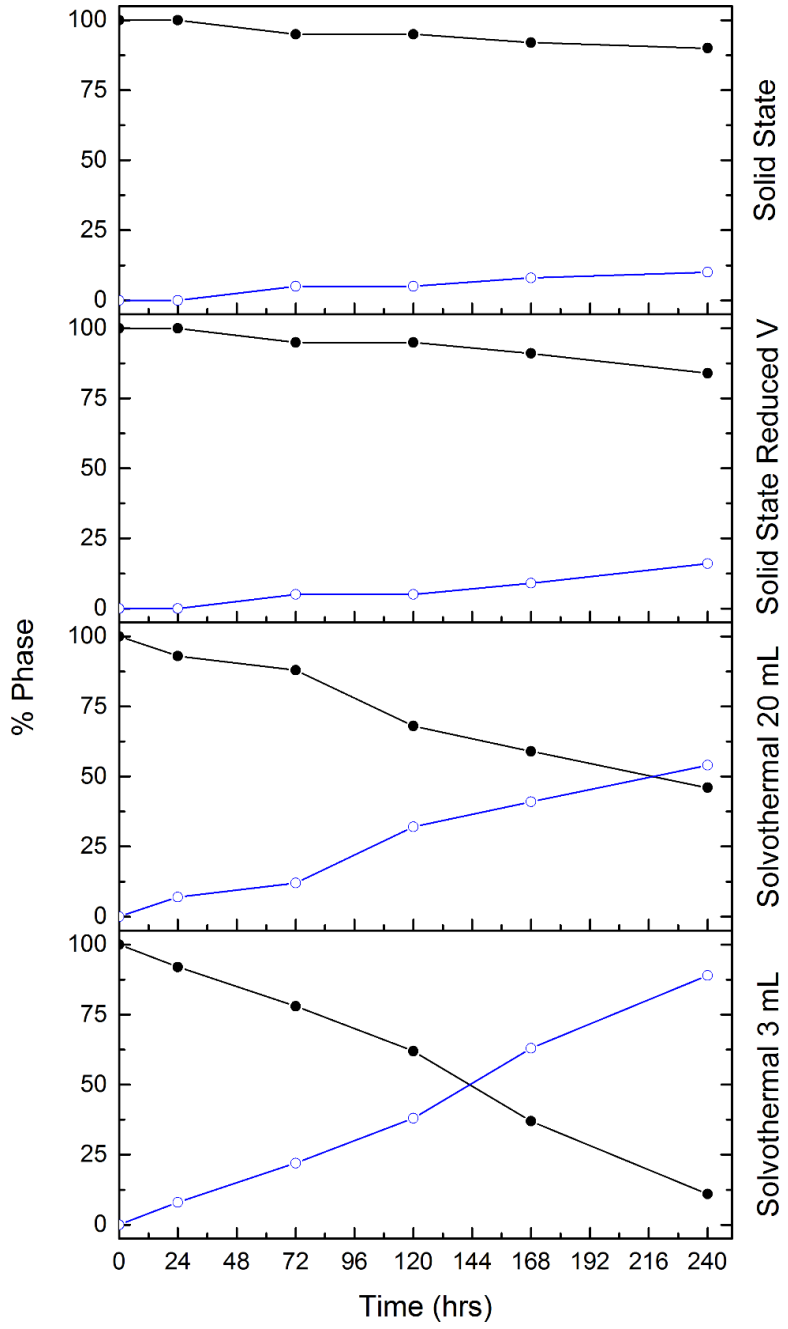

Figure 3-16. Fluorination rates over time for the fluorination of $Sr_2Co_2O_5$ using XeF_2 as a fluorine source under different experimental conditions. The blue lines show the % of $Sr_2Co_2O_5F$ at any given time.

From Figure 3-16 and Table 3-7, it is quite clear that fluorination occurs at a much faster rate under solvothermal conditions than in the solid state reactions. It appears that the fluorination rates are constant with all four methods. Interestingly, when lowering the temperature from 125 °C to 100 °C, the fluorination of $Sr_2Co_2O_5$ under solvothermal conditions with 3 mL of acetonitrile is still incomplete after 10 days. A cursory glance at the fluorination rates in Figure 3-16 point to a rate first order in XeF_2, an idea that will be discussed further. The small temperature change results in a very large decrease in reactivity. Neither of the solid state reactions produced more than approximately 20% of the oxyfluoride $Sr_2Co_2O_5F$ after 10 days.

Table 3-7. Percent formation of $Sr_2Co_2O_5F$ via the fluorination of $Sr_2Co_2O_5$ over time using four different methods. The total percent of unreacted $Sr_2Co_2O_5$ is the difference between the listed value below and 100.

Time	Solvothermal (3 mL)	Solvothermal (20 mL)	Solid State (45 mL)	Solid State (10 mL)
24	10	7	< 3	< 3
72	24	12	4	5
120	38	28	6	7
168	62	41	9	11
240	88	55	11	17

In the solid state reactions, there are two possible pathways for fluorination to occur as shown in equations 3-5, 3-6 and 3-7, with the first one being much more likely based on thermodynamic arguments.

$$XeF_2 \rightarrow Xe + 2F^{\bullet} \quad (3\text{-}5)$$

$$XeF_2 \rightarrow XeF^{+} + F^{-} \quad (3\text{-}6)$$

$$F^{\bullet}/F^{-} + Sr_2Co_2O_5\square_1 \rightarrow Sr_2Co_2O_5F_1 \quad (3\text{-}7)$$

The concentration of $F^{\bullet}$ is directly related to the temperature of the reaction as well as the vapor pressure of XeF_2 because it is in equilibrium with XeF_2 (g) below 115 °C. The vapor pressure of XeF_2 was explicitly measured by Chernick at Argonne national Lab and can be described by the equation presented in (3-8) where P_{mm} is the vapor pressure in mmHg and T is the reaction temperature (*72*).

$$\log P_{mm} = \frac{-3057.67}{T} - 1.23521 \log T + 13.969736 \quad (3\text{-}8)$$

For instance, the vapor pressure of XeF_2 is 25.34 mmHg and 394.1 mmHg at 50 °C and 100 °C, respectively, using equation (3-8). The formation of atomic fluorine is much more likely in this reaction because formation of the fluorine anion requires the presence of a Lewis acid, for example performing the reaction in a Pyrex flask. The acidic sites (B_2O_3 and Al_2O_3) polarize the linear XeF_2 molecule, allowing for reaction with the highly electrophilic XeF^{+} (*73*). At higher temperatures, the equilibrium shifts to purely atomic Xe and $F^{\bullet}$. Corroborating evidence for the radical species acting as the fluorination agent is given by the increase in reaction rate as the experimental volume is decreased from 45 mL to 10 mL, lowering the

mean path required for reactants to interact. Using simple ideal-gas law equations, the partial pressure of $F^{\bullet}$ is 4.5 times higher in the reduced volume case.

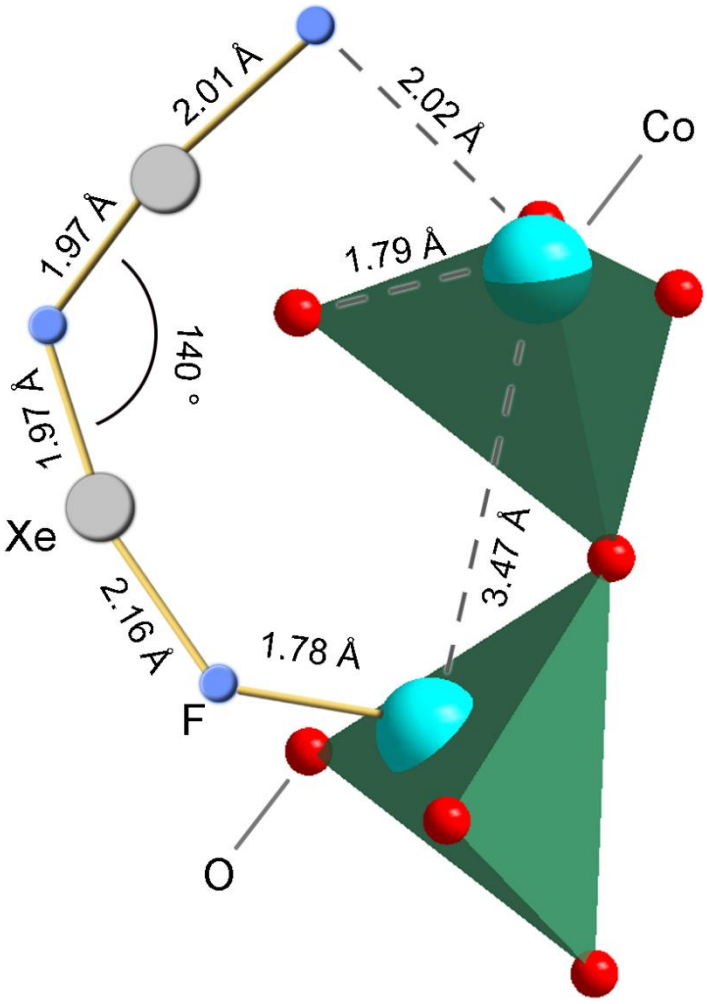

Figure 3-17. Possible bonding interaction between XeF_2 and two adjacent CoO_4 tetrahedra in the brownmillerite structure $Sr_2Co_2O_5$. A full description is presented in the text. Bond lengths were obtained from the literature (*20*, *28*, *66*, *74*, *75*).

Deducing the mechanism of the solvothermal reactions is a bit more difficult because of the possible reactants. As mentioned previously, and discussed in much more detail further, the electrophilic XeF^+ is formed in the presence of Lewis acids. In the case of the fluorination of $Sr_2Co_2O_5$, Co^{3+} near the surface can act as a hard Lewis acid (Figure 3-17), forming a weak bond with one of the fluorine atoms and generating the electrophile XeF^+ while oxidizing the Co^{3+} to Co^{3+}/Co^{4+}. The electrophile can then participate in a one electron radical transfer, resulting in the release of Xe gas and the local abstraction of fluorine into the vacancies in the unit cell of $Sr_2Co_2O_5$ (*66*). This reactivity is visualized in Figure 3-17, where the XeF^+ ion interacts with XeF_2, forming the bent $Xe_2F_3^+$ electrophile (*66*, *75*). When the $Xe_2F_3^+$ approaches an open face of the CoO_4 tetrahedra in $Sr_2Co_2O_5$, a fluorine atom can form a bond with the acidic Co^{3+}. This is shown in the picture as the F^{1-} Co bond with length 1.78 Å. Because of the geometry of both the bent $Xe_2F_3^+$ and the offset tetrahedra, the terminal fluorine in $Xe_2F_3^+$ is now within about 2 Å of another Co^{3+}. This Lewis acid site may promote further local formation of $Xe_2F_3^+$ with XeF_2, essentially creating a cascade fluorination effect. Since this cascade effect occurs in solution, this mechanism also validates the experimentally observed results (*66*, *76*, *77*). When the volume of acetonitrile was increased from 3 mL to 20 mL while the mass of XeF_2 was kept constant in the solvothermal reactions, the overall concentration of XeF_2 and any electrophilic XeF_2 species is lowered by a factor of nearly 7. Refer to the paragraphs on the reactivity of XeF_2 in the presence of Lewis acids further in this chapter for more information.

Increasing the fluorination power of XeF_2 by forming adducts with strong Lewis acids was also investigated in hopes of reducing reaction times and allowing for higher throughput. Considering that the chemistry of XeF_2 is starkly different than the chemistry of BF^{4-} or NMe_4F, the Lewis acid used had to be strong with appropriate orbital energies. The F^{1-} anion - for example, in NMe_4F - is exceptionally basic, and for that reason also very rare. When the ion is bound through Lewis interactions to a good Lewis acid like BF_3 or PF_5, any possible secondary basicity interactions are reduced, effectively lowering the fluorinating power relative to the F^{1-} anion. An even further reduction in basicity occurs in XeF_2 where the central Xe^{II} atom is electron deficient. Because of this reduced basicity, XeF_2 more readily forms ionic salts with strong Lewis acids (denoted LF_5 below), according to equations 3-9 and 3-10 below.

$$XeF_2 + LF_5 \rightarrow XeF^+ + LF_6^- \quad (3\text{-}9)$$

$$2XeF_2 + LF_5 \rightarrow Xe_2F_3^+ + LF_6^- \quad (3\text{-}10)$$

These two species, XeF^+ and $Xe_2F_3^+$, are both highly electrophilic and easily reduced by a single electron to form the strong fluorination agents $XeF^\bullet$ and $Xe_2F_3^\bullet$, respectively.

To test the hypothesis that adding a Lewis acid to a solution of XeF_2 in MeCN increases the fluorinating power of the solution, reactions were set up using NbF_5 and $AlCl_3$. A 1M solution of XeF_2 in acetonitrile was prepared by dissolving 0.845 g (5 mmol) XeF_2 in 5 mL of anhydrous acetonitrile in a glass vial in the glovebox. A teflon stir bar was added to promote dissolution. Half of the solution was then

transferred to a second vial using a volummetric pipette. 0.939 g (5 mmol) NbF_5 or 0.667 g (5 mmol) $AlCl_3$ were added separately to the vials. After vigorous reaction, especially for $AlCl_3$, the solutions turned pale yellow. Following complete dissolution of the Lewis acid, 0.373 g (1 mmol) of $Sr_2Co_2O_5$ was added. The vials were then stirred for 1 and 3 days, after which the product was washed three times with anhydrous acetonitrile and diffractograms were collected. According to the diffractograms, only pure phase $Sr_2Co_2O_5$ was present after all reactions with XeF_2-Lewis acid fluorine sources.

There are two possible reasons why the fluorination rates were substantially suppressed after addition of NbF_5 or $AlCl_3$ to XeF_2. The first explanation is that neither of these materials are strong enough Lewis acids to form ionic salts with XeF_2, instead forming more covalent type interactions. This idea is corroborated by the fact that both $AlCl_3$ and NbF_5 form polymeric units that must crack to create the ionic XeF_2 adduct. The other possible explanation is the lack of knowledge on the stability of highly reactive fluorinating agents in MeCN. Considering that XeF_2 adducts with NbF_5 and $AlCl_3$ should be colorless, the yellow solution and fierce bubbling may have represented the oxidation and/or fluorination of MeCN - shown in equation (3-11).

$$XeF_2 + NbF_5 \rightarrow [XeF]^+[NbF_6]^- + CH_3CN \rightarrow Xe + H^+ + NbF_6^- + CH_2FCN \quad (3\text{-}11)$$

As very little is known on the stability of XeF_2 adducts in acetonitrile - many of these compounds have been intensely studied in dry HF - further experiments must be first completed to identify the side reactions occurring with the solvent.

Alternatively, a transition to using HF as the solvent is possible; however, as the driving force for the creation of this solvothermal method was to lower the energy requirements and safety precautions of the experiment, using HF as a solvent would appear to be moving backwards in that regard.

3.5 Chapter Conclusions

In this chapter, multiple different synthetic methods for the preparation of complex, metastable oxyfluoride materials are discussed. The synthesis of $SrFeO_2F$ resulted in a large thermal parameter for the O/F lattice site, a sure sign of anion disorder in the structure. However, a large preference for cis-FeO_4F_2 coordination was demonstrated when $SrFeO_2F$ was synthesized using the soft-chemistry approached described herein, as opposed to the complete randomization in the previous higher temperature synthesis report. Further studies on this material, may result in a completely anion ordered structure.

Fluorination of the T' type $La_4Ni_3O_8$ phase previously synthesized in Chapter 2 of this thesis using a low temperature, multistep synthetic method was also discussed. Two distinct oxyfluoride phases, $La_4Ni_3O_8F_1$ and $La_4Ni_3O_8F_2$, were prepared. Structure characterization and Rietveld refinement was performed on synchrotron and NPD patterns of $La_4Ni_3O_8F_2$, while high-resolution diffraction patterns were elusive for $La_4Ni_3O_8F_2$ due to the poor crystallinity. Cell parameters and space groups were confirmed by electron diffraction studies. Stoichiometry and Ni oxidation states were investigated using ICP and XANES, respectively.

The chapter concludes with a presentation of a solvothermal fluorination method that does not result in metal oxide admixtures – a common problem with solid state fluorination methods. The power of the method is demonstrated with the synthesis of $Sr_2Co_2O_5F$ at a much lower temperature than previously reported.

3.6 Future work on this topic

Due to the robust nature of the solvothermal fluorination method presented, a future direction of the project could focus on the synthesis of metastable oxyfluorides tailored for certain properties, including second harmonic generation or Li-ion cathode materials. Depending on the diffusion pathways available in a target phase, many different compounds could be synthesized with this method, especially those structural types with anion vacancies or large interstitial zones (Brownmillerite, Aurivillius, etc). Applying the ideas of structure *vs.* function by modulating the transition metal oxidation states or the crystal structure in these phases via fluorination may lead to the direct tuning of physical or magnetic properties of the target phases.

A very different direction of this project could rely on developing methods to intercalate or exchange sulfur in a topotactic regime. The recent literature has shown sulfurization to be a very interesting method in synthesizing functional materials, yet there are no – as of this writing – papers on the topotactic intercalation of sulfur (*78–80*). A topotactic sulfurization reaction could be imagined where triphenylphosphine is used as the sulfur transport reagent, especially for reactions where the driving force is the formation of triphenylphosphine oxide after exchange.

REFERENCES

REFERENCES

(1) Ranmohotti, K. G. S.; Josepha, E.; Choi, J.; Zhang, J.; Wiley, J. B. Topochemical manipulation of perovskites: low-temperature reaction strategies for directing structure and properties. *Adv. Mater.* **2011**, *23*, 442–60.

(2) Mcintyre, R. A.; Falster, A. U.; Li, S.; Simmons, W. B.; Connor, C. J. O.; Wiley, J. B. Opening a Perovskite to Valence Manipulation : Two-Step Topotactic Route to a New Mixed-Valence Titanate, $Na_{1-x+y}Ca_{x/2}LaTiO_4$. *J. Am. Chem. Soc.* **1998**, *7863*, 217–218.

(3) Li, R. K.; Greaves, C. Double-layered ruthenate $Sr_3Ru_2O_7F_2$ formed by fluorine insertion into $Sr_3Ru_2O_7$. *Phys. Rev. B* **2000**, *62*, 3811–3815.

(4) Troyanchuk, I.; Kasper, N.; Mantytskaya, O.; Shapovalova, E. High-pressure synthesis of some perovskite — Like compounds with a mixed anion type. *Mater. Res. Bull.* **1995**, *30*, 421–425.

(5) Yoo, C.-Y.; Kim, S.-J. Dimensional modification of oxyfluoride lattice: Preparation and structure of $A'ANb_2O_6F$ (A′=Na, K; A=Ca, Sr). *J. Phys. Chem. Solids* **2008**, *69*, 1475–1478.

(6) Berry, F. J.; Ren, X.; Heap, R.; Slater, P.; Thomas, M. F. Fluorination of perovskite-related $SrFeO_{3-\delta}$. *Solid State Commun.* **2005**, *134*, 621–624.

(7) Berry, F. J.; Heap, R.; Helgason, Ö.; Moore, E. a; Shim, S.; Slater, P. R.; Thomas, M. F. Magnetic order in perovskite-related $SrFeO_2F$. *J. Phys. Condens. Matter* **2008**, *20*, 215207.

(8) Isobe, M.; Li, J.-Q.; Matsui, Y.; Izumi, F.; Kanke, Y.; Takayama-Muromachi, E. Synthesis, crystal structures and superconductivity of new copper oxyfluorides, $Sr_2RCu_2O_5F$ (R = Y,La,Nd,Sm,Gd,Dy,Er and Yb). *Phys. C Supercond.* **1996**, *269*, 5–14.

(9) Alekseeva, A. M.; Abakumov, A. M.; Rozova, M. G.; Antipov, E. V.; Hadermann, J. Synthesis and crystal structure of the $Sr_2MnGa(O,F)_6$ oxyfluorides. *J. Solid State Chem.* **2004**, *177*, 731–738.

(10) Tong, W.; Yoon, W.-S.; Hagh, N. M.; Amatucci, G. G. A Novel Silver Molybdenum Oxyfluoride Perovskite as a Cathode Material for Lithium Batteries. *Chem. Mater.* **2009**, *21*, 2139–2148.

(11) Ravez, J. The Inorganie Fluoride and Oxyfluoride Ferroelectrics. *J. Phys. III* **1997**, *7*, 1129–1144.

(12) Mizoguchi, H.; Orita, M.; Hirano, M.; Fujitsu, S.; Takeuchi, T.; Hosono, H. NbO_2F: An oxyfluoride phase with wide band gap and electrochromic properties. *Appl. Phys. Lett.* **2002**, *80*, 4732.

(13) Isobe, M.; Li, J.-Q.; Matsui, Y.; Izumi, F.; Kanke, Y.; Takayama-Muromachi, E. Synthesis, crystal structures and superconductivity of new copper oxyfluorides, $Sr_2RCu_2O_5F$ (R = Y,La,Nd,Sm,Gd,Dy,Er and Yb). *Phys. C Supercond.* **1996**, *269*, 5–14.

(14) Amatucci, G. G.; Pereira, N. Fluoride based electrode materials for advanced energy storage devices. *J. Fluor. Chem.* **2007**, *128*, 243–262.

(15) Greaves, C.; Kissick, J. L.; Francesconi, M. G.; Aikens, L. D.; Gillie, L. J. Synthetic strategies for new inorganic oxide fluorides and oxide sulfates. *J. Mater. Chem.* **1999**, *9*, 111–116.

(16) Aikens, L. D.; Li, R. K.; Greaves, C. The synthesis and structure of a new oxide fluoride, $LaSrMnO_4F$, with staged fluorine insertion. *Chem. Commun.* **2000**, 2129–2130.

(17) Francesconi, M. G.; Slater, P. R.; Hodges, J. P.; Greaves, C.; Edwards, P. P.; Al-Mamouri, M.; Slaski, M. Superconducting $Sr_{2-x}A_xCuO_2F_{2+\delta}$ (A=Ca, Ba): Synthetic Pathways and Associated Structural Rearrangements. *J. Solid State Chem.* **1998**, *135*, 17–27.

(18) Slater, P. R.; Gover, R. K. B. Synthesis and structure of the new oxide fluoride $Sr_2TiO_3F_2$ from the low temperature fluorination of Sr_2TiO_4: an example of a staged fluorine substitution/insertion reaction. *J. Mater. Chem.* **2002**, *12*, 291–294.

(19) Aikens, L. D.; Gillie, L. J.; Li, R. K.; Greaves, C. Staged fluorine insertion into manganese oxides with Ruddlesden–Popper structures: $LaSrMnO_4F$ and $La_{1.2}Sr_{1.8}Mn_2O_7F$. *J. Mater. Chem.* **2002**, *12*, 264–267.

(20) Weinstock, B.; Weaver, E. E.; Knop, C. P. The Xenon-Fluorine System. *Inorg. Chem.* **1966**, *5*, 2189–2203.

(21) Saratovsky, I.; Lockett, M. A.; Rees, N. H.; Hayward, M. A. Preparation of $Sr_7Mn_4O_{13}F_2$ by the topotactic reduction and subsequent fluorination of $Sr_7Mn_4O_{15}$. *Inorg. Chem.* **2008**, *47*, 5212–7.

(22) Cordier, S.; Roisnel, T.; Poulain, M. Synthesis and characterization of the novel $Nb_3O_5F_5$ niobium oxyfluoride: the term n=3 of the $Nb_nO_{2n-1}F_{n+2}$ series. *J. Solid State Chem.* **2004**, *177*, 3119–3126.

(23) Prodjosantoso, A. .; Kennedy, B. .; Vogt, T.; Woodward, P. . Cation and anion ordering in the layered oxyfluorides $Sr_{3-x}A_xAlO_4F$ (A=Ba, Ca). *J. Solid State Chem.* **2003**, *172*, 89–94.

(24) Brink, F. J.; Withers, R. L.; Cordier, S.; Poulain, M. An electron diffraction and bond valence sum investigation of oxygen/fluorine ordering in $Nb_nO_{2n-1}F_{n+2}$, n=3. *J. Solid State Chem.* **2006**, *179*, 341–348.

(25) Tsujimoto, Y.; Tassel, C.; Hayashi, N.; Watanabe, T.; Kageyama, H.; Yoshimura, K.; Takano, M.; Ceretti, M.; Ritter, C.; Paulus, W. Infinite-layer iron oxide with a square-planar coordination. *Nature* **2007**, *450*, 1062–5.

(26) Chen, W. M.; Hong, W.; Geng, J. F.; Wu, X. S.; Ji, W.; Li, L. Y.; Qui, L.; Jin, X. Iodometric titration for determining the oxygen content of samples doped with Fe and Co. *Phys. C Supercond.* **1996**, *270*, 349–353.

(27) Sears, V. F. Neutron scattering lengths and cross sections. *Neutron News* **1992**, *3*, 26–37.

(28) Shannon, R. D. Revised effective ionic radii and systematic studies of interatomic distances in halides and chalcogenides. *Acta Crystallogr. Sect. A* **1976**, *32*, 751–767.

(29) Tassel, C.; Kageyama, H. Square planar coordinate iron oxides. *Chem. Soc. Rev.* **2012**, *41*, 2025–35.

(30) Hayward, M. A.; Rosseinsky, M. J. Cool conditions for mobile ions. *Nature* **2007**, *450*, 960.

(31) Beurmann, P. Phase transitions in the $SrSnO_3$–$SrFeO_3$ solid solutions: X-ray diffraction and Mössbauer studies. *J. Solid State Chem.* **2003**, *174*, 392–402.

(32) Woo, H.; Tyson, T. a; Croft, M.; Cheong, S.-W. Evidence for spin clusters and glassy behaviour in $Bi_{1-x}Ca_xMnO_3$ (x = 0.875). *J. Phys. Condens. Matter* **2004**, *16*, 2689–2705.

(33) Hyett, G.; Barrier, N.; Clarke, S. J.; Hadermann, J. Topotactic oxidative and reductive control of the structures and properties of layered manganese oxychalcogenides. *J. Am. Chem. Soc.* **2007**, *129*, 11192–201.

(34) Bhowmik, R. N.; Ranganathan, R. Anomaly in cluster glass behaviour of $Co_{0.2}Zn_{0.8}Fe_2O_4$ spinel oxide. *J Mag. Mater.* **2002**, *248*, 101–111.

(35) Hjøllum, J.; Madsen, M. B. Fit:o) - A Mossbauer spectrum fitting program. *arXiv* **2011**.

(36) Inaguma, Y.; Greneche, J. Structure and Mo 1 ssbauer Studies of F-O Ordering in $PbFeO_2F$. *Chem. Mater.* **2005**, 1386–1390.

(37) Blaha, P.; Schwarz, K.; Madsen, G. K. H.; Kvasnicka, D.; Luitz. WIEN2k, An Augmented Plane Wave + Local Orbitals Program for Calculating Crystal Properties, 2001.

(38) Blochl, P. E. Projector augmented-wave method. *Phys. Rev. B* **1994**, *50*, 17953.

(39) Perdew, J. P.; Chevary, J. A.; Vosko, S. H.; Jackson, K. A.; Pederson, M. R.; Singh, D. J.; Fiolhais, C. Atoms, Molecules, Solids, and Surfaces: Applications of the Generalized Gradient Approximation for Exchange and Correlation. *Phys. Rev. B* **1992**, *46*, 6671.

(40) Kresse, G.; Hafner, J. Ab initio molecular dynamics for liquid metals. *Phys. Rev. B* **1993**, *47*, 558.

(41) Adamson, A. W. Domain representations of orbitals. *J. Chem. Educ.* **1965**, *42*, 140.

(42) Urusov, V. S.; Orlov, I. P. State-of-art and Perspectives of the Bond-Valence Model in Inorganic Crystal Chemistry. *Crystallogr. Reports* **1999**, *44*, 736–760.

(43) Poltavets, V. V; Lokshin, K. A.; Croft, M.; Mandal, T. K.; Egami, T.; Greenblatt, M. Crystal structures of $Ln_4Ni_3O_8$ (Ln = La, Nd) triple layer T'-type nickelates. *Inorg. Chem.* **2007**, *46*, 10887–91.

(44) Poltavets, V. V.; Lokshin, K. A.; Egami, T.; Greenblatt, M. The oxygen deficient Ruddlesden–Popper $La_3Ni_2O_{7-\delta}$ (δ=0.65) phase: Structure and properties. *Mater. Res. Bull.* **2006**, *41*, 955–960.

(45) Poltavets, V. V; Lokshin, K. A.; Dikmen, S.; Croft, M.; Egami, T.; Greenblatt, M. $La_3Ni_2O_6$: a new double T'-type nickelate with infinite $Ni^{1+/2+}O_2$ layers. *J. Am. Chem. Soc.* **2006**, *128*, 9050–1.

(46) Poltavets, V.; Greenblatt, M.; Fecher, G.; Felser, C. Electronic Properties, Band Structure, and Fermi Surface Instabilities of Ni^{1+}/Ni^{2+} Nickelate $La_3Ni_2O_6$, Isoelectronic with Superconducting Cuprates. *Phys. Rev. Lett.* **2009**, *102*, 046405.

(47) Hayward, M. A.; Green, M. A.; Rosseinsky, M. J.; Sloan, J. Sodium Hydride as a Powerful Reducing Agent for Topotactic Oxide Deintercalation: Synthesis and Characterization of the Nickel(I) Oxide $LaNiO_2$. *J. Am. Chem. Soc.* **1999**, *121*, 8843–8854.

(48) Blakely, C. K.; Bruno, S. R.; Poltavets, V. V. Low-temperature solvothermal approach to the synthesis of $La_4Ni_3O_8$ by topotactic oxygen deintercalation. *Inorg. Chem.* **2011**, *50*, 6696–700.

(49) Lacorre, P. Passage from T-type to T′-type arrangement by reducing $R_4Ni_3O_{10}$ to $R_4Ni_3O_8$ (R = La, Pr, Nd). *J. Solid State Chem.* **1992**, *97*, 495–500.

(50) Wen, X.-D.; Cahill, T. J.; Gerovac, N. M.; Bucknum, M. J.; Hoffmann, R. Playing the quantum chemical slot machine: an exploration of ABX_2 compounds. *Inorg. Chem.* **2010**, *49*, 249–60.

(51) Al-Mamouri, M.; Edwards, P. P.; Greaves, C.; Slaski, M. Synthesis and superconducting properties of the strontium copper oxyfluoride $Sr_2CuO_2F_{2+\delta}$. *Nature* **1994**, *369*, 382–384.

(52) ApRoberts-Warren, N.; Crocker, J.; Dioguardi, a. P.; Shirer, K. R.; Poltavets, V. V.; Greenblatt, M.; Klavins, P.; Curro, N. J. NMR evidence for spin fluctuations in the bilayer nickelate $La_3Ni_2O_6$. *Phys. Rev. B* **2013**, *88*, 075124.

(53) ApRoberts-Warren, N.; Dioguardi, A. P.; Poltavets, V. V.; Greenblatt, M.; Klavins, P.; Curro, N. J. Critical spin dynamics in the antiferromagnet $La_4Ni_3O_8$ from ^{139}La nuclear magnetic resonance. *Phys. Rev. B* **2011**, *83*, 014402.

(54) Peterson, V. K. Lattice parameter measurement using LeBail versus structural (Rietveld) refinement: A caution for complex, low symmetry systems. *Powder Diffr.* **2012**, *20*, 14–17.

(55) Tripathi, R.; Ramesh, T. N.; Ellis, B. L.; Nazar, L. F. Scalable synthesis of tavorite $LiFeSO_4F$ and $NaFeSO_4F$ cathode materials. *Angew. Chem. Int. Ed. Engl.* **2010**, *49*, 8738–42.

(56) Li, J.; Chen, Z.; Lam, K.; Mulley, S.; Proserpio, D. M.; Strutturale, C. $Rb_2Hg_3Te_4$: A New Layered Compound Synthesized from Solvothermal Reactions. **1997**, *1669*, 684–687.

(57) Dong, Y.; Xie, H.; Song, J.; Xu, M.; Zhao, Y.; Goodenough, J. B. The Prepared and Electrochemical Property of Mg Doped $LiMnPO_4$ Nanoplates as Cathode Materials for Lithium-Ion Batteries. *J. Electrochem. Soc.* **2012**, *159*, A995–A998.

(58) Choi, D.; Wang, D.; Bae, I.-T.; Xiao, J.; Nie, Z.; Wang, W.; Viswanathan, V. V; Lee, Y. J.; Zhang, J.-G.; Graff, G. L.; Yang, Z.; Liu, J. $LiMnPO_4$ nanoplate grown via solid-state reaction in molten hydrocarbon for Li-ion battery cathode. *Nano Lett.* **2010**, *10*, 2799–805.

(59) Schaak, R. E.; Mallouk, T. E. Perovskites by Design: A Toolbox of Solid-State Reactions. *Chem. Mater.* **2002**, *14*, 1455–1471.

(60) Blakely, C. K.; Bruno, S. R.; Davis, J. D.; Poltavets, V. V. Synthesis and Electrochemical Properties of Novel Co^{2+}/Co^{3+} Layered Ordered Rock-Salt Structure Type $Li_{0.75}Ca_{0.25}CoO_2$. *ECS Trans.* **2013**, *45*, 3–10.

(61) Wu, S.-H.; Liu, H.-Y. Preparation of α-$LiFeO_2$-based cathode materials by an ionic exchange method. *J. Power Sources* **2007**, *174*, 789–794.

(62) Slater, P. R.; Hodges, J. P.; Francesconi, M. G.; Greaves, C.; Slaskic, M. Fluorination of the Ruddlesden – Popper type cuprates , LnACuO (Ln = La , Nd ; A = Ca , Sr). *Structure* **1997**, *7*, 2077–2083.

(63) Stavber, G.; Zupan, M.; Stavber, S. Solvent-free fluorination of organic compounds using N–F reagents. *Tetrahedron Lett.* **2007**, *48*, 2671–2673.

(64) Berry, F. J.; Ren, X.; Heap, R.; Slater, P.; Thomas, M. F. Fluorination of perovskite-related $SrFeO_{3-\delta}$. *Solid State Commun.* **2005**, *134*, 621–624.

(65) Sheng, J.; Tang, K.; Liang, Z.; Wang, Y.; Wang, D.; Zhang, W. Solvothermal fluorination: A new chemical fluorination method to insert fluorine into Sr_2CuO_3 and $NdSr_2Cu_2O_{6-\delta}$. *Mater. Chem. Phys.* **2009**, *115*, 483–487.

(66) Tramšek, M.; Žemva, B. Synthesis , Properties and Chemistry of Xenon(II) Fluoride. **2006**, 105–116.

(67) Barbara Grüttner, Michael F. A. Dove, Alan F. Clifford, G. J. and H. S. *Inorganic Chemistry in Liquid Hydrogen Cyanide and Liquid Hydrogen Fluoride*; Elsevier, 1971.

(68) Dukat, W.; Holloway, J. H.; Hope, E. G.; Townson, P. J.; Powell, R. L. The reactions of xenon difluoride with “inert” solvents. *J. Fluor. Chem.* **1993**, *62*, 293–296.

(69) Sullivan, E.; Hadermann, J.; Greaves, C. Crystallographic and magnetic characterisation of the brownmillerite $Sr_2Co_2O_5$. *J. Solid State Chem.* **2011**, *184*, 649–654.

(70) Sullivan, E.; Greaves, C. Fluorine insertion reactions of the brownmillerite materials $Sr_2Fe_2O_5$, Sr_2CoFeO_5, and $Sr_2Co_2O_5$. *Mater. Res. Bull.* **2012**, *47*, 2541–2546.

(71) Taguchi, H.; Shimada, M.; Koizumi, M. The Effect of Oxygen Vacancy on the Magnetic Properties in the System $SrCoO_{3-x}$. *J. Solid State Chem.* **1979**, *225*, 221–225.

(72) Schreiner, F.; McDonald, G. N.; Chernick, C. L. Vapor pressure and melting points of xenon difluoride and xenon tetrafluoride. *J. Phys. Chem.* **1968**, *72*, 1162–1166.

(73) Ramsden, C. A. Xenon difluoride in the organic laboratory: a tale of substrates, solvents and vessels. *Arkivoc* **2013**, *2014*, 109.

(74) Stout, J. W.; Reed, S. A. The Crystal Structure of MnF_2 , FeF_2 , CoF_2 , NiF_2 and ZnF_2. *J. Am. Chem. Soc.* **1954**, *76*, 5279–5281.

(75) Nakajima, T.; Tressaud, A.; Zemva, B. Advanced Inorganic Fluorides. *Handb. Clin. Neurol. / Ed. by P.J. Vinken G.W. Bruyn* **2008**, *90*, IX–X.

(76) Brown, D. R.; Clegg, M. J.; Downs, A. J.; Fowler, R. C.; Minihan, A. R.; Norris, J. R.; Stein, L. The dixenon(1+) cation: formation in the condensed phases and characterization by ESR, UV-visible, and Raman spectroscopy. *Inorg. Chem.* **1992**, *31*, 5041–5052.

(77) Nabiev, S. S.; Ostroukhova, I. . Raman study of molecular dynamics of inorganic fluoroxidizers in nonaqueous solutions- Part 1 . Xenon difluoride in acetonitrile. *Spectrochmica Acta* **1993**, *49*, 1527–1535.

(78) Lu, P.; Lu, N.; Wang, J.; Kim, M. J.; Xia, Y. Site-selective sulfurization of bromide-capped palladium nanocubes by polysulfide and the underlying mechanism. *Nanotechnology* **2014**, *25*, 014003.

(79) Liu, X.; Liu, Z.; Lu, J.; Wu, X.; Chu, W. Silver sulfide nanoparticles sensitized titanium dioxide nanotube arrays synthesized by in situ sulfurization for

photocatalytic hydrogen production. *J. Colloid Interface Sci.* **2014**, *413*, 17–23.

(80) Tang, X.; Ye, H.; Hu, H. Sulfurization synthesis and photocatalytic activity of oxysulfide $La_3NbS_2O_5$. *Trans. Nonferrous Met. Soc. China* **2013**, *23*, 2644–2649.

Chapter 4 : MuRE – A multistep topotactic synthetic method

4.1 Literature Background on α-$NaFeO_2$ type phases

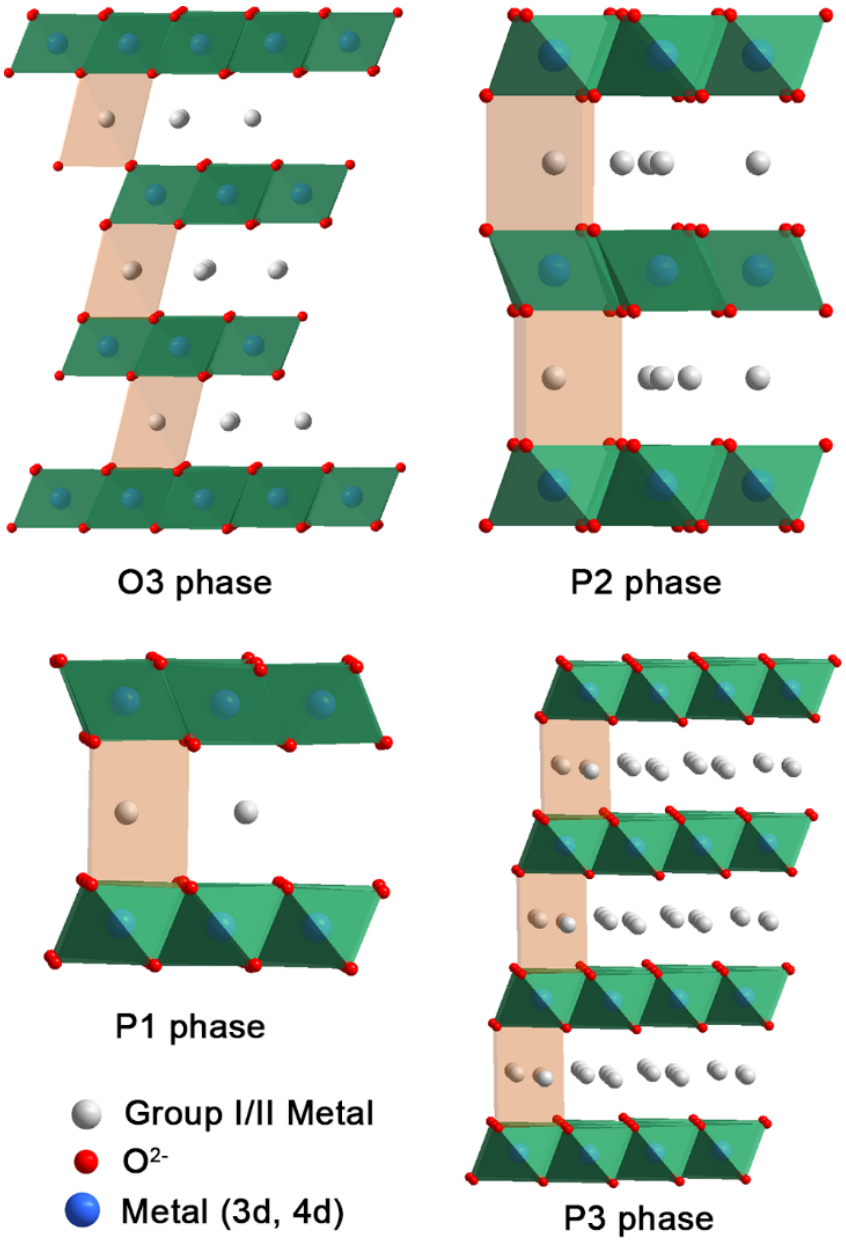

Figure 4-1. Different structure variations found in the α-$NaFeO_2$ system based on the coordination of the alkali metal – O for octahedral and P for trigonal prismatic. A further description of the naming convention is given in the text.

At first glance, the α-$NaFeO_2$ structure presented in Figure 4-1 appears to be a simple rock-salt superstructure with alternating layers of NaO_6 and FeO_6 octahedrally coordinated planes. However, the actual crystal structure and coordination geometry of phases in this family are highly dependent on the stoichiometry of the sample; for example, $Na_{0.76}CoO_2$ and $Na_{0.75}CoO_2$ adopt different structural motifs (P2 and O1, respectively) with very similar stoichiometries (*1*, *2*). Before proceeding, the subtle differences in structures for the α-$NaFeO_2$ family of compounds must be closely examined.

Originally presented by Delmas, a simple hexagonal packing scheme with three distinct oxygen positions (A, B, C) can be used to identify the cation geometry between $(MO_2)_n$ sheets. Assuming the oxygen in the $(MO_2)_n$ sheets are in the A and B positions, only two possibilities exist for the position of the third oxygen sheet: B or C. When the third oxygen is located in the B position, either ABBA or ABBCCA stacking motifs can exist depending on the position of the fourth oxygen (either A or C), resulting in a trigonal prismatic coordination for the alkali metals between the $(MO_2)_n$ sheets. On the other hand, when the third oxygen is located on a C position, an ABCABC stacking pattern is created with the alkali metals adopting octahedral symmetry. The final case, which will not be further explored here, exists when the third oxygen lies in the A position leading to an ABAB stacking pattern that only occurs with A_2MO_2 stoichiometry and alkali metals in tetrahedral coordination. As viewed down the *c* axis, the two and three layer phases can be easily distinguished. In the two layer phases, all of the M ions lie in

the same positions on the *a-b* plane; however, in the three layer system the M ions are staggered based on hexagonal packing into three distinct *a-b* coordinates.

Once the geometry of the alkali cation is established as either O (octahedral) or P (trigonal prismatic), the number of $(MO_2)_n$ repeating units per unit cell is appended to give the structural type. Finally, a prime is added after the geometry notation to inform of the presence of a monoclinic distortion of the unit cell. Often, after a monoclinic distortion, the unit cell can be described using a one layer cell (similar to the P1 structure in Figure 4-1).

The majority of known phases adopting the α-$NaFeO_2$ type structure or one of its deviations are shown pictorially in Figure 4-2. The dotted line running with slight curvature towards the top right of the figure separates phases with P type structure and geometry from those of O type. Different color markers represent different transition metals. This Rouxel type diagram presents a relationship between bond ionicity and A atom size that makes it easy to see when the trigonal prismatic environment is dominant: large alkali/alkaline earth metals in the A position, when vacancies in the A position are present, and when the lattice is more covalent than ionic (*3*). The bond ionicities were calculated using Pauling's formula (*4*):

$$I_b=1 - \exp(-0.25(\Delta X)^2) \qquad (4\text{-}1)$$

Where ΔX refers to the difference in electronegativity between the atoms in the bond being studied (*5*). For example, the bond ionicity of $NaCoO_2$ can be calculated by multiplying the iconicity of Na-O by the ionicity of Co-O. Using the electronegativity values of Na (0.93), Co (1.88), and O (3.44) in Equation 4-1 gives

ionicities of 0.793 for Na-O and 0.456 for Co-O (*4*). Multiplying these values gives a total bond iconicity for $NaCoO_2$ of 0.361, as shown in Figure 4-2.

As there are exceptions to the trends shown in Figure 4-2, a theoretical plot of compounds yet to be produced is a bit forward. For example, in the material $K_{0.70}CrO_2$, K^{1+} adopts octahedral coordination, contrary to the bond ionicities. Similarly, $Na_{0.70}MnO_2$ shows Na^{1+} in trigonal prismatic coordination while firmly placed in the octahedral coordination coordinate of the plot. These anomalies are generally a result of either superstructural ordering or mixing of cations in different positions.

This is a fairly rudimentary calculation of bond ionicity, which takes advantage of the direct relationship between electronegativity difference and bond ionicity. A more rigorous definition would be a self-contained atomic structure calculation based on atomic radius and charge neutrality.

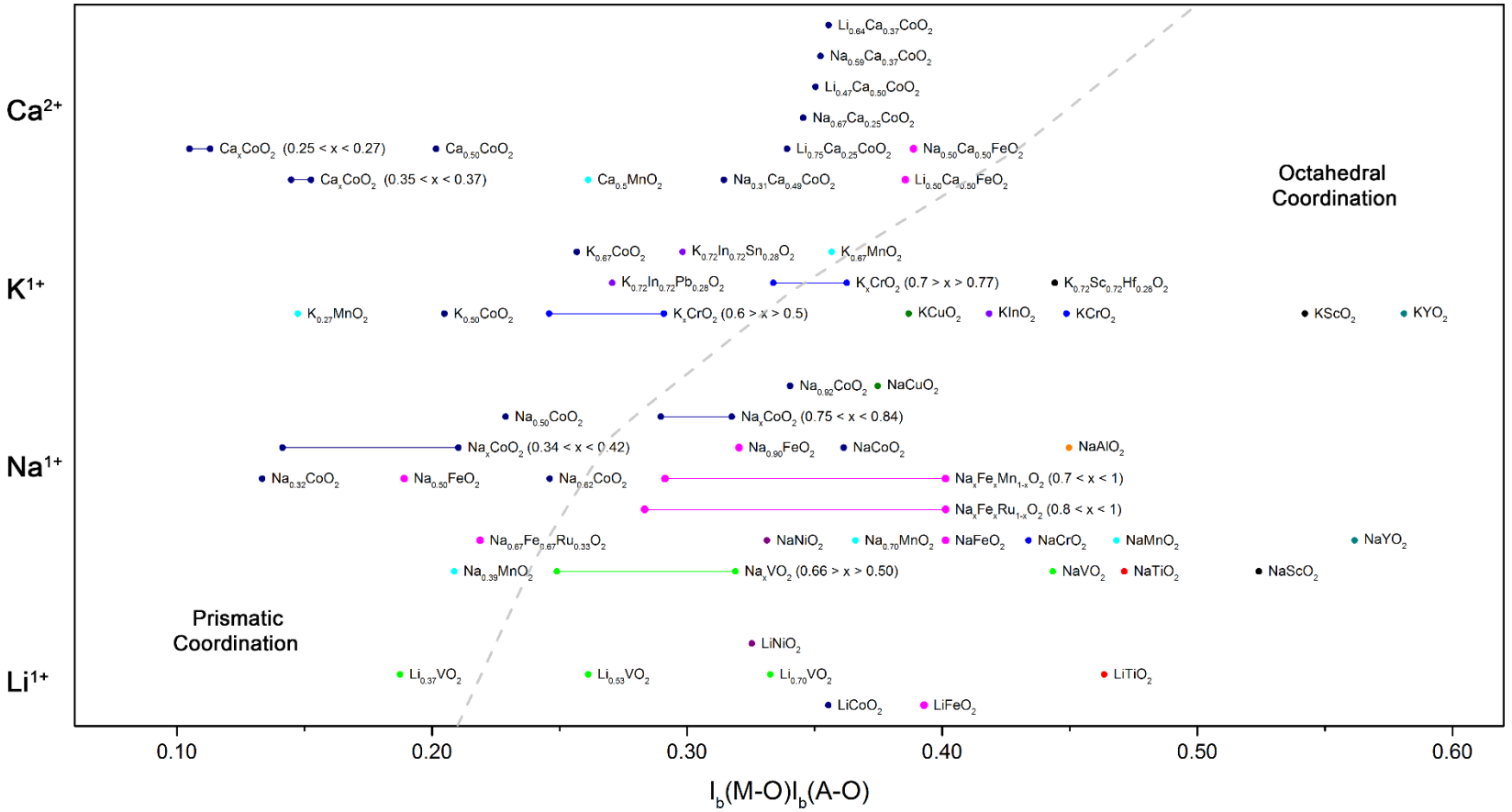

Figure 4-2. Rouxel type plot of bond ionicities *vs.* alkali metal/alkaline earth metal. Dotted line separates P type (left side) from O type phases. Bond ionicities were calculated using the Pauling method (Equation 4-1) (*4*).

4.1a Review of α-$NaFeO_2$ type and similar structures

The following sections give a brief survey of the literature as pertaining to phases with the α-$NaFeO_2$ type structure categorized by where the transition metal falls in the periodic table.

The preparation and characterization of quantum spin systems on perfectly geometrically frustrated lattices is a subject of considerable interest (*6*). $NaTiO_2$ is a canonical two-dimensional frustrated S=1/2 system, and as such may be a model for the quantum spin fluid ground state proposed by Anderson (*7*). $NaTiO_2$ adopts the α-$NaFeO_2$ structure which is an ordered variant of the rock-salt structure. In this structure, layers of edge-sharing TiO_6 octahedra and edge-sharing NaO_6 octahedra alternate along the rock-salt [111] direction. In $NaTiO_2$, there exists a structural transition from the high-temperature (HT) rhombohedral phase (space group $R\bar{3}m$) to the low-temperature (LT) monoclinic phase (space group C2/m) through a broad, continuous transition from 220 K and 250 K (*8*). $NaTiO_2$ formally contains d^1 Ti^{3+} with S=1/2 arranged on a triangular lattice with a separation of about 3.04 Å.

The main body of literatures is focused on how different synthetic routes influence the physical properties of Na_xTiO_2. A range of synthetic procedures - from solid state reactions to soft chemistry - have been applied to prepare this compound; however, it has been shown that different synthetic pathways result in a different Na content, causing a change in the Ti^{3+}/Ti^{4+} ratio (*7*, *9*, *10*).

Depending on the synthesis route, different starting materials such as Na_2O, Na_2O_2, Na and n-butyl sodium, and anatase TiO_2 or Ti_2O_3 have been used. Generally, the high temperature solid-state methods result in sodium deficient phases due to the high sodium vapor pressure above 700 °C. The analogous Li^{1+} phase can be prepared by reducing anatase with ^{n}ButLi in hexane at room temperature. However, efforts to intercalate the larger Na^{1+} ion using sodium naphthalide in tetrahydrofuran failed (*7*). Independent of synthetic method chosen, phases in the entire Na_xTiO_2 oxidation range crystalize in the hexagonal $R\bar{3}m$ space group with cell parameters *a* = 3.00 - 3.05 Å and *c* = 16.23 - 16.44 Å. Because of the incredibly low solubility of Na_xTiO_2 in concentrated acid and HF, a direct correlation between cell parameters and sodium stoichiometry was established (*7*). Due to the sensitivity of the *a* lattice parameter to the oxidation state of titanium, sodium concentration can be calculated based solely on the lattice parameters from high resolution diffractograms. This relationship has been explored throughout the Na deficient range; a convenient way to prepare stoichiometrically pure $Na_{1.0}TiO_2$ (*a* = 3.04365 Å, *c* = 16.2539 Å) by reacting sodium deficient Na_xTiO_2 with sodium metal at 300 °C for an extended period of time was first reported by Clarke (*7*). Afterward, additional Na was washed out with liquid NH_3.

The observed χ_m at room temperature for $NaTiO_2$ is very small and relatively temperature independent. However, on lowering the temperature, the magnetic susceptibility starts to decrease steeply at 260 K followed by a gentle tail(*8*). Since

no hysteresis on cooling and heating was observed, the transition is believed to be second order caused by a shift of the TiO_6 and NaO_6 planes relative to each other. Heat capacity measurements were also consistent with a second order phase transition at 260 K (*9*). A similar metal-metal bonding derived transition has been reported for early transition metal oxides, including V_2O_3 and Ti_2O_3 (*11*). If these transitions are similar in nature, the magnetic features of $NaTiO_2$ are dictated by correlated electrons, not by the spin frustration present in the structure. The magnetic susceptibility of off-stoichiometry Na_xTiO_2 depends strongly on the *a* lattice parameter and the synthetic route used to prepare the material. For example, the magnetic susceptibility of $Na_{1.2}TiO_2$ falls off at 260 K while the susceptibility of $Na_{0.9}TiO_2$ is temperature independent across all temperature regions. Further investigations into the dependence of molar susceptibility on alkali metal stoichiometry would be noteworthy and allow for more concrete determination of Na^{1+} content.

The synthesis of $NaScO_2$ has been reported once in the literature by the Veilhaber group (*12*). Na_2O_2 and Sc_2O_3 were intimately fixed and fired at 600 °C, resulting in phase pure material. No properties investigation was reported. The overall lack of literature precedence is most likely due to the extreme scarcity of scandium on the open market and the difficulty in preparing metallic Sc (*13*).

V_2O_3 and VO_2 vanadium oxides were intensively studied in the 1970s owing to the metal to insulator transition resulting from the presence of V^{3+} ($3d^2$) and V^{4+} ($3d^1$) ions in the corundum and rutile structures, respectively (*14*). The possibility

to introduce these ions into the layered oxide structure is therefore expected to lead to a new family of materials with highly correlated electrons. The Na_xVO_2 system has been researched only very recently, certainly owing to the very reducing character of the trivalent vanadium ions that makes its synthesis difficult (*15*).

Synthesis of $NaVO_2$ required two consecutive steps. Initially, $NaVO_3$ was synthesized via the solid state reaction of Na_2CO_3 and V_2O_5 by heating to the melting point (630 °C). Afterward, $NaVO_3$ powder was reduced chemically under H_2 at 700 °C for 8 hours. As trivalent vanadium in$NaVO_2$ is hyper-sensitive to both oxygen and moisture, the synthesis and characterization must be completed with great care.

Vanadium oxides with layered (α-V_2O_5 and $Na_{1+x}V_3O_8$) or tunnel (β-$Na_xV_2O_5$) structures have been demonstrated to reversibly cycle up to 1.6 Na (225 mAh/g), although the average cell potential is low and capacity retention is poor (*16*–*19*). Layered Na_xVO_2 (x = 0.7, 1) are reported to cycle 0.5 Na reversibly with a specific capacity of 130 mAh/g (*20*). Voltage profiles indicate that sodium vacancy ordering occurs in the layer as a function of Na content, a phenomena that creates two-phase and solid-solution. When $NaVO_2$ is cycled against a Na metal anode above 3V, a phase transition similar to that seen in $LiCoO_2$ occurs that reduces the specific capacity upon subsequent cycling (*20*). Recently, the prismatic phase P2-$Na_{0.70}VO_2$ has shown tolerance towards cycling at high voltage compared to O3-$NaVO_2$ (*21*). The high electronic conductivity of P2-$Na_{0.70}VO_2$ is believed as the

origin of the reduced polarization considering that O3-$NaVO_2$ is electronically insulating.

Recently, rechargeable batteries with high energy density and low cost are in great demand as energy sources for various applications. Lithium ion batteries (LIBs) are being widely used in portable electronics and are considered as promising power sources for future electric vehicles. However, the large-scale commercialization of electric vehicles using LIBs might be hampered significantly due to the relatively high cost and limited resources of lithium. In contrast, the earth abundance of sodium (2.75%) is about three orders of magnitude higher than that of lithium (0.002%). Because of this abundance, rechargeable sodium-ion batteries (SIBs) are being considered as promising energy storage systems for large-scale and cost sensitive applications. Many layered Na intercalated compound with general formula $NaMO_2$ (M = V, Cr, Mn, CO, Ni) are considered as potential cathode materials for SIBs (*22–26*). Among them $NaCrO_2$ is the most promising (*27*). Electrochemical cycling of Na^{1+} in $NaCrO_2$ shows a flat and smooth charge/discharge voltage plateau similar to widely commercialized $LiCoO_2$. In addition, $NaCrO_2$ has higher thermal stability at the charged state compared to $LiCoO_2$ and even $LiFePO_4$, providing a safer cathode material that is not prone to thermal runaway. Interestingly, the analogous Li^{1+} phase with the same layered structure is electrochemically inactive, due to the presence of Cr^{6+} in tetrahedral coordination upon deintercalation of Li^{1+}.

The electrochemical performance of $NaCrO_2$ as a cathode material has been extensively studied by several groups. The compound shows a reversible capacity of 110 mAh/g between 2.5 and 3.6 V vs Na^{1+} / Na) with good capacity retention, demonstrating that half of Na^{1+} can be reversibly extracted and inserted back per $NaCrO_2$ (*28*). Komaba attributed the high reversibility of $NaCrO_2$ to the mismatch between the size of Cr^{6+} ions and the interstitial tetrahedral site of the $NaCrO_2$ structure (*29*, *30*). Most of the research dedicated to $NaCrO_2$ looks at structural changes during electrochemical Na (de)intercalation (*27*).

The synthesis of $NaCrO_2$ is straightforward: a stoichiometric mixture of Cr_2O_3 and Na_2CO_3 is heated at 900 °C under flowing argon for 5 hours, resulting in a O3 type structure (C2/m, *a* = 5.0178 Å, *b* = 2.8828 Å, *c* = 5.9027 Å and ß = 106.97 °) (*31*). Structural changes of $Na_{1-x}CrO_2$ during electrochemical Na deintercalation in was investigated in real time by in situ diffraction using a specially designed electrochemical cell (*27*). According to the variations in Bragg peak positions, the removal of Na^{1+} from the layered $NaCrO_2$ results in consecutive structural phase transitions between three solid solutions. For $Na_{1-x}CrO_2$, when $x < 0.08$, the solid solutions crystalize in the O3 type structure with octahedrally coordination Na^{1+}. Further Na^{1+} removal results in the emergence of a second phase with the O'3-type structure with a monoclinic structure. In the $0.08 \leq x < 0.2$ range, two line phases coexist, while for $x = 0.25$ the dominant phase is $Na_{0.74}CrO_2$. When a third of the Na^{1+} is deintercalated from the structure, the P3 type phase begins to come

in due to the larger separation of the CrO_2 slabs. As x increases to 0.40 and greater, only the P3-type $NaCrO_2$ is present.

The archetype compound of this crystal structure, α-$NaFeO_2$, is a relatively well studied compound, including magnetic, electrochemical, and ionic conductivity measurements (*32*, *33*). $NaFeO_2$ is one of the oldest documented synthesized solid-state materials, first being described in 1888 by Bernheim (*34*). The sodium mobility in this structure has been investigated multiple times through different types of topotaxy including hydrolysis, oxidation, cation exchange, and proton exchange (*35*–*38*). Just as in other similar layer phases described in these thesis, the large difference in the covalent M-O bonds and the ionic A-O bonds allows for topotactic access to the A cations. The vacant tetrahedral positions in the rock salt structure also provides hopping intermediate positions for the A cations, which is generally understood to be the source of the high ionic conductivity reported (*32*).

The synthesis of α-$NaFeO_2$ is easily accomplished - a sodium precursor (NaOH or Na_2O_2) in 10% molar excess is intimately mixed with Fe_2O_3 then fired in air at 500 °C for 24 hours. Any excess sodium precursor is easily removed by washing with anhydrous methanol. Oxidation with Br_2 in MeCN, a very common oxidation method used to deintercalate Na from these layered phases, resulted in a $Na_{0.90}FeO_2$ stoichiometry. Further deintercalation results in decomposition of the phase.

A very nice study on the ionic conductivity of α-$NaFeO_2$ was completed by Blesa in 1999 (*32*). The ionic conductivity of the alpha ferrite was compared to a very common sodium ion conductor $NaInO_2$, where α-$NaFeO_2$ showed a four orders of magnitude increase in ionic conductivity (5.5×10^{-5} S/cm) over $NaInO_2$ (7.9×10^{-9} S/cm) (*32*). As the mechanism of Na^{1+} conductivity is the same in both of these compounds - movement through a vacant tetrahedral position between the two octahedral sites - the increase in ionic conductivity must be caused by a crystallochemical reason. The sodium indate would appear to be a better conductor based on a larger unit cell volume (146.40 $Å^3$ vs 127.56 $Å^3$); however, the increased crystal radius of In^{3+} is substantially larger than Fe^{3+} (0.80 Å vs 0.64 Å), resulting in a smaller total free space for Na^{1+} movement (*32*, *39*, *40*).

The magnetic properties of $NaFeO_2$ are very complicated, with two different low temperature magnetic phases (*33*). The rich magnetic properties of this material can be described by the common vein of many of these layered transition metal oxides with Cd-I_2 type layers: frustrated systems with multiple different competing couplings of approximately equal magnitude. The 4d analog $NaRuO_2$ has also been synthesized although very little characterization has been reported (*41*). In general, when a less electronegative ion is substituted, the metallic conductivity is enhanced due to the reduced directionality in the bonding nature of the material.

Of the main group metals and metalloids, $NaInO_2$ and related species are the most studied by far. Neither Al or B form layered α-$NaFeO_2$ type phases of formula AMO_2 due to their small crystal radii - the tunnel ß-$NaFeO_2$ type phases are more

thermodynamically preferred in these cases. Furthermore, slight doping of both Sn^{4+} and Pb^{2+} for In^{3+} in the $AInO_2$ layered structure has been reported as alkali solid electrolytes although higher doping led to phase disproportionation or non-stoichiometry (*42*, *43*). The most obvious difference between the literature reports of $NaInO_2$ and related phases and the transition metal AMO_2 phases is the lack of magnetic investigation - the spin frustration present in the strongly correlated transition metal materials has been alleviated by diamagnetic In^{3+}; however, a somewhat rich suite of properties has been published recently.

Synthesis of $NaInO_2$ is straightforward: equimolar amounts of Na_2CO_3 and In_2O_3 were fired at 900 °C for 1 hr to avoid Na loss due to vaporization, resulting in the O3 type structure with *a* = 3.227 Å and *c* = 16.38 Å (*40*). The analogous Li^{1+} containing phase can be produced similarly by mixing Li_2CO_3 with In_2O_3 and sintering at 1000 °C (*44*). Topotactic cation exchange of H^{1+} for Na^{1+}, as well as anion exchange of S^{2-} for O^{2-}, have been reported, giving phases with $H_{0.6}Na_{0.4}InO_2$ and $NaInS_2$ respectively (*40*, *45*). A rarely used technique in solid state chemistry, the low temperature facile exchange of H^{1+} for alkali metals in extended solids employing molten benzoic acid saw great success in this system. Trivial isolation of the ion exchange product from the sodium benzoate carboxylate salt was completed by washing with hot methanol and water, affording the O3 type $H_{0.6}Na_{0.4}InO_2$ pure phase material with a slightly compressed *c* parameter (16.35 Å) relative to the parent phase. Attempts at further ion exchange by increasing the temperature above the melting point of benzoic acid (> 180 °C) led to phase

decomposition most likely caused by layer exfoliation as a result of hydrogen binding to only one oxygen as opposed to the octahedrally coordinated Na^{1+} it replaced (*45*).

In recent literature reports, $NaInX_2$ (X = O, S) has been heavily investigated as a photocatalyst for water splitting and organic molecule degradation. A series of $Na_{1-x}(Li,K)_xInO_{,2}$ (0.2 >= x >= 0) were synthesized by the previously mentioned solid state route then impregnated with $Ru_3(CO)_{12}$ in tetrahydrofuran solution (*46*). After oxidation in air at 400 °C, 1% RuO_2 by weight was loaded on the indates. $NaInO_2$ was chosen as the scaffold for RuO_2 impregnation due to its layered structure, which has been previously reported to allow for ideal RuO_2 particle dispersion (*46*, *47*). A closed system hooked up to a gas chromatograph was set up where 250 mg of the solid was suspended in distilled water then illuminated with a Hg-Xe lamp. The highest water splitting activity was found for the pristine RuO_2 impregnated $NaInO_2$ (0.8 μmol/hr) followed by K^{1+} doped $Na_{1-x}K_xInO_2$ (0.7 μmol/hr). Without RuO_2 particles on the surface, no catalytic activity was observed for $NaInO_2$ under any conditions. Interestingly, Sato *et al.* also studied the effects of $NaInO_2$ crystallinity on catalytic activity, finding that a calcination temperature of 1200 °C led to the highest catalytic activity rates due to the highly crystalline nature of the $NaInO_2$ sample prepared at this temperature. Both higher and lower calcination temperatures led to the formation of jagged particles which increased the occurrence of surface trap states, reducing catalytic activity by crippling charge separation rates. With further optimization, impregnated $NaInO_2$ may be a viable

catalyst for water oxidation, paving the way for more widespread use of H_2 as a green energy source (*46*).

$NaInO_2$ has also been investigated as a potential organic molecule decomposition catalyst because of the efficient separation of excitons attributed to the layered α-$NaFeO_2$ structure. The photocatalytic activity of $NaInO_2$ for methylene blue decomposition under UV light was studied by Nomani *et al* (*48*). $NaiNO_2$ was impregnated with 0.5% RuO_2, NiO, and Pt, then suspended in a methylene blue solution. Photocatalytic activity was monitored via UV-Vis absorption spectroscopy due to the strong absorbance of methylene blue at 650 nm. After 60 minutes, all four samples demonstrated methylene blue decomposition while the Pt impregnated sample completely discolored the solution. When codoped with RuO_2, NiO, or Pt, the $NaNiO_2$ powder showed a substantial increase in photocatalytic activity due to the enhanced photoinduced electron hole spatial separation; therefore, the recombination rate of the hole-electron pairs was greatly reduced. Using previous literature reports of the photocatalytic decomposition of methylene blue, two mechanisms can be proposed (*49*). After photoinduced generation of an electron-hole pair the holes in the valence band can react with H_2O to produce ·OH or the electrons in the conduction band can react with dissolved O_2 to produce superoxide radicals. Either of these radical species has been shown to quickly decompose methylene blue under illumination.

4.1b Dependence of oxidation state on properties

The most studied system by far, Na_xCoO_2 demonstrates a rich range of properties depending on the Na concentration (*50*). Considering the oxidation state of Co can be very finely controlled through chemical or electrochemical deintercalation of Na from the crystal lattice, thereby controlling the hole density, Na_xCoO_2 presents a replete system to study the structure-properties relationship in a frustrated triangular lattice.

In general, Na_xCoO_2 ($x >= 0.60$) phases are prepared using classic solid state methods. Stoichiometric amounts of Co metal and a 10% excess sodium source (NaOH, Na_2O_2) were intimately ground under inert atmosphere and fired under O_2 atmosphere. A large body of literature has been devoted to the topotactic methods of Na intercalation and deintercalation into the Na_xCoO_2 framework to specifically tune the Co oxidation state. These tools give great structural control to the inorganic chemist because it allows for the synthesis of phases with similar stoichiometries yet different atomic coordinations. For example, $Na_{0.50}CoO_2$ is easily synthesized, crystallizing in both P'3 and P2 type symmetries depending on the reaction conditions. When $NaCoO_2$ (O3) is oxidized with I_2 in anhydrous MeCN for two days, $Na_{0.50}CoO_2$ (P'3) is produced. These two structures - O3 and P'3 - are easily converted by shifting the CoO_2 layers about 1 Å parallel to the *a* axis. On the other hand, oxidation with I_2 under the same conditions results in the two-layer P2 type $Na_{0.50}CoO_2$ phase. Furthermore, single crystals of P1 type $Na_{0.51}CoO_2$ were synthesized when $NaCoO_2$ (P2) was chemically oxidized with

H_2O_2. Structural control of the highly oxidized cobaltate, $Na_{0.34}CoO_2$, is similarly available: oxidation of O3 $NaCoO_2$ with Br_2 in MeCN afforded O3 $Na_{0.34}CoO_2$. Overall phase composition can be further tuned by modifying oxidation time or intercalating Na using common reducing agents such as Na-benzophenone.

At first glance, it appears that any Na_xCoO_2 ($0.34 <= x <= 1$) with either octahedral or prismatic coordination can be easily chemically synthesized. As seen in Table 4-1, this is not the case. For the two layer system (P2 type phases), solid solution phases with trigonal prismatic symmetry are easily synthesized across essentially the entire range of x values except for a small island of instability at high Na compositions. As reported by the Cava group, the three layer system shows much narrower solid solution limits with two major subgroups: octahedral coordination when $x > 0.75$ and $x < 0.4$ sandwiching prismatic P1 type structures when $0.75 > x > 0.4$ (*51*). Intercalation and deintercalation of Na in the three layer system is therefore much more complicated, as synthesis of phases outside of the solid solution limits of each structural type generally leads to biphasic products.

In these frustrated cobaltates, interplanar length seems to play a key role in material properties - larger distances between CoO_2 planes reduce interplanar interactions relative to intraplanar interactions. Two competing forces dictate how the interplanar distance changes depending on the stoichiometry of these phases: Coulombic interactions between Na^{1+}/$Co^{3+/4+}$ and O, and the O^{2-} - O^{2-} repulsion in adjacent CoO_2 layers. As the NaO_2 layer becomes Na^{1+} deficient, an increase in repulsion between adjacent CoO_2 layers accompanied with a decrease in

Coulombic interactions leads to an increase in interplanar spacing in both the two-layer and three-layer systems. This increase is accompanied by shorter intraplanar Co-Co distances and Co-O bond lengths due to the smaller crystal radii of Co^{4+} relative to Co^{3+} (*39*).

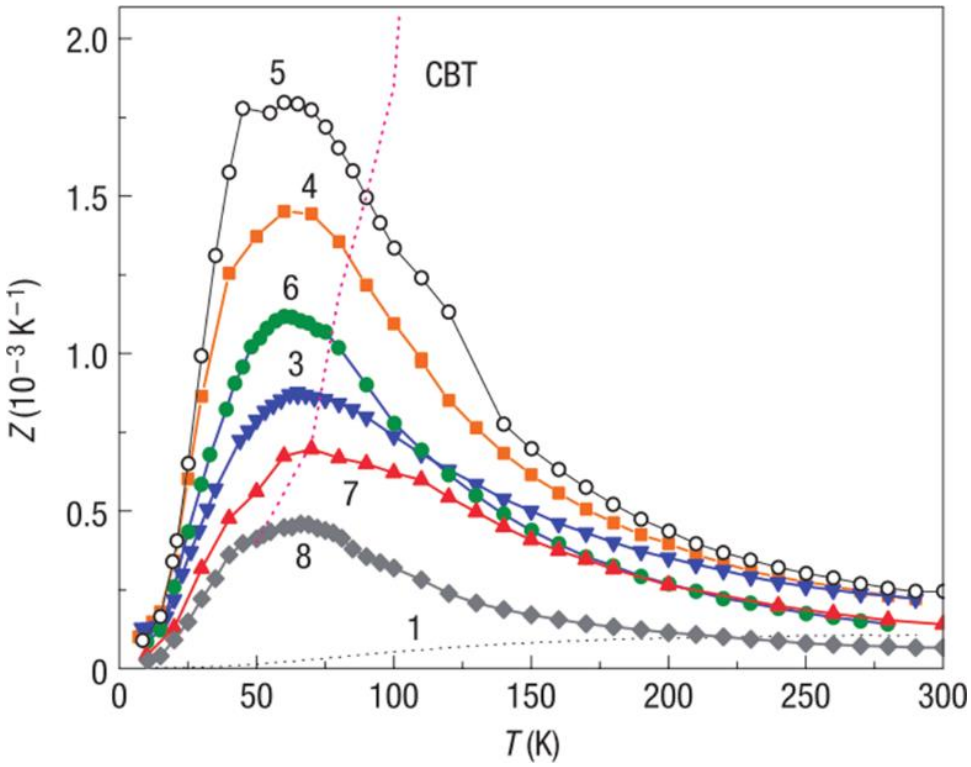

Figure 4-3. Graph of the figure-of-merit Z values for the in Na_xCoO_2 series of layered cobaltates. Used with permission from (*52*).

Table 4-1. Summary of structure types, space groups, cation coordination, and the Co oxidation state in the three layer and two layer families of the Na_xCoO_2 system.

Composition	A Coordination	Structure Type	Space Group	Co Oxidation State
Three Layer Family				
$NaCoO_2$ (*53*)	Octahedral	O3	$R\bar{3}m$	3+
$Na_{0.92}CoO_2$ (*2*)	Octahedral	O3	$R\bar{3}m$	3.08+
$Na_{0.75}CoO_2$ (*2*)	Trigonal Prismatic	P'1	C2/m	3.25+
$Na_{0.67}CoO_2$ (*54*)	Trigonal Prismatic	P'1	C2/m	3.33+
$Na_{0.60}CoO_2$ (*2*)	Trigonal Prismatic	P'1	C2/m	3.40+
$Na_{0.52}CoO_2$ (*53*)	Trigonal Prismatic	P'1	C2/m	3.48+
$Na_{0.50}CoO_2$ (*2*)	Trigonal Prismatic	P'1	C2/m	3.50+
$Na_{0.32}CoO_2$ (*2*)	Octahedral	O3	$R\bar{3}m$	3.68+
Two Layer Family				
$NaCoO_2$ (*1*)	Trigonal Prismatic	P2	$P6_3/mmc$	3+
$Na_{0.85}CoO_2$ (*1*)	Trigonal Prismatic	P2	$P6_3/mmc$	3.15+
$Na_{0.80}CoO_2$ (*1*)	Trigonal Prismatic	P2	$P6_3/mmc$	3.20+
$Na_{0.76}CoO_2$ (*1*)	Trigonal Prismatic	P2	$P6_3/mmc$	3.24+
$Na_{0.71}CoO_2$ (*53*)	Trigonal Prismatic	P2	$P6_3/mmc$	3.29+
$Na_{0.63}CoO_2$ (*1*)	Trigonal Prismatic	P2	$P6_3/mmc$	3.37+
$Na_{0.53}CoO_2$ (*53*)	Trigonal Prismatic	P2	$P6_3/mmc$	3.47+
$Na_{0.50}CoO_2$ (*55*)	Trigonal Prismatic	P2	$P6_3/mmc$	3.50+
$Na_{0.34}CoO_2$ (*1*)	Trigonal Prismatic	P2	$P6_3/mmc$	3.66+

When Co is in the 3+ oxidation state – $NaCoO_2$ – an unremarkable nonmagnetic, nonmetallic material exists. However, when slightly oxidized, Na_xCoO_2 ($1 >= x >= 0.80$) exhibits highly interesting thermoelectric properties. Lee et al recently published a comprehensive study of the thermopower (S) and figure of merit (Z - Equation 4-2), in which they found a direct relation between the thermoelectric properties and Na doping in the structure (Figure 4-3).

$$Z=S^2/\rho\kappa \qquad (4\text{-}2)$$

The curves in Figure 4-3 represent different x values in Na_xCoO_2 according to the following: 1(x = 0.71), 3(x = 0.80), 4(x = 0.85), 5(x = 0.88), 6(x = 0.89), 7(x = 0.96), 8(x = 0.97). At approximately 60 K, a maximum Z is reached for all samples with $Na_{0.88}CoO_2$ having the highest Z of 1.8×10^{-3}. A large jump in the in-plane resistivity between samples 6 and 7 is responsible for the dramatic drop in Z for Na_xCoO_2 where $x > 0.95$. However, resistivity curves with metallic like shape were observed across the doping region studied. The authors propose that the jump in resistivity in samples close to the ideal $NaCoO_2$ stoichiometry is due to charge carrier segregation into layers, thus leading to a lower degree of electrical connection between layers. Understanding the reason for a 40 fold increase in the figure of merit for $Na_{0.88}CoO_2$ relative to $NaCoO_2$ is far from complete, intimately depending on both charge carrier interactions as well as the geometric frustration inherent to the structure.

When 25% of the Na is deintercalated from $NaCoO_2$, effectively oxidizing Co to 3.33+, a curious metallic state manifests. The in-plane susceptibility of $Na_{0.75}CoO_2$ follows Curie-Weiss law above 25 K, yet the resistivity is linear with temperature above 25 K. Essentially, from the susceptibility data, it appears that in $Na_{0.75}CoO_2$ the magnetic susceptibility is dictated by the total number of positive spin carriers, whereas in a metal the susceptibility would quickly fall as the temperature decreased due to lack of population of aligned spins. This mixture of Curie-Weiss paramagnetic susceptibility with metallic resistivity has garnered $Na_{0.75}CoO_2$ (and similar Na composition) the title “Curie-Weiss metal”.

Further oxidation of the sodium cobalt oxide lattice results in the x = 0.5 phase $Na_{0.50}CoO_2$, an insulator that separates the two metallic regions on either side. Deintercalation of Na^{1+} from $Na_{0.74}CoO_2$ gives $Na_{0.50}CoO_2$ with a hexagonal structure (a = 2.81 Å, c = 11.1 Å, P2 type), with Na^{1+} occupying both 2b and 2c sites with near equality. An orthorhombic supercell was established from faint reflections in the neutron diffraction data corresponding with perfectly ordered Na^{1+} atoms – a structural feature that defies an obvious explanation. A low temperature structural study of $Na_{0.50}CoO_2$ identified the reason for the Na^{1+} ordering below 300 K: induced Na^{1+} ordering based on charge ordering of the $Co^{3+/4+}$ ions in the lattice (*55*). The Na^{1+} ordering was confirmed by thermal conductivity measurements. As in most layered oxides of this structural type, the thermal conductivity is primarily carried by phonons; therefore, in an ordered material the phonon mean free path would be much longer than a disordered structure. The in-plane thermal

conductivity of $Na_{0.50}CoO_2$ does indeed increase below the disorder to order transition temperature to 300 W/mK, a similar value to that of quartz and diamond.

Synthesis of the highly oxidized $Na_{0.34}CoO_2$ was accomplished by reacting $Na_{0.74}CoO_2$ with Br_2 in MeCN. The structure is similar to that of $Na_{0.92}CoO_2$ and α-$NaFeO_2$ - three layer structure with octahedrally coordinated Na^{1+} (O3). The magnetic properties of $Na_{0.34}CoO_2$ were reported in the literature - molar susceptibility independent of temperature - but were never explained due to a serendipitous discovery of superconductivity in 2003. A collaboration of materials science groups in Japan were working on layered cobaltates and measuring the magnetic properties of $Na_{0.34}CoO_2$ to try and further elucidate the reason for the independent susceptibility; however, they handled the highly water-sensitive sample in air, allowing 1.47 water molecules per formula unit to intercalate into the 12k sites of the structure. Magnetization measurements in a field of 1000 Oe showed a large diamagnetic signal below 5 K (Figure 4-4). This superconductivity is postulated to occur because of the large increase between CoO_2 layers upon intercalation of two layers of water, effectively localizing the 2d CoO_2 layers similar to the CuO_2 square planar superconductors. A direct comparison between these two structural types is null, as the CoO_2 slabs adopt a frustrated triangular lattice while the CuO_2 square planes are ordered antiferromagnetically.

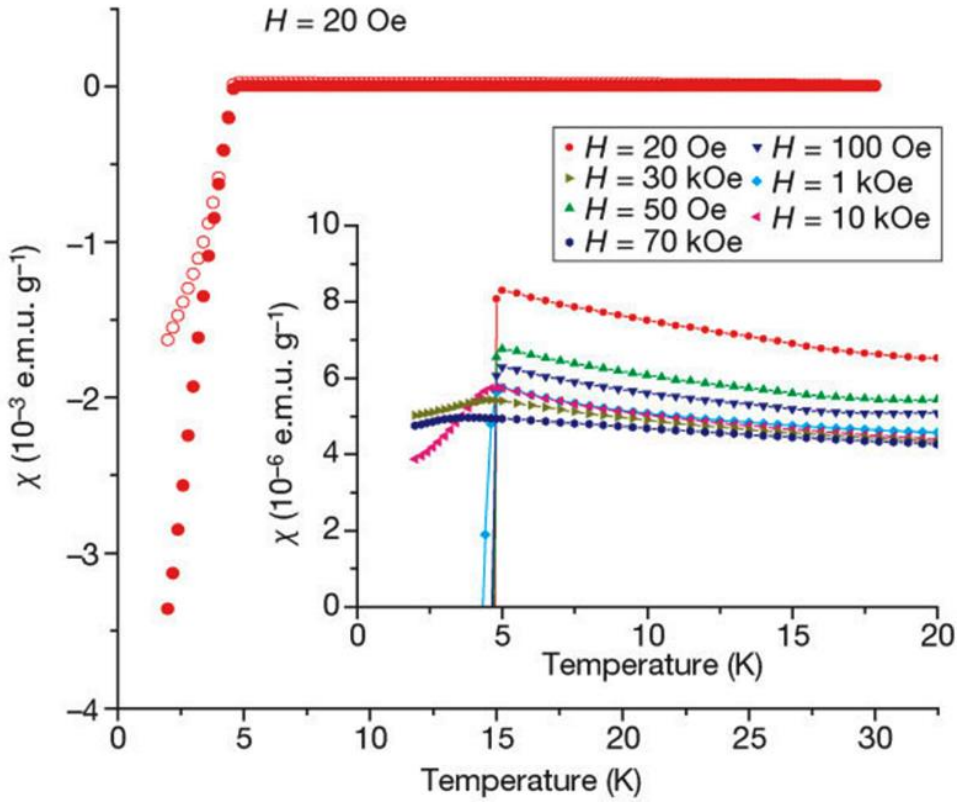

Figure 4-4. Magnetic susceptibility (x) of $Na_xCoO_2 \cdot yH_2O$. Filled circles, zero-field cooling; open circles, field cooling. The susceptibility was measured in a magnetic field of 20 Oe. The inset shows x measured under various magnetic fields by the zero-field cooling process. Reused without adaptation from (*56*).

There have been multiple accounts of directly controlling the Na^{1+} stoichiometry in Na_xCoO_2 by intercalating Na^{1+} back into the structure after oxidation. This has been used extensively at higher x values in hopes of increasing the thermopower of Na_xCoO_2, and has allowed for the large scale synthesis of $Na_{0.88}CoO_2$.

In an attempt to develop more rugged structures, Wiley et al initially proposed the aliovalent exchange of a divalent alkaline earth metal for two alkali metals in

the $NaCoO_2$ family of compounds (*53*, *57*). Compared to previous reports of aliovalent exchange predominately performed in aqueous solutions, the ability to synthesize moisture sensitive materials in molten salt fluxes with controlled vacancies is obviously useful to the solid state chemist. Lamellar calcium cobalt oxides were prepared by intimately mixing the sodium precursor Na_xCoO_2 (x = 1, 0.71, 0.6, 0.53, 0.52) with an excess of anhydrous $Ca(NO_3)_2$ in an evacuated, sealed Pyrex tube and heated at 310 °C for 48 hrs (Equation 4-3, Table 4-2) (*53*, *57*).

$$Na_xCoO_2 + x/2\ Ca(NO_3)_2 \rightarrow \quad Ca_{x/2}CoO_2 + xNaNO_3 \qquad (4\text{-}3)$$

The $Ca_{x/2}CoO_2$ phases were isolated by washing out the nitrate byproduct with anhydrous methanol then stored under inert atmosphere. Interestingly, except for $Ca_{0.52}CoO_2$, the calcium product phases and the reactant sodium phases were indexed in the same space groups, demonstrating the topotactic nature of the reactions. In the case of $Ca_{0.52}CoO_2$, the monoclinic distortion from O3 → P’3 can be reversed by a shift in the CoO_2 layers along the *a* axis. The reason for this transformation, originally proposed by Delmas, is due to the enhanced thermal stability of the A cations in trigonal prismatic coordination as the CoO_2 interlayer spacing increases.

Table 4-2. Unit cell parameters of sodium parent phases and calcium exchange phases discussed in this chapter (*53*, *57*). Notice the topotactic nature of the aliovalent exchange preserves the structural type between sodium and calcium phases.

Precursor	Unit cell (Å)	Exchange Product	Unit cell (Å)
$NaCoO_2$ (O3)	*a* = 2.886 *c* = 15.600	$Ca_{0.52}CoO_2$ (P'3)	*a* = 4.881 *b* = 2.826 *c* = 5.654 ß = 105.8 °
$Na_{0.70}CoO_2$ (P2)	*a* = 2.834 *c* = 10.882	$Ca_{0.35}CoO_2$ (P2)	*a* = 2.812 *c* = 10.87
$Na_{0.60}CoO_2$ (P'3)	*a* = 4.904 *b* = 2.827 *c* = 5.709 ß = 106.1 °	$Ca_{0.30}CoO_2$ (P'3)	*a* = 4.870 *b* = 2.811 *c* = 5.664 ß = 106.6 °
$Na_{0.53}CoO_2$ (P2)	*a* = 2.820 *c* = 11.05	$Ca_{0.27}CoO_2$ (P2)	*a* = 2.812 *c* = 10.87
$Na_{0.52}CoO_2$ (P'3)	*a* = 4.889 *b* = 2.821 *c* = 5.751 ß = 106.2 °	$Ca_{0.26}CoO_2$ (P'3)	*a* = 4.961 *b* = 2.805 *c* = 5.671 ß = 106.7 °

As shown herein and elsewhere, as a compound with an α-$NaFeO_2$ type layered structure is oxidized by removing the A cations, approaching the stoichiometry $A_{0.50}MO_2$, a general crystallinity loss is observed. In the case of Co, the culprit of this decomposition is the presence of a majority of Co^{4+}, not vacancies in the AO_2 layers. However, since the oxidation state of Co is preserved during aliovalent exchange, a larger number of vacancies are created in the AO_2 layer while preserving less than ½ of the Co sites in the Co^{4+} oxidation state; therefore, structural deformations due to the presence of Co^{4+} are avoided. Furthermore, the

Ca^{2+} ions act as structural pillars – the strong interaction between Ca^{2+} and O^{2-} between layers effectively holds the structure together. This observation was experimentally demonstrated by comparing the CoO_2 interplanar distance upon different Ca^{2+} concentrations in Ca_xCoO_2 – the interplanar distance (approximately 5.43 Å) is both constant and independent of Ca^{2+} stoichiometry (*53*).

Multiple reports of the aliovalent exchange of Sr^{2+} for Na^{1+} have recently surfaced in the arXiv repository, focusing on the phase $Sr_{0.35}CoO_2$ (*58*, *59*). Polycrystalline samples of $Sr_{0.35}CoO_2$ were synthesized in a similar fashion as the analogous Ca^{2+} compounds reported herein and elsewhere: $Sr(NO_3)_2$ and $Na_{0.7}CoO_2$ were intimately mixed and allowed to react at 310 °C for two days in air. The publications report on an interesting phenomenon occurring in $Sr_{0.35}CoO_2$ where the annealing temperature has a direct correlation on the band structure of the material. When the sample is annealed at 400 °C under O_2, a metallic state arises with exceptionally low resistivity; however, when annealed in air at 300 °C, the material is a standard semiconductor. The authors propose that the difference in oxygen stoichiometry generated between the two firing conditions is the cause for this change in resistivity without any further investigation. In reality, and in agreement with decomposition products found when performing the Ca^{2+} exchange with Na_xCoO_2 at T > 350 °C, decomposition of the phase at the grain boundaries is most likely leading to a decrease in resistivity. Obvious impurities found in the PXD patterns reported support this idea.

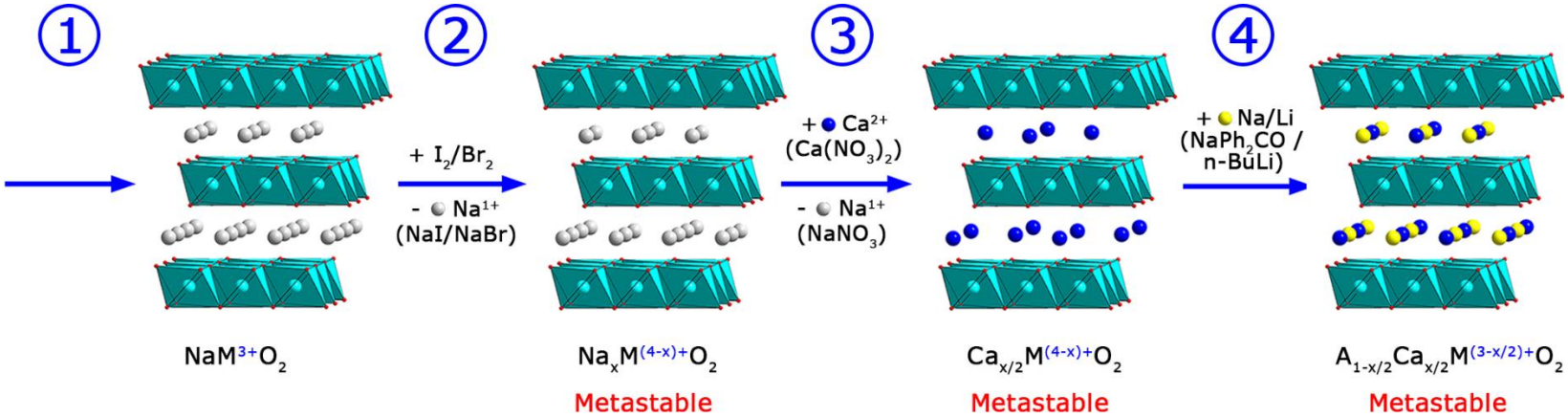

Figure 4-5. Schematic of the general four step MuRE method. In the chemical formulae, M represents any 3d transition metal. Colored spheres represent the following atoms: grey – Na^{1+}, teal – M^{x+}, blue – Ca^{2+}, yellow – Na^{1+}/Li^{1+}. MO_6 octahedra are shown in teal for clarity.

4.2 The multistep reductive exchange (MuRE) method

The general four step MuRE method is depicted in Figure 4-5. The procedure begins with the synthesis of the $NaM^{3+}O_2$ precursor phase by the appropriate solid state methods described previously in this review. Sodium containing phases were chosen over Li^{1+} or K^{1+} because all $NaM^{3+}O_2$ phases with 3d transition metals crystallizing in the α-$NaFeO_2$ type structure are well ordered and easily synthesized. The second step of the procedure is applicable when a final stoichiometry other than $A_{0.5}A'_{0.5}MO_2$ is desired because the Na^{1+} content in the structure before aliovalent exchange directly determines the final phase stoichiometry. Depending on the stability of the transition metal in the 3+/4+ oxidation state, different amounts of Na^{1+} can be deintercalated from the structure using common oxidants (*i.e*. I_2, Br_2, $NOBF_4$, NO_2BF_4), resulting in Na_xCoO_2 ($1 >= x > 0$). The third step of the procedure is the aliovalent exchange of Ca^{2+} for 2 Na^{1+}, thereby creating vacancies in the AO_2 planes of the structure. Multiple groups have shown success in the exchange of Sr^{2+} for Na^{1+} as well, although partial aliovalent exchange for any alkaline earth cation has not been reported (*58*). Due to the metastability of these phases and the desire for topotactic exchange with structure retention, the aliovalent exchange is performed at as low of a temperature possible by exploiting the eutectic between $Ca(NO_3)_2$ and $NaNO_3$ (214 °C). The final step, intercalation of alkali metals into the vacancies created during the aliovalent exchange, results in structures with transition metals in the 2+/3+ oxidation states while maintaining the layered α-$NaFeO_2$ structure. Because complete exchange of

Ca^{2+} for Na^{1+} occurs, the final product can contain any alkali metal. An example set of reactions for the synthesis of $A_xCa_{0.25}CoO_2$ is presented in Equations 4-4 – 4-8. The side products after alkali intercalation using ^{n}BuLi or the sodium benzophenone ketyl, octane and benzophenone, are written to balance the reaction only. The actual side products are a much more complex mixture that is outside of the scope of this review.

$$1/3\ Co_3O_4 + NaOH + 1/12\ O_2 \rightarrow NaCoO_2 + 0.5\ H_2O \quad (4\text{-}4)$$

$$NaCoO_2 + 0.25\ I_2 \rightarrow Na_{0.5}CoO_2 + 0.5\ NaI \quad (4\text{-}5)$$

$$Na_{0.5}CoO_2 + 0.25\ Ca(NO_3)_2 \rightarrow Ca_{0.25}CoO_2 + 0.5\ NaNO_3 \quad (4\text{-}6)$$

$$Ca_{0.25}CoO_2 + 0.75\ ^{n}BuLi \rightarrow Li_{0.75}Ca_{0.25}CoO_2 + 3/8\ C_8H_{18} \quad (4\text{-}7)$$

$$Ca_{0.25}CoO_2 + 0.67\ C_{13}H_{10}ONa \rightarrow Na_{0.67}Ca_{0.25}CoO_2 + 0.67C_{13}H_{10}O \quad (4\text{-}8)$$

The diffractograms of the extremely air sensitive samples $Li_{0.75}Ca_{0.25}CoO_2$ and $Na_{0.67}Ca_{0.25}CoO_2$ were both measured with the diffractometer in an N_2 filled purgebox at a 0.5 s scan rate to minimize any oxidation or hydrolysis. Complete filling all vacancies was not possible in some cases – especially when the larger Na^{1+} ion was intercalated. This trend will be discussed further but may be caused by large particle size, which leads to a core-shell type situation where the shell is much more intercalated than the core resulting in an overall non-stoichiometric phase.

All compounds were prepared in a nitrogen filled glovebox and, if needed, transported to a furnace in a sealed alumina tube. NaOH (Alfa Aesar, 99%), Na_2CO_3 (Sigma Aldrich, 99.9%), Br_2 (Jade Chemical, ACS Grade), I_2 (Jade Chemical, ACS), Co metal (Alfa Aesar, 99.99%), Na metal (Mallinckrodt, ACS Grade), n-BuLi (Sigma Aldrich, 1.6M in hexanes), and benzophenone (Sigma Aldrich, 99%) were used as received without further purification. $Ca(NO_3)_2 \bullet 4H_2O$ (Sigma Aldrich, 99.9%) was thermally treated at 500 °C in dry air for 2 hours to afford anhydrous $Ca(NO_3)_2$.

Synthesis methods for the precursor phases are presented in the following few paragraphs. 1.600 g (40 mmol) NaOH and 2.63 g (10.91 mmol) Co_3O_4 were ball milled for 30 minutes, then fired at 500 °C for 120 hours under O_2, affording pure phase $NaCoO_2$ after washing out excess of NaOH with anhydrous methanol. $Na_{0.74}CoO_2$ was prepared by heat treatment of a mixture of 1.908 g (18 mmol) Na_2CO_3 with 3.77 g (15.66 mmol) Co_3O_4 for 48 hrs at 850 °C under O_2 flow. The more oxidized cobaltates (x = 0.50, 0.34) were synthesized in 5 g batches by room temperature reaction with a 10 molar excess of I_2 and Br_2 in acetonitrile for 96 hrs and 108 hrs, respectively. The NaI/NaBr was removed by washing with dry acetonitrile. $Na_{0.74}CoO_2$ can also be prepared by the staged deintercalation of Na^{1+} from $NaCoO_2$ using I_2 in acetonitrile; however, the solid state method is more facile. The sodium cobaltates were stored in a glovebox to prevent hydrolysis over time from reaction with atmospheric water.

The aliovalent exchange of calcium for sodium was completed by intimately mixing the sodium precursor with 4 equivalents of previously dried $Ca(NO_3)_2$ in a glovebox, then firing the powder under O_2 for 48 hours at 310 °C. The reaction products were washed with water to remove the nitrate salts, then dried under vacuum and stored in a nitrogen filled desiccators.

Calcium exchange phases containing Fe as the transition metal were synthesized similarly with one change – the calcium exchange was performed at 225 °C rather than 310 °C to avoid decomposition.

Topotactic chemical intercalation of Na and Li into the vacancies of the layered framework was performed using standard organometallic reducing agents at room temperature in the glove box. A 20 mL glass vial was charged with 250 mg of the calcium phase and 10 molar excess of either 1.6 M ^{n}BuLi in hexanes or 1M Na-benzophenone in THF, depending on the desired product, and a magnetic stir bar. The reaction was allowed to stir for up to 10 days depending on the phase and final composition desire. After the reaction was complete, the final products were washed with 5 20 mL aliquots of pentane for the Li intercalation or THF for the Na intercalation reactions to remove excess starting material.

$NaFeO_2$ was prepared by grinding 10 g (62.6 mmol) Fe_2O_3 and 5.1 g (125 mmol) NaOH under N_2, heating the mixture in an alumina boat to 330 °C over 5 hours, holding at 330 °C for 10 hours, then raising the temperature to 500 °C and firing for 48 hours under O_2. The product was washed with anhydrous ethanol under N_2 to remove excess NaOH.

All Powder X-ray diffraction (PXD) patterns were obtained on a Bruker D8-Advanced New from 15°- 75° 2θ with Cu radiation (λ = 1.5418 Å), a 2mm beam slit, and a step size of 0.02° 2θ. A plastic dome with a lead coated air-scattering slit was mounted on a zero-background sample holder (Si wafer) to afford the air-tight sample holder used during all measurements.

Inductively-Coupled Plasma Atomic Emission Spectroscopy (ICP-OES) was used to determine the elemental composition of the synthesized compounds on a Varian Vista-MPX CCD. Standard solutions of 1ppm, 10ppm, and 100ppm were prepared from stock solutions of 1000 ppm Li, Na, Ca, and Co obtained from Sigma Aldrich (Puratronic Tracert, standardized). Samples were run in quintuplicate to afford the emission intensity used to derive concentration from calibration curves of the standards.

Thermogravimetric Analysis (TGA) and Differential Scanning Calorimetry (DSC) measurements were performed on a Netsch Jupiter STA-449 F3 TGA/DSC instrument with ultrapure N_2 as a buffer gas. Buoyancy effects were corrected for using an empty alumina sample holder as a blank. Measurements were run with a 5 °C/min step size.

The average magnetic moment of Co in each of the samples was determined using a Quantum Design MPMS. Samples were prepared in gel capsules under N_2 in a glovebox to avoid oxidation. Susceptibility vs. temperature (χ vs. T) was measured at both 1000 Oe and 50000 Oe while susceptibility vs. magnetic field (χ

vs. H) measurements were taken in a scanning field from -50000 Oe to 50000 Oe at 5 K and 300 K.

Electrochemical cycling performance of the lithiated calcium cobaltates was completed using a coin cell type setup with a Celgard 2400 membrane, a 1 M $LiPF_6$ ins EC:DC electrolyte, and a Li metal anode. The cells were prepared in an Ar filled glovebox, then connected to a potentiostat in galvanostatic mode. The voltage was scanned from 3 V to 4.5 V with a step rate of 0.042 mV/s, equivalent to a C/10 scanning rate, for 4 cycles and a step rate of 0.42 mV/s (1C rate) for 50 cycles. Electrochemical performance of the sodium intercalated analogs was also investigated using the same experimental setup with a Na chip used as the anode instead of Li.

4.3 $Fe^{2.5+}$ Phases prepared with the MuRE method

The initial phase, $NaFeO_2$, was prepared by ball milling 10 g (62.6 mmol) of Fe_2O_3 with 5.01 g (125 mmol) NaOH in agate jars for 1 hour at 400 rpm. The jars were opened under nitrogen and the contents were placed in an alumina boat. The boat was loaded into a tube furnace and the following heating profile was initiated under O_2: raise to 330 °C at 65 °C/hour and hold for 10 hours to allow the sodium hydroxide to melt without crawling up the sides of the boat, heat to 500 °C at 100 °C/hour, and hold for 48 hours. This procedure was modified from the literature method only in the fact that the sodium hydroxide was allowed to melt before increasing the temperature. Refinement of phase pure $NaFeO_2$ obtained from this procedure is presented in Figure 4-6.

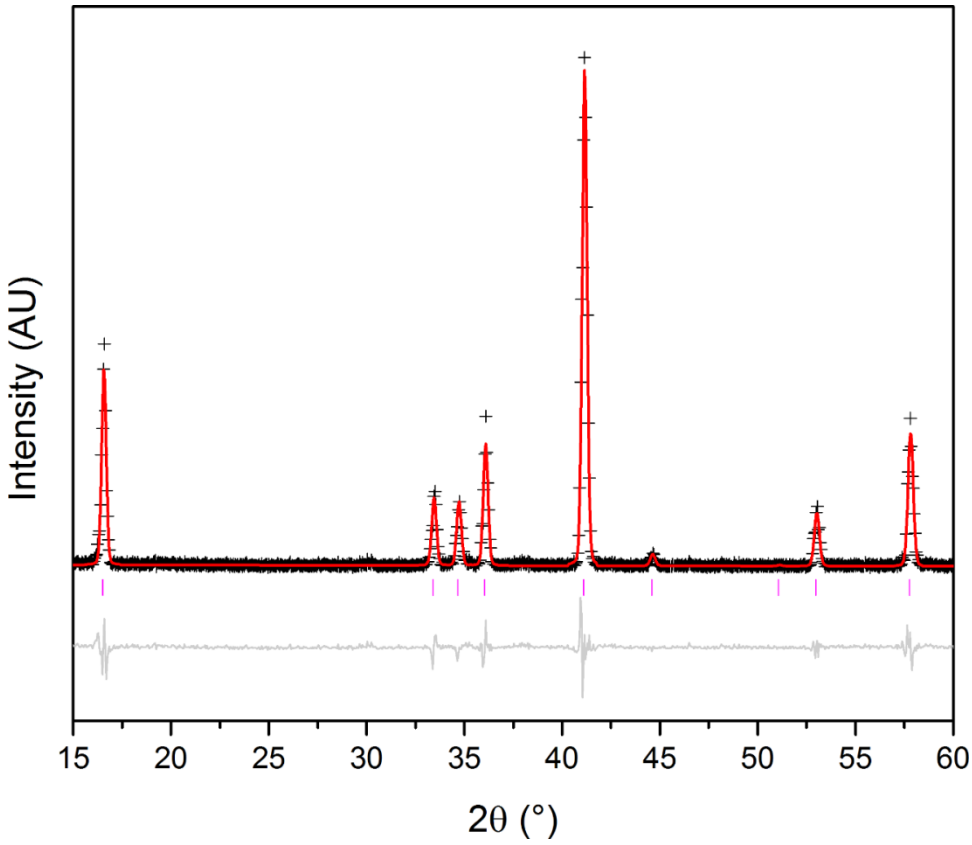

Figure 4-6. Rietveld refinement PXD data for α-$NaFeO_2$ performed using the GSAS software package. Peak anisotropy from preferred orientation is shown in the difference plot (grey line).

The refinement of $NaFeO_2$ converged with χ^2 = 1.43 and R_{wp} = 2.87%. The refined cell parameters ($R\bar{3}m$, *a* = 3.0248(2) Å, *c* = 16.093(1) Å) matched well with the previously reported cell parameters ($R\bar{3}m$, *a* = 3.0251 Å, *c* = 16.094 Å) (*33*). A small amount of peak anisotropy was present in all peaks – a slight decrease in the fitting statistics was observed when preferred orientation along the (003) plane was used in the refinement. The standard hexagonal setting with atomic positions

Na (0 0 0), Fe (½ ½ ½), and O (0.2338 0.2338 0.2338) was used. Since the compound diffracts very well, possible impurities of Fe_3O_4 or Fe_2O_3 are not apparent in the diffractogram. To check for purity of the sample, low temperature magnetization curves were obtained in a 1000 Oe field. The magnetic data closely matched previous reports, verifying the purity of the sample.

4.3a $Ca_{0.50}FeO_2$ characterization and intercalation

Initial attempts at Ca-for-Na exchange were unsuccessful because of the decomposition of the produced phase ($Ca_{0.50}FeO_2$) to Fe_2O_3 and CaO at 310 °C under O_2, as confirmed in the impure PXD where the main peak for Fe2O3 is seen approximately 27° 2θ. Once the reaction temperature was lowered to 225 °C – just above the eutectic temperature of $Ca(NO_3)_2$ and $NaNO_3$ - pure phase $Ca_{0.50}FeO_2$ was produced after 48 hours under O_2 (*60*). The powders were intimately ground in the glovebox before firing, but were not pelletted for the first reaction. When pelletted, the reaction speed increased dramatically, resulting in pure phase material after just 24 hours. After the products cooled to room temperature, the material was ground with a mortar and pestle under anhydrous methanol to remove the $NaNO_3$ present after exchange. The final stoichiometry was determined by ICP-OES. PXD patterns of the Fe family of compounds prepared using the MuRE method are presented in Figure 4-7.

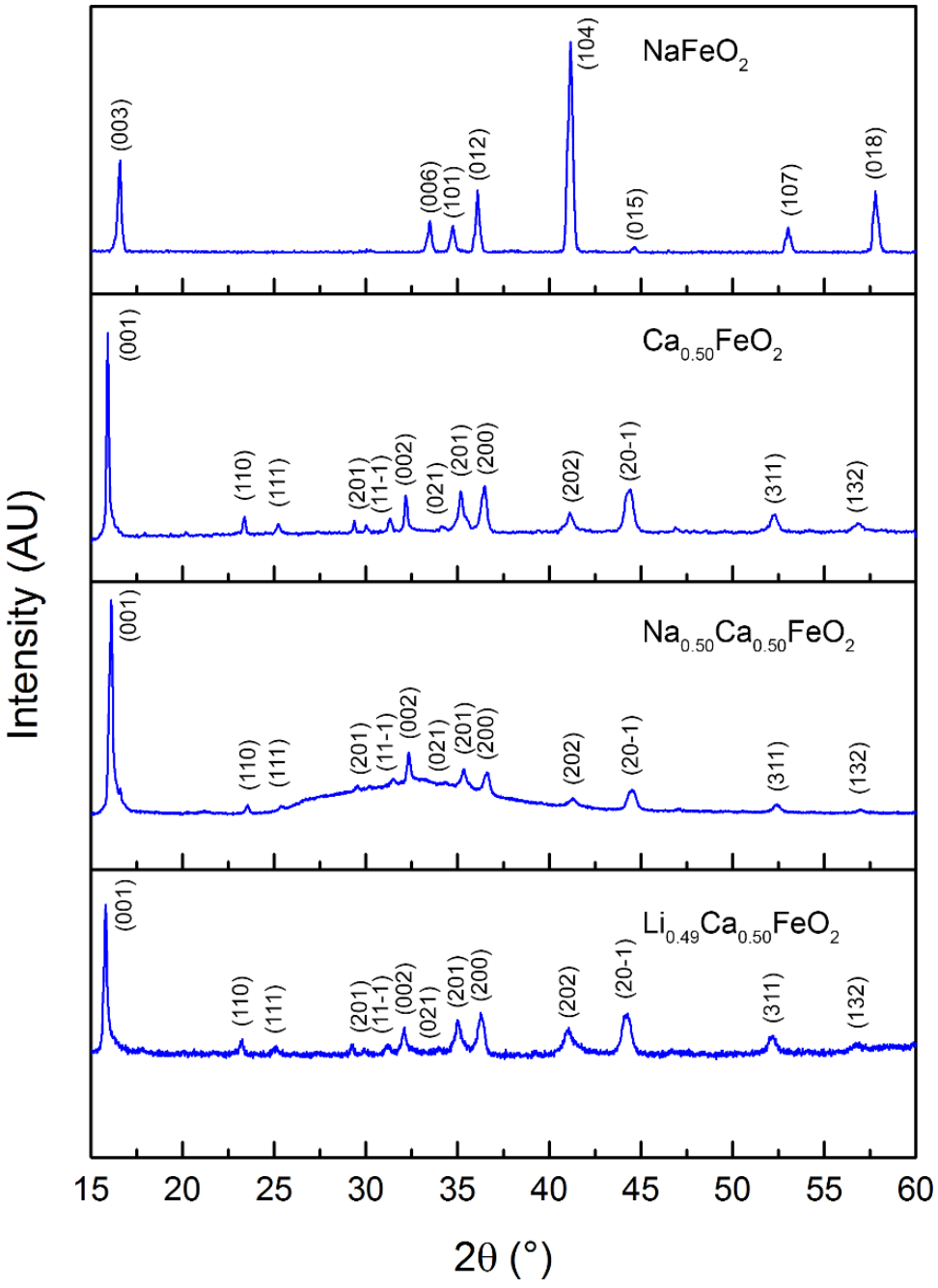

Figure 4-7. PXD spectra of the Fe based family of materials prepared using the MuRE method presented in this chapter. The background (broad hump, peak near 16 °2θ) in $Na_{0.50}Ca_{0.50}FeO_2$ was due to the dome-type sample holder used during collection.

Table 4-3. Cell parameters of $Ca_{0.50}FeO_2$ obtained from the LeBail refinement of powder X-ray and neutron diffraction data at different temperatures (*61*). Full Rietveld refinement was undertaken as well.

Method	a (Å)	b (Å)	c (Å)	ß (°)
PXD	5.1743(8)	5.9532(4)	5.8215(3)	73.21(2)
NPD 75K	5.1453(3)	5.9442(7)	5.8060(1)	73.19(4)
NPD 12 K	5.1321(1)	5.9385(4)	5.7924(2)	73.16(3)

Indexing of $Ca_{0.50}FeO_2$ was successful, resulting in a C2/m monoclinic unit cell with *a* = 5.1743(8) Å, *b* = 5.9532(1) Å, *c* = 5.8215(3) Å, and ß = 73.21(2) °. Rietveld refinement of $Ca_{0.50}FeO_2$ was completed on both PXD and NPD patterns (75 K and 12 K) obtained at Oak Ridge National Lab on the POWGEN beam line in collaboration with Dr. Jason Hodges. Rietveld refinement of the PXD data converged with χ^2 = 1.79. The cell parameters obtained from refinement of the diffraction data sets are presented in Table 4-3 – the small discrepancy between the PXD and NPD derived cell parameters is due to the measurement temperatures: the PXD spectra were recorded at 298 K, while the NPD data was recorded at both 75 K and 12 K.

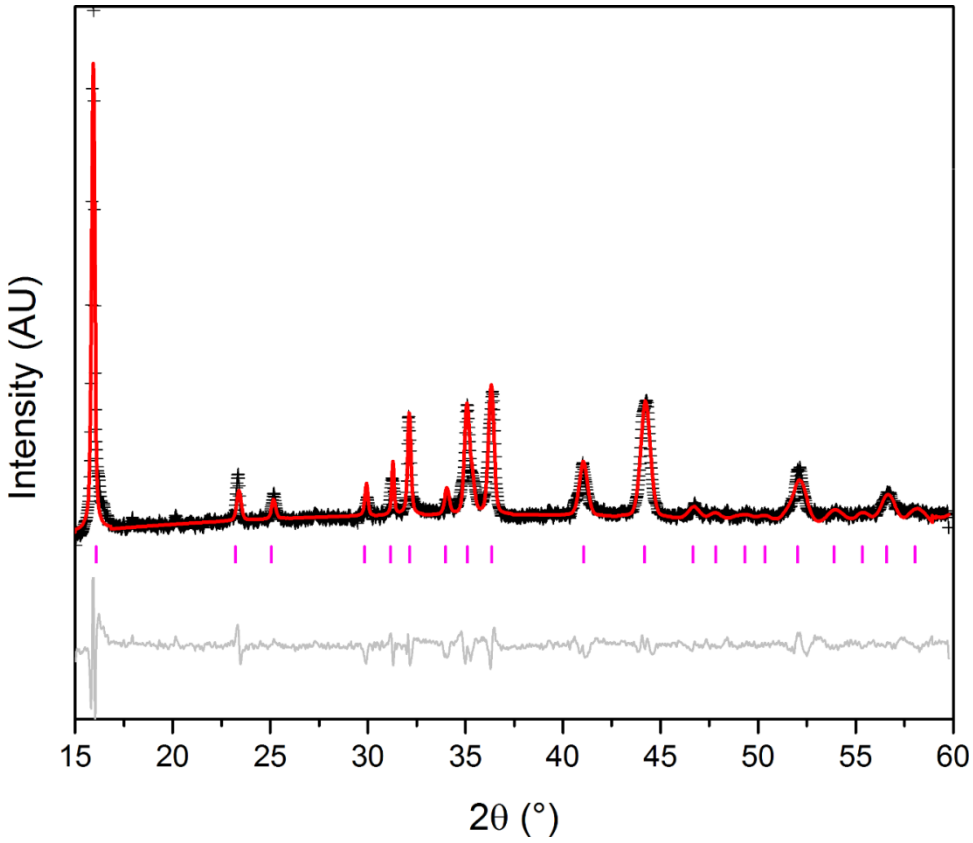

Figure 4-8. Rietveld refinement of the PXD data of $Ca_{0.50}FeO_2$ showing the observed pattern (black crosses), refined fit (red trace), difference curve (grey below), and Bragg diffraction positions (magenta tickmarks, below).

PXD least squares refinement of the $Ca_{0.50}FeO_2$ diffraction pattern was straightforward and converged with the following statistics: $\chi^2 = 1.79$, $R_{wp} = 5.89$ %, and $R_p = 6.72$ % as seen in Figure 4-8. A small amount of non-systematic peak anisotropy was observed in the pattern, attributed to a mixture of preferred orientation and peak broadening as a result of a smaller particle size distribution. Atomic positions of $Ca_{0.50}FeO_2$ in the C2/m space group were refined as well and

are presented in Table 4-4. The large thermal parameters obtained are a consequence of the relatively poor diffraction pattern statistics. Observed and calculated Bragg positions are compared in Table 4-4. Due to the unreliable refinement, the model obtained from this PXD data was further used in the neutron refinements. It is difficult to directly compare the structures of $NaFeO_2$ and $Ca_{0.50}FeO_2$ based on cell parameters due to the large differences in unit cell symmetry; however, the layered structure was preserved as seen from the atomic positions and diffraction pattern.

Refinement of the neutron data was exceptionally difficult for two reasons: poor counting statistics at low d spacing and large angle-dependent peak asymmetry. These problems were overcome by careful profile refinement, which will be explained over the next few paragraphs.

Table 4-4. Refined atomic positions for $Ca_{0.50}FeO_2$ obtained by Rietveld refinement of NPD data.

Atom	Wyckoff Position	X	y	z	U_{iso} 10^2 (Å^2)	Occ.
Ca^{2+}	2 b	0	0	0.5	0.0184(2)	0.50
Fe^{3+}	2 a	0	0	0	0.0161(3)	0.50
Fe^{3+}	2 c	0.5	0	0	0.0153(1)	0.50
O^{2-}	8 j	0.36	0.25	0.2	0.0212(7)	0.34
O^{2-}	4 i	0.17	0	0.21	0.0216(8)	0.33

Table 4-5. Observed and calculated Bragg reflections for $Ca_{0.50}FeO_2$ in the C2/m space group as proof of correct indexing. Indexing of the PXD data was done using the TOPAS software package.

Calculated °2θ	Observed °2θ
15.887	15.897
23.342	23.338
25.112	25.121
29.866	29.815
31.361	31.358
32.144	32.148
34.081	34.082
35.161	35.165
36.323	36.243
40.976	40.978
44.375	44.382
46.823	46.901
47.822	47.815
49.375	49.402
50.197	50.185
52.019	52.017
54.259	54.248
55.535	55.521
56.519	56.498
57.892	57.885

Initially, the cell parameters obtained from the PXD refinement of $Ca_{0.50}FeO_2$ were added as a phase to GSAS, followed by the addition of the two NPD histograms for $Ca_{0.50}FeO_2$ recorded at 75 K and 12 K. Since the NPD data was recorded as time of flight, a diffractometer constant of 22778.326 s was used to convert the time of flight data to d-spacing with Equation 4-9.

$$t = DIFC*d + DIFA*d^2 + ZERO \quad (4\text{-}9)$$

In the above formula, DIFC can be approximated if the total neutron path length and the scattering angle are known by combining the Bragg Law with the de Broglie relationship (where m is the neutron mass, *h* is Planck's constant, t is total flight time, and L is total flight path):

$$t = (\frac{2m}{h})L\sin\theta d \quad (4\text{-}10)$$

When m and h are populated with 939.565 MeV/c_2 and 4.13567 x 10^{-15} eVs, respectively, the following relationship is obtained:

$$t = 505.56L\sin\theta d \quad (4\text{-}11)$$

From this relationship, when DIFA and ZERO are 0 – common with many neutron sources – DIFC can be approximated by $505.56L\sin\theta$. When multiple histograms are taken at different wavelengths, DIFC must be constantly refined for the lower resolution histogram and fixed for the higher resolution histogram to prevent divergence from the high correlation of DIFC to lattice parameters. Similarly, DIFA can be introduced to the refinement if a large difference in source

wavelengths are incorporated – the quadratic dependence of DIFA on the scattering angle fits the small shift in total flight path between longer wavelength (longer flight length) and shorter wavelength (less absorption, shorter path). In the case of $Ca_{0.50}FeO_2$, DIFA was refined after the profile refinement but did not increase the refinement fit to any appreciable degree. The background was then refined with a minimum number of terms (6 due to the complexity of the background at low d-spacing) using the Chebyshev profile.

After the histogram related constants were inserted, atom positions and occupancies were added according to Table 4-5. The peak profile was then characterized as pseudo-voight – the weighted average of Gaussian and Lorentzian peak profiles. Using this profile type required the refinement of six parameters denoted sig-0, sig-1, sig-2 for the Gaussian part, and gam-0, gam-1, gam-2 for the Lorentzian part of the profile as show in Equations 4-12 and 4-13, respectively.

$$\sigma^2 = \sigma_0^2 + \sigma_1^2 d^2 + \sigma_2^2 d^4 \quad (4\text{-}12)$$

$$\gamma = \gamma_0 + \gamma_1 d + \gamma_2 d^2 \quad (4\text{-}13)$$

These parameters are much more important than they initially look – especially sig-1 and gam-1 due to their linear relationship to d-spacing. In general, with a stationary detector, peak broadening is related to d-spacing by a constant over the whole d space. Refinement of sig-1 and gam-1 directly describes this constant, creating a profile where the peak width naturally increases as the d-spacing

decreases. Unfortunately, these parameters alone do not account for anisotropic peak broadening, which also has a d space dependence. The addition of two terms to the Lorentzian Equation can account for anisotropic deviations with a linear relationship to d space.

$$\gamma = \gamma_0 + \gamma_1 d + \gamma_2 d^2 + (\gamma_{1e} d + \gamma_{2s} d^2)\cos\theta + \gamma_L \qquad (4\text{-}14)$$

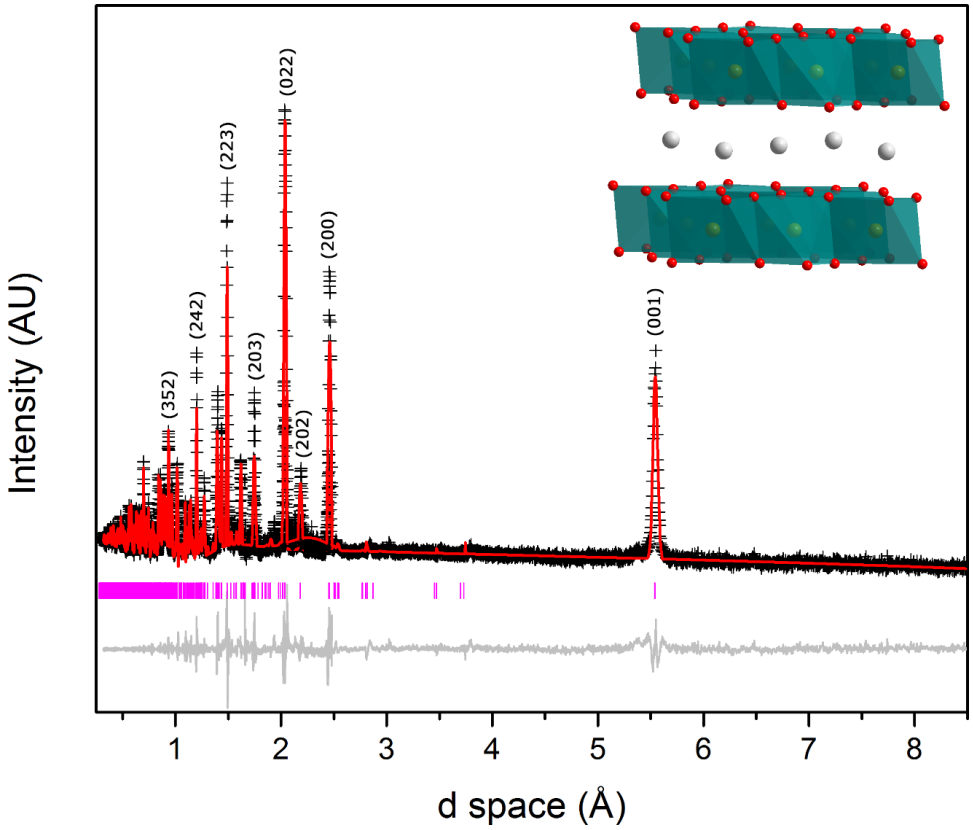

Figure 4-9. Rietveld refinement of NPD of $Ca_{0.50}FeO_2$ collected at 75 K showing the observed pattern (crosses), fit pattern (red trace), difference curve (grey line, below), and Bragg positions (magenta tickmarks). The refined unit cell is present in the top right corner showing the topotactically preserved layered structure.

Incorporating the γ1e (g1ec), γL (L11), and γ2s (g2ec) parameters adds a second set of terms similar to the first that are shifted depending on the diffraction angle. Considering the phase being refined – $Ca_{0.50}FeO_2$ – incorporation of anisotropic broadening (commonly caused by stacking faults) was scientifically reasonable. A summary of the profile parameter values used for the refinements at 12 K and 75 K are given in Table 4-6. Both datasets include diffraction data collected with 1.066 Å and 3.731 Å radiation to cover a large d space range.

Table 4-6. Values for profile fitting parameters used in the Rietveld refinement of $Ca_{0.50}FeO_2$ NPD data collected at both 75 K and 12 K.

Parameter	Value
sig-0	0.0000
sig-1	3022.5
sig-2	2081.8
gam-0	0.0000
gam-1	713.12
gam-2	0.0000
g1ec	-77.098
g2ec	41.231
L11	0.0000

Even with the extra profile parameters included to describe the peak anisotropy from stacking faults and other broadening features, the low d space fit at 75 K is fairly poor (Figure 4-9). As expected, the low d spacing profile fit at 12 K is substantially better because of the lower lattice thermal energy (Figure 4-10). There was also a problem refining oxygen positions due to the signal to noise ratio, resulting in skewed octahedra.

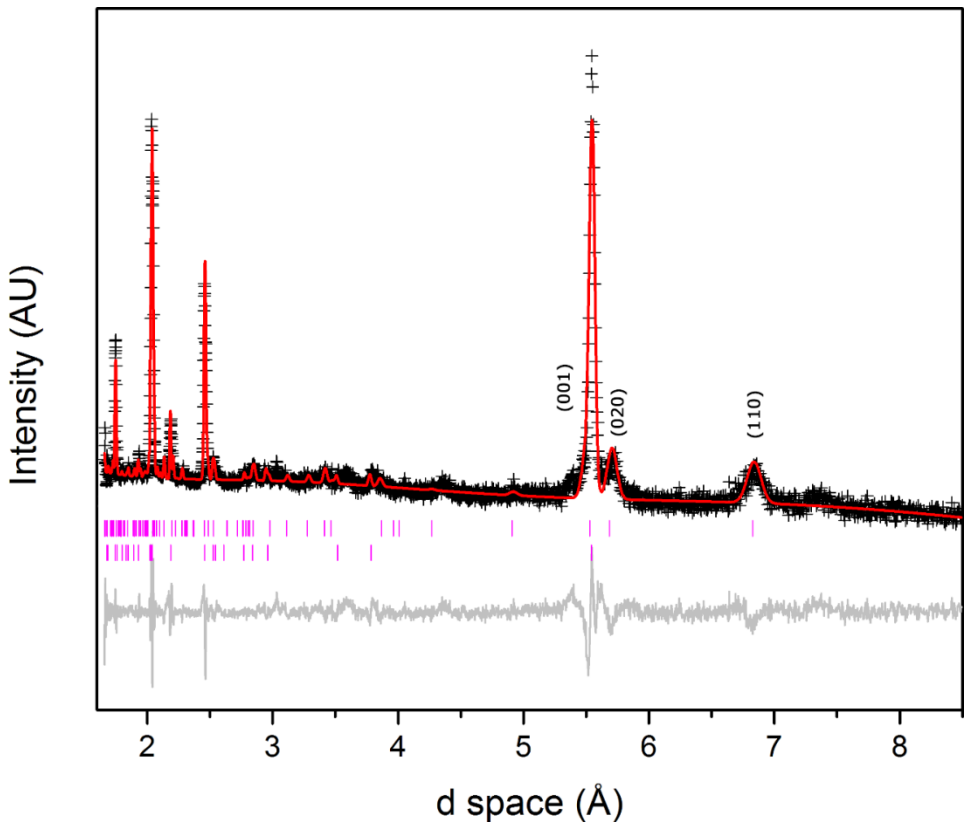

Figure 4-10. Rietveld refinement of NPD of $Ca_{0.50}FeO_2$ showing the observed pattern (crosses), fit pattern (red trace), difference curve (grey, below), and Bragg positions (tickmarks, below). The second line of magenta tickmarks represents the magnetic cell observed. The first few reflections of the magnetic cell are labeled.

The appearance of a magnetic cell in the low temperature NPD pattern was not surprising considering $NaFeO_2$ has two very distinct magnetic cells at low temperatures (*33*). However, one $NaFeO_2$ magnetic cell is incommensurate and one is commensurate with the parent rhombohedral unit cell, a main difference found in the low temperature magnetic unit cell of $Ca_{0.50}FeO_2$. The incommensurate nature of the $Ca_{0.50}FeO_2$ magnetic cell made Rietveld refinement extremely difficult. A LeBail refinement was completed on the magnetic cell, resulting in the cell parameters presented in Table 4-7 (*62*). Higher quality NPD patterns obtained at multiple temperatures between 5 K and 25 K (reason for this temperature discussed further) are needed to establish the magnetic propagation vector and moment direction, as well as to investigate the possibility of multiple magnetic states.

Table 4-7. A comparison of the nuclear and incommensurate magnetic cell parameters of $Ca_{0.50}FeO_2$ obtained from refinement of NPD data.

Cell Parameter	Nuclear Cell	Magnetic Cell	% Change
a (Å)	5.1321	8.9378	+74
b (Å)	5.9385	11.435	+93
c (Å)	5.7924	5.7952	0
ß (°)	73.16	73.02	-1.2
Volume (Å^3)	168.96	566.47	+330

An educated guess at the nature of the magnetic cell would point to a ferromagnetic nearest-neighbor interaction with coupling constant J_{NN}, an antiferromagnetic next-nearest-neighbor interaction J_{NNN}, and an antiferromagnetic nearest-neighbor interplanar interaction J_{IP} when viewed looking down the frustrated triangular lattice. If the next-nearest-neighbor interaction was not present, the FeO_2 layers would be dominated by ferromagnetic interactions; hence, the J_{NNN} gives rise to the frustration of the lattice. This description of the magnetic cell is similar to that of one of the magnetic superstructures of $NaFeO_2$ (*36*). A corroboration of further NPD and magnetic measurements at low temperatures (between 5 K and 25 K) could be used to determine the effect of JIP and how the antiferromagnetic influence changes based on temperature.

The sodium intercalated product of $Ca_{0.50}FeO_2$ – $Na_{0.50}Ca_{0.50}FeO_2$ – was synthesized by first placing 250 mg $Ca_{0.50}FeO_2$ (2.32 mmol) in a clean 50 mL round bottom flask in the glovebox with a magnetic stir bar. A 1 M solution of Na-benzophenone in THF was prepared by adding 0.4598 g (20 mmol) Na metal and 3.664 g (20 mmol) benzophenone to 20 mL of THF while stirring. 10 mL of the 1 M solution of Na-benzophenone was added to the round bottom flask and the reaction was stirred for 10 days. Initially, to check for product purity and intercalation rates, aliquots were taken every day and analyzed via ICP. A full year-long reaction scaled up 25x in a 1 L round bottom flask was completed as well, resulting in pure phase material.

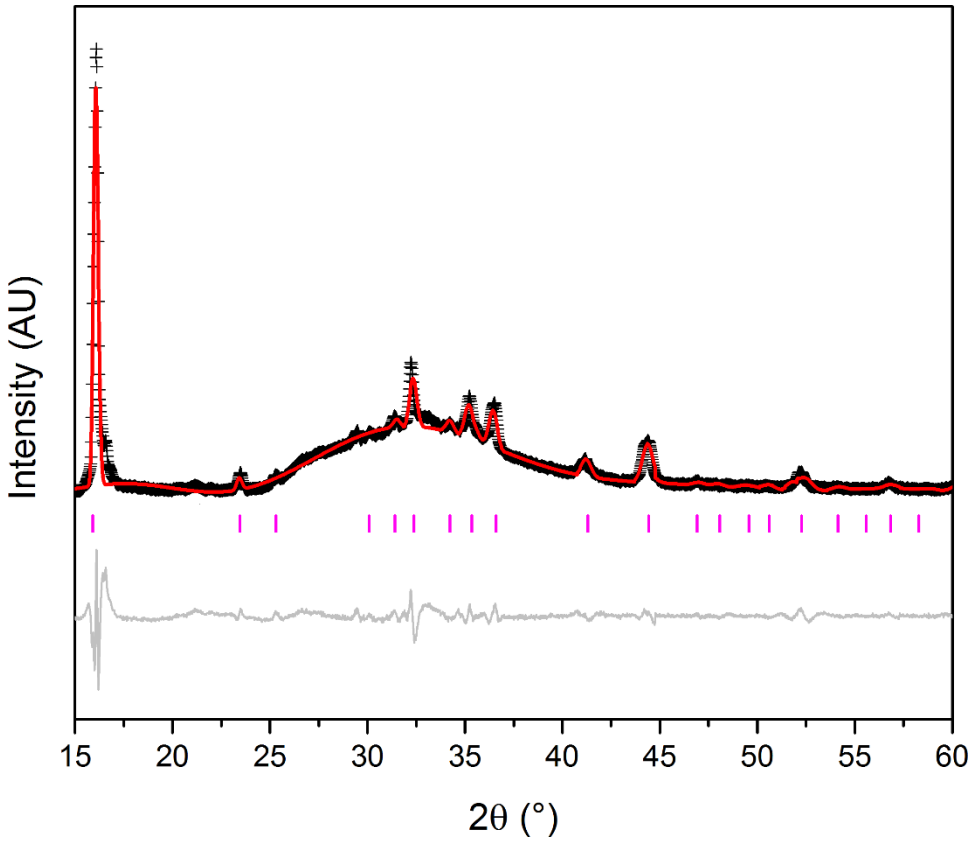

Figure 4-11. Refinement of PXD of $Na_{0.50}Ca_{0.50}FeO_2$. Contribution from the sample holder is the reason for the unindexed peaks/amorphous background.

The background of $Na_{0.50}Ca_{0.50}FeO_2$ is due to the domed sample holder used to collect the diffractogram of the exceptionally air-sensitive sample. Many of the diffractograms collected on air-sensitive samples and presented in this thesis were obtained on a standard low background Si sample holder while the diffractometer was located in an inert purgebox. When a diffractogram of $Na_{0.50}Ca_{0.50}FeO_2$ was collected in this way, the pattern showed obvious sample hydrolysis due to excessive peak broadening and loss of crystallinity as the theta angle increased.

The sample was then loaded into a dome sample holder that was assembled inside of a purified atmosphere glovebox to assure a constant and completely inert atmosphere. However, the sample holder diffracted as well, leading to the unindexed peaks and large hump-like background found in the PXD spectrum.

Refinement of PXD data for $Na_{0.50}Ca_{0.50}FeO_2$ was also difficult due to both the poor counting statistics of lab diffractometer data as well as the large background contribution from the sample holder (Figure 4-11). The $Ca_{0.50}FeO_2$ model previously refined was used as a starting basis for the refinement of $Na_{0.50}Ca_{0.50}FeO_2$. The refinement did converge when all occupancies were fixed at values obtained from ICP data; however, with very poor refinement criteria of χ^2 = 7.85 and R_{wp} = 19.76%. Thermal parameters were refined then closed as the final refinement diverged when thermal parameters were open (Table 4-8).

The Li-intercalated product $Li_{0.50}Ca_{0.50}FeO_2$ was also successfully synthesized; however, according to diffraction data a very small peak (<5%) that could not be indexed was always present. This peak was not seen in the other diffraction patterns and may be a sign of short range ordering of Li^{1+} or Ca^{2+} in the lattice. Stoichiometry was confirmed by ICP analysis. Refinement of the PXD data converged with χ^2 = 2.23 and R_{wp} = 5.64%. Refined atomic positions for $Li_{0.50}Ca_{0.50}FeO_2$ are presented in Table 4-9. The atomic positions are very similar to those of $Na_{0.50}Ca_{0.50}FeO_2$ and $Ca_{0.50}FeO_2$, verifying the topotactic nature of the reaction.

Table 4-8. Atomic positions for $Na_{0.50}Ca_{0.50}FeO_2$ from Rietveld refinement of PXD data.

Atom	Wyckoff Position	x	y	z	10^2 U_{iso} ($Å^2$)	Occ.
Ca^{2+}	2b	0	0	0.5	0.51(3)	0.5000
Na^{1+}	4i	0.49	0	0.52	3.1(2)	0.5108
Fe^{3+}	2a	0	0	0	0.82(4)	0.5000
Fe^{3+}	2c	0.5	0	0	0.64(1)	0.5000
O^{2-}	8j	0.36	0.23	0.20	2.1(2)	0.335
O^{2-}	4i	0.17	0	0.21	1.8(1)	0.335

Table 4-9. Atomic positions for $Li_{0.50}Ca_{0.50}FeO_2$ from Rietveld refinement of PXD data

Atom	Wyckoff Position	X	y	z	10^2 U_{iso}($Å^2$)	Occ.
Ca^{2+}	2b	0	0	0.5	0.86(3)	0.5000
Li^{1+}	8j	0.47	0.08	0.57	2.6(1)	0.4821
Fe^{3+}	2a	0	0	0	0.79(7)	0.5000
Fe^{3+}	2c	0.5	0	0	0.61(4)	0.5000
O^{2-}	8j	0.35	0.22	0.21	1.5(3)	0.3784
O^{2-}	4i	0.15	0	0.20	1.4(2)	0.3025

A comparison of the cell parameters of $Ca_{0.50}FeO_2$ and the intercalated compounds follows similar trends established in the previous cobaltate literature (Table 4-10). The *a*-*b* plane is very similar among all three compounds with a slight expansion in the Na^{1+} doped material due to the larger size of Na^{1+} compared to Li^{1+}. The *c* parameter contracted slightly after intercalation of $Ca_{0.50}FeO_2$, caused by the attraction between the intercalated alkali metals and the O^{2-} of the CoO_2 slabs. FeO_2 interplanar distances followed expected trends as well, as shown in Table 4-11.

The interplanar distances between Fe atoms in the Fe containing phases are compared in Table 4-11. The distances trend as would be expected from chemical intuition. After the aliovalent exchange of Ca^{2+} for Na^{1+} the interplanar distance decreased nearly 1 Å due to the larger Coulombic interaction between Ca^{2+} and O^{2-} and the increase of bond covalency over the Na^{1+} - O^{2-} bonding. After alkali metal ions were intercalated into the vacancies created during the exchange the interplanar distance decreased slightly. It appears that the Ca^{2+} ions act as pillars in the structure essentially locking the interplanar distance regardless of further ion intercalation.

Table 4-10. Cell parameters comparison of $Ca_{0.50}FeO_2$ and the intercalated products $Na_{0.50}Ca_{0.50}FeO_2$ and $Li_{0.50}Ca_{0.50}FeO_2$.

Compound	a (Å)	b (Å)	c (Å)	ß (°)
$Ca_{0.50}FeO_2$	5.1743(8)	5.9532(4)	5.8215(3)	73.21(2)
$Na_{0.50}Ca_{0.50}FeO_2$	5.1796(4)	5.9643(6)	5.8025(2)	73.24(2)
$Li_{0.50}Ca_{0.50}FeO_2$	5.1733(3)	5.9482(7)	5.8044(1)	73.12(4)

Table 4-11. FeO_6 interplanar distance comparison in the Fe compounds prepared with the MuRE method.

Compound	Interplanar Distance (Å)
$NaFeO_2$	5.6354
$Ca_{0.50}FeO_2$	5.5165
$Na_{0.50}Ca_{0.50}FeO_2$	5.5052
$Li_{0.50}Ca_{0.50}FeO_2$	5.4931

4.3b Magnetic measurements of $Fe^{2.5+}$ phases

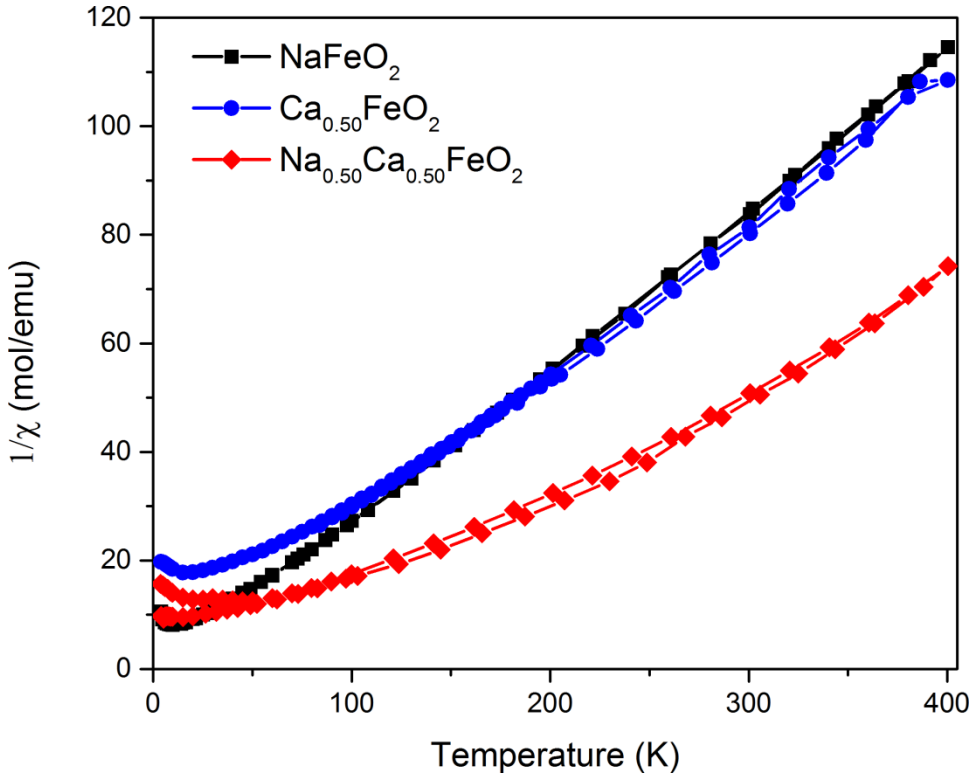

Figure 4-12. DC magnetic susceptibility data collected for $NaFeO_2$, $Ca_{0.50}FeO_2$, and $Na_{0.50}Ca_{0.50}FeO_2$ collected under a 1000 Oe field.

The magnetic susceptibility observed for $NaFeO_2$, $Ca_{0.50}FeO_2$, and $Na_{0.50}Ca_{0.50}FeO_2$ is presented in Figure 4-12. The $NaFeO_2$ susceptibility curve shows an antiferromagnetic transition with Neel temperature T_N = 17 K, matching the previous literature reports (*33*). Above the antiferromagnetic transition, $NaFeO_2$ appears to follow Curie-Weiss law in the range measured; however, after analyzing the first derivative of the trace, it is apparent that a very broad tail exists above 100 K. This tail may be due to an increase in competition between the coupling

constants J_{NN}, J_{NNN}, and J_{IP} at higher temperatures. Similarly to the parent phase $NaFeO_2$, $Ca_{0.50}FeO_2$ also shows a kink in the susceptibility data at T_N = 23 K. The divergence from Curie-Weiss behavior is even more apparent in the trace of $Ca_{0.50}FeO_2$. The smaller interplanar distance between FeO_2 slabs, in $Ca_{0.50}FeO_2$ relative to $NaFeO_2$ leads to an increase in the J_{IP} coupling. This coupling causes frustration not only in the FeO_2 planes but between planes and manifests in short-range spin fluctuations that cause the non-CW behavior across the measured region.

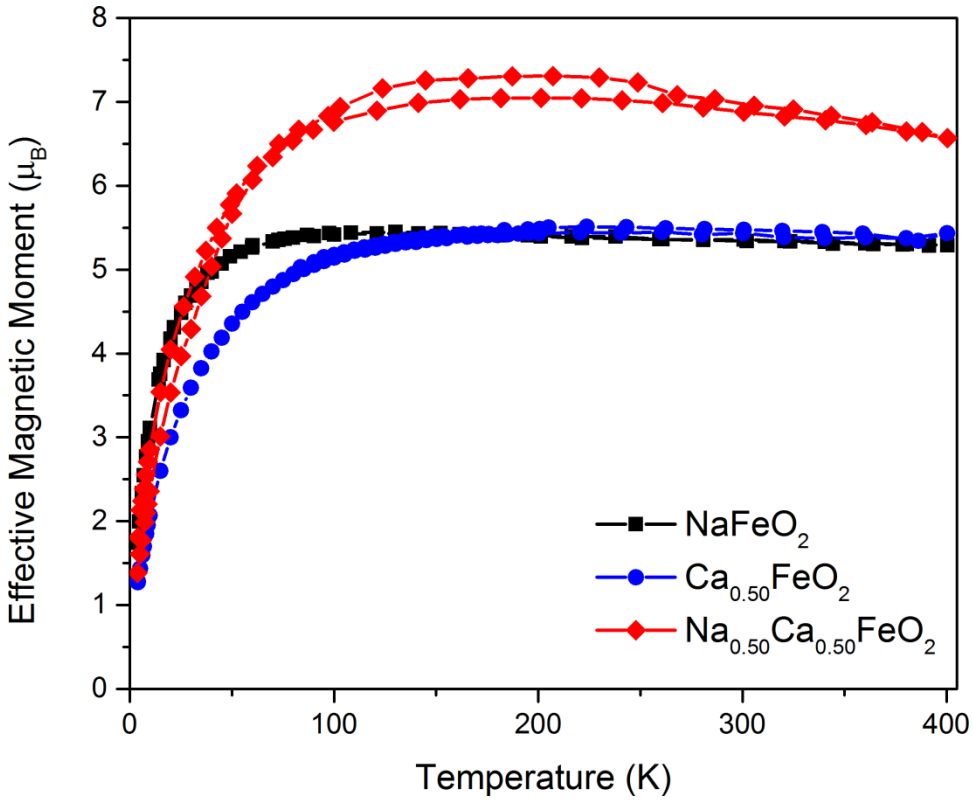

Figure 4-13. Effective magnetic moment for $NaFeO_2$, $Ca_{0.50}FeO_2$, and $Na_{0.50}Ca_{0.50}FeO_2$ calculated from magnetic susceptibility data.

The short-range fluctuations present in $Ca_{0.50}FeO_2$ manifest in the effective magnetic moment at low temperature (Figure 4-13). The effective moment of 5.92 bohr magnetons expected for an Fe^{3+} ion was realized at a much lower temperature in $NaFeO_2$ than $Ca_{0.50}FeO_2$, as expected for a less frustrated system.

The reduced phase $Na_{0.50}Ca_{0.50}FeO_2$ showed very different susceptibility data than the parent and intermediate phases in its synthesis. A large bifurcation between the zero-field cooled and field cooled traces at low temperature becomes apparent below 35 K. This bifurcation is typical of a spin glass state, especially due to the nearly linear slope of the field cooled curve at low temperature - a sign of a stochastic temperature dependence on time-frozen spins. The effective magnetic moment plot of $Na_{0.50}Ca_{0.50}FeO_2$ is even more interesting. As the temperature is increased, enough thermal energy is present to break any short range spin fluctuations present in the system. However, above 50 K, the effective magnetic moment is much higher than the expected μ_S for a mixed $Fe^{2+/3+}$ system or the μ_L of an Fe^{2+} system. The high spin value may be a result of the large spin orbit-coupling present in octahedral Fe^{2+} and a small superparamagnetic Fe or Fe_3O_4 impurity. Further studies, including AC magnetization or a Langevin plot, can be used to identify superparamagnetic Fe/Fe_3O_4. A Langevin fit of the M vs H presented in Figure 4-14 was completed to investigate the existence of the superparamagnetic impurity.

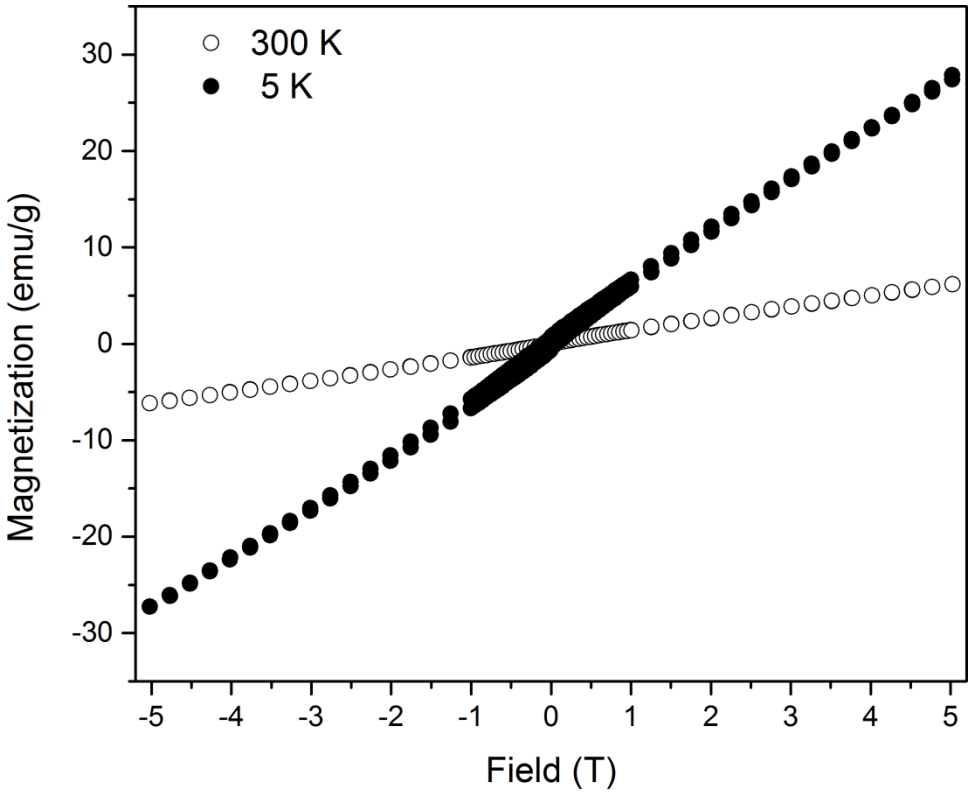

Figure 4-14. Dependence of magnetization on applied field of $Na_{0.50}Ca_{0.50}FeO_2$ collected at 300 K and 5 K.

The field dependence curve of $Na_{0.50}Ca_{0.50}FeO_2$ is shown at 300 K and 5 K in Figure 4-14. To further understand the nature of the large bifurcation in the M vs. T curve as well as the nearly linear M vs. H curve at 5 K, a purely academic investigation into the possibility of superparamagnetic nanoparticles was undertaken. The data presented in the following few paragraphs coupled with Mossbauer spectroscopy would cement the cause of the interesting magnetic results mentioned. However, a Langevin fit of the 5 K M vs H curve resulted in a saturation magnetization of 27.02 g/emu and a particle mass of 1.27 x 10^{-19} g

according to Equation 4-15 (*63*). The variables C and x_c represent the saturation magnetization in g/emu and the particle mass in g respectively. Based on a 5.05 g/mL density for Fe_3O_4 and a spherical particle assumption, a 2.894 nm particle diameter was calculated.

$$y=y_0+ C(\coth(x-x_c) - \frac{1}{(x-x_c)}) \quad (4\text{-}15)$$

From the M vs. H curve, a very small coercivity of approximately 25 Oe is present. By definition, a superparamagnetic material must have 0 coercivity; however, as this value is dependent on the instrument response and accuracy, many materials that shows coercivities less than 50 Oe are reported as superparamagnetic in the literature. Since blocking temperatures for Fe_3O_4 are reported as low as 10 K for 3.8 nm particles, it appears that the positive coercivity may be a result of the superparamagnetic Fe_3O_4 particles present with a diameter less than 3 nm (*63*, *64*). The saturation magnetization value of 27.02 emu/g observed is very low compared to literature reports of between 36 and 50 emu/g (*65*, *66*). It is also possible that a complex ferrite or a mixture of nanoparticles are the sources of the possible superparamagnetism at low temperature, a phenomena that has been reported previously (*67*, *68*).

4.3c Electrochemical cycling of $Li_{0.50}Ca_{0.50}FeO_2$

In the recent literature, cycling of the $Fe^{2+/3+}$ oxidation state has been notoriously difficult due to the insulating nature of the materials that restricted

current flow across the cell. This problem was thrown into the spotlight when $LiFePO_4$ was initially proposed as a Li^{1+} cathode material (*69*–*72*).

In the olivine type phase $LiFePO_4$, Li^{1+} diffusion occurs along unideminsional tunnels – generally unacceptable as a feature of a cathode material due to defects inherent in most structural types (*73*). However, in the olivine structure, the diffusion channels are never blocked by point defects (Li/Fe cation disorder) or stacking faults across crystal lattice when the particle size is sub-micron (*74*). The two-phase charging reaction of $LiFePO_4$, given in Equation 4-16, also presents another materials limitation: the constant charging voltage of 3.45 V limits both the electronic and ionic conductivities of the material due to collection of the products of reaction at the surface of the particles (*69*). This problem has been alleviated through multiple pathways, including reduction of particle size, while the most success has been seen by coating the particles in a layer of a Li-permeable material (i.e. carbon) that allows the Li to be removed from the surface (*72*, *75*).

$$LiFePO_4 \rightarrow FePO_4 + Li^{1+} + e^{1-} \qquad V = 3.45\ V \tag{4-16}$$

The electrochemical cycling performance of $Li_{0.50}Ca_{0.50}FeO_2$ was tested using a coin cell type setup against Li metal. The full experimental details of this setup can be found in the appendix section of this thesis.

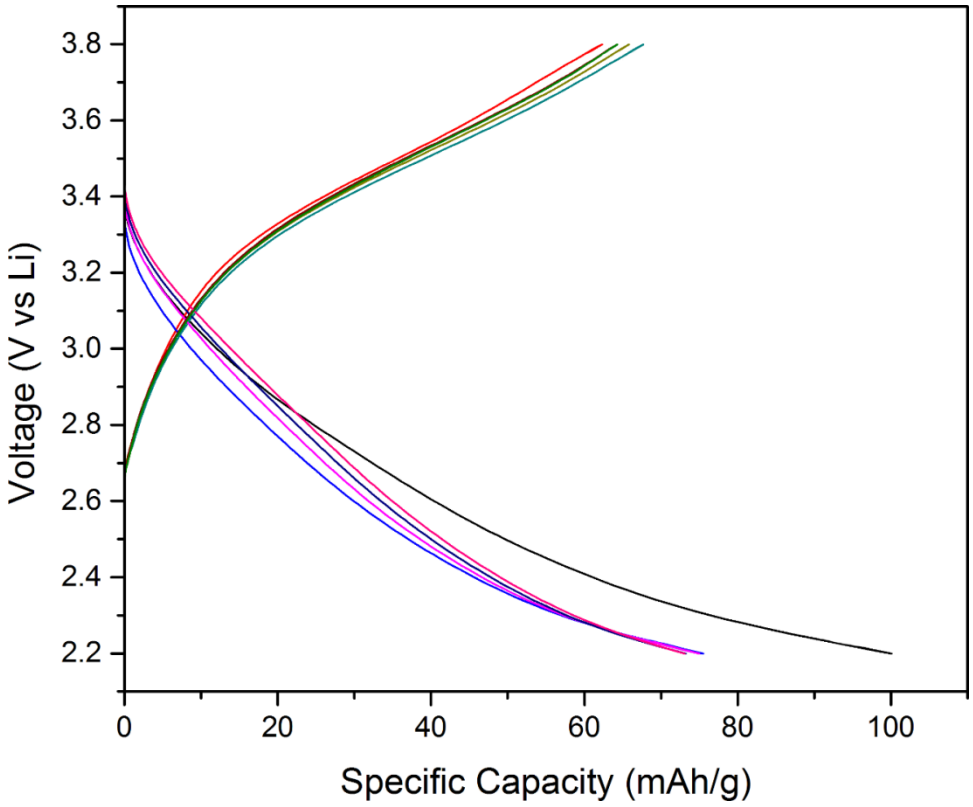

Figure 4-15. Partially optimized charge-discharge curve of $Li_{0.50}Ca_{0.50}FeO_2$ cycled from 2.2 V to 3.8 V vs. a Li-metal anode.

Similar to $LiFePO_4$, initial electrochemical testing of $Li_{0.50}Ca_{0.50}FeO_2$ resulted in very poor performance. $Li_{0.50}Ca_{0.50}FeO_2$ was prepared for electrochemical characterization in an Ar-filled glovebox by grinding the powder with 20% by weight acetylene black (Alfa Aesar, 99.9%) to increase overall conductivity of the sample. In general, 1 g of sample material was used during sample preparation. A sufficient amount (4-6 mL) of N-methyl-2-pyrrolidone was added to wet the powder, creating a very thick consistency. A syringe was used to drop 2 mL of this slurry onto battery grade aluminum foil and was flattened to a height of approximately 300 microns

using a doctor blade tool. The aluminum foil was then heated to 130 °C under a partial vacuum of 500 mmHg for a minimum of 12 hours to completely remove the solvent and densify the spread material. A die press was used in the glovebox to cut 12.7 cm discs from the coated aluminum foil. These discs will now be referred to as “active material”. The active material was loaded into the bottom of a split coin cell, followed by a Celgard polyethylene membrane, 1 mL of 1 M $LiClO_4$ in ethylene carbonate, and a Li-metal anode. The cell was closed, pressed, and hooked up to a potentiostat as demonstrated in the appendix of this thesis. Cycling $Li_{0.50}Ca_{0.50}FeO_2$ under these conditions from 2.5 V to 4 V resulted in a total cycled capacitance of approximately 10 mAh/g.

Initial optimization of the cycling performance of this material was achieved by altering the sample preparation method. Multiple literature reports have looked at the importance of intimate contact between the conductive filler (carbon) and the cathode material being tested (*76*–*78*). Taking this into account, $Li_{0.50}Ca_{0.50}FeO_2$ was ball-milled with acetylene black and N-methyl-2-pyrrolidone for 1 hr in agate jars at 400 rpm. The resulting liquid was similar in consistency to thick paint and had no indication of clumping or inhomogeneity (as found when the materials were hand-ground together). Further changes made to the experimental setup included the substitution of $LiClO_4$ for $LiPF_6$ as the electrolyte, which has been shown to be much more compatible with Fe-based cathode materials (*79*, *80*), as well as modifying the electrolyte solvent by replacing ethylene carbonate with a 4:3:3 ethylene carbonate:dimethyl carbonate:diethyl carbonate (MTI-XTL). A custom

program module that allowed for easy processing of cyclic voltammetry data led to more accurate charge-discharge curves as well because it introduced the ability to add background contributions to the analysis.

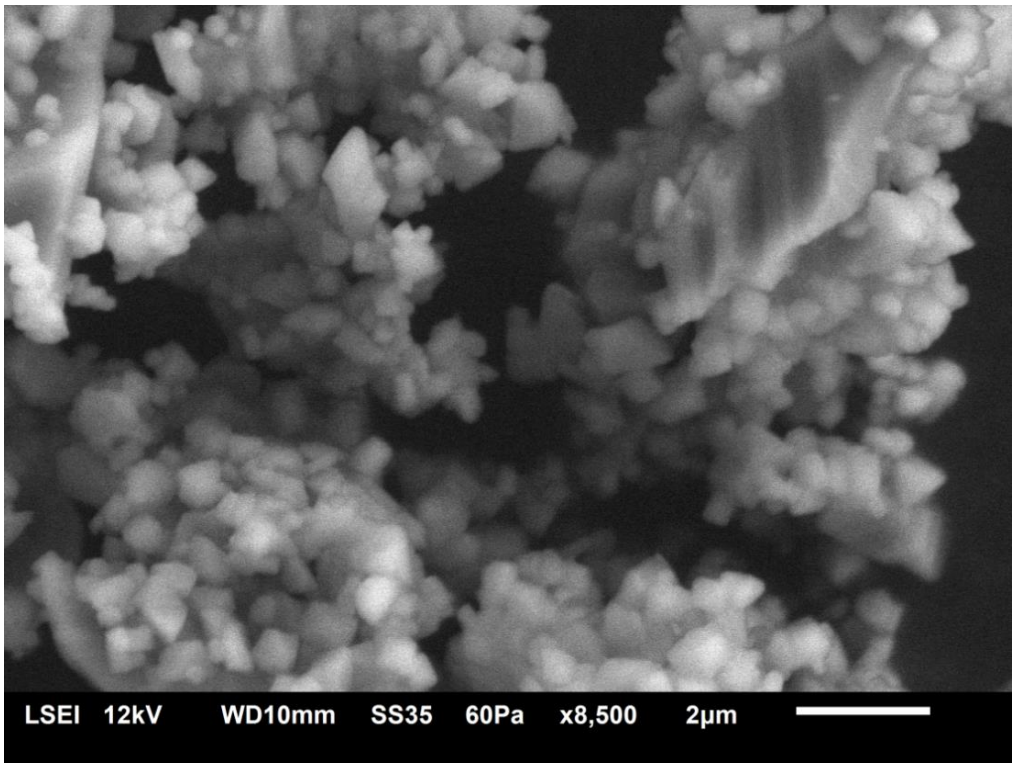

Figure 4-16. Secondary electron SEM of $Ca_{0.50}FeO_2$ prepared using the MuRE method.

Once these optimizations were made, the charge-discharge curves for $Li_{0.50}Ca_{0.50}FeO_2$ presented in Figure 4-15 were obtained. The large capacitance demonstrated in the black trace in the figure can be attributed to the formation of a secondary electrolyte interface (SEI) layer, a phenomenon that has been

reported and studied many times in the literature (*81–83*). After formation of the SEI layer, a maximum capacitance of 70 mAh/g is achieved, followed by 2% capacitance degradation per cycle. Reasons for this degradation may be physical (flaking of the material from the Al foil, large particle size, low conductivity) or chemical (soluble SEI layer, chemical instability).

The particle size of the sample is an obvious problem that, when optimized, may lead to a 25% increase in cycled capacity and retention (*84*). As seen in the SEM micrograph presented in Figure 4-16, the $Ca_{0.50}FeO_2$ particles are approximately 1 micron after grinding; however, very large crystals are still present. Because $Ca_{0.50}FeO_2$ is insulating, only the surface of these large crystals will cycle Li^{1+}. As these are a large percentage of the total volume with a relatively small surface area, the presence of these large crystals skews the data substantially. The synthesis of smaller particles of $Ca_{0.50}FeO_2$ via some kind of microemulsion or aqueous exchange may take advantage of solvent exfoliation and result in higher true cycling capacity and retention.

4.4 $Co^{2+/3+}$ phases prepared with the MuRE method

The following few sections describe and characterize the phases prepared with the MuRE method with Co as the transition metal.

4.4a Structure characterization of $A_xCa_yCoO_2$ phases

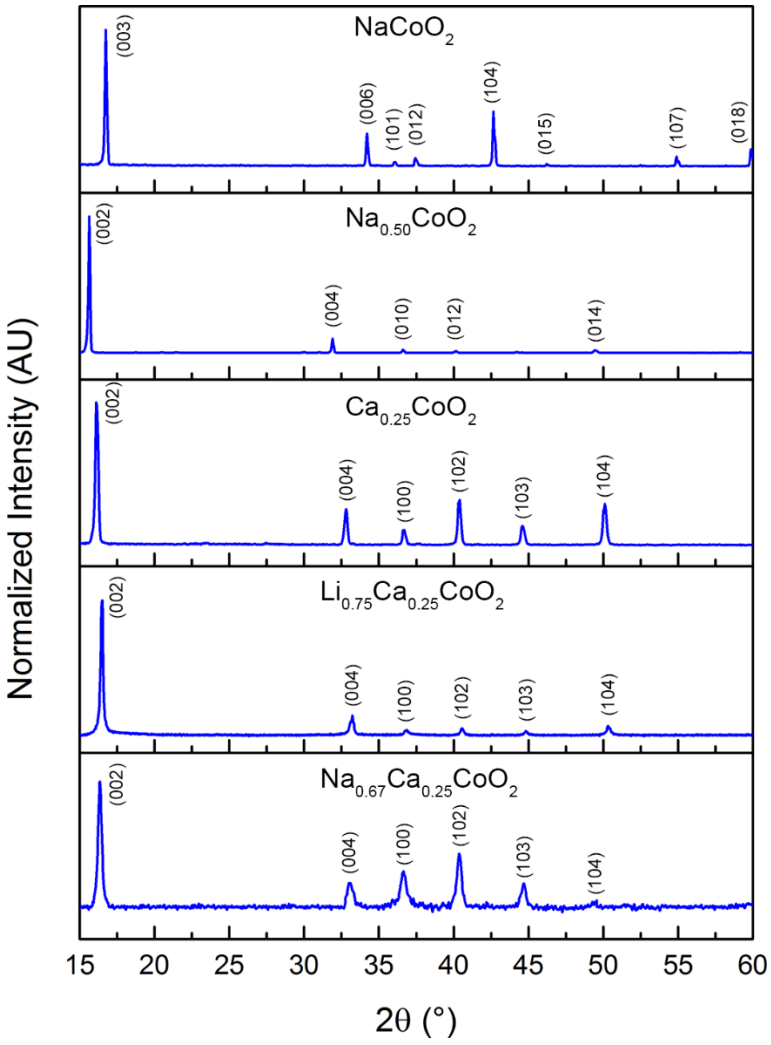

Figure 4-17. PXD spectra of the $Na_{0.50}CoO_2$ based family of materials prepared using the MuRE method presented in this chapter.

Intercalation of Li^{1+} into the P2 type $Ca_{0.25}CoO_2$ led to a slight expansion of the unit cell in the *a*-*b* plane coinciding with a nearly 1 Å contraction in the c direction. Larger Coulombic attraction between the Li^{1+} and O^{2-} from the CoO_2 layers is the reason for this contraction. A much smaller contraction in the *c* axis after Na^{1+} intercalation was observed due to a combination of the larger size of Na^{1+} and the lack of complete filling of all vacancies during intercalation. Both intercalated phases were indexed in the hexagonal $P6_3/mmc$ space group, proving the topotactic nature of the MuRE method (Figure 4-17).

Table 4-12. Refined atomic positions of $Li_{0.75}Ca_{0.25}CoO_2$ based on the $Ca_{0.25}CoO_2$ model. Li^{1+} and Ca^{2+} shared atomic sites in the refinement because the statistics were not high enough to try and separate them into different positions.

Atom	Wycoff site	x	y	z	$10^2 U_{iso}(Å^2)$
Li1/Ca1	2b	0	0	0.25	3.2
Li2/Ca2	2c	0.1650(1)	0.3304(4)	0.25	4.7
Co	2a	0	0	0	2.4
O	4f	1/3	2/3	0	2.8

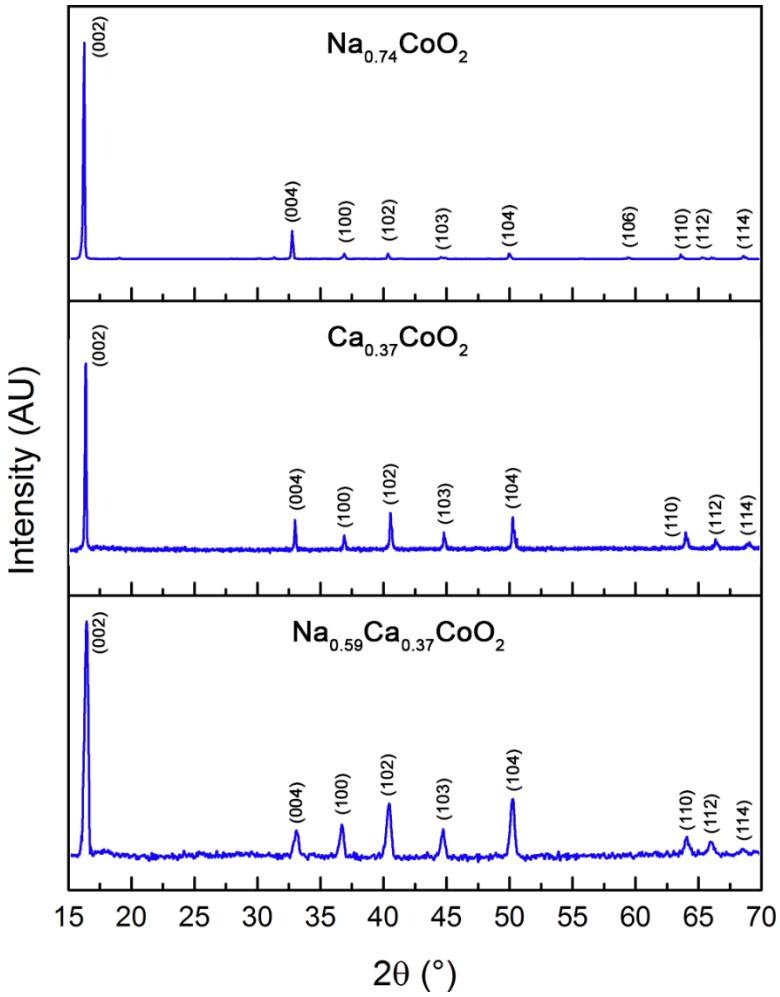

Figure 4-18. PXD patterns of the intercalated materials in the $Na_{0.74}CoO_2$ family prepared using the MuRE method.

Rietveld refinement of PXD data of $Li_{0.75}Ca_{0.25}CoO_2$ was performed in the $P6_3/mmc$ space group with Li^{1+} and Ca^{2+} in trigonal prismatic coordination. All peaks were indexed in this model with very moderate fitting statistics (χ^2 = 1.997, R_{wp} = 7.86% R_p = 5.99%). Peak profile functions were refined using the LeBail method followed by Rietveld refinement of atomic positions and thermal

parameters. Atomic occupancies were not refined, as the data did not have sufficiently good statistics to reliably extract the occupancies of lighter elements. A final unit cell of *a* = 2.817 Å *c* = 10.794 Å was produced with atomic positions presented in Table 4-12. Rietveld refinement of $Na_{0.67}Ca_{0.25}CoO_2$ resulted in a unit cell of *a* = 2.828 Å and *c* = 10.851 Å with similar atomic positions and convergence criteria (χ^2 = 2.297, R_{wp} = 9.94% R_p = 7.22%). As apparent from the atomic thermal parameters, the diffraction data was not of high enough quality for proper Rietveld refinement.

In general, the PXD patterns obtained for the MuRE prepared compounds were of too poor quality to perform reliable Rietveld refinements. Preferred orientation and very large anisotropy in the *c* direction of the phases led to intense main peaks with the majority of the other Bragg diffractions lost in the background. Furthermore, PXD patterns were saturated with fluorescence from Co, a common problem with Cu radiation sources (*85*). Voltage discrimination was used to enhance the diffraction quality to a degree where peaks were visible; however, changing the voltage window too far resulted in anomalous and malformed peaks. Rietveld refinement diverged easily, especially when trying to include the small Bragg reflections in the patterns; therefore, LeBail refinement was employed to obtain the cell parameters of all phases, which are presented in Table 4-13. Rietveld refinement of atomic positions and occupancies would require much higher resolution data to understand if any Li^{1+} ordering is present. The refinement of $Li_{0.75}Ca_{0.25}CoO_2$ and $Na_{0.67}Ca_{0.25}CoO_2$ was completed for example purposes

only and cannot be assumed to be correct due to the poor signal to noise ratio. Rietveld refinement of the Fe-containing phases was possible because of the neutron diffraction data and the lesser degree of anisotropy in the crystal structure.

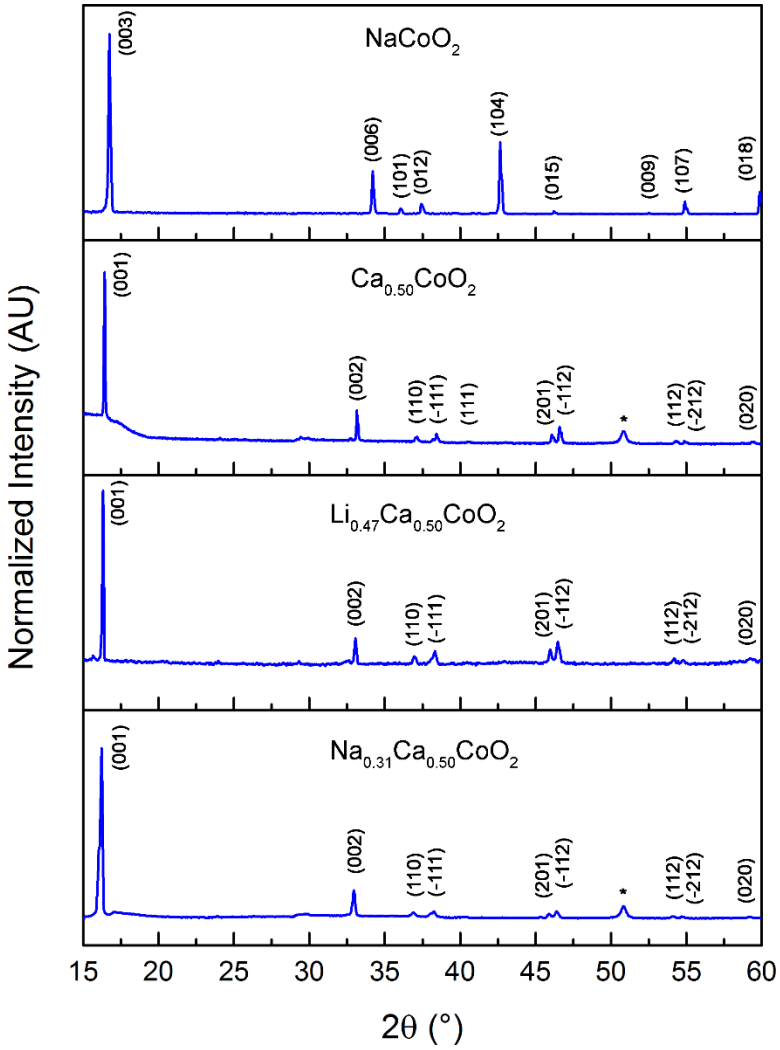

Figure 4-19. PXD spectra of the $NaCoO_2$ based family of materials prepared using the MuRE method presented in this chapter. The broad background and marked (*) peaks are due to the sample holder used.

PXD patterns for the rest of the Co containing compounds prepared with the MuRE method are presented in Figures 4-18 and 4-19. It is apparent that the layered structure is preserved throughout the MuRE series of reactions in all of the compounds. As some samples were exceptionally air sensitive – showing slow hydrolysis in the purge box – diffraction patterns were collected using a dome-type sample holder. Because of the large intensity of the main peak, the amorphous background is much less prominent in these patterns.

Table 4-13. Cell parameters of the materials with transition metals in the 2+/3+ oxidation state couple prepared with the MuRE method next to the cation coordination type and Co oxidation state.

Compound	Space Group	Unit Cell (Å, ß in °)	Structure Type	Co Oxidation State
$Li_{0.47}Ca_{0.50}Co_{1.00}O_2$	C2/m	*a* = 4.789 *b* = 4.027 *c* = 5.696 ß = 107.5	O'3	+2.53
$Na_{0.31}Ca_{0.50}Co_{1.00}O_2$	$R\bar{3}m$	*a* = 2.831 *c* = 16.288	O3	+2.69
$Li_{0.64}Ca_{0.37}Co_{1.00}O_2$	$P6_3/mm_c$	*a* = 2.818 *c* = 10.820	P2	+2.62
$Na_{0.59}Ca_{0.37}Co_{1.00}O_2$	$P6_3/mm_c$	*a* = 2.856 *c* = 10.809	P2	+2.67
$Li_{0.75}Ca_{0.25}Co_{1.00}O_2$	$P6_3/mm_c$	*a* = 2.817 *c* = 10.794	P2	+2.75
$Na_{0.67}Ca_{0.25}Co_{1.00}O_2$	$P6_3/mm_c$	*a* = 2.828 *c* = 10.851	P2	+2.83

Further structural studies of $Na_{0.31}Ca_{0.50}CoO_2$ must be completed, as the unit cell can also be indexed in the C2/m space group with cell parameters *a* = 4.873 Å, *b* = 3.866 Å, *c* = 5.422 Å, and ß = 89.94 °. Likewise, $Li_{0.47}Ca_{0.50}CoO_2$ can be indexed in both $R\bar{3}m$ and C2/m. High resolution diffraction is needed to understand whether this is a monoclinic distortion or some other type of atomic ordering. The low intensity peaks that should be present if the space group is monoclinic would be apparent with a better signal to noise ratio.

Interplanar [CoO_2] spacing for the Na_xCoO_2, $Ca_{x/2}CoO_2$, and the intercalated $A_{1-x}Ca_{x/2}CoO_2$ are phases are presented in Table 4-14. Since the interplanar spacings are based on Rietveld refinement of powder diffraction data collected on a lab diffractometer with rather poor statistics or by interpolating based on the powder diffraction pattern d spacing (main peaks are all 00c), there is a large uncertainty in the values. The following discussion is purely academic in nature. As discussed previously, the layer spacing in the Na_xCoO_2 materials is completely dependent on x, increasing nearly linearly with oxidation of Co^{3+} to Co^{4+}. After intercalation of the alkali metals back into the $Ca_{x/2}CoO_2$ phases, a decrease in the [CoO_2] separation is observed. As the vacancies created during the aliovalent exchange step are filled with cations, Coulombic attraction between the Na^{1+}/Li^{1+} and Ca^{2+} and the O^{2-} ions draw the layers together. However, the Ca^{2+} pillars appear to lock the interplanar distance into a narrow region (5.429 Å – 5.439 Å) depending on the alkali metal intercalated and the x value in $A_{1-x/2}Ca_{x/2}CoO_2$.

Table 4-14. CoO_6 interplanar spacings for all Co-containing layer phases prepared with the MuRE method

Material	$[CoO_2]$ separation (Å)
$NaCoO_2$ (*53*)	5.200
$Na_{0.71}CoO_2$ (*53*)	5.441
$Na_{0.53}CoO_2$ (*53*)	5.529
$Ca_{0.50}CoO_2$ (*53*)	5.438
$Ca_{0.35}CoO_2$ (*53*)	5.436
$Ca_{0.25}CoO_2$	5.438
$Li_{0.47}Ca_{0.50}Co_{1.00}O_2$	5.429
$Na_{0.31}Ca_{0.49}Co_{1.00}O_2$	5.431
$Li_{0.64}Ca_{0.37}Co_{1.00}O_2$	5.435
$Na_{0.59}Ca_{0.37}Co_{1.00}O_2$	5.433
$Li_{0.75}Ca_{0.25}Co_{1.00}O_2$	5.437
$Na_{0.67}Ca_{0.25}Co_{1.00}O_2$	5.430

Crystallite size was calculated using the Whole Powder Pattern modeling (WPPM) method with the PM2K software package. Microscopy measurements were not performed due to the air and water sensitivity of the samples; however, previous literature reports demonstrate the efficacy of WPPM in determining crystallite size distribution for phases of high symmetry (*86*, *87*). A lognormal

function was chosen to describe the particle size, given in Equation 4-17. Thermodynamically this assumption is reasonable as well, considering that small grains will generally form convex shapes (sphere, cube, etc) that can be easily described using a single parameter. The lognormal function employed for this size distribution study is a combination of the lognormal mean μ and the lognormal variance σ:

$$g_l(D)=\frac{1}{D\sigma(2\pi)^{1/2}}\exp[-(\ln D-\mu)^2/2\sigma^2] \qquad (4\text{-}17)$$

where D is the diameter of the spherical particle. A more in-depth description of the lognormal function and the Fourier transform of said function used in the PM2K software suite is given by Scardi and Leoni, but can also be found in Chapter 5 of this thesis (*88*).The precursor sodium cobalt oxide phases all had respective size distributions above 1 micron. After undergoing aliovalent exchange, the particle size distribution shifted to approximately 500 +/- 100 nm, most likely due to layer exfoliation, which is common in layered materials. Particle size distributions of the final phases prepared with the MuRE method where Co is in the 2+/3+ oxidation state were grouped near 120 +/- 20, showing a large decrease after each topotactic operation was completed on the structure (Table 4-15). The particle size distribution given by PM2K is the average platelet height parameter, which agrees well with SEM (Figure 4-20).

Table 4-15. Particle size distributions obtained using the WPPM algorithms implemented in the PM2K software suite. PM2K results gave the shortest length (height of platelet) for platelet type particles.

Material	Space Group	Particle Size (nm) from PM2K	Particle Size (nm) from SEM
$NaCoO_2$	$R\bar{3}m$	> 1 µm	-
$Ca_{0.50}CoO_2$	C2/m	512 ± 95	-
$Li_{0.47}Ca_{0.50}CoO_2$	C2/m	119 ± 12	-
$Na_{0.31}Ca_{0.50}CoO_2$	$R\bar{3}m$	128 ± 21	-
$Na_{0.74}CoO_2$	$P6_3/mmc$	> 1 µm	900 - 1100
$Ca_{0.37}CoO_2$	$P6_3/mmc$	502 ± 259	650 - 725
$Li_{0.64}Ca_{0.37}CoO_2$	$P6_3/mmc$	114 ± 52	-
$Na_{0.59}Ca_{0.37}CoO_2$	$P6_3/mmc$	157 ± 17	148 - 205
$Na_{0.51}CoO_2$	$P6_3/mmc$	> 1 µm	-
$Ca_{0.25}CoO_2$	$P6_3/mmc$	800 ± 235	-
$Li_{0.75}Ca_{0.25}CoO_2$	$P6_3/mmc$	130 ± 70	-
$Na_{0.67}Ca_{0.25}CoO_2$	$P6_3/mmc$	143 ± 10	-
$NaFeO_2$	$R\bar{3}m$	> 1 µm	600 - 800
$Ca_{0.50}FeO_2$	C2/m	> 1 µm	550 - 750
$Li_{0.49}Ca_{0.50}FeO_2$	C2/m	117 ± 29	-
$Na_{0.50}Ca_{0.50}FeO_2$	C2/m	514 ± 244	475 - 575

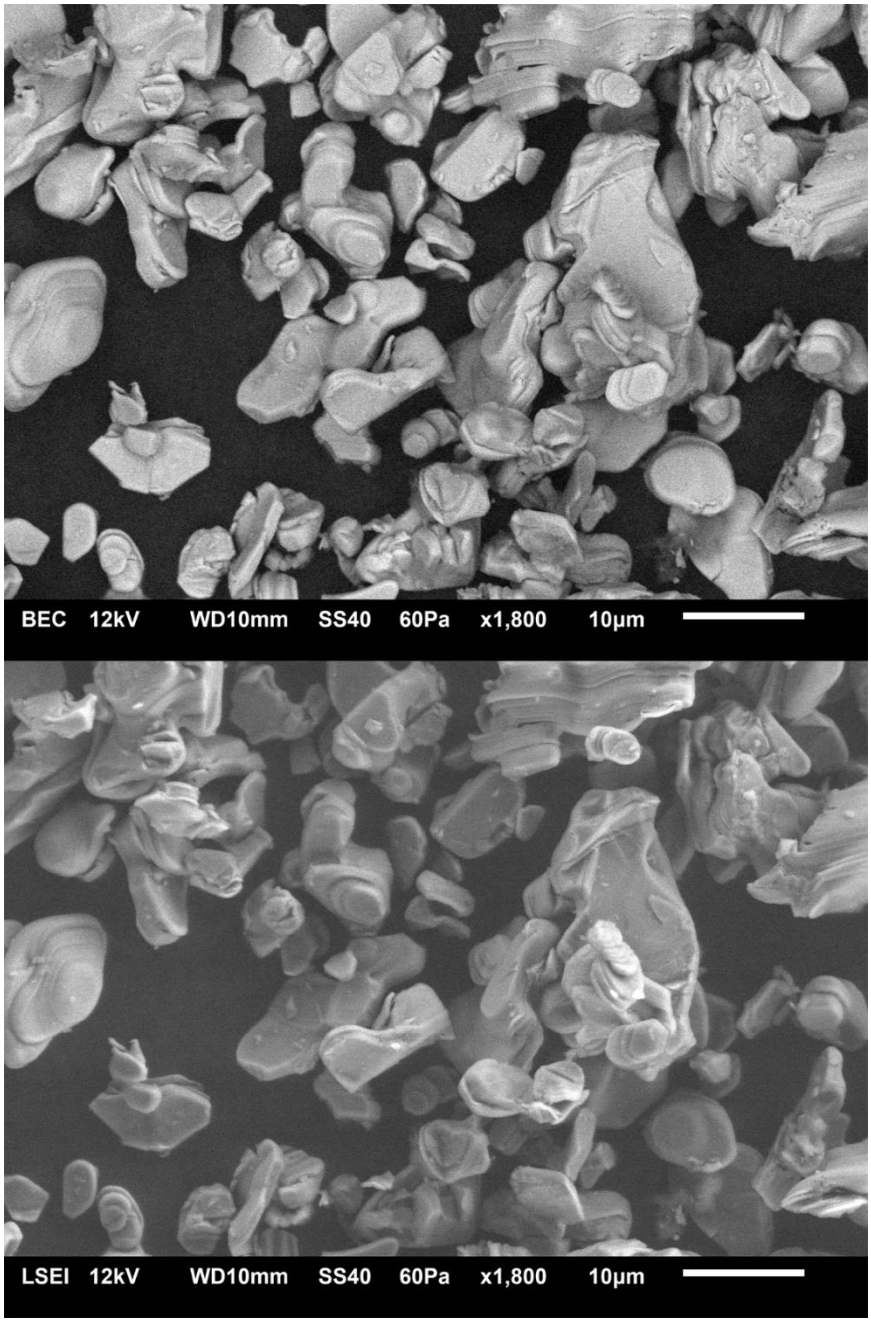

Figure 4-20. SEM image of $Na_{0.59}Ca_{0.37}CoO_2$ using back scattered electrons (top) and secondary electrons (bottom) showing the large anisotropy in crystal dimensions resulting in platelets. Clearly, the ridges on the larger particles are actually many different platelets.

4.4b Thermal analysis and stability investigation

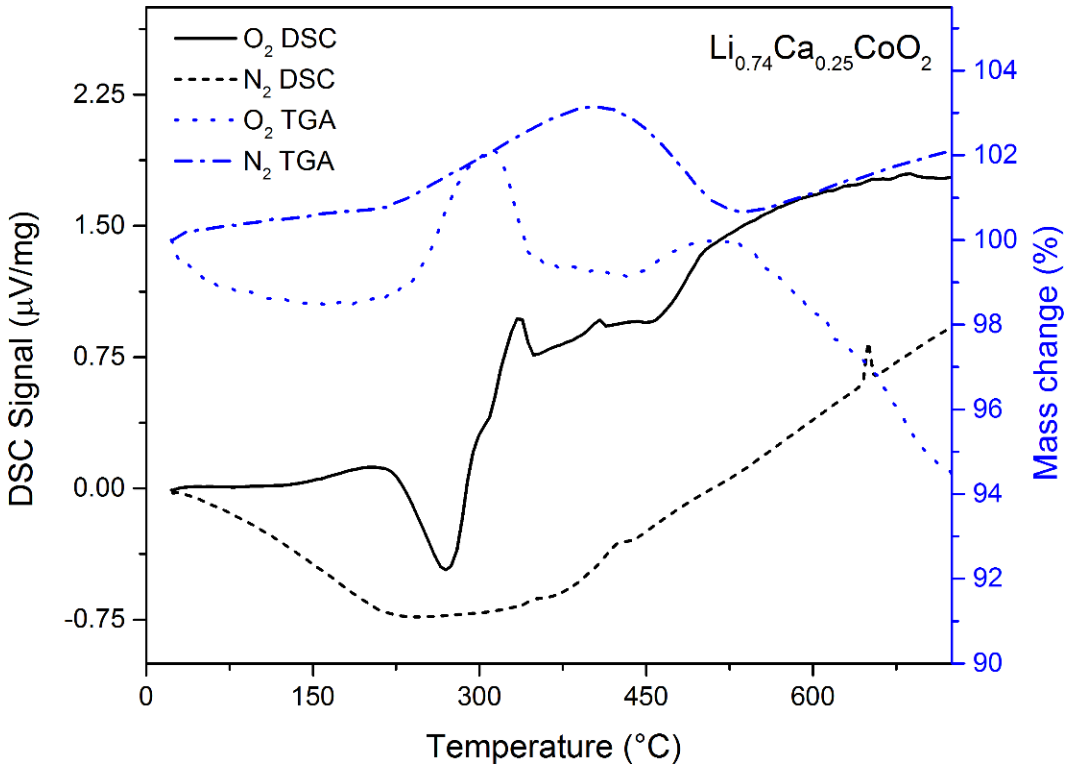

Figure 4-21. TGA and DSC curves of $Li_{0.75}Ca_{0.25}CoO_2$ under O_2 and N_2 atmospheres. Negative signals in the DSC are exothermic.

It is important to note the role of Ca^{2+} as "pillars" between the MO_2 layers, effectively stabilizing the structures with M^{2+} ions. Theoretical investigations into the reasons for ordering in these layered phases have pointed to large differences in elastic energy as the driving force to overcome the entropy required for ordering. For example, since the ionic radii of Ca^{2+} in an octahedral environment (1.15 Å) is much larger than that of Fe^{2+} (High spin (HS) - 0.92 Å), the radii ratio R(Fe^{2+}/Ca^{2+})

= 0.80, well below the maximum empirical value of 0.86 required for layered ordering (*39*, *89*). Since the Fe^{2+} radii is similar to that of Li^{1+} (0.90 Å) – generating a radii ratio $R(Fe^{2+}/Li^{1+})$ = 1.01 - the direct synthesis of layered compounds without Ca^{2+} pillars is impossible because disorder in the resulting structure would be energetically favored.

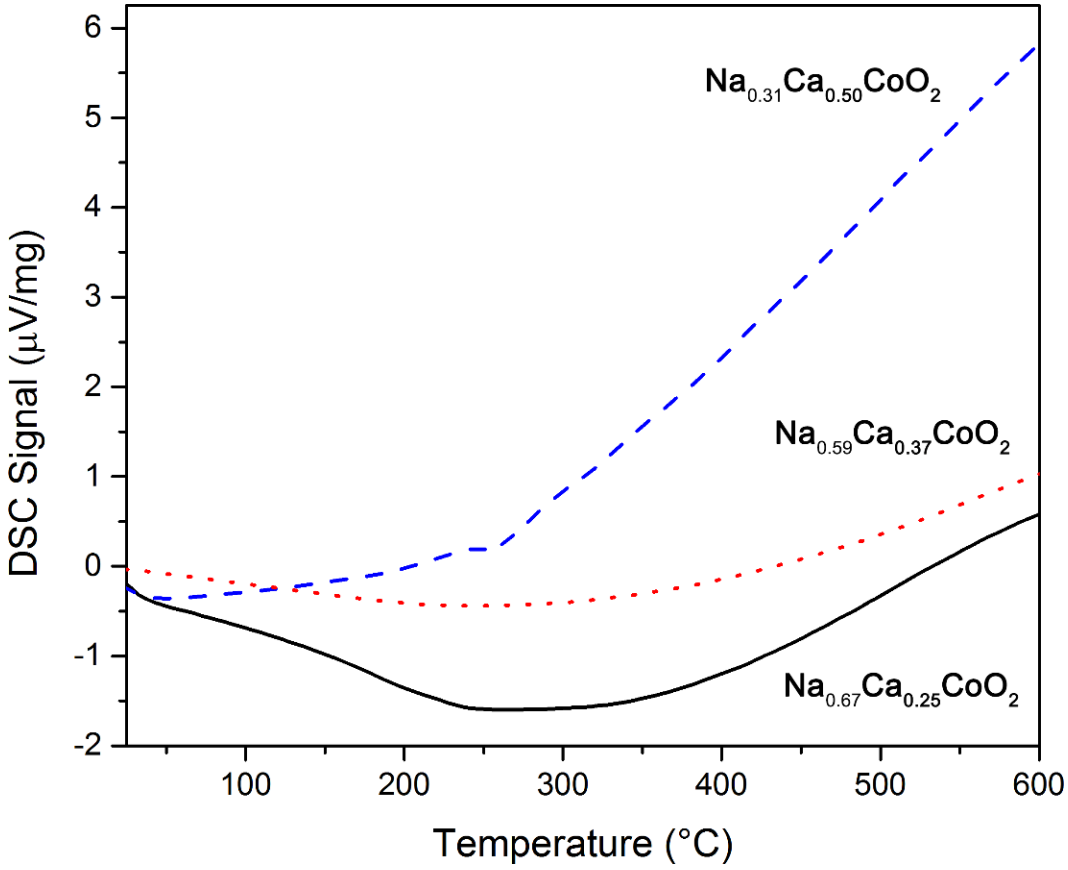

Figure 4-22. DSC curves of the Na^{1+} intercalated products of Ca_xCoO_2 (x = 0.50, 0.37, 0.25) under an N_2 atmospheres. Negative signals in the DSC are exothermic.

The TGA plot for $Li_{0.75}Ca_{0.25}CoO_2$, shown in Figure 4-21, has a very interesting mass gain feature under N_2 at 425 °C. This feature was ruled out as either instrumentally anomalous or systematic in nature, considering it is reproducible in $Li_{0.75}Ca_{0.25}CoO_2$ and was not seen for any Na^{1+} intercalated phases or in the TGA of $Li_{0.75}Ca_{0.25}CoO_2$ collected under Ar. As the resulting product of this mass gain is not discernible using PXD due to the poor spectral quality, the hypothesis that Li_3N is formed during heating is proposed. Previous literature reports of Li metal under N_2 show a very sharp onset reaction and mass gain at approximately 180 °C (*90*). The DSC curve under O_2 may lend some credence towards this hypothesis, especially since the exothermic peak at 275 °C may represent the burning of Li in air to form Li_2O. NPD or SPXD would lend more insight into the produced phase, and determine whether phase separation occurs and Li_3N is a separate material or if Li_3N is intercalated into the layered structure.

As the DSC plots of the Li^{1+} intercalated phases were poisoned by the formation of Li_3N, the metastability of the phases was studied using the Na^{1+} intercalated compounds. DSC curves for the three Na^{1+} materials with reduced Co transition metals are presented in Figure 4-22. The DSC curves of these layered phases with disordered cations show very broad transitions; however, upon zooming in, more information on the stability of the materials can be elucidated.

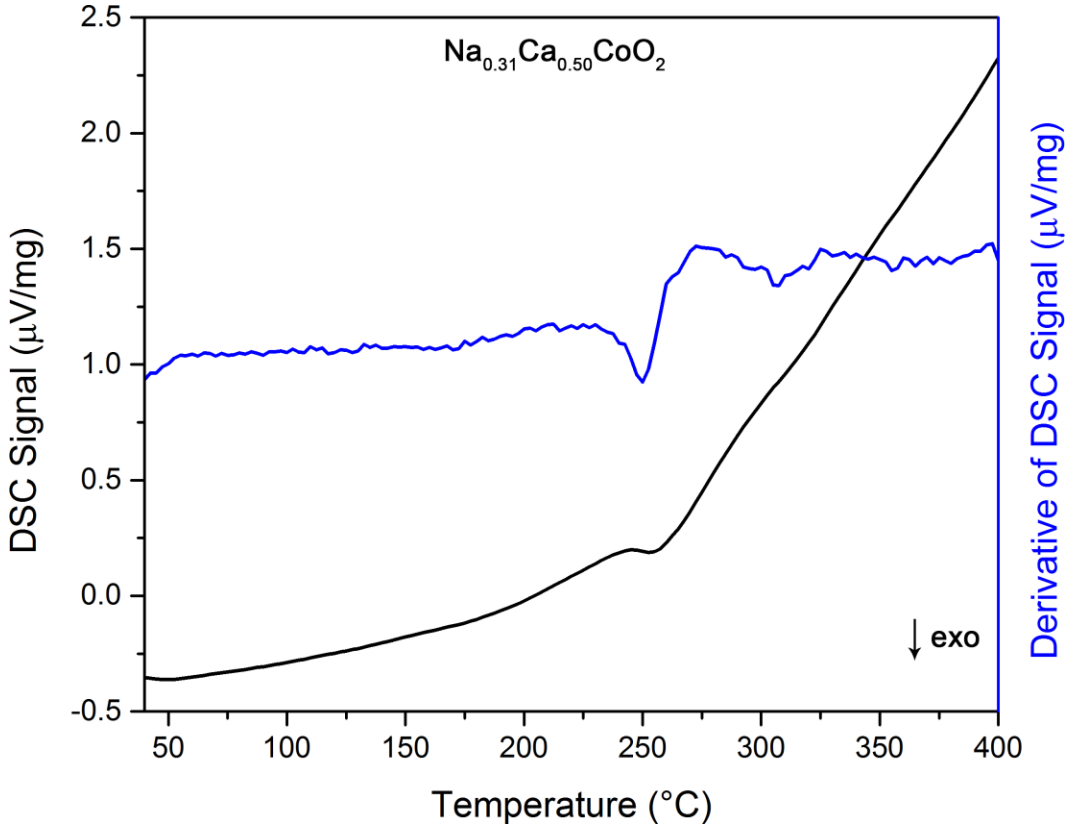

Figure 4-23. Magnified differential scanning calorimetry trace of $Na_{0.31}Ca_{0.50}CoO_2$ with the first derivative of the trace.

A magnified view of the DSC curve of $Na_{0.31}Ca_{0.50}CoO_2$ is presented in Figure 4-23 to investigate the true metastability of phases prepared by the MuRE method. In general, there are two types of solid state materials: high-temperature (thermodynamic) phases and low-temperature (kinetic) phases. The kinetic phases can be further split into two subgroups – metastable and low-temperature – where the metastable phases cannot be directly prepared, while the low-temperature phases are easily prepared using conventional solid state techniques at low temperatures. One of the easiest ways to distinguish between these two

types of kinetic phases is to look closely at the DSC curves for an exothermic signal at low temperature. This signal points to the transformation of a metastable phase into a truly low-temperature phase. Unfortunately, due to the nature of metastable phases – especially in terms of disorder and artificial defect density – the exothermic signals can be very broad or faint in magnitude.

For the case of $Na_{0.31}Ca_{0.50}CoO_2$, a clear exothermic signal is apparent at 250 °C in the DSC curve collected under an Ar environment. To appreciate whether the signal is a manifestation of a slight change in background or a true exothermic signal, the first derivative of the trace is also presented – again demonstrating that $Na_{0.31}Ca_{0.50}CoO_2$ is indeed a metastable material. Powder X-ray diffraction of $Na_{0.31}Ca_{0.50}CoO_2$ after heating to 250 °C under Ar showed a complete loss of crystallinity – assumed to be an effect of this transition to the low-temperature phase.

4.4c Magnetic properties – completing the phase diagram

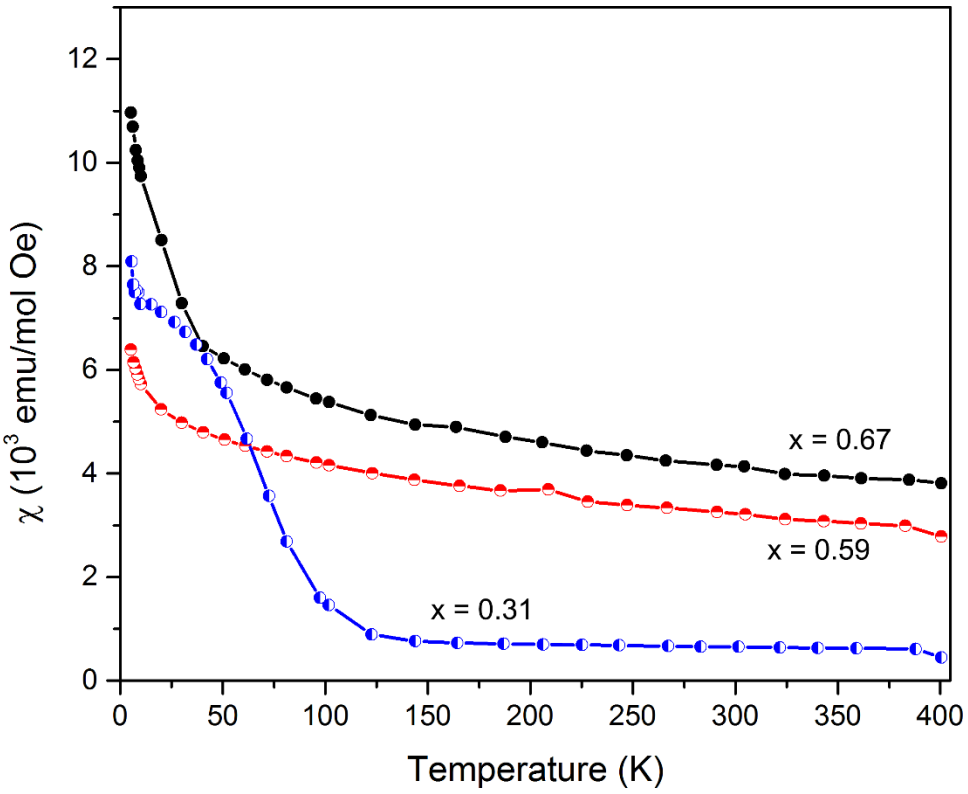

Figure 4-24. Molar magnetic susceptibility of the Na^{1+} intercalated cobaltates synthesized with the MuRE method obtained under an applied field of 0.1 T.

Investigation into the magnetic properties of the materials with exceptionally low oxidation states produced by the MuRE method will greatly increase the knowledge base of these triangular frustrated species and the impact of A cation stoichiometry on their fundamental properties. Preliminary magnetic measurements of the $Co^{2+/3+}$ materials present similar features to the $Co^{3+/4+}$ Na_xCoO_2 materials (Figures 4-24 and 4-25). For example, the molar susceptibility

of $Na_{0.31}Ca_{0.50}Co^{2.69+}O_2$ is temperature independent, very similar to $Na_{0.30}Co^{3.7+}O_2$. However, the magnetic susceptibility data between 60 K and 150 K follows Curie-Weiss law with theta = 58.4 K and C = 0.08403 cm^3K/mol. The positive Weiss constant is indicative of ferromagnetic interactions in the ground state. Above this temperature the susceptibility appears to vary from the CW model and is independent of temperature, indicative of a bad-metal state. Under a 5 T magnetic field the compound appears to be a standard paramagnet, but at 0.1 T, cusps in the magnetization at 10 K and 45 K become apparent. The origin of these cusps is unknown, although a spin glass state of asperomagnets is most likely present between 10 K and 45 K. This hypothesis is substantiated by the bifurcation between the ZFC and FC curves and characteristic magnetization curves of a spin glass at 5 K denoted by the non-linear dependence of magnetization on field at high field. Under high magnetic field a thermal randomization of the spins destroys the spin-glass network, resulting in a paramagnetic signal. The uptick in molar magnetization below 10 K may correlate to local short-range dominance of the ferromagnetic contribution of the spin glass state. DFT calculations are underway to investigate the magnetic ground state of this material. The cusps in the magnetization data may point to charge ordering of the doped electrons similar to $Na_{0.50}CoO_2$, a charge ordered insulator.

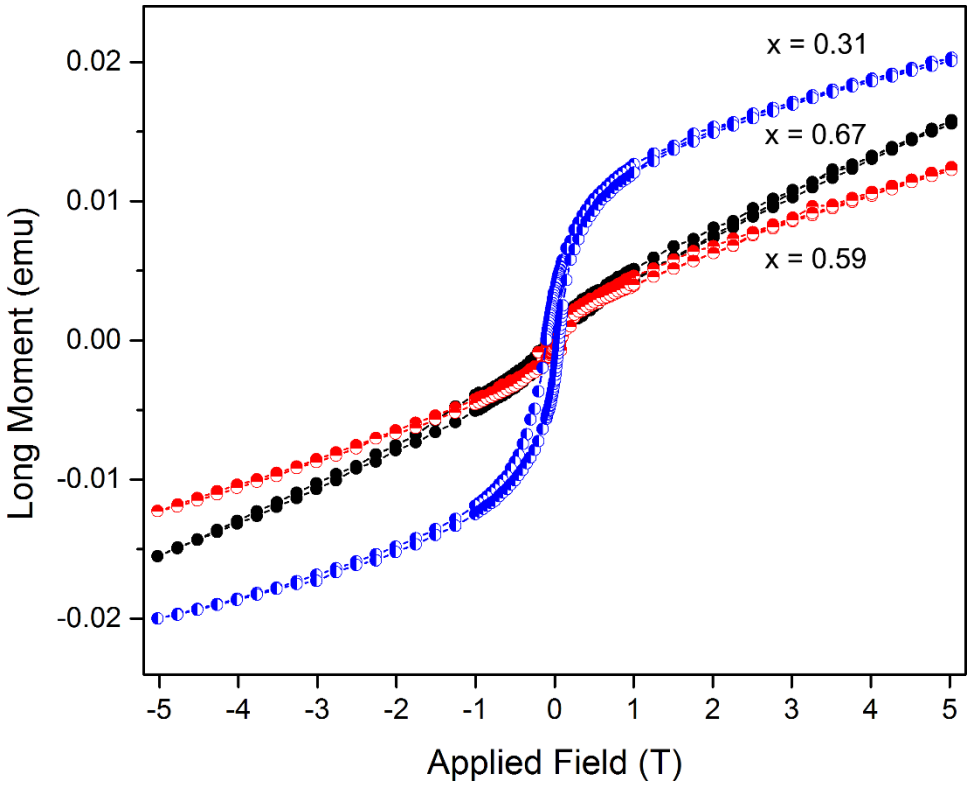

Figure 4-25. Magnetization dependence on field traces of the Na^{1+} intercalated cobaltates synthesized with the MuRE method obtained at 5 K.

The $Co^{2.83+}$ material $Na_{0.67}Ca_{0.25}CoO_2$ appears to follow Curie-Weiss law in the temperature range 60 K - 400 K, but upon further inspection of the first derivative of the susceptibility, deviation across the whole range becomes obvious. The combination of the very slight 'S' shape of the field dependence curve with no hysteresis in the M vs. H loop and the minor bifurcation in the susceptibility data below 10 K between the FC and ZFC curves suggests the presence of superparamagnetic cobalt nanoparticles in the sample with an approximate particle size of 2 nm. No cobalt impurities were seen via powder diffraction. The sharp transition at 50 K in the susceptibility curve may be caused by charge

ordering of the HS Co^{2+} and LS Co^{3+} present. Heat capacity and low temperature diffraction measurements are needed to identify if this transition is a first or second order phase transition.

$Na_{0.59}Ca_{0.37}CoO_2$, where Co is in the +2.67 oxidation state, is composed of the nonmagnetic LS Co^{3+} and the paramagnetic HS Co^{2+} ions in a 2:1 ratio. Assuming the simple model where Co^{2+} carries all of the charge and Co^{3+} is not in an intermediate spin state, thus eliminating Co^{2+}/Co^{3+} coupling, the susceptibility follows Curie-Weiss law between 80 K and 400 K with a negative Weiss constant of -117 K. This relatively large negative Weiss constant points to a strong antiferromagnetic correlation between the spins in $Na_{0.59}Ca_{0.37}CoO_2$. The uptick at 18 K in the susceptibility curve and the slight 'S' shape lacking hysteresis in the field dependence curve point to a very small impurity of cobalt nanoparticles that are formed during the reductive intercalation step undetected by diffraction techniques. Interestingly, considering that only 33% of the $Co^{2+/3+}$ ions are magnetic, a possible charge ordering state may exist where the magnetic frustration in the CoO_2 layers is completely relieved by having 2 Co^{3+} and 1 Co^{2+} per triangular subunit. Low temperature diffraction may shed light on whether this scenario exists below 20 K, correlating with the transition present in the susceptibility data.

To complete the Na_xCoO_2 magnetic phase diagram presented earlier with properties observed for the novel $Co^{2+/3+}$ materials would be premature at this point; however, heat capacity and resistivity measurements will shed light on the

nature of the magnetic features present. Very preliminary additions to the 2.5+/3+ region of the magnetic phase diagram include charge ordering near +2.80, an asperomagnetic spin glass (possible Mott insulator depending on the resistivity results) at +2.69, and a Curie-Weiss paramagnet at +2.67. These additions can be seen in Figure 4-26. Because the Na^{1+} stoichiometry is easily tuned through chemical deintercalation, a highly detailed magnetic phase diagram is possible.

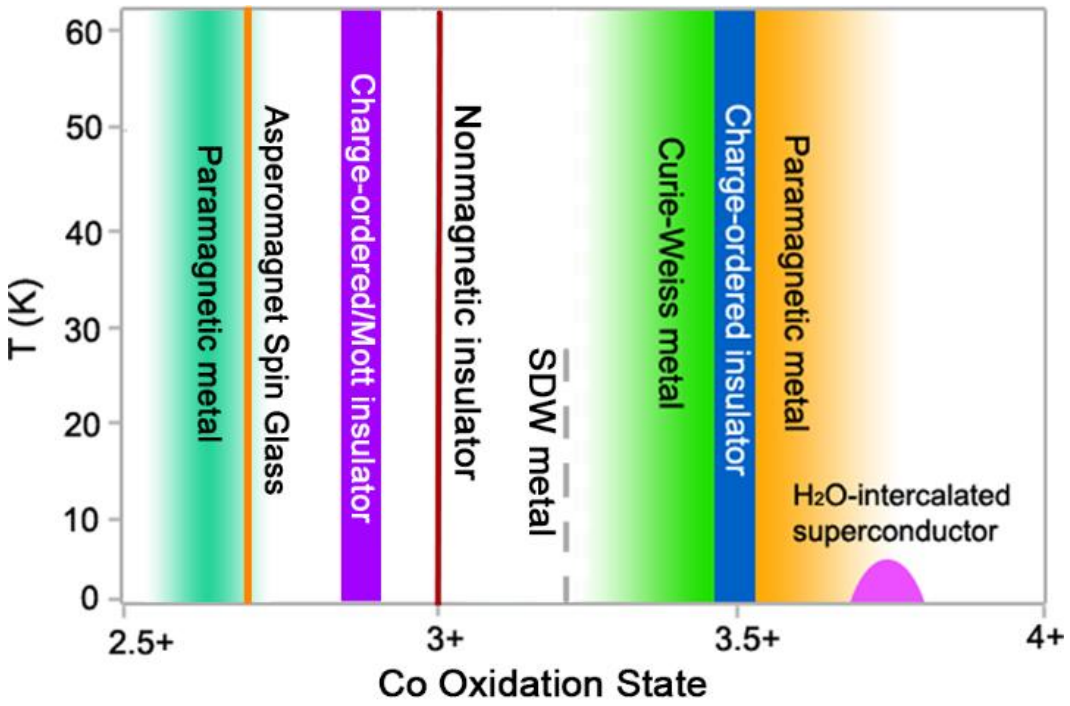

Figure 4-26. Low-temperature magnetic phase diagram of layered oxide phases with Co in different oxidation states

4.4d Electrochemical cycling of layered cobaltates

When designing new cathode materials for portable devices, three general requirements should be adhered to: high operating voltage, multi-dimensional ion pathways, and long cycle lifetimes (Table 4-16). Other important factors, including cell safety, are generally considered an engineering problem, although toxic elements should be avoided whenever possible. Currently, the two most common Li-ion cathode materials are $LiCoO_2$ and $LiFePO_4$, with specific energies of 0.546 kWh/kg and 0.581 kWh/kg, respectively (*91*, *92*). Both of these materials suffer from inherent drawbacks: $LiCoO_2$ can only reversibly cycle 0.5 Li^{1+} per formula unit and is composed of expensive Co, while the synthesis of $LiFePO_4$ is challenging and industrially complicated (*75*).

When $LiCoO_2$ is charged and more than 0.5 Li^{1+} is removed, a monoclinic structural modification occurs where CoO_2 planes shift relative to LiO_2 planes, leading to a degradation of the cycling capacity (*93*–*95*). To add rigidity to $LiCoO_2$, one could imagine placing 'chemical pillars' that connect the CoO_2 layers and limit their movement in the *a*-*b* plane. This idea, the topotactic modification of an α-$NaFeO_2$ type structure, can be easily achieved using the MuRE method previously described herein, shown to be successful with $Li_{0.75}Ca_{0.25}CoO_2$ (*96*). Starting with the O3 type $NaCoO_2$, the aliovalent exchange of Ca^{2+} for 2 Na^{1+} leads to a product with 'chemical pillars' between the CoO_2 layers: $Ca_{0.50}CoO_2$. The doubly-charged Ca^{2+} ion locks the CoO_2 layers together at a fixed distance – shown by the constant interplanar distance independent of Ca stoichiometry in the Ca_xCoO_2 layered

materials (*53*). Li^{1+} can then be intercalated into $Ca_{0.50}CoO_2$ while retaining the 'chemical pillars', giving a final product of $Li_{0.47}Ca_{0.50}CoO_2$.

Table 4-16. Electrochemical properties of common Li-ion cathode materials compared to the novel cobaltates presented in this thesis.

Material	Li+ Cycled	Average Voltage (V)	Specific Capacity (mAh/g)	Specific Energy (kWh/kg)	Specific Energy vs $LiCoO_2$
$LiCoO_2$	0.50	3.9	140	0.546	1.00
$LiMn_2O_4$	0.50	4.0	148	0.592	1.08
$LiFePO_4$	1	3.3	176	0.581	1.06
$LiCo_{1/3}Ni_{1/3}Mn_{1/3}O_2$	0.50	3.6	150	0.540	1.02
$Li_{0.47}Ca_{0.50}CoO_2$	0.47	3.54	111	0.388	0.71
$Li_{0.63}Ca_{0.37}CoO_2$	0.63	3.54	159	0.562	1.03
$Li_{0.75}Ca_{0.25}CoO_2$	0.75	3.58	190	0.680	1.25

A key difference between $LiCoO_2$ and $Li_{0.47}Ca_{0.50}CoO_2$ is the oxidation state of Co, having been reduced from 3+ to 2+/3+. When employed as a cathode material, the average charging voltage *vs.* lithium for each cathode is given in Equations 4-18 and 4-19 below, demonstrating the effect of oxidation state on voltage.

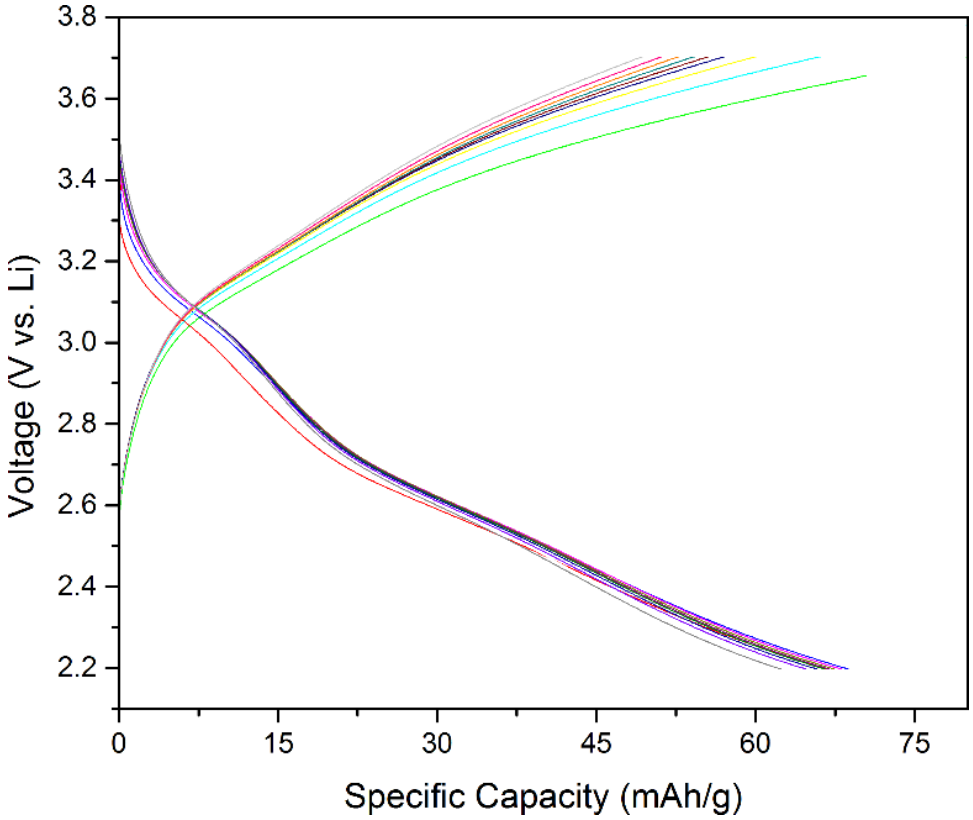

Figure 4-27. Charge-discharge curves of $Li_{0.47}Ca_{0.50}CoO_2$ showing two separate discharge events at 2.9 V and 3.2 V vs Li metal.

$$LiCo^{3+}O_2 \rightarrow \quad Li_{0.5}Co^{3.5+}O_2 + 1/2Li \qquad E_{cell} = 3.9\ V \qquad (4\text{-}18)$$

$$Li_{0.47}Ca_{0.50}Co^{2.53+}O_2 \rightarrow \quad Ca_{0.50}Co^{3+}O_2 + 0.47Li \qquad E_{cell} = 3.5\ V \qquad (4\text{-}19)$$

Using charging voltage as a guide, $Li_{0.47}Ca_{0.50}CoO_2$ has a capacity approximately 10% less than that of $LiCoO_2$; however, due to the added weight of Ca^{2+} in the structure, the specific capacity is 22% less, resulting in a total decrease in specific energy of approximately 30% when 0.47 equivalents of Li are cycled. Figure 4-27 shows initial cycling results for $Li_{0.47}Ca_{0.50}CoO_2$ at a rate of C/5 in a

coin cell type setup. The first cycle capacity of 75 mAh/g decreases upon further cycling and stabilizes at 50 mAh/g, 45% of the theoretical capacity. As the charging voltage is essentially fixed, an increase in specific energy must be accomplished by increasing the number of Li^{1+} cycled per formula unit or decreasing the molar mass of the compound. Interestingly, the discharge curve for $Li_{0.47}Ca_{0.50}CoO_2$ has two well defined intercalation peaks, while the charging curve has only one. It appears that the presence of these two curves is the manifestation of two redox couples involved – the cycling of the $Co^{2+/3+}$ oxidation couple and the $Co^{3+/4+}$ oxidation couple. This is one of few examples of multiple redox couple cycling in a Li-ion battery cathode material (*97*, *98*).

Because the MuRE method allows for control over the number of vacancies created in the A position of the AMO_2 structure, a starting material with a large number of vacancies will translate to a final product with a relatively large amount of intercalated Li^{1+}. For example, if $NaCoO_2$ is first oxidized to $Na_{0.50}CoO_2$ then the Na^{1+} ions are exchanged for Ca^{2+}, followed by Li^{1+} intercalation, the highly lithiated phase $Li_{0.75}Ca_{0.25}CoO_2$ is formed (*96*). The combination of formula mass decrease between $Li_{0.50}Ca_{0.50}CoO_2$ (114.44 g/mol) and $Li_{0.75}Ca_{0.25}CoO_2$ (106.08 g/mol), as well as an increase in Li^{1+} cycled per formula unit, leads to a specific capacity of 190 mAh/g for $Li_{0.75}Ca_{0.25}CoO_2$ and a total specific energy increase of 0.292 kWh/kg. Experimentally, it was demonstrated that $Li_{0.75}Ca_{0.25}CoO_2$ can be charged with an unoptimized first cycle capacity of approximately 115 mAh/g – well below the theoretical maximum 190 mAh/g (*96*). Upon subsequent cycles the charging

capacity diminished rapidly, attributed to the formation of an SEI layer with poor Li^{1+} conductivity (Figure 4-28). Varying the experimental cycling conditions, including electrolyte, solvent, loading content, and step rate, is currently underway to optimize the experimental specific capacity.

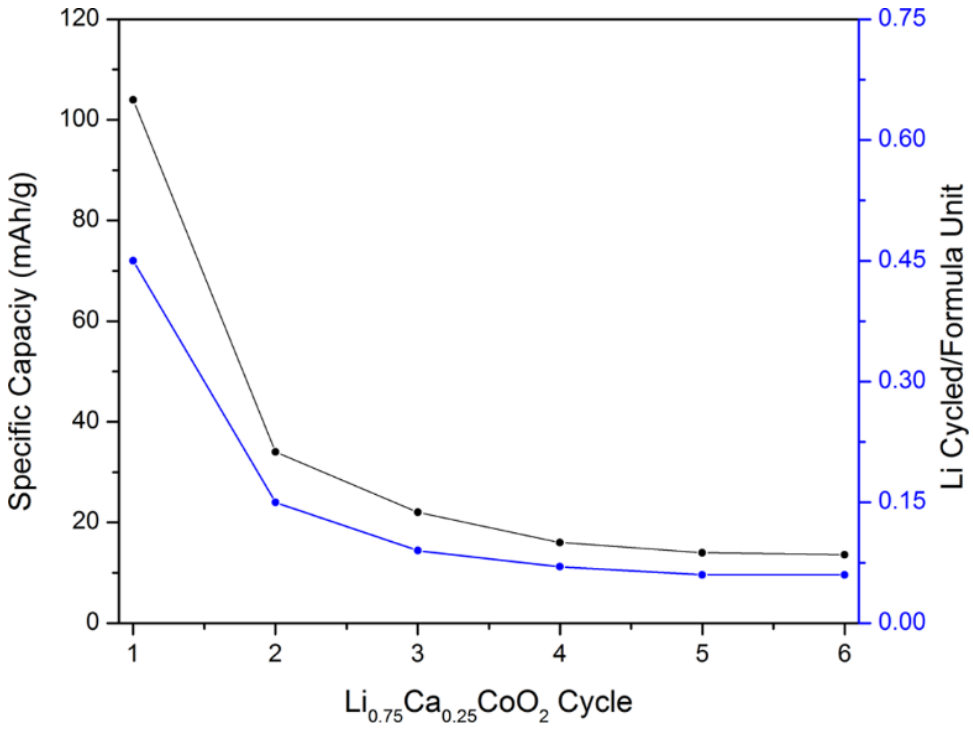

Figure 4-28. Per-cycle capacity of $Li_{0.75}Ca_{0.25}CoO_2$ measured at a C/5 rate against a Li metal anode.

Overall, the highest specific capacity can be achieved by beginning with the oxidized phase $Na_{0.34}CoO_2$ and employing the MuRE process. After Li^{1+} intercalation, a product with a theoretical stoichiometry of $Li_{0.83}Ca_{0.17}CoO_2$ is possible; however, experimentally this proves difficult. Aliovalent exchange of Ca^{2+}

for Na^{1+} on $Na_{0.34}CoO_2$ results in nearly pure phase $Ca_{0.17}CoO_2$ with a Co_2O_3 admixture. Upon reductive intercalation, the structure quickly decomposes at room temperature. The high concentration of oxidizing Co^{4+} in the structure, as well as the ease of CoO_2 plane shifting caused by a lack of interplanar Coulombic attraction, is attributed to the extreme instability of the phase. Further experiments may show some viability in electrochemical insertion of Li^{1+}. If synthesized, $Li_{0.83}Ca_{0.17}CoO_2$ would have a specific capacity of 216 mAh/g and a specific energy of 0.788 kWh/kg, nearly 1.5x greater than $LiCoO_2$.

4.4e Intercalation kinetics investigation

Intercalation kinetics were monitored over time to understand the relationship between layer stacking and alkali metal geometry with cation insertion in the host lattice (Table 4-17). Aliquots of both Li^{1+} and Na^{1+} intercalation solutions with different Ca_xCoO_2 (x = 0.50, 0.37, 0.25) host phases were taken every 24 hours. Alkali metal content was determined in triplicate with ICP. The smaller Li^{1+} is more mobile during intercalation due to fewer in-space interactions with the large and double-charged Ca^{2+}. As becomes quickly apparent, insertion of Na^{1+} into the O3 type $Ca_{0.50}CoO_2$ structure is much slower than in the P2 type $Ca_{0.35}CoO_2$ or $Ca_{0.25}CoO_2$ structures. After 120 hours, both P2 phases had nearly 90% Na^{1+} occupancy, whereas only 60% of the theoretical limit of Na^{1+} intercalation into $Ca_{0.50}CoO_2$ was achieved. In the O3 structural types Na^{1+} and Ca^{2+}, both share the same structural position (3b) as opposed to the P2 structure where both the 2b

and 2c sites are occupied by cations in the AO_2 layer. The two positions in the P2 structure can be differentiated by their relation to the CoO_6 octahedra: prisms in the 2b site shared edges with CoO_6 octahedra while prisms in the 2c site share faces with CoO_6 octahedra. In the majority of P2 type Na_xCoO_2 phases, Na^{1+} occupies the edge sharing site with a 2:1 preference. In the O3 stacking type, all AO_6 octahedra share edges with CoO_6 octahedra. We believe Na^{1+} diffusion is limited in the O3 type phase because of Coulombic repulsion between Na^{1+} and Ca^{2+} upon intercalation into the lone 3b site. This repulsion occurs to a lesser degree in the P2 type phases where Na^{1+} and Ca^{2+} can occupy two different structural sites. Na^{1+} phases prepared by the MuRE method were intercalated for 240 hrs and 360 hrs, in which final compositions were identical between the two reaction times. Li^{1+} intercalation into the O3 phase is much less hindered, although after 120 hours vacancies were still present in $Li_{0.47}Ca_{0.50}CoO_2$.

Table 4-17. Compound stoichiometry over intercalation time for the preparation of the reduced phases presented in the manuscript. Bolded numbers are stopping points for the preparation each compound.

Compound	x after time (hrs)					
	24	**48**	**72**	**96**	**120**	**240**
$Li_xCa_{0.50}CoO_2$	0.212	0.371	0.435	0.475	**0.489**	0.498
$Li_xCa_{0.37}CoO_2$	0.446	0.523	0.591	0.627	**0.642**	0.638
$Li_xCa_{0.25}CoO_2$	0.268	0.313	0.475	0.682	**0.751**	0.762
$Na_xCa_{0.50}CoO_2$	0.062	0.078	0.123	0.153	0.199	**0.313**
$Na_xCa_{0.37}CoO_2$	0.295	0.218	0.275	0.495	0.542	**0.593**
$Na_xCa_{0.25}CoO_2$	0.174	0.183	0.325	0.389	0.472	**0.665**

4.5 Possibility of lower oxidation states with extended MuRE

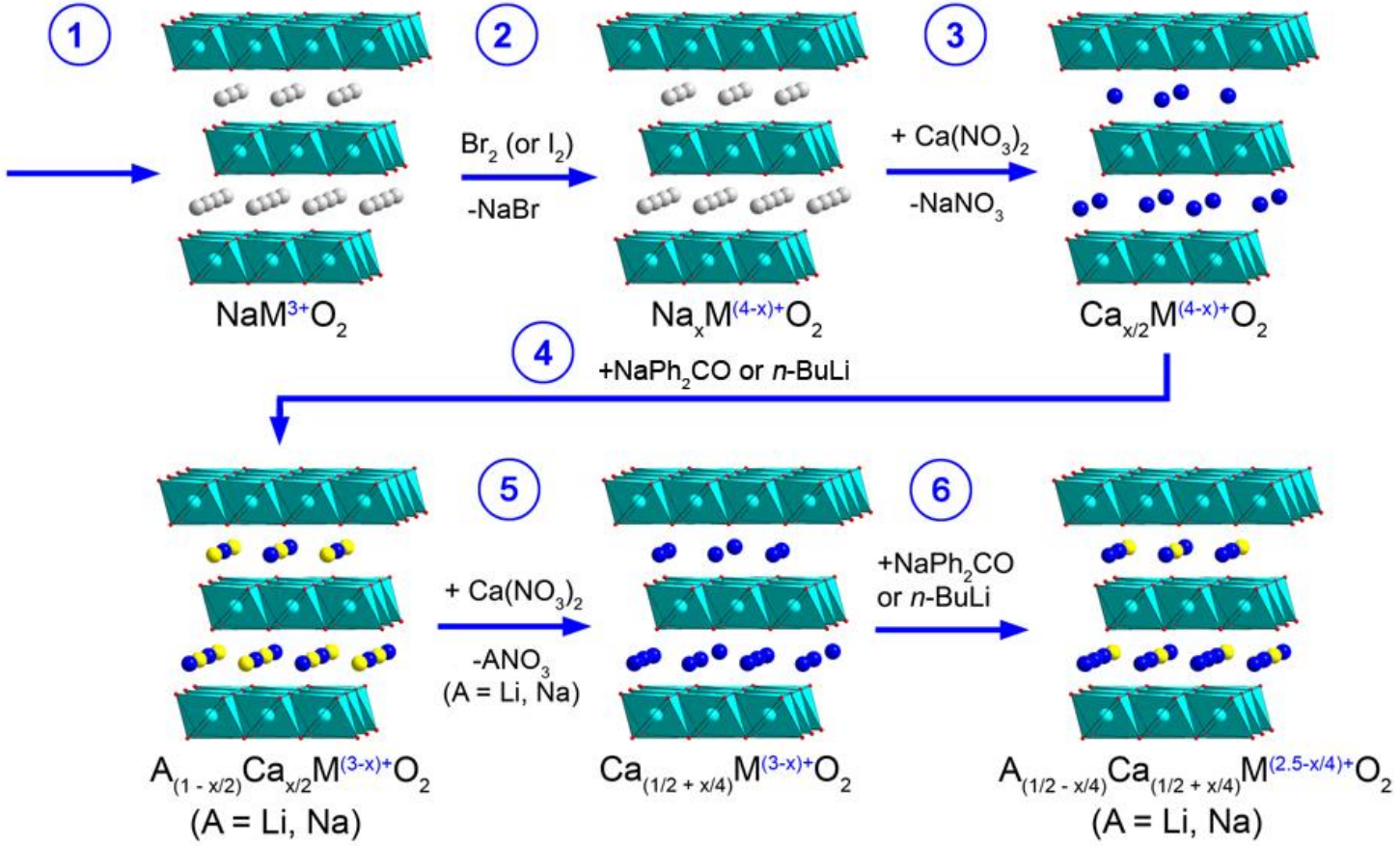

Figure 4-29. A schematic diagram demonstrating the theoretical extendibility of the MuRE method to produce phases with transition metal oxidation states between 2+ and 2.5+.

By extrapolating on the aforementioned reductive-intercalation approach, it seems possible to produce layered materials of the α-$NaFeO_2$ type structure with Co oxidation states below 2.5 – the limit of the reductive-intercalation technique. As shown in Figure 4-29, aliovalent exchange of Ca^{2+} for A^{1+} in the intercalated compound (Step 5) will lead to a higher Ca^{2+} content ($Ca_{0.75}$ when x = 1) than was possible when starting with $Na_{x=1}CoO_2$ ($Ca_{0.50}$ when x = 1). Alkali metals could then be intercalated into the Ca^{2+} enriched material (Step 6), effectively lowering the oxidation state of Co to below 2.5+. Theoretically, the aliovalent exchange followed by intercalation could be repeated ad infinitum as the Co oxidation state approaches 2+, effectively producing $CaCoO_2$. Similar compounds, $Ca_3Co_4O_9$ and Ca_2CoO_3, which have misfit layered structures that resemble the layered materials presented herein, are being explored for interesting thermoelectric properties (*99*, *100*).

4.6 Chapter conclusions

A multistep, topotactic synthesis method for the preparation of phases with Cd-I_2 type frustrated layers was presented. A series of compounds was synthesized with transition metals in uniquely low oxidation states for the type of crystal structure. Structural and stoichiometry characterization was presented to validate the method and demonstrate the true topotactic nature via the retention of crystal structure across the multiple synthetic steps. Intercalation kinetics, electrochemical characterization, and TGA analysis discussions are presented. Use of the MuRE method will allow for deeper fundamental insights into magnetically frustrated systems and how the competing coupling pathways in these systems can be modulated.

4.7 Future work on this topic

The future direction of this research project has the potential to branch into many other projects. Because the synthetic method is so versatile, and can be applied to other structural types, a purely fundamental solid state project looking at the synthesis of new phases and crustal structures could be approached. As many of the compounds produced with the MuRE method - either the layered α-NaFeO2 type or other structural motifs - will exhibit interesting characteristics and novel properties, full characterization of these materials is necessary.

More specifically, the MuRE method can be used to synthesize new Li-ion cathode materials with the possibility of 2 electron transfer. Using transition metals with multiple oxidation states - V or Mn, for example - would facilitate this chemistry. Furthermore, lighter transition metals will have a larger theoretical specific capacity.

The MuRE method can also be used as a technique to synthesize materials for thermoelectric devices. Increasing phonon and electron scattering by introducing vacancies and multiple different ions in the same crystallographic position are achievable with the MuRE method. Future direction could focus on using Co and a 5d transition metal with a mixture of alkali metal and alkaline earth metals in the A position.

Further structural investigations using high-resolution diffraction techniques - either synchrotron or neutron diffraction - are necessary to fully understand the location of atoms in the phases prepared using the MuRE method. Low

temperature neutron diffraction studies may lead to the characterization of long-range atom ordering.

REFERENCES

REFERENCES

(1) Huang, Q.; Foo, M.; Pascal, R.; Lynn, J.; Toby, B.; He, T.; Zandbergen, H.; Cava, R. Coupling between electronic and structural degrees of freedom in the triangular lattice conductor Na_xCoO_2. *Phys. Rev. B* **2004**, *70*, 184110.

(2) Viciu, L.; Bos, J.; Zandbergen, H.; Huang, Q.; Foo, M.; Ishiwata, S.; Ramirez, a.; Lee, M.; Ong, N.; Cava, R. Crystal structure and elementary properties of Na_xCoO_2 (x=0.32, 0.51, 0.6, 0.75, and 0.92) in the three-layer $NaCoO_2$ family. *Phys. Rev. B* **2006**, *73*, 1–10.

(3) Rouxel, J.; Danot, M.; Bichon, J. Intercalation Compounds NaxTiS2 - General Structural Study of Na_xTiS_2 and K_xTiS_2 Phases. *Bull. Soc. Chim. Fr.* **1971**, 3930.

(4) Pauling, L. *The Nature of the Chemical Bond*; 3rd ed.; 1948.

(5) Lucovsky, G. Transition from thermally grown gate dielectrics to deposited gate dielectrics for advanced silicon devices: A classification scheme based on bond ionicity. *J. Vac. Sci. Technol. A Vacuum, Surfaces, Film.* **2001**, *19*, 1553.

(6) Mamiya, M.; Kataoka, K.; Kikuchi, S.; Terajima, Y.; Tokiwa, K.; Akimoto, J. Synthesis and structure analysis of a new titanium oxide having an intergrowth structure between ramsdellite-type and calcium ferrite-type. *J. Phys. Chem. Solids* **2012**, *73*, 1460–1462.

(7) Clarke, S. J.; Fowkes, A. J.; Harrison, A.; Ibberson, R. M.; Rosseinsky, M. J. Synthesis , Structure , and Magnetic Properties of $NaTiO_2$. *Society* **1998**, *4756*, 372–384.

(8) Ouyang, S.-D.; Quan, Y.-M.; Liu, D.-Y.; Zou, L.-J. A Comparative Investigation on the JT Effect in Triangular Compounds of $NaMnO_2$, $NaNiO_2$ and $NaTiO_2$. *Chinese Phys. Lett.* **2011**, *28*, 067102.

(9) Takeda, K.; Miyake, K.; Takeda, K.; Hirakawa, K. Phase Transition in $NaTiO_2$: A Candidate for S=1/2 Traingular Heisenberg Antierromagnet. *J. Phys. Soc. Japan* **1992**, *61*, 2156–2157.

(10) Dhariwal, M.; Maitra, T.; Singh, I. Comparative study of $NaTiO_2$ and $NaNiO_2$ using first principle calculations. **2013**, *824*, 824–825.

(11) Reid, A.; Sabine, T.; Wheeler, D. Neutron Diffraction and Other Studies of Magnetic Ordering in Phases Based on Cr_2O_3, V_2O_3, and Ti_2O_3. **1972**, *409*, 400–409.

(12) Hoppe, R.; Schepers, B.; Rohrborn, H.-J.; Vielhaber, E. Uber Oxoscandate: $LiScO_2$ und $NaScO_2$. *Zeitschrift fur Anorg. und Allg. Chemie* **1965**, *339*, 130–143.

(13) *US Geological Survey Mineral Commodity Summaries*; 2008; pp. 1–2.

(14) Morosan, E.; Natelson, D.; Nevidomskyy, A. H.; Si, Q. Strongly correlated materials. *Adv. Mater.* **2012**, *24*, 4896–923.

(15) McQueen, T.; Stephens, P.; Huang, Q.; Klimczuk, T.; Ronning, F.; Cava, R. Successive Orbital Ordering Transitions in $NaVO_2$. *Phys. Rev. Lett.* **2008**, *101*, 166402.

(16) Ragupathy, P.; Shivakumara, S.; Vasan, H. N.; Munichandraiah, N. Preparation of Nanostrip V_2O_5 by the Polyol Method and Its Electrochemical Characterization as Cathode Material for Rechargeable Lithium Batteries. *J. Phys. Chem. C* **2008**, *112*, 16700–16707.

(17) Sathiya, M.; Prakash, a S.; Ramesha, K.; Tarascon, J. M.; Shukla, A. K. V_2O_5-anchored carbon nanotubes for enhanced electrochemical energy storage. *J. Am. Chem. Soc.* **2011**, *133*, 16291–9.

(18) Whittingham, M. S.; Song, Y.; Lutta, S.; Zavalij, P. Y.; Chernova, N. A. Some transition metal (oxy)phosphates and vanadium oxides for lithium batteries. *J. Mater. Chem.* **2005**, *15*, 3362.

(19) Li, L.; Kim, S.; Wang, W.; Vijayakumar, M.; Nie, Z. A New Vanadium Redox Flow Battery Using Mixed Acid Electrolytes. *Rev. Lit. Arts Am.* **2010**.

(20) Didier, C.; Guignard, M.; Denage, C.; Szajwaj, O.; Ito, S.; Saadoune, I.; Darriet, J.; Delmas, C. Electrochemical Na-Deintercalation from $NaVO_2$. *Electrochem. Solid-State Lett.* **2011**, *14*, A75.

(21) Guignard, M.; Didier, C.; Darriet, J.; Bordet, P.; Elkaïm, E.; Delmas, C. P2-Na_xVO_2 system as electrodes for batteries and electron-correlated materials. *Nat. Mater.* **2013**, *12*, 74–80.

(22) Miyazaki, S. Chemical and Electrochemical Deintercalations of the Layered AMO_2, *Synthetic Metals* **1983**, 6, 211-217.

(23) Saint, J. A.; Doeff, M. M.; Wilcox, J. Electrode Materials with the $Na_{0.44}$ MnO_2 Structure : Effect of Titanium Substitution on Physical and Electrochemical Properties. **2008**, 3404–3411.

(24) Li, H. H.; Yabuuchi, N.; Meng, Y. S.; Kumar, S.; Breger, J.; Grey, C. P.; Shao-horn, Y. Changes in the Cation Ordering of Layered O3 $Li_xNi_{0.5}Mn_{0.5}O_2$ during Electrochemical Cycling to High Voltages : An Electron Diffraction Study. *Society* **2007**, 2551–2565.

(25) Yuan, D.; He, W.; Pei, F.; Wu, F.; Wu, Y.; Qian, J.; Cao, Y.; Ai, X.; Yang, H. Synthesis and electrochemical behaviors of layered $Na_{0.67}[Mn_{0.65}Co_{0.2}Ni_{0.15}]O_2$ microflakes as a stable cathode material for sodium-ion batteries. *J. Mater. Chem. A* **2013**.

(26) Cheng, F.; Liang, J.; Tao, Z.; Chen, J. Functional materials for rechargeable batteries. *Adv. Mater.* **2011**, *23*, 1695–715.

(27) Zhou, Y.-N.; Ding, J.-J.; Nam, K.-W.; Yu, X.; Bak, S.-M.; Hu, E.; Liu, J.; Bai, J.; Li, H.; Fu, Z.-W.; Yang, X.-Q. Phase transition behavior of $NaCrO_2$ during sodium extraction studied by synchrotron-based X-ray diffraction and absorption spectroscopy. *J. Mater. Chem. A* **2013**, *1*, 11130.

(28) Miyazaki, S.; Kikkawa, S.; Koizumi, M. Chemical and electrochemical deintercalations of the layered compounds $LiMO_2$ (M = Cr, Co) and $NaM'O_2$ (M' = Cr, Fe, Co, Ni). *Synth. Metails* **1983**, *6*, 211–217.

(29) Komaba, S.; Takei, C.; Nakayama, T.; Ogata, A.; Yabuuchi, N. Electrochemical intercalation activity of layered $NaCrO_2$ vs. $LiCrO_2$. *Electrochem. commun.* **2010**, *12*, 355–358.

(30) Komaba, S.; Nakayama, T.; Ogata, A.; Shimizu, T.; Takei, C.; Takada, S.; Hokura, A.; Nakai, I. Electrochemically Reversible Intercalation of Layered $NaNi_{0.5}Mn_{0.5}O_2$ and $NaCrO_2$. In *ECS Transactions*; ECS, 2009; pp. 43–55.

(31) Elliston, P. R.; Blazey, K. W. Magnetic and Optical Study of $NaCrO_2$. *J. Phys. Chem. Solids* **1974**, *36*, 877–881.

(32) Blesa, M.; Moran, E.; Leon, C.; Santamaria, J.; Tornero, J. D.; Mendendez, N. α-$NaFeO_2$: ionic conductivity and sodium extraction. *Solid State Ionics* **1999**, *126*, 81–87.

(33) McQueen, T.; Huang, Q.; Lynn, J.; Berger, R.; Klimczuk, T.; Ueland, B.; Schiffer, P.; Cava, R. Magnetic structure and properties of the S=5/2 triangular antiferromagnet α-$NaFeO_2$. *Phys. Rev. B* **2007**, *76*, 1–7.

(34) Rousseau, J.; Bernheim, R. Synthesis of $NaFeO_2$. *Compt Rend* **1888**, *170*, 240.

(35) Blesa, M. C.; Morán, E.; Menéndez, N.; Tornero, J. D.; Torrón, C. Hydrolysis of sodium orthoferrite α-$NaFeO_2$. *Mater. Res. Bull.* **1993**, *28*, 837–847.

(36) Blesa, M.; Moran, E.; Amador, U.; Andersern, N. H. Crystal and Magnetic Structures of a Nickel-Rich Ferrite Obtained by Ionic Exchange from α-$NaFeO_2$. *J. Solid State Chem.* **1997**, *129*, 123–129.

(37) Blesa, M. C.; Morán, E.; Tornero, J. D.; Menéndez, N.; Mata-Zamora, E.; Saníger, J. M. A new route to γ-Fe_2O_3 via an intermediate oxyhydroxide. The reaction of α-$NaFeO_2$ with benzoic acid. *J. Mater. Chem.* **1999**, *9*, 227–231.

(38) Blesa, M.; Amador, U.; Moran, E.; Menendez, N.; Torenero, J.; Synthesis and characterization of nickel and magnesium ferrites obtained from α-$NaFeO_2$. *Solid State Ionics* **1993**, *63-65*, 429–436.

(39) Shannon, R. D. Revised effective ionic radii and systematic studies of interatomic distances in halides and chalcogenides. *Acta Crystallogr. Sect. A* **1976**, *32*, 751–767.

(40) Fukuzaki, K.; Kohiki, S.; Matsushima, S.; Oku, M.; Hideshima, T.; Watanabe, T.; Takahashi, S.; Shimooka, H. Preparation and characterization of $NaInO_2$ and $NaInS_2$. *J. Mater. Chem.* **2000**, *2*, 779–782.

(41) Shikano, M.; Delmas, C.; Darriet, J. $NaRuO_2$ and $Na_xRuO_2.yH_2O$: new oxide and oxyhydrate with two dimensional RuO_2 layers. *Inorg. Chem.* **2004**, *43*, 1214–6.

(42) Agrawal, R. C.; Gupta, R. K.; Superionic solids : composite electrolyte phase – an overview. *J. Mater. Sci.* **1999**, *4*, 1131–1162.

(43) Delmas, C.; Maazaz, A.; Fouassier, C.; Reau, J.-M.; Hagenmuller, P. Influence de l'environnement de l'ion alcalin sur sa mobilite dans les structures a feuillets $A_x(LXM_{1-x})O_2$. *Mater. Res. Bull.* **1979**, *14*, 329–335.

(44) Kawakami, S.; Sasaki, M.; Tabata, H.; Shimooka, H.; Kohiki, S.; Matsushima, S.; Oku, M.; Shishido, T. Comparison of electronic structure of $LiInO_2$ with $NaInO_2$. *J. Alloys Compds.* **2003**, *359*, 278–280.

(45) Hernan, L.; Macias, M.; Morales, J. Topotactic exchange of layered $NaInO_2$ by protons. *Mater. Res. Bull.* **1990**, *25*, 1169–1174.

(46) Sato, J.; Kobayashi, H.; Saito, N.; Nishiyama, H.; Inoue, Y. Photocatalytic activities for water decomposition of RuO_2-loaded $AInO_2$ (A=Li, Na) with d10 configuration. *J. Photochem. Photobiol. A Chem.* **2003**, *158*, 139–144.

(47) Ogura, S.; Kohno, M.; Sato, K.; Inoue, Y. Effects of RuO_2 on activity for water decomposition of a $RuO_2/Na_2Ti_3O_7$ photocatalyst with a zigzag layer structure. *J. Mater. Chem.* **1998**, *7*, 2335–2337.

(48) Chem, W.; Chem, J.; Denki, S.; Mb, T. Photocatalytic activity for methylene blue decomposition of $NaInO_2$. *J. Mater. Sci.* **2004**, *9*, 6367–6370.

(49) Diebold, U. The surface science of titanium dioxide. *Surf. Sci. Rep.* **2003**, *48*, 53–229.

(50) Ong, N. P.; Cava, R. J. Electronic frustration on a triangular lattice. *Science* **2004**, *305*, 52–3.

(51) Foo, M.; Wang, Y.; Watauchi, S.; Zandbergen, H.; He, T.; Cava, R.; Ong, N. Charge Ordering, Commensurability, and Metallicity in the Phase Diagram of the Layered Na_xCoO_2. *Phys. Rev. Lett.* **2004**, *92*, 1–4.

(52) Lee, M.; Viciu, L.; Li, L.; Wang, Y.; Foo, M. L.; Watauchi, S.; Pascal, R. a; Cava, R. J.; Ong, N. P. Large enhancement of the thermopower in Na_xCoO_2 at high Na doping. *Nat. Mater.* **2006**, *5*, 537–40.

(53) Cushing, B. L.; Wiley, J. B. Topotactic Routes to Layered Calcium Cobalt Oxides. *J. Solid State Chem.* **1998**, *391*, 385–391.

(54) Ono, Y.; Ishikawa, R.; Miyazaki, Y.; Ishii, Y.; Morii, Y.; Kajitani, T. Crystal Structure, Electric and Magnetic Properties of Layered Cobaltite β-Na_xCoO_2. *J. Solid State Chem.* **2002**, *166*, 177–181.

(55) Huang, Q.; Foo, M. L.; Lynn, J. W.; Zandbergen, H. W.; Lawes, G.; Wang, Y.; Toby, B. H.; Ramirez, A. P.; Ong, N. P.; Cava, R. J. Low temperature phase transitions and crystal structure of $Na_{0.5}CoO_2$. *J. Phys. Condens. Matter* **2004**, *16*, 5803–5814.

(56) Takada, K.; Sakurai, H.; Takayama-muromachi, E. Superconductivity in two-dimensional CoO_2 layers. **2003**, *422*, 53–55.

(57) Cushing, B. L.; Falster, A. U.; Simmons, W. B.; Wiley, J. B. A multivalent ion exchange route to lamellar calcium cobalt oxides. *Chem Comm* **1996**, *2*, 2635–2636.

(58) Yang, H. X.; Shi, Y. G.; Guo, Y. Q.; Liu, X.; Xiao, R. J.; Physical properties, strontium ordering and structural modulation in layered hexagonal $Sr_{0.35}CoO_2$. *arXiv* **2005**, 1–16.

(59) Xiao, R. J.; Yang, H. X.; Xu, L. F.; Zhang, H. R.; Electronic structure and electron energy-loss spectra of $Sr_{0.35}CoO_2$. *arXiv* **2006**, 1–16.

(60) Gomez, J. C.; Calvet, N.; Starace, A. K.; Glatzmaier, G. C. $Ca(NO_3)_2$ — $NaNO_3$ - KNO_3 Molten Salt Mixtures for Direct Thermal Energy Storage Systems in Parabolic Trough Plants. *J. Sol. Energy Eng.* **2013**, *135*, 021016.

(61) Peterson, V. K. Lattice parameter measurement using LeBail versus structural (Rietveld) refinement: A caution for complex, low symmetry systems. *Powder Diffr.* **2012**, *20*, 14–17.

(62) Peterson, V. K. Lattice parameter measurement using LeBail versus structural (Rietveld) refinement: A caution for complex, low symmetry systems. *Powder Diffr.* **2012**, *20*, 14–17.

(63) Parvin, K. Synthesis and magnetic properties of monodisperse Fe_3O_4 nanoparticles. *J. Appl. Phys.* **2004**, *95*, 7121.

(64) Rumpf, K.; Granitzer, P.; Morales, P. M.; Poelt, P.; Reissner, M. Variable blocking temperature of a porous silicon/Fe_3O_4 composite due to interactions of the magnetic nanoparticles. *Nanoscale Res. Lett.* **2012**, *7*, 445.

(65) Sun, J.; Zhou, S.; Hou, P.; Yang, Y.; Weng, J.; Li, X.; Li, M. Synthesis and characterization of biocompatible Fe_3O_4 nanoparticles. **2006**, 2–10.

(66) Ghandoor, H. El; Zidan, H. M.; Khalil, M. M. H.; Ismail, M. I. M. Synthesis and Some Physical Properties of Magnetite (Fe_3O_4). **2012**, *7*, 5734–5745.

(67) Yuan, H. L.; Wang, Y. Q.; Zhou, S. M.; Liu, L. S.; Chen, X. L.; Lou, S. Y.; Yuan, R. J.; Hao, Y. M.; Li, N. Low-Temperature Preparation of Superparamagnetic $CoFe_2O_4$ Microspheres with High Saturation Magnetization. *Nanoscale Res. Lett.* **2010**, *5*, 1817–1821.

(68) Lak, A.; Kraken, M.; Ludwig, F.; Kornowski, A.; Eberbeck, D.; Sievers, S.; Litterst, F. J.; Weller, H.; Schilling, M. Size dependent structural properties of FeO-Fe_3O_4 nanoparticles. *Nanoscale* **2013**, *5*, 12286–95.

(69) Ouyang, C.; Shi, S.; Wang, Z.; Huang, X.; Chen, L. First-principles study of Li ion diffusion in $LiFePO_4$. *Phys. Rev. B* **2004**, *69*, 1–5.

(70) Zaghib, K.; Goodenough, J. B.; Mauger, a.; Julien, C. Unsupported claims of ultrafast charging of $LiFePO_4$ Li-ion batteries. *J. Power Sources* **2009**, *194*, 1021–1023.

(71) Chung, S.-Y.; Bloking, J. T.; Chiang, Y.-M. Electronically conductive phospho-olivines as lithium storage electrodes. *Nat. Mater.* **2002**, *1*, 123–8.

(72) Yuan, L.-X.; Wang, Z.-H.; Zhang, W.-X.; Hu, X.-L.; Chen, J.-T.; Huang, Y.-H.; Goodenough, J. B. Development and challenges of $LiFePO_4$ cathode material for lithium-ion batteries. *Energy Environ. Sci.* **2011**, *4*, 269.

(73) Gu, Y.-J.; Zeng, C.-S.; Wu, H.-K.; Cui, H.-Z.; Huang, X.-W.; Liu, X.-B.; Wang, C.-L.; Yang, Z.-N.; Liu, H. Enhanced performance and high energy density of $LiFePO_4$ based lithium ion batteries. *Mater. Lett.* **2007**, *61*, 4700–4702.

(74) Wagemaker, M.; Singh, D. P.; Borghols, W. J. H.; Lafont, U.; Haverkate, L.; Peterson, V. K.; Mulder, F. M. Dynamic solubility limits in nanosized olivine $LiFePO_4$. *J. Am. Chem. Soc.* **2011**, *133*, 10222–8.

(75) Konarova, M.; Taniguchi, I. Synthesis of carbon-coated $LiFePO_4$ nanoparticles with high rate performance in lithium secondary batteries. *J. Power Sources* **2010**, *195*, 3661–3667.

(76) Li, H.; Chen, G.; Zhang, B.; Xu, J. Advanced electrochemical performance of $Li[Ni(_{1/3-x})FexCo_{1/3}Mn_{1/3}]O_2$ as cathode materials for lithium-ion battery. *Solid State Commun.* **2008**, *146*, 115–120.

(77) Palomares, V.; Goñi, A.; Muro, I. G. De; de Meatza, I.; Bengoechea, M.; Cantero, I.; Rojo, T. Conductive additive content balance in Li-ion battery cathodes: Commercial carbon blacks vs. in situ carbon from $LiFePO_4$/C composites. *J. Power Sources* **2010**, *195*, 7661–7668.

(78) Wu, N. L. Impact of Current Collector on High- Rate Performance of Li-ion Battery Electrodes. *Society* 2011.

(79) Licht, S. A High Capacity Li-Ion Cathode: The Fe(III/VI) Super-Iron Cathode. *Energies* **2010**, *3*, 960–972.

(80) Tarascon, J. M.; Delacourt, C.; Prakash, a S.; Morcrette, M.; Hegde, M. S.; Wurm, C.; Masquelier, C. Various strategies to tune the ionic/electronic properties of electrode materials. *Dalton Trans.* **2004**, 2988–94.

(81) Becker, D.; Cherkashinin, G.; Schmid, S.; Hausbrand, R.; Jaegermann, W. Mechanistic investigation of SEI formation : Study of solvent adsorption on in-situ prepared thin film cathode surfaces. *Surf. Sci.* 2011.

(82) Cherkashinin, G.; Nikolowski, K.; Ehrenberg, H.; Jacke, S.; Dimesso, L.; Jaegermann, W. The stability of the SEI layer, surface composition and the oxidation state of transition metals at the electrolyte-cathode interface impacted by the electrochemical cycling: X-ray photoelectron spectroscopy investigation. *Phys. Chem. Chem. Phys.* **2012**, *14*, 12321–31.

(83) Mukhopadhyay, A.; Tokranov, A.; Xiao, X.; Guo, F.; Hurt, R. H.; Sheldon, B. W. Irreversible stress development due to SEI formation and self discharge kinetics of graphitic thin film anodes in Li-ion battery. *Stress Int. J. Biol. Stress* 2011.

(84) Malik, R.; Burch, D.; Bazant, M.; Ceder, G. Particle size dependence of the ionic diffusivity. *Nano Lett.* **2010**, *10*, 4123–7.

(85) Fransen, M. J. 1 and 2 dimensional detection systems and the problem of sample fluorescence in X-ray diffractometry. *Adv. X-ray Anal.* **2004**, *47*, 224–231.

(86) Blakely, C. K.; Bruno, S. R.; Baum, Z. J.; Poltavets, V. V. Effects of ball milling and thermal annealing on size and strain of $ASnO_3$ (A = Ba, Sr) ceramics. *Solid State Sci.* **2013**, *15*, 110–114.

(87) Ahmed, J.; Blakely, C. K.; Bruno, S. R.; Poltavets, V. V. Synthesis of $MSnO_3$ (M=Ba, Sr) nanoparticles by reverse micelle method and particle size distribution analysis by WPPM. *Mater. Res. Bull.* **2012**, *47*, 2282–2287.

(88) Leoni, M.; Scardi, P. Nanocrystalline domain size distributions from powder diffraction data research papers. *J. Appl. Crystallogr.* **2004**, *37*, 629–634.

(89) Schougaard, S. B.; Bréger, J.; Jiang, M.; Grey, C. P.; Goodenough, J. B. $LiNi_{0.5+\delta}Mn_{0.5-\delta}O_2$ High-Rate, High-Capacity Cathode for Lithium Rechargeable Batteries. *Adv. Mater.* **2006**, *18*, 905–909.

(90) Jeppson, D. W.; Ballif, J. L.; Yuan, W. W.; Chou, B. E. *Lithium Literature Review: Lithium's Properties and Interactions*; 1978; p. 111.

(91) Mizushima, K.; Jones, P. C.; Wisemna, P. J.; Goodenough, J. B. Li_xCoO_2 (0<x<=1): A new cathode material for batteries of high energy density. *Mater. Res. Bull.* **1980**, *15*, 783–789.

(92) Goodenough, J. B.; Kim, Y. Challenges for Rechargeable Li Batteries. *Chem. Mater.* **2010**, *22*, 587–603.

(93) Gupta, R.; Manthiram, A. Chemical Extraction of Lithium from Layered $LiCoO_2$. *J. Solid State Chem.* **1996**, *491*, 483–491.

(94) Kim, Y.; Veith, G. M.; Nanda, J.; Unocic, R. R.; Chi, M.; Dudney, N. J. High voltage stability of $LiCoO_2$ particles with a nano-scale Lipon coating. *Electrochim. Acta* **2011**, *56*, 6573–6580.

(95) Jhu, C.-Y.; Wang, Y.-W.; Wen, C.-Y.; Shu, C.-M. Thermal runaway potential of $LiCoO_2$ and $Li(Ni_{1/3}Co_{1/3}Mn_{1/3})O_2$ batteries determined with adiabatic calorimetry methodology. *Appl. Energy* **2012**, *100*, 127–131.

(96) Blakely, C. K.; Bruno, S. R.; Davis, J. D.; Poltavets, V. V. Synthesis and Electrochemical Properties of Novel Co^{2+}/Co^{3+} Layered Ordered Rock-Salt Structure Type $Li_{0.75}Ca_{0.25}CoO_2$. *ECS Trans.* **2013**, *45*, 3–10.

(97) Park, Y.-U.; Seo, D.-H.; Kim, B.; Hong, K.-P.; Kim, H.; Lee, S.; Shakoor, R. a; Miyasaka, K.; Tarascon, J.-M.; Kang, K. Tailoring a fluorophosphate as a novel 4 V cathode for lithium-ion batteries. *Sci. Rep.* **2012**, *2*, 704.

(98) Li, X.; He, W.; Xiao, Z.; Peng, F.; Chen, J. Ionothermal synthesis and rate performance studies of nanostructured $Li_3V_2(PO_4)_3$/C composites as cathode materials for lithium-ion batteries. *J. Solid State Electrochem.* **2013**, *17*, 1991–2000.

(99) Masset, a.; Michel, C.; Maignan, a.; Hervieu, M.; Toulemonde, O.; Studer, F.; Raveau, B.; Hejtmanek, J. Misfit-layered cobaltite with an anisotropic giant magnetoresistance: $Ca_3Co_4O_9$. *Phys. Rev. B* **2000**, *62*, 166–175.

(100) Asahi, R.; Sugiyama, J.; Tani, T. Electronic structure of misfit-layered calcium cobaltite. *Phys. Rev. B* **2002**, *66*, 155103.

Chapter 5 : Particle size analysis using Whole Powder Pattern Modeling

5.1. Introduction to particle size analysis

As nanostructured materials are more widely studied in the literature, a better technique to extract physical parameters from powder diffraction data has evolved - Whole Powder Pattern Modeling (WPPM) (*1*). Compared to standard line profile analysis techniques (LPA) like the Scherrer formula (equation 5-1), WPPM methods do not solely rely on peak width and shape factors in calculating physical properties like particle size distribution (*2*). In the Scherrer equation, the average domain size D is directly related to the dimensionless shape factor K which is dependent on the shape of the crystallites and the incident x-ray wavelength and indirectly related to the peak line breadth in radians ß at FWHM and the Bragg angle θ This equation always calculates the lower bound for the particle size because of the intrinsically complicated nature of nanostructure materials. The width of a peak in an x-ray diffractogram is dependent on both instrumental effects and crystallite characteristics: size, strain, dislocations, twinning, anti-phase grain boundaries, and heterogeneities in the chemical makeup. Because the Scherrer formula only includes crystallite size as the determinant for peak width, it can only provide a correct particle size distribution when the sample is perfectly crystalline and dispersed (when every other contribution to peak width is essentially zero).

$$D = \frac{K\lambda}{\beta\cos\theta} \qquad (5\text{-}1)$$

Rather than basing particle size analysis on peak breadth, WPPM methods use a bottom-up approach (*1*). A least squares analysis - similar in idea to Rietveld refinement - is used to create a synthetic powder pattern based on the refined parameters that contribute to peak width, mentioned previously. This pattern is iterated through and modulated during each refinement cycle until the synthetic pattern matches the observed pattern. Assuming the diffractogram statistics are reasonably high, all real contributions to peak width can be quantified using WPPM.

The PM2K software suite was used in the following studies to employ the WPPM methods (*3*). PM2K is a customizable software package that allows plug-ins to be written and run simultaneously - for example, both WPPM and Rietveld analysis can be run on the same powder pattern at the same time and each iteration can be compared. Current plugins that have been created include: Rietveld-Caglioti, Fundamental Parameter Approach of instrumental broadening, size broadening including lognormal, delta, and York distributions, strain broadening to identify dislocations via Wilkens, Green, and Houska functions, effective broadening using the Harmonics model, Faulting with Warren equations, antiphase boundary identification with Wilson-soldos models, and grain surface relaxation. First, an input file is written by the user in a pseudo-visual basic type code which includes peak locations and reflections as well as sample and instrument parameters. Then, certain parameters are locked or unlocked

depending on which physical phenomena are being investigated, followed by least squares iteration.

For those interested in learning more about the PM2K software package: a full user manual with examples has been compiled, printed, and bound. It is located in Prof. Viktor Poltavets' office.

5.2 Effects of milling and annealing on stannate nanoparticles

Alkaline earth metal stannates $ASnO_3$ (A = Ba, Sr) are actively investigated for multiple applications. Thin hetero-junction films of $BaSnO_3$ with other oxides have been studied as gas sensors for CO, CH_3SH, and liquefied petroleum gas (*4*–*7*). When structurally similar $BaTiO_3$ and $BaSnO_3$ perovskites are combined, multifunctional sensors are formed with the capacity to detect temperature, acetylene, and ethylene under standard conditions (*8*). $BaSnO_3$ also shows promise in photocatalysis, has room temperature luminescence properties, and operate as ceramic dielectrics (*9*–*11*). The efficiency of stannates in these applications is directly linked to the grain size, leading to a push to develop synthetic methods that result in smaller particle sizes.

The conventional ceramic method results in large, coarse-grained particles with a non-uniform size distribution. Nano-sized $ASnO_3$ materials have been produced through low temperature routes including: hydrothermal and sol-gel methods (*12*), lyothermal synthesis (*8*), coprecipitation (*13*), and a peroxide procedure (*14*). Inorganic nitrate, oxalate, and acetate precursors are predominately used in the low temperature synthesis (150 °C – 200 °C) of nanoparticles due to their low thermal stability. There are very few systematic size-tuning studies of ternary oxides in the literature and, to the best of our knowledge, none that focus on the $ASnO_3$ perovskite materials or the exploration of the effects of ball milling on particle size and strain.

The importance of particle size in cutting-edge devices has recently been realized in the optimization of the semiconductor charge collector in dye-sensitized solar cells (DSSCs). Both particle size and crystallite strain are important factors in the efficiency of a DSSC, where particle size dictates electron diffusion coefficients (D), electron recombination times (τ), and charge injection efficiency, while crystallite strain is correlated to surface trap states and an overall decrease in injection efficiency (*15*). Thus, there is a need in facile preparation techniques which would allow for the precise control of both particle size and crystallite strain.

Particle size and strain analysis is commonly performed by studying X-ray diffraction peak broadening with the Scherrer equation (*16*, *17*). A seminal study on ZnO samples prepared from different precursor salts clearly defined a correlation between the chemical nature of the initial precursor (nitrate, oxalate, acetate, or carbonate) and the microstrutural properties of the obtained ceramic, including the crystallite shape, size, strain, and stacking faults (*18*). While widely employed, the Scherrer equation utilizes only one or two reflections rather than all applicable reflections in the pattern. A further disadvantage of the Scherrer formula is the assumption that diffraction peaks are rectangular – an essential shortcoming that is fixed when the WPPM algorithms are used. Since diffraction peak shape depends on the combination of particle shape and size distributions, as well as strain of different origins, improvement of the WPPM model is an ongoing effort. The WPPM approach models all peaks to extract microstructural features and information from the entire pattern, rather than a subset, by combining pattern-

fitting techniques based on both integral breadth and Fourier methods. Because the diffraction pattern peaks are modelled directly, the WPPM particle size and crystallite strain analysis is a powerful and accurate method in microstructure determination.

In this case study, the preparation of $ASnO_3$ (A = Ba, Sn) nanoparticles by high-impact ball milling and a study of the particle size and strain dependence on milling time and further annealing temperature is presented. The underlying idea was to prepare nanoparticles by a simple method and decrease strain by thermal annealing while preserving small particle size.

5.2a Experimental methods and WPPM input

$BaCO_3$ (Alfa Aesar, 99%), $SrCO_3$ (Alfa Aesar, 99%), and SnO_2 (Strem Chemical, 99%) were used as staring materials without further purification. For the milling experiments, a Fritsch planetary ball mill was used with 18 mL steel jars and 4 10mm tungsten carbide balls per jar. Milling was done in five minute increments with one minute rest at 500 rpm for an appropriate time as described below. All samples were stored under a N_2 atmosphere after preparation.

For the synthesis of $BaSnO_3$ and $SrSnO_3$, stoichiometric amounts of the appropriate metal carbonate and SnO_2 were intimately mixed using an agate mortar and pestle for 30 minutes, then fired at 1200 °C for 24 hours in air with a 6 hour heating ramp. The material was then reground and fired for an additional 16 hours, resulting in approximately 20 g of pure phase material - enough for all further

studies. From this bulk material, 3 g aliquots were ball milled in steel jars according to the procedure mentioned above for the following specific time durations: 30 minutes, 1 hour, 2 hours, 4 hours, and 8 hours. The 8 hour sample was then split into 10 equivalent samples, each fired in air with a 3 hour heating ramp to an array of temperatures (200 °C - 1000 °C with a 100 °C step), and held for 24 hours. Powder X-ray Diffraction (PXD) patterns were taken of these thermally treated samples in order to correlate the effect of thermal annealing on grain size and crystallite strain.

PXD patterns were obtained on a Bruker D8 Advanced New diffractometer equipped with a LynxEye detector using Cu radiation with a $K_{\alpha 1}$ wavelength of 1.5418 Å at room temperature. Diffraction patterns were collected from 10 - 80° 2Θ with a step size of 0.02° at 25 °C for all materials. The instrumental line broadening profile was developed using the standard reference material LaB_6 provided by NIST measured under identical conditions as the sample material. Due to the high symmetry of both materials, seven reflections were recorded for $BaSnO_3$ ($Pm\bar{3}m$, a = 4.1084(2) Å) and six for $SrSnO_3$ ($Pm\bar{3}m$, a = 4.0252(3) Å). Rietveld refinement and structure analysis were completed using the Bruker Topas software suite (*19*). Peak positions, areas, unit cell parameters, and crystallite parameters were refined one by one, then locked, followed by a complete refinement of all parameters to obtain the final unit cell dimensions. The patterns were initially refined based on ICSD entries 43138 and 27047 for $BaSnO_3$ and $SrSnO_3$ respectively, using the Bruker Topas software suite.

Thermogravimetric analysis (TGA) and differential scanning calorimetry (DSC) measurements were performed using a Netsch Jupiter 449 F3 TGA/DSC on 10-20 mg samples with a platinum sample holder. Ultra-high purity (99.999%) nitrogen was used as the protective gas for all experiments. Buoyancy effects were corrected via subtraction of a blank measurement under identical experimental conditions and TGA analysis was used to confirm oxygen stoichiometry of the starting ceramic materials.

Microstructural features of the samples were analyzed using a JEOL-2200FS high-resolution transmission electron microscope (HRTEM), and elemental analysis was obtained using an Oxford Inca EDX analyzer attached to the aforementioned TEM instrument. The PM2K software suite, based on the principle of WPPM, was used to analyze the particle size distribution and particle strain features using the assumption of a lognormal distribution of particles and a Lorentzian peak shape (*3*).

Necessary parameters for the extraction of size and strain from the powder diffraction pattern were obtained using both the PM2K and TOPAS software suites. The major assumptions using this modeling method include: minimum peak overlap in the diffraction pattern, high counting statistics, and a Lorentzian peak shape. Considering the highly symmetric nature of the materials studied herein, the spacing between hkl peaks led to zero line overlap in the pattern, accompanied by a very high signal-to-noise ratio. A lognormal size distribution was used to calculate the particle size of the ball-milled and thermally treated samples. There

is precedence in the literature for the use of a lognormal distribution of particle sizes for nanoparticles used in different chemical methods, including catalysis (*7*). This assumption is thermodynamically reasonable, considering that small grains form simple convex shapes (sphere, cube) that can be described using a single parameter (*20*).

The lognormal function employed for this size distribution study is a combination of the lognormal mean μ and the lognormal variance σ:

$$g_l(D)=\frac{1}{D\sigma(2\pi)^{1/2}}\exp[-(\ln D-\mu)^2/2\sigma^2] \quad (5\text{-}2)$$

where D is the diameter of the spherical particle. A more in-depth description of the lognormal function and the Fourier transform of said function used in the PM2K software suite is given by Scardi and Leoni (*1*, *3*, *20*). The instrument profile component of the powder x-ray diffraction pattern was modeled with the Caglioti formula to parametize the FWHM and Lorentzian fractions (*21*):

$$FWHM^2 = W + V\tan(\theta) + U\tan^2(\theta) \quad (5\text{-}3)$$

$$\eta_{Lorentz} = a + b\theta_{deg} + c\theta_{deg}^2 \quad (5\text{-}4)$$

where θ is half of the Bragg angle 2θ. The W, V, U, a, b, and c parameters were refined by PM2K to optimize the Caglioti profile function, and then fixed, as we assumed that the instrumental contribution is constant for the instrument and is not dependant on the sample (*22*).

PXD patterns for both $BaSnO_3$ and $SrSnO_3$ were obtained on the same instrument with identical experimental setups to avoid the introduction of

instrument discrepancy. Using the indexing obtained from the respective refinements, the spectra were loaded into the PM2K program with an input file specifying the Caglioti parameters previously established, the cell parameters of the respective phases, a function to refine zero error and sample displacement, a four parameter Chebyshev background function, and the peak indices and relative intensities. All variables except for the background, peak intensities, and sample displacement were initially locked and then released over a series of iterations to obtain a final whole pattern refinement. Once a suitable refinement fit value was obtained, a lognormal size distribution function was added to the input file.

5.2b Effect of impact milling on particle size and strain

PXD diffraction patterns of the ceramics $BaSnO_3$ (cubic symmetry, $Pm\bar{3}m$ space group, a = 4.1084(2) Å) and $SrSnO_3$ (cubic symmetry, $Pm\bar{3}m$ space group, a = 4.0252(3) Å) fired at 1200 °C were refined using the Bruker Topas software suite and agree with previously reported results (*23*). TGA and elemental analysis via EDS both confirmed phase pure oxygen stoichiometric $BaSnO_3$ and $SrSnO_3$ starting materials.

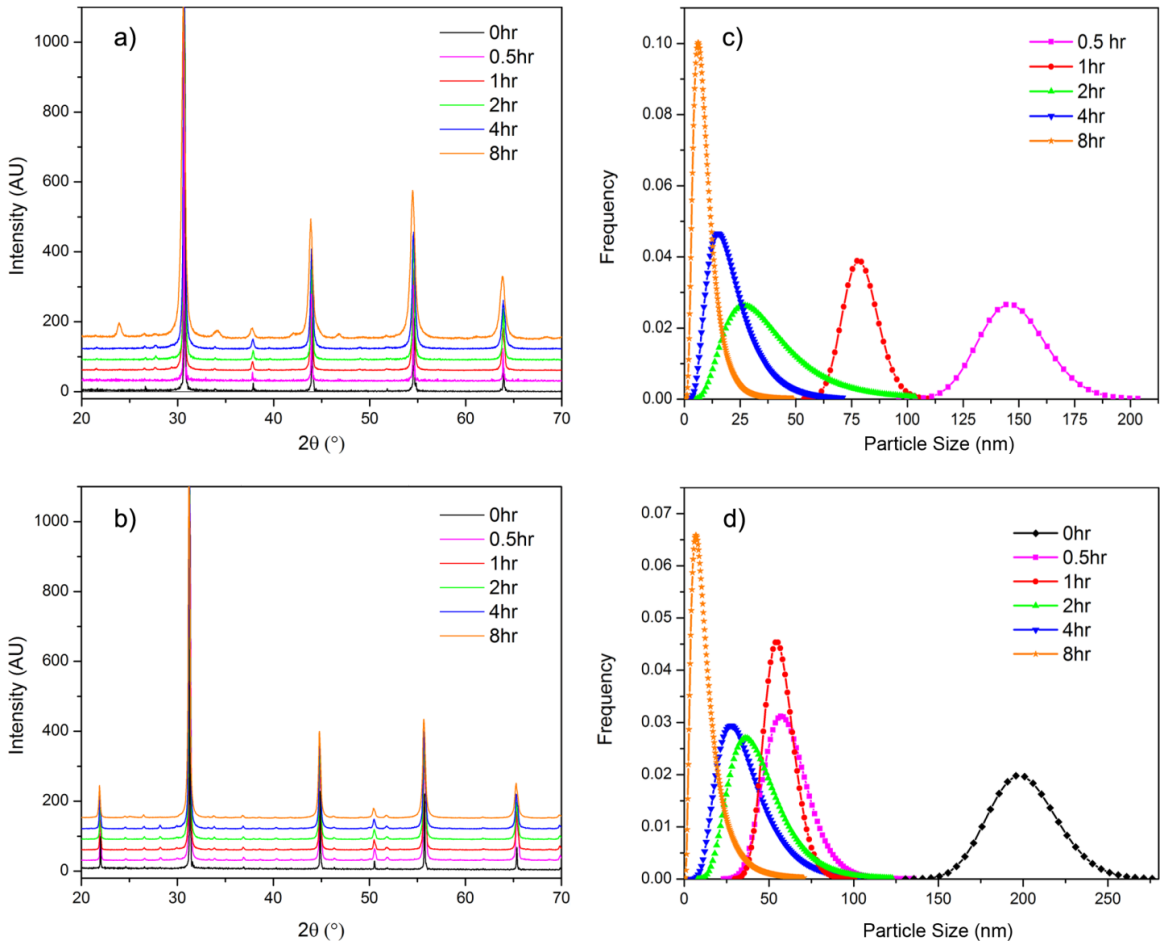

Figure 5-1. Powder x-ray diffraction patterns of a) $BaSnO_3$ and b) $SrSnO_3$, as well as the corresponding calculated particle size distributions in c) and d), respectively.

Microstructure and particle size analysis of the ceramic compounds were completed using the PM2K and TOPAS software suites, calculating particles sizes of 680 ± 400 nm and 201 ± 246 nm, and strain values of 0.0072% and 0.0113% for un-milled, ceramic $BaSnO_3$ and $SrSnO_3$, respectively. These results were verified with TEM imaging showing overall cubic particles with a large size

variance. The particle size values agree with those previously reported in the ternary stannate ceramics literature (*24*).

The ball milling conditions, extracted particle sizes, and calculated crystallite strain values of ceramic $BaSnO_3$ and $SrSnO_3$ samples milled for different times ranging from 30 minutes to 8 hours are listed in Table 5-1. As expected, the extracted average particle size is inversely related to milling time, culminating in particles of sub 20 nanometer size (Figure 5-1) - ideal for applications in the nano-tech industry, such as in solar cells, battery materials, and fuel cells (*25*). Microstructural strain associated with the $ASnO_3$ stannates milled for different time lengths was investigated using the Williamson-Hall plots ($B\cos(\theta)$ vs $\sin(\theta)$), shown in Figure 5-2. The slope of the fitted line is directly related to the strain of the material, given by the equation:

$$B\cos(\theta) = \frac{\lambda}{D_v} + 4\varepsilon_s \sin(\theta) \qquad (5\text{-}5)$$

where D_V is the average diameter (nm) and ε_S is the crystallite strain (*26*).

Table 5-1. Particle sizes and crystallite strain values calculated using the PM2K software for $BaSnO_3$ and $SrSnO_3$ samples milled for different time periods.

Milling (hr)	Particle Size (nm)		ε_{str}	
	$BaSnO_3$	**$SrSnO_3$**	**$BaSnO_3$**	**$SrSnO_3$**
0	680 ± 400	201 ± 246	0.00715	0.00817
0.5	147 ± 44	62 ± 16	0.03808	0.04798
1	94 ± 30	56 ± 23	0.04921	0.11225
2	32 ± 17	45 ± 22	0.07343	0.12566
4	24 ± 21	37 ± 19	0.14135	0.14105
8	9.4 ± 2	14 ± 4	0.18133	0.18939

Multiple hkl indices were analyzed for both samples out to 85° 2Θ There is a variable amount of scatter away from the fitting lines, especially at longer milling times, which is indicative of anisotropic microstructural characteristics that can be a result of high-impact ball milling. The non-superimposible nature of the fitting lines lend credence to the fact that after milling, non-cuboid particles resulted. The extracted strain values for the twelve compounds are listed in Table 5-1, clearly following a constant trend of higher strain under longer milling conditions.

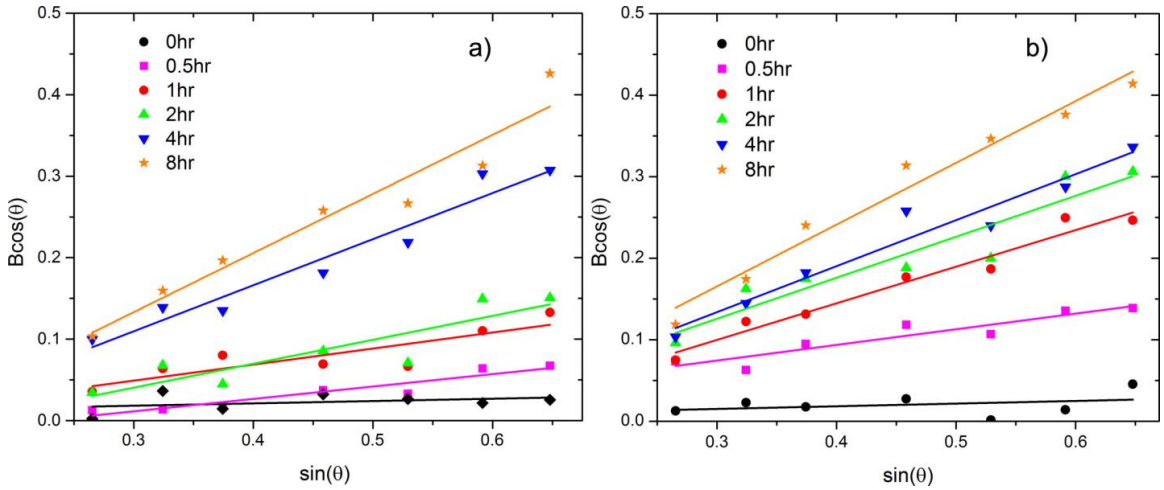

Figure 5-2. Williamson-Hall plots of a) $BaSnO_3$ and b) $SrSnO_3$ obtained using the WPPM methods. The particle strain can be extracted from the slope of the line using equation (5-5).

5.2c Direct control over size and strain with annealing

After milling for 8 hours, samples of both $BaSnO_3$ and $SrSnO_3$ were subjected to thermal annealing (200 °C - 1000 °C) for 24 hours. The powder diffraction patterns were analyzed to extract both average crystallite size and crystallite strain after thermal annealing (Table 5-2 and Figure 5-3). As the annealing temperature increased from 200 °C to 600 °C, crystallite strain decreased 38% and 44% for $BaSnO_3$ and $SrSnO_3$ respectively. From 600 °C to the highest thermal treatment temperature, 1000 °C, crystallite strain decreased 58% and 28%, resulting in a total crystallite strain reduction of 71% and 59% for $BaSnO_3$ and $SrSnO_3$, respectively. Thermal annealing was reproducible and verified by TEM microscopy measurements, shown in Figure 5-4.

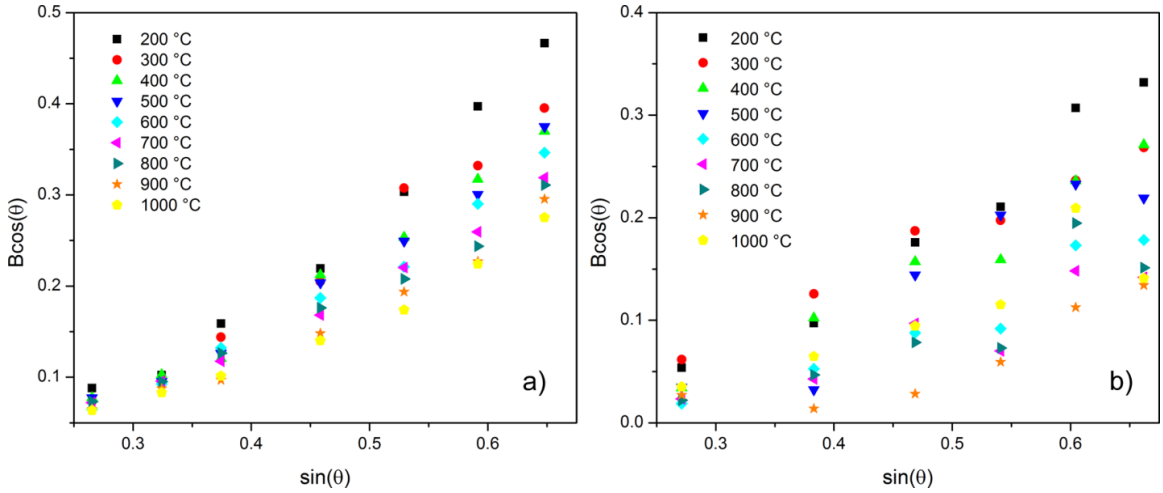

Figure 5-3. Williamson-Hall plots of $BaSnO_3$ and $SrSnO_3$ particles after thermal annealing for 24 hrs at various temperatures. The particle strain can be extracted from the slope of the line using equation (5-5).

Current DSSCs utilize nanometer size metal-oxide films that have been coated with a light-absorbing dye to facilitate the conversion of solar energy to electrical energy via photon capture by the dye, followed by relaxation and elecron injection into the metal-oxide substrate. In recent literature, the relationships between particle size and electron diffusion coefficients, as well as recombination lifetimes have been studied by numerous prominent groups (*15*, *27*, *28*). The Yanagida group in Japan correlated a smaller TiO_2 particle size to increased effective light absorption of the cell due to the larger surface area, leading to an increase in the number of photogenerated electrons (*15*). As the TiO_2 particle size approached 14 nm, both the charge injection efficiency and a shorter diffusion length caused efficiency losses in the cell. The ability to control the particle size of the metal-oxide

film is paramount when attempting to optimize the electron diffusion coefficients, recombination lifetimes, and effective light absorption of a DSSC. During the thermal treatment study, particular attention was paid to the effect of temperature on both particle size and strain of the crystallites. The information on controlling particle size and strain gleaned from this study can be used to directly increase the efficiency of DSSCs.

5.2d Concluding remarks and observations

The ability to specifically control crystallite size has been shown to be an invaluable tool in the development of cutting-edge materials technology, including solar cells. In this paper, we have shown that the precise control of the particle size of $ASnO_3$ (A = Ba, Sn) can be accomplished using simple solid state methods. Both particle size and crystallite strain were extracted from the powder diffraction patterns by employing the WPPM algorithm via the PM2K software. This allowed for a systematic approach to decreasing overall crystallite strain while maintaining sub-hundred nm particle sizes. This technique can be easily extended to specifically fabricate other technologically useful materials to investigate the properties of different particle sizes and strains.

Table 5-2. Particle sizes and crystallite strain values calculated using the PM2K software for $BaSnO_3$ and $SrSnO_3$ samples thermally treated for 24 hours at varied temperatures.

Temp. (°C)	Particle Size (nm)		E_{str}	
	$BaSnO_3$	**$SrSnO_3$**	**$BaSnO_3$**	**$SrSnO_3$**
200	15 ± 6	13 ± 5	0.20068	0.18795
300	14 ± 2	20 ± 12	0.15872	0.14559
400	22 ± 14	49 ± 35	0.18002	0.14657
500	24 ± 10	51 ± 12	0.15574	0.14748
600	51 ± 28	46 ± 15	0.12521	0.10604
700	59 ± 13	63 ± 38	0.12009	0.08103
800	60 ± 25	81 ± 27	0.12910	0.08083
900	58 ± 12	108 ± 56	0.05360	0.07510
1000	63 ± 44	128 ± 95	0.05192	0.07646

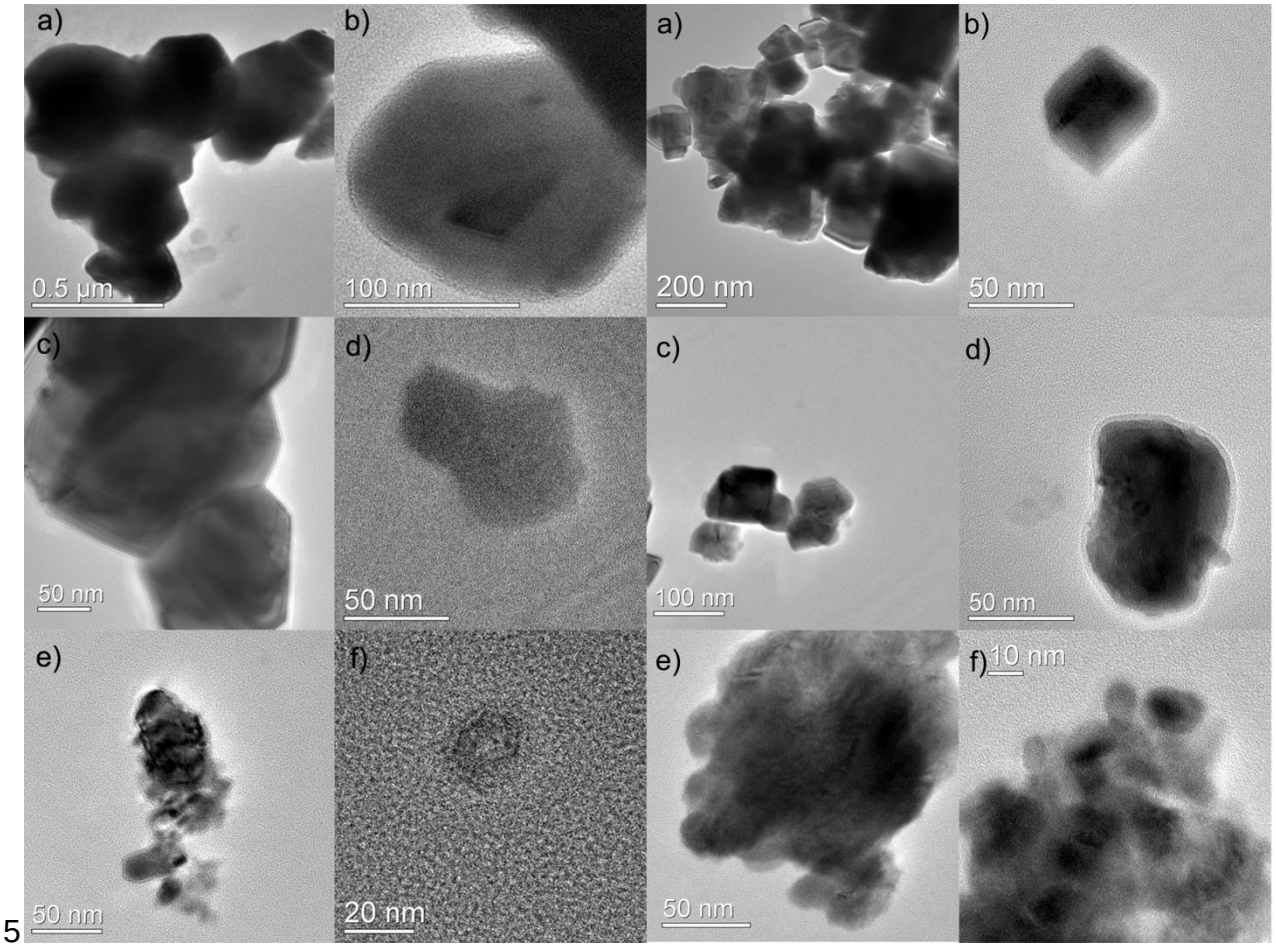

Figure 5-4. The left 6 TEM micrograms represent $BaSnO_3$, while the right 6 vertical panels show $SrSnO_3$ particles. The labels a) - f) refer to milling times: a) none, b) 30 min, c) 1 hr, d) 2 hr, e) 4hr, and f) 8 hr.

5.3 Using WPPM to characterize synthesized nanoparticle

As previously shown, WPPM methods work well to describe particles greater in size than 15 nm produced by impact milling, which results in very broad peaks due to the decrease in particle size and the introduction of multiple forms of strain to the crystallites. This second study looks at the efficacy of WPPM when the particles are nanosized and essentially free of strain. The following synthesis was in collaboration with Dr. Jahangeer Ahmed.

5.3a Direct synthesis of stannate nanoparticles

$ASnO_3$ nanoparticles (A = Ba or Sr) were synthesized using the microemulsion method via two procedures. In procedure I, one microemulsion system was composed of (1-hexadecyl) trimethylammonium bromide as the surfactant, 1-butanol as the co-surfactant, 2,2,4-trimethylpentane as the oil phase, and 0.1M of $Ba(NO_3)_2$ or $Sr(NO_3)_2$ and 0.1M of $SnCl_4$ as the aqueous phases. The second microemulsion system had an identical composition, with the exception of the aqueous phase, which was NH_4OH (28% of NH_3). The above two microemulsions were mixed slowly on a magnetic stirrer before adding 0.5 M ammonium carbonate drop by drop to maintain the stoichiometry of the loaded reactions at room temperature. The resulting precipitates were centrifuged and washed several times with a methanol and chloroform mixture (1:1 ratio) to remove the organic moieties and dried at 80 °C for 2 hrs. Powder X-ray diffraction patterns show that ACO_3 (A = Ba or Sr) was obtained with orthorhombic crystal structure and

amorphous tin based compound. The above product was used a precursor for the synthesis of $ASnO_3$ (A = Ba or Sr) nanoparticles at 650 °C.

In procedure II, microemulsion one had the same composition as the first procedure, while the second contained an aqueous phase of 0.5 M $(NH_4)_2CO_3$ rather than NH_4OH (28% of NH_3). The resulting precipitate was centrifuged and washed as given above. These precipitates were used as a precursor for the synthesis of $ASnO_3$ (A = Ba or Sr) nanoparticles at 650 °C.

The amorphous tin component and barium carbonate obtained after centrifugation from the first procedure was annealed at 650 °C in air for 60 hrs, resulting in the formation of $BaSnO_3$ nanoparticles with a small amount of impurity (3 %). All reflections of the pattern could be indexed on the basis of a cubic unit cell. The cell parameter was refined using the Bruker Topas software suite, and the refined lattice parameter of the $BaSnO_3$ nanoparticles was found to be 4.116(3) Å, which closely matches with the lattice parameter previously reported (*14*). Thermal analysis of the synthesized precursors under flowing oxygen shows a weight loss corresponding to one water molecule and one molecule of carbon dioxide. The final decomposed product was analyzed as $BaSnO_3$.

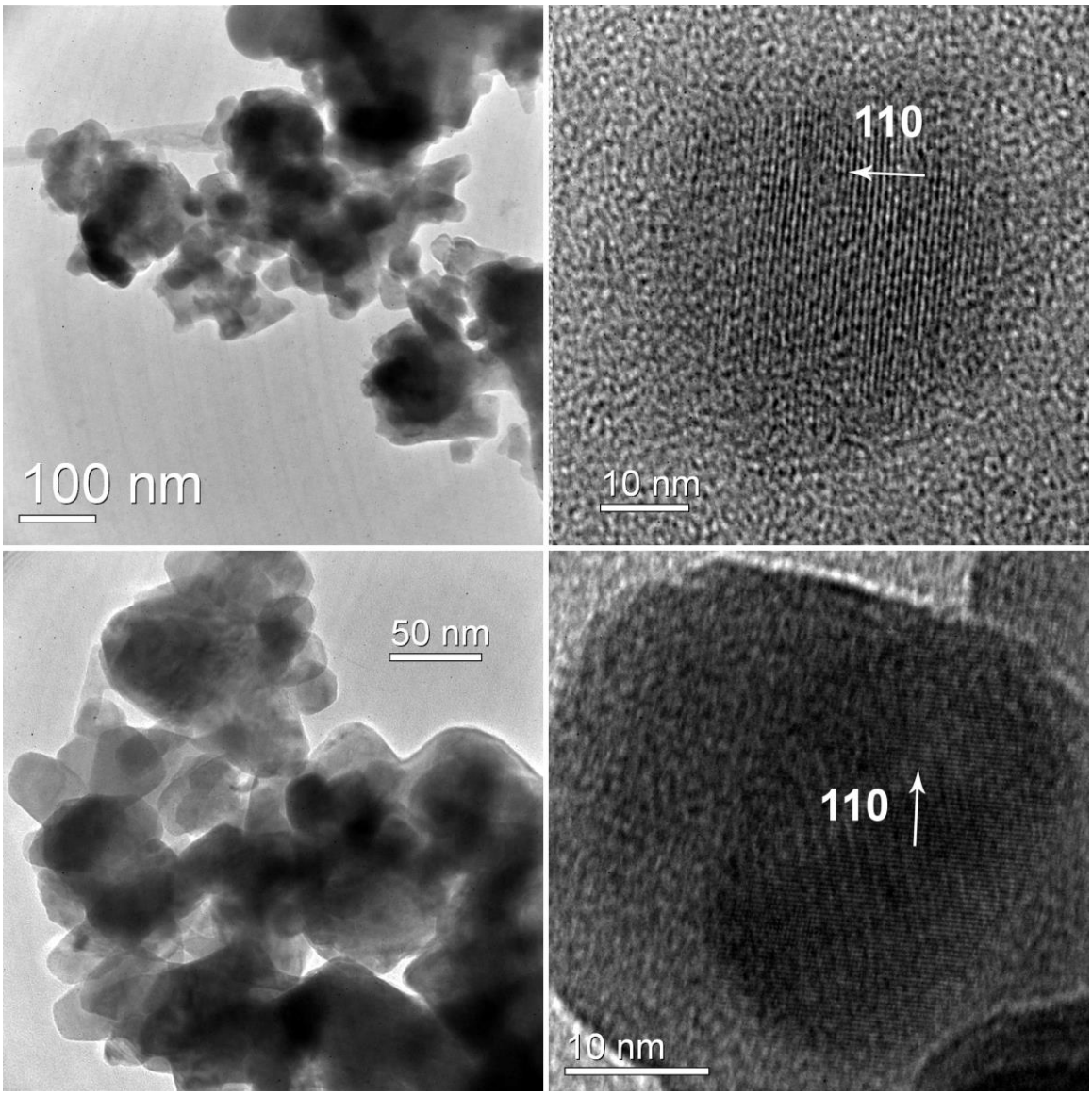

Figure 5-5. TEM (top, left) and HRTEM (top, right) micrographs of $BaSnO_3$ nanoparticles synthesized using procedure I, and TEM (bottom, left) and HRTEM (bottom, right) micrographs of $BaSnO_3$ nanoparticles synthesized using procedure II. Both materials were fired at 650 °C for 60 hrs.

5.3b Microscopy investigation of particle size

Figure 5-5 shows the TEM micrographs of the synthesized $BaSnO_3$ nanoparticles using both procedures. The microscopy studies showed the formation of spherical shaped nanoparticles with an average size of 15 nm. High resolution transmission electron microscopic (HRTEM) studies confirm the formation of nanospheres of $BaSnO_3$ particles with a lattice spacing of 2.916 Å, which is consistent with that of the (110) plane of $BaSnO_3$. The average size of the barium stannate nanoparticles obtained at 650 °C via the second procedure was found to be ~ 40 nm. The HRTEM image of the nanoparticle obtained via the second procedure with a fringe value was consistent with the 110 plane of $BaSnO_3$.

Similarly, TEM micrographs for $SrSnO_3$ are represented in Figure 5-6. TEM studies show the formation of $SrSnO_3$ nanoparticles with an average size of 25 nm. The long aging time of the reaction may be responsible for the agglomeration of the nanoparticles.

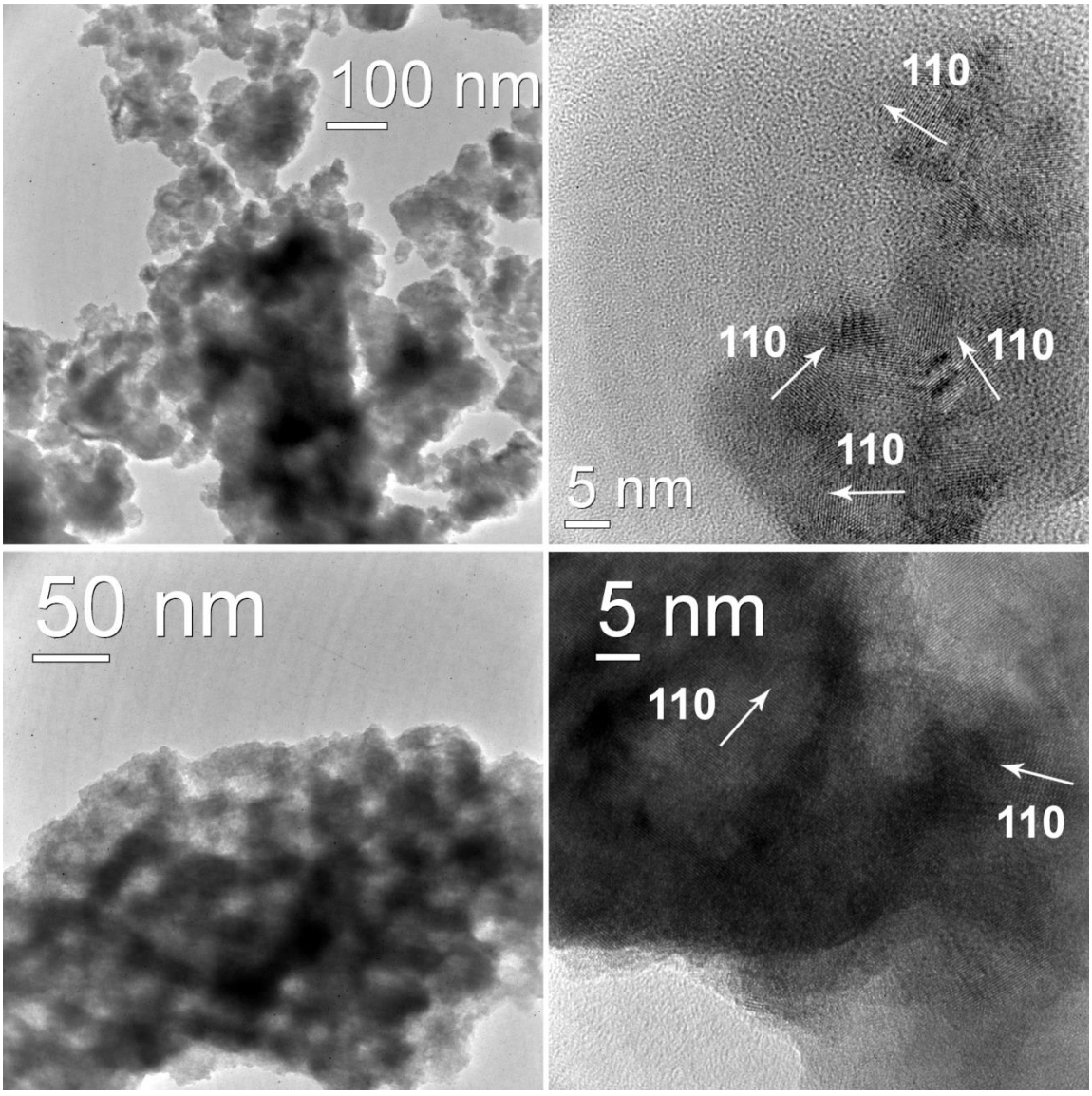

Figure 5-6. (a) & (b) TEM and HRTEM micrographs of $SrSnO_3$ nanoparticles synthesized at 650 °C for 72 hr (obtained from procedure I), (c) & (b) TEM and HRTEM micrographs of $SrSnO_3$ nanoparticles.

5.3c Particle size distributions of stannate nanoparticles

PXD patterns for both $BaSnO_3$ and $SrSnO_3$ were obtained on the same instrument with identical experimental setups. The patterns were initially refined based on ICSD entries 43138 and 27047 for $BaSnO_3$ and $SrSnO_3$ respectively, using the Bruker Topas software suite. Using the indexing obtained from these refinements, the spectra were loaded into the PM2K program with an input file specifying the Caglioti parameters previously established, the cell parameters of the respective phases, a function to refine zero error and sample displacement, a four parameter Chebyshev background function, and the peak indices and relative intensities. All variables except for the background, peak intensities, and sample displacement were initially locked and then released over a series of iterations to obtain a final whole pattern refinement. Once a suitable refinement fit value was obtained, a lognormal size distribution function was added to the input file, resulting in the size distribution shown in Figure 5-7.

Particle size distributions of 15.8 ± 4.2 and 18.4 ± 8.3 were calculated for $BaSnO_3$ and $SrSnO_3$ respectively, using PM2K. The results obtained from the WPPM algorithm agreed well with the TEM particle size analysis shown in Figure X, validating the use of WPPM as a tool for calculating particle size distribution on cubic as-prepared nanoparticles with simple crystal morphology.

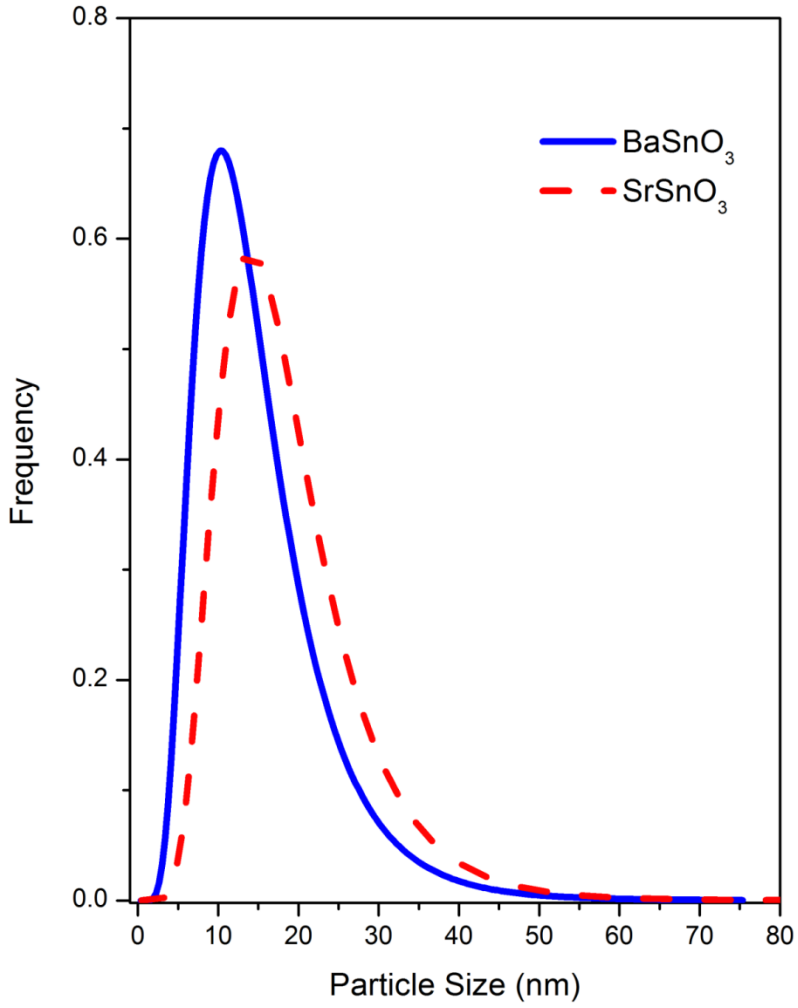

Figure 5-7. Particle size distributions of the prepared $BaSnO_3$ and $SrSnO_3$ nanoparticles obtained using the WPPM method.

5.4 Efficacy of WPPM on lower symmetry oxides

The previous two case studies on the use of WPPM have focused on highly symmetric cubic oxide particles of varying sizes. The following study on delafossite $CuAlO_2$ nanoparticles investigates the modeling functions on much lower symmetry materials, where preferred orientation can also lead to large peak asymmetry. The synthesis of the nanoparticles was in collaboration with Dr. Jahangeer Ahmed.

5.4a Introduction to delafossite type $CuAlO_2$

Delafossite $CuAlO_2$ belongs to a family of transparent conducting oxides (TCOs) - oxides with low electrical resistivity and high visual light transparency - that show promise in multiple applications including liquid crystal displays, touch screens, gas sensors, thermoelectric devices, solar cells, dilute magnetic semiconductors, light-emitting diodes, etc (*29*–*34*). $CuAlO_2$ nanoparticles have also been used as thermo-catalysts in the thermal photo-catalytic reactions for the evolution of hydrogen gas from water splitting (*33*). The most well-known TCOs, ZnO and In_2O_3, are n-type semiconductors; therefore, the synthesis of a p-type conducting oxide allows for the preparation of p-n junctions - the source of many interesting semiconductor properties in cutting edge technology (*35*, *36*). Essentially, a p-n junction photovoltaic using $CuAlO_2$ and In_2O_3 would allow visible light to pass through the cell while producing electricity via the absorption of ultraviolet radiation (*37*).

$CuAlO_2$ has a layered crystal structure with Cu atoms between AlO_2 layers forming O-Cu-O pillars (*38*). $CuAlO_2$ has indirect and direct band gaps of 1.2 and 3.6 eV respectively, high transparency (80%) in the visible region, and high light-to-electricity conversion efficiencies in solar cells (*31*, *39*). Photocurrents ranging from 0.02 mA/cm^2 to 0.08 mA/cm^2 have been observed when $CuAlO_2$ nanoparticles (300 nm) were used as the photocathode materials in p-type DSSCs, while delafossite $CuGaO_2$ nanoplates produced comparatively high photocurrents (0.384 mA/cm^2) in the region of visible light using polypyridyl $Co^{3+/2+}$(dtb-bpy) as the electrolyte and the organic P1 dye (*38*, *40*).

Delafossite $CuAlO_2$ is thermodynamically unstable below 1000 °C in air, easily decomposing to the Cu^{2+} compounds CuO and $CuAl_2O_4$ under these conditions (*41*). Synthesis of polycrystalline $CuAlO_2$ is typically achieved by firing a stoichiometric mixture of Al_2O_3 and Cu_2O at 1100 °C under argon or air atmosphere.

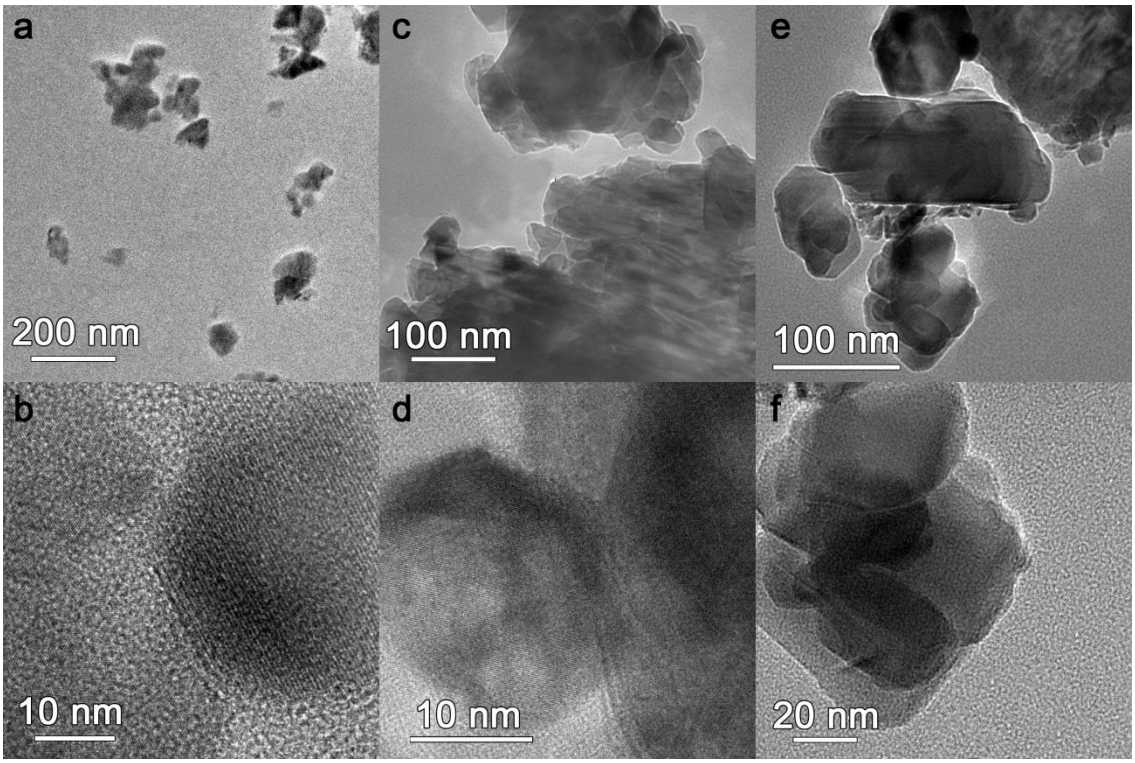

Figure 5-8. Transmission electron microscopy pictures of $CuAlO_2$ nanoparticles prepared at 775 °C under a controlled partial oxygen pressure atmosphere (a,b), 800 °C under ultrapure N_2 (c,d), and 950 °C under ultrapure N_2 (e,f).

Various techniques have been used to produce $CuAlO_2$ nanoparticles including sol-gel, mechanical alloying, hydrothermal, field emission process, and electro-spinning methods (*32*, *42–44*). $CuAlO_2$ nanostructured semiconducting materials were synthesized by using boehmite (ϒ-AlOOH) nanorods loaded with Cu(II) acetate as a nanoprecursor at 1150 °C in air (*30*). $CuAlO_2$ nanowires (50 nm diameter) and nanoparticles (35 nm) were produced via a porous anodic alumina oxide (AAO) template at 900 °C and citrate route at 1000 °C, respectively (*45*).

Considering that most syntheses reported require very high reaction temperatures (> 1000 °C) or complex instrumentation or templating, the production of bulk quantities of pure phase $CuAlO_2$ nanoparticles is still a serious challenge.

5.4b Synthesis of nanoparticle $CuAlO_2$

Aqueous solutions of 0.1 M $Cu(NO_3)_2 \cdot 2.5H_2O$ and 0.1 M $Al(NO_3)_3 \cdot 9H_2O$ were mixed in stoichiometric amounts and then transferred to a porcelain crucible containing citric acid (0.15 mol) and ethylene glycol (10 ml). Initially, a sky blue transparent solution was apparent. The solution was allowed to gel for three days at room temperature before being undergoing thermal treatment at 350 °C for 6 hr in air to remove the chelating organics, which resulted in a fine black powder of copper (II) oxide and an amorphous aluminum based compound as determined by PXD. The fine black powders were then fired at 775 °C for 12 hrs in air, leading to the formation of CuO and $CuAl_2O_4$. This product was further treated at 800 °C in ultrapure N_2 for 48 hr, affording pure $CuAlO_2$ nanoparticles.

5.4c Particle size distribution of $CuAlO_2$ nanoparticles

A lognormal size distribution of spherical nanoparticles was used as previously described (Equation 5-2). The results obtained from the WPPM algorithm showed uniform size distribution, as well as strong correlation with the TEM studies (Figure 5-8). The average sizes of the $CuAlO_2$ nanoparticles were calculated to be 35 ± 9 nm for the $CuAlO_2$ nanoparticles prepared at 775 °C under controlled partial

oxygen pressure, 39 ± 14 nm for the nanoparticles prepared at 800 °C under ultrapure N_2, and 43 ± 17 nm for the $CuAlO_2$ nanoparticles prepared at 950 °C under ultrapure N_2 (Figure 5-9). These values agree well with the particle sizes observed from microscopy measurements; however, the WPPM method appears to give the shortest length for anisotropic crystallite sizes.

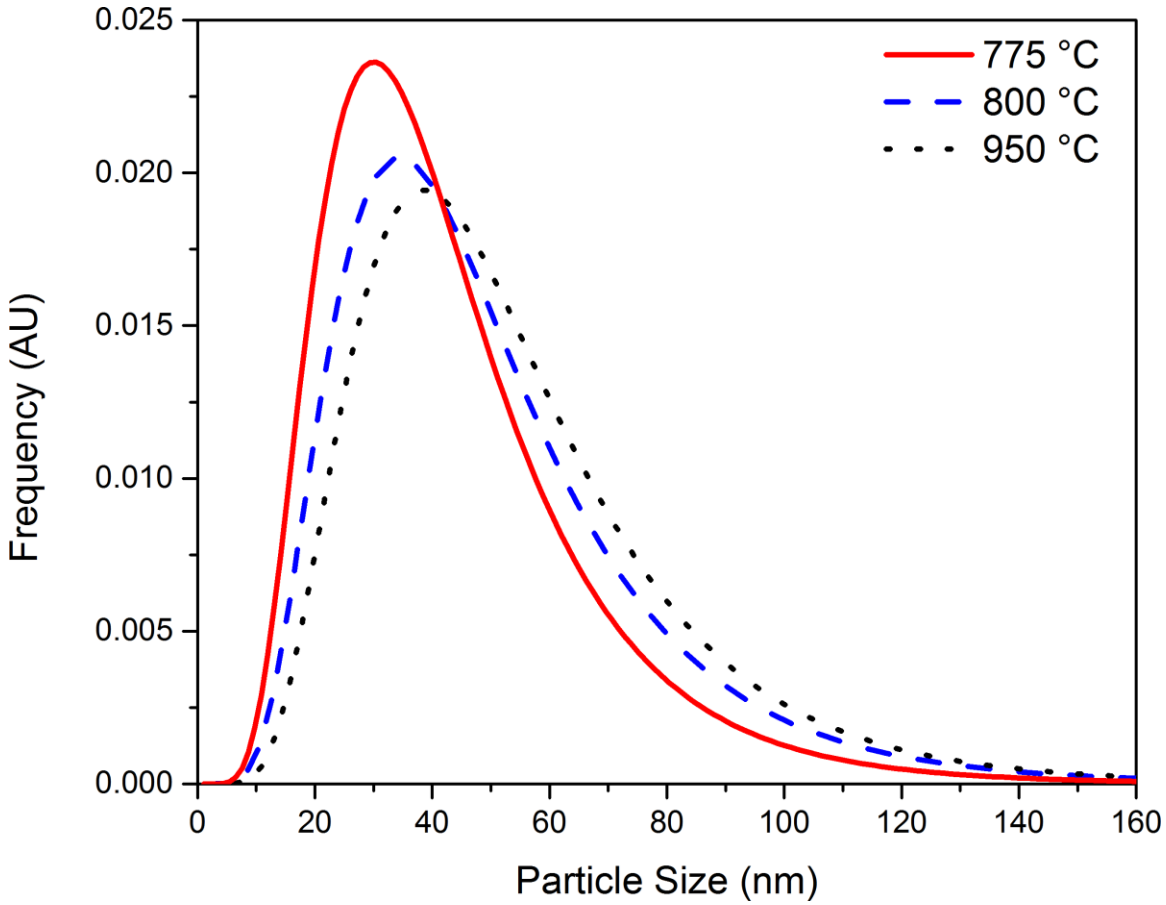

Figure 5-9. Particle size distribution of $CuAlO_2$ nanoparticles prepared at 775 °C, 800 °C, and 950 °C. Distribution plots calculated using the PM2K software package.

5.5 Chapter conclusions

The WPPM method as implemented in PM2K is much more effective at calculating the particle size of both nano- and micro-sized particles than the Scherrer formula, as shown in the three case studies presented. TEM micrograms were used as experimental proof that the particle size distributions calculated using WPPM were accurate. In conclusion, a combination of WPPM and controlled thermal annealing may allow for very precise control over both particle size and strain of nanoparticles used in advanced functional materials.

REFERENCES

REFERENCES

(1) Leoni, M.; Scardi, P. Nanocrystalline domain size distributions from powder diffraction data research papers. *J. Appl. Crystallogr.* **2004**, *37*, 629–634.

(2) Patterson, A. The Scherrer Formula for X-Ray Particle Size Determination. *Phys. Rev.* **1939**, *56*, 978–982.

(3) Leoni, M.; Confente, T.; Scardi, P. PM2K: a flexible program implementing Whole Powder Pattern Modelling. *Zeitschrift für Krist. Suppl.* **2006**, *2006*, 249–254.

(4) Lampe, U.; Gerblinger, J.; Meixner, H. Carbon-monoxide sensors based on thin films of $BaSnO_3$. *Sensors Actuators B Chem.* **1995**, *25*, 657–660.

(5) Chu, X. Dilute CH_3SH-sensing characteristics of $BaSnO_3$ thick film sensor. *Mater. Sci. Eng. B* **2004**, *106*, 305–307.

(6) Ostrick, B.; Fleischer, M.; Lampe, U.; Mexines, H. Preparation of stoichiometric barium stannate thin films: Hall measurements and gas sensitivities. *Sensors Actuators B Chem.* **1997**, *44*, 601–606.

(7) Hodjati, S.; Vaezzadeh, K.; Petit, C.; Pitchon, V.; Kiennemann, a. NO_x sorption–desorption study: application to diesel and lean-burn exhaust gas (selective NO_x recirculation technique). *Catal. Today* **2000**, *59*, 323–334.

(8) Deepa, A. S.; Vidya, S.; Manu, P. C.; Solomon, S.; John, A.; Thomas, J. K. Structural and optical characterization of $BaSnO_3$ nanopowder synthesized through a novel combustion technique. *J. Alloys Compd.* **2011**, *509*, 1830–1835.

(9) Yuan, Y.; Lv, J.; Jiang, X.; Li, Z.; Yu, T.; Zou, Z.; Ye, J. Large impact of strontium substitution on photocatalytic water splitting activity of $BaSnO_3$. *Appl. Phys. Lett.* **2007**, *91*, 094107.

(10) Mizoguchi, H.; Woodward, P. M.; Park, C.-H.; Keszler, D. a. Strong near-infrared luminescence in $BaSnO_3$. *J. Am. Chem. Soc.* **2004**, *126*, 9796–800.

(11) Bao, M.; Li, W.; Zhu, P. Study on the dielectric properties of oxide-doped $Ba(Ti,Sn)O_3$ ceramics prepared from ultrafine powder. *J. Mater. Sci.* **1993**, *28*, 6617–6621.

(12) Udawatte, C. P.; Yoshimura, M. Preparation of well-crystallized $BaSnO_3$ powders under hydrothermal conditions. *Mater. Lett.* **2001**, *47*, 7–10.

(13) Udawatte, C. P.; Kakihana, M.; Yoshimura, M. Preparation of pure perovskite-type $BaSnO_3$ powders by the polymerized complex method at reduced temperature. *Solid State Ionics* **1998**, *108*, 23–30.

(14) Pfaff, G. Wet chemical synthesis of $BaSnO_3$ and Ba_2SnO_4 powders. *J. Eur. Ceram. Soc.* **1993**, *12*, 159–164.

(15) Nakade, S.; Saito, Y.; Kubo, W.; Kitamura, T.; Wada, Y.; Yanagida, S. Influence of TiO_2 Nanoparticle Size on Electron Diffusion and Recombination in Dye-Sensitized TiO_2 Solar Cells. *Society* **2003**, 8607–8611.

(16) Hoffmann, M. J.; Hammer, M.; Endriss, A.; Lupascu, D. C. Correlation between microstructure, strain behavior, and acoustic emission of soft PZT ceramics. *Acta Mater.* **2001**, *49*, 1301–1310.

(17) Audebrand, N.; Auffrédic, J.-P.; Louër, D. An X-ray Powder Diffraction Study of the Microstructure and Growth Kinetics of Nanoscale Crystallites Obtained from Hydrated Cerium Oxides. *Chem. Mater.* **2000**, *12*, 1791–1799.

(18) Audebrand, N.; Auffre, J.; Loue, D. X-ray Diffraction Study of the Early Stages of the Growth of Nanoscale Zinc Oxide Crystallites Obtained from Thermal Decomposition of Four Precursors. General Concepts on Precursor-Dependent Microstructural Properties. *Society* **1998**, *4756*, 2450–2461.

(19) Lu, W.; Schmidt, H. Hydrothermal synthesis of nanocrystalline $BaSnO_3$ using a SnO2•xH2O sol. *J. Eur. Ceram. Soc.* **2005**, *25*, 919–925.

(20) Scardi, P.; Leoni, M. Diffraction line profiles from polydisperse crystalline systems. *Acta Crystallogr. Sect. A Found. Crystallogr.* **2001**, *57*, 604–613.

(21) Caglioti, G.; Paoletti, A.; Ricci, F. P. Choice of collimators for a crystal spectrometer for neutron diffraction. *Nucl. Instruments* **1958**, *3*, 223–228.

(22) *Diffraction Analysis of the Microstructure of Materials*; Mittemeijer, E. J.; Scardi, P., Eds.; Springer Berlin Heidelberg: Berlin, Heidelberg, 2004; Vol. 68.

(23) Azad, A.; Hashim, M.; Baptist, S. Phase evolution and microstructural development in sol-gel derived $MSnO_3$ (M = Ca , Sr and Ba). *Mater. Sci.* **2000**, *5*, 5475 – 5483.

(24) Azad, A.-M.; Liew, L.; Shyan, W.; Yen, P. T. Synthesis, processing and microstructural characterization of $CaSnO_3$ and $SrSnO_3$ ceramics. *J. Alloys Compd.* **1999**, *282*, 109–124.

(25) Sharma, N.; Shaju, K. M.; Rao, G. V. S.; Chowdari, B. V. R. Anodic behaviour and X-ray photoelectron spectroscopy of ternary tin oxides. *J. Power Sources* **2005**, *139*, 250–260.

(26) Williamson, G.; Hall, W. X-Ray Line Broadening from Filed Aluminum and Wolfram. *Acta Metall.* **1953**, *1*, 22–31.

(27) Films, T.; Wallenberg, R.; Hagfeldt, A.; Sundstrom, V.; Yartsev, A. P. Particle Size and Crystallinity Dependent Electron Injection in Fluorescein 27-Sensitized TiO_2 Films*. Phys. Chem. B* **2003**, 1370–1375.

(28) O'Hayre, R.; Nanu, M.; Schoonman, J.; Goossens, A.; Wang, Q.; Grätzel, M. The Influence of TiO_2 Particle Size in TiO_2/$CuInS_2$ Nanocomposite Solar Cells. *Adv. Funct. Mater.* **2006**, *16*, 1566–1576.

(29) Vanaja, K. A.; Ajimsha, R. S.; Asha, A. S.; Jayaraj, M. K. p-type electrical conduction in α-$AgGaO_2$ delafossite thin films. *Appl. Phys. Lett.* **2006**, *88*, 212103.

(30) Thu, T. V.; Thanh, P. D.; Suekuni, K.; Hai, N. H.; Mott, D.; Koyano, M.; Maenosono, S. Synthesis of delafossite $CuAlO_2$ p-type semiconductor with a nanoparticle-based Cu(I) acetate-loaded boehmite precursor. *Mater. Res. Bull.* **2011**, *46*, 1819–1827.

(31) Ghosh, C. K.; Popuri, S. R.; Mahesh, T. U.; Chattopadhyay, K. K. Preparation of nanocrystalline $CuAlO_2$ through sol–gel route. *J. Sol-Gel Sci. Technol.* **2009**, *52*, 75–81.

(32) Li, G.; Zhu, X.; Lei, H.; Jiang, H.; Song, W.; Yang, Z.; Dai, J.; Sun, Y.; Pan, X.; Dai, S. Preparation and characterization of $CuAlO_2$ transparent thin films prepared by chemical solution deposition method. *J. Sol-Gel Sci. Technol.* **2010**, *53*, 641–646.

(33) Smith, J.; Van Steenkiste, T.; Wang, X.-G. Thermal photocatalytic generation of H_2 over $CuAlO_2$ nanoparticle catalysts in H_2O. *Phys. Rev. B* **2009**, *79*, 041403.

(34) Zheng, X. G.; Taniguchi, K.; Takahashi, A.; Liu, Y.; Xu, C. N. Room temperature sensing of ozone by transparent p-type semiconductor $CuAlO_2$. *Appl. Phys. Lett.* **2004**, *85*, 1728.

(35) Ferromagnetism, R.; Lu, Y.; Hsu, Y. Cu^{2+} doped ZnO Nanocrystals: Visible-Light-Driven Photoactivity and. *Society* **2011**, *104*, 2418.

(36) Libera, J. A.; Hryn, J. N.; Elam, J. W. Indium Oxide Atomic Layer Deposition Facilitated by the Synergy between Oxygen and Water. *Energy* 60439.

(37) Robertson, J.; Gillen, R.; Clark, S. J. Advances in understanding of transparent conducting oxides. *Thin Solid Films* **2012**, *520*, 3714–3720.

(38) Yu, M.; Natu, G.; Ji, Z.; Wu, Y. p-Type Dye-Sensitized Solar Cells Based on Delafossite $CuGaO_2$ Nanoplates with Saturation Photovoltages Exceeding 460 mV. **2012**.

(39) Gillen, R.; Robertson, J. Band structure calculations of $CuAlO_2$, $CuGaO_2$, $CuInO_2$, and $CuCrO_2$ by screened exchange. *Phys. Rev. B* **2011**, *84*, 035125.

(40) Nattestad, A. Dye-sensitized $CuAlO_2$ photocathodes for tandem solar cell applications. *J. Photonics Energy* **2011**, *1*, 011103.

(41) Kumekawa, Y.; Hirai, M.; Kobayashi, Y.; Endoh, S.; Oikawa, E.; Hashimoto, T. Evaluation of thermodynamic and kinetic stability of $CuAlO_2$ and $CuGaO_2$. *J. Therm. Anal. Calorim.* **2009**, *99*, 57–63.

(42) Deng, Z.; Zhu, X.; Tao, R.; Dong, W.; Fang, X. Synthesis of $CuAlO_2$ ceramics using sol-gel. *Mater. Lett.* **2007**, *61*, 686–689.

(43) Banerjee, A. N.; Maity, R.; Chattopadhyay, K. K. Preparation of p-type transparent conducting $CuAlO_2$ thin films by reactive DC sputtering. *Mater. Lett.* **2004**, *58*, 10–13.

(44) Zhao, S.; Li, M.; Liu, X.; Han, G. Synthesis of $CuAlO_2$ nanofibrous mats by electrospinning. *Mater. Chem. Phys.* **2009**, *116*, 615–618.

(45) Mo, R.; Liu, Y. Synthesis and properties of delafossite $CuAlO_2$ nanowires. *J. Sol-Gel Sci. Technol.* **2010**, *57*, 16–19.